

Copyright  
by  
Seung Ryul Na  
2015

**The Dissertation Committee for Seung Ryul Na Certifies that this is the approved  
version of the following dissertation:**

**Molecular Level Interactions of Large Area 2D-Materials**

**Committee:**

---

Kenneth M. Liechi, Supervisor

---

Rui Huang

---

K. Ravi-Chandar

---

Nanshu Lu

---

Rodney S. Ruoff

**Molecular Level Interactions of Large Area 2D-Materials**

**by**

**Seung Ryul Na, B.E.; M.S.**

**Dissertation**

Presented to the Faculty of the Graduate School of

The University of Texas at Austin

in Partial Fulfillment

of the Requirements

for the Degree of

**Doctor of Philosophy**

**The University of Texas at Austin**

**May 2015**

## **Dedication**

To my family



## **Acknowledgements**

The author would like to express sincere appreciation to his supervisor, Professor Kenneth M. Liechti for his valuable technical and personal guidance and for the freedom to try any interesting experiment. Whenever the author met to discuss experimental difficulties, his broad experience and insightful ideas turned into breakthroughs in my experiments. Being a Ph.D. student in Dr. Liechti's group was indeed a great honor.

The author would like to thank Professor Rui Huang, Professor K. Ravi-Chandar, Nanshu Lu and Professor Rodney S. Ruoff. I am grateful to Professor Rui Huang for his passionate interest and suggestions for my research work. His ideas hit the mark, resulting in significant improvements in my research. I am grateful to Professor Ravi-Chandar, who presented an excellent fracture mechanics course to me and allowed me to use his digital image correlation system and other experiments facilities. In addition, I would like to thank Professor Nanshu Lu, who encouraged me whenever I discussed my experiments with her. I am grateful to Professor Ruoff, currently working in S. Korea as IBS Director and Distinguished Professor in Ulsan National Institute of Science and Technology, for allowing me to use the WITec Raman microscope and high-quality graphene supplies during two years.

I would also like to acknowledge the assistance provided by Dr. Deji Akinwande in the Department of Electrical and Computer Engineering at UT Austin for fabricating graphene samples and Dr. Michael Krische in the Department of Chemistry at UT Austin and Dr. Yves J. Chabal, affiliated with the Department of Material Science from UT Dallas, for their fabrication of SAM samples. Special thanks to the department of energy (DE-FG02-06ER46303), National Science Foundation (CMMI-1130261), the

Nanomanufacturing Systems for Mobile Computing and Energy Technologies (EEC-1160494) for financial support during my Ph.D.

There are a lot of colleagues who have been with me in Austin for several years. Without their help and encouragement, I could not have completed this work so effectively. First of all, I would like to mention Shravan Gowrishankar, who worked alongside me for several years. As a labmate, working with him was an excellent experience and increased my productivity. My special thanks to Thomas Mauchien for helping me determine the material properties of the epoxy. Most of all, I would like to mention Dr. Ji Won Suk who prepared the graphene samples that used in my experiments. In spite of all the difficulties in preparing graphene samples, he not only gave me high quality and sufficient samples for the challenging tests, but also shared his experience and knowledge with me about graphene and various materials. My special thanks are to Dr. Se-Hyuk Im, Dr. Do-Chul Yang, Dr. Suk-Kyu Ryu and many others in the Korean society in Austin.

I must mention my undergraduate research assistants, Boris Doynov, Adam Christopherson and Daniel E. Sarceno, who helped with several verification steps. In spite of the fact that these were difficult and time-consuming, they always provided me with excellent supplementary data to support my experiments.

I have no doubts that my work would not have been accomplished without the unconditional support and the love of my wife, my kids, my mother, my mother-in-law and father-in-law, my brother, and my sister-in-law. In particular, Kil-A, my best friend and wife, made many sacrifices to support me and take care of our kids for seven years. This work could not have been accomplished without her support. I love you.

# **Molecular Level Interactions of Large Area 2D-Materials**

Seung Ryul Na, Ph.D.

The University of Texas at Austin, 2015

Supervisor: Kenneth M. Liechti

Two-dimensional materials such as self-assembled monolayers (SAMs), graphene, etc. are candidate materials for improving the performance of microelectronics components and MEMS/NEMS devices. In view of their relatively large in-plane dimensions, surface forces are likely to dominate their behavior. The purpose of the current work was to extract not only the adhesion energy (or steady state fracture toughness) but also the traction-separation relation associated with interactions between various two-dimensional materials and substrates. In particular, interactions between SAMs terminated by carboxyl and diamine (COOH/NMe<sub>2</sub>) groups, hydroxylated silicon surfaces, graphene and silicon, graphene and its seed copper and graphene and epoxy over large areas was considered. Traction-separation relations, which are a continuum description of such molecular interactions, were determined by a direct method, which makes use of measurements of crack tip opening displacements; an inverse approach where the key parameters are extracted by comparing measured global parameters with finite element solutions and a hybrid approach in which the direct method was supplemented by finite element analysis. Furthermore, the surface free energy of graphene was measured by contact angle measurements.

The most striking observation across all the interactions that were considered is that the interaction ranges were much larger than those attributed to van der Waals forces.

While van der Waals models might have been at play between graphene and its seed copper foil and graphene and epoxy, the adhesion energies were surprisingly high. This coupled with the long interaction range suggests that roughness effects modulated the basic force field. Interactions between graphene and silicon and hydroxylated silicon surfaces may have been due to capillary and/or electrostatic again possibly modulated by roughness. The interactions between COOH and NMe<sub>2</sub> SAMs became stronger under vacuum, which may have induced chemical bonding, and tougher under mixed-mode loading.

## Table of Contents

List of Tables .....	xiii
List of Figures .....	xv
Chapter 1 Introduction .....	1
1.1 Self-Assembled Monolayers .....	1
1.1.1 General Structure and Deposition .....	2
1.1.2 Detection of SAMs .....	2
1.1.2 Self-Assembled Monolayers for Friction Control .....	3
1.1.3 Self-Assembled Monolayers for Adhesion Control .....	4
1.2 Wafer Bonding .....	6
1.3 Graphene .....	9
1.2.1 Creating Graphene .....	10
1.2.2 Electrical Properties .....	11
1.2.3 Mechanical Properties .....	11
1.2.4 Optical Behavior and Chemical Resistance .....	13
1.2.5 Transfer of Graphene .....	14
1.4 Traction-Separation Relations .....	15
1.5 Research Scope .....	17
Chapter 2 Experimental Procedures .....	20
2.1 Sample Preparation .....	21
2.1.1 Silicon Wafers .....	21
Silicon Surface Preparation .....	21
2.1.2 Deposition of Self-assembled Monolayers .....	23
2.1.3 Growth of Graphene on Copper and its Wet-transfer to Silicon .....	25
2.2 Thin Film Diagnostics .....	26
2.2.1 X-ray Photoelectron Spectroscopy .....	26
2.2.2 Atomic Force Microscopy .....	27
2.2.3 Ellipsometry .....	28

2.2.4 Raman Spectroscopy.....	28
2.3 Fracture Samples.....	29
2.4 Fracture Experiments.....	30
2.4.1 Wedge Tests.....	30
Infrared Crack Opening Interferometry.....	31
Mode I Wedge Fracture Experiments.....	34
2.4.2 Double Cantilever Beam Test.....	35
2.4.3 Mixed-Mode Fracture.....	37
2.5 Contact Angle Measurement.....	39
2.5 Traction Separation Relations.....	42
Chapter 3 Interactions between Self-Assembled Monolayers.....	46
3.1 SAM Diagnostics.....	46
3.1.1 XPS.....	46
3.1.2 AFM.....	48
3.1.3 Ellipsometry.....	48
3.1.4 Contact Angles.....	49
3.1.5 Fabrication of Si/COOH/NMe <sub>2</sub> /Si Laminates.....	50
3.2 Mode I Fracture.....	50
3.3 Mixed Mode Fracture.....	53
3.4 Fracture Surface Analysis.....	55
3.5 Discussion.....	56
Chapter 4 Hydrophilic Bonding between Silicon Strips.....	59
4.1 Sample Preparation.....	59
4.2 Mode I Wedge Experiments.....	61
4.2.1 Results.....	62
4.3 Surface Analysis.....	65
4.4 Cohesive Zone Modeling.....	68
4.5 Conclusions.....	75

Chapter 5 Surface Energy of Graphene .....	77
5.1 Measurement of the Contact Angle. ....	77
5.1.1 Cleaning and Sample Preparation .....	78
5.1.2 Calibration of the Contact Angle Goniometer .....	79
5.2 Substrate Effect .....	79
5.2.1 Silicon .....	80
5.2.2 Copper .....	81
5.3 Layer Effect .....	83
5.4 Contamination of Graphene .....	84
5.5 PMMA on Silicon .....	85
5.6 Surface Energy of graphene .....	86
5.7 Conclusions .....	89
Chapter 6 Interactions between Graphene and Silicon .....	91
6.1 Wedge Experiments .....	92
6.2 Fracture Surface Characterization .....	96
6.3 Traction-Separation Relations for Interactions between Graphene and Silicon .....	99
<i>Specimen Response</i> .....	100
<i>Delamination Resistance Curves</i> .....	100
<i>Traction-Separation Relations</i> .....	102
6.4 Analysis .....	104
6.5 Conclusions .....	107
Chapter 7 Selective Mechanical Transfer of Graphene .....	109
7.1 Selective Transfer .....	109
<i>Sample Fabrication</i> .....	110
<i>Graphene/Copper Delamination</i> .....	111
<i>Graphene/Epoxy Delamination</i> .....	115
<i>Other Delamination Modes</i> .....	117
<i>Identification of Delamination Modes</i> .....	118
7.2 Analysis .....	118

<i>Beam Theory Analysis</i> .....	119
<i>Cohesive Zone Modeling</i> .....	120
7.3 DISCUSSION .....	126
7.4 CONCLUSIONS .....	129
Chapter 8 Conclusions and Future Work.....	132
FIGURES .....	138
TABLES .....	255
References.....	265
Vita .....	279



## List of Tables

Table 2.1	The surface energy components of four liquids.....	255
Table 3.1	The RMS roughness of CF <sub>3</sub> , COOH, and NMe <sub>2</sub> -terminated SAMs.	256
Table 3.2	Comparisons of the measured and expected thickness of the SAMs [161].....	256
Table 4.1	Material properties of silicon and a summary of the key parameters of the traction-separation relations for hydrophilic bonding.....	257
Table 4.2	Master traction separation relation for hydrophilic bonding. ....	258
Table 5.1	Summary of the surface free energy components of four solid surfaces. The liquids used in the tests were water (W), glycerin (G), toluene (T) and diiodomethane (D), the latter two being apolar liquids. T and D indicate apolar liquid used in the calculation. The two liquid method was used for graphene on copper. ....	259
Table 6.1	Summary of key parameters for the traction-separation relations of graphene on silicon in each of the three experiments. ....	260
Table 6.2	The traction-separation relation parameters that were used in the finite element analysis of graphene/silicon interactions.....	261
Table 7.1	The effect of loading rate on the fracture path in the selective separation of graphene from copper or epoxy. ....	262
Table 7.2	Material properties of epoxy at different loading rates of 2 /s and 12 /s. .....	262
Table 7.3	Material properties and geometry of each material .....	263
Table 7.4	The values of the parameters associated with the traction-separation relations that were extracted by simulation. ....	263

Table 7.5	The RMS roughness along the rolling and transverse directions of graphene on epoxy. ....	264
-----------	--	-----

## List of Figures

- Figure 1.1 A schematic of a SAM on silicon showing the head group, backbone group, and functional group of each molecule. Red spheres represent oxygen atoms, blue hydrogen, black carbon, gray silicon, and orange covalent bonding between carbon and silicon. ....138
- Figure 1.2 Water drops on (a) hydrophilic and (b) hydrophobic surfaces (ref. Wikipedia).....138
- Figure 1.3 Transparency of both monolayer and bilayer graphene by Nair *et al.* [68]: (a) Optical observation of a 50  $\mu\text{m}$  aperture covered by monolayer and bilayer graphene. (b) Transmittance spectrum of monolayer graphene in hollow symbols. ....139
- Figure 1.4 Various forms of the traction-separation relation: (a) Constant traction model suggested by Dugdale [81]. (b) Nonlinear relation by Needleman [96] (c) Trapezoidal shape suggested by Tvergaard *et al.* [97]. (d) Bilinear form by Geubelle *et al.* [98].....140
- Figure 2.1 The crystal structure of silicon: Red solid lines present the Si(111) plane and yellow lines represent the unit cell associated with the diamond cubic structure on the [111] plane by Lilliestr le *et al.* [236].....141
- Figure 2.2 Termination of the hydrogen on various silicon surfaces by Ciampi *et al.* [120]: (a) Dihydride-termination on Si(100). (b) monohydride-termination on Si(111). ....141

Figure 2.3	RMS roughness vs. $\text{NH}_4\text{F}$ etching time. The Si(111) surfaces of silicon strips treated for 30 minutes in a piranha solution and then etched in ammonium fluoride solution for various etching times. The RMS roughness was measured by AFM. The optimum treatment was from three to five minutes, which yielded approximately 0.4 nm RMS roughness. ....	142
Figure 2.4	Schematics of the three SAMs considered in this work. Pink is for silicon, green for carbon, white for hydrogen, blue for nitrogen, and orange for oxygen from Wakamatsu [114]. (a) 10-undecylenic trifluoroethyl ester SAM ( $\text{CF}_3$ SAM), (b) 10-undecylenic acid ( $\text{COOH}$ SAM), (c) 10-undecylenic $\text{N,N}'$ -dimethylamino ethyl amide ( $\text{NMe}_2$ SAM).....	143
Figure 2.5	The schematic outlines the series of steps that were required to produce the $\text{COOH}$ and $\text{NMe}_2$ SAMs on Si(111). ....	144
Figure 2.6	Wet transfer of graphene to the Si(111) surfaces of silicon strips: (a) Following the deposition of graphene on copper foil, PMMA is deposited on the graphene and the copper foil is then etched away leaving graphene with a PMMA backing. (b) The graphene/PMMA bilayer is scooped up by a silicon strip. (c) The PMMA layer was removed in an acetone bath. (d) The PMMA residue is evaporated at a high temperature in an inert gas ( $\text{Ar}/\text{H}_2$ ) chamber. (e) Graphene has been completely transferred to the silicon strip.....	145
Figure 2.7	Example of an XPS survey scan on a $\text{CF}_3$ SAM. ....	146
Figure 2.8	An AFM tapping mode scan on a silicon wafer. The overall RMS roughness was 0.264 nm. ....	147

Figure 2.9	The Raman spectrum associated with CVD-grown graphene that was transferred to a silicon strip. The G and 2D peaks are clearly visible at $1583\text{ cm}^{-1}$ and $2693\text{ cm}^{-1}$ , respectively. ....	148
Figure 2.10	(a) A scenario for ionic bonding between COOH and NMe <sub>2</sub> SAMs [114]. (b) Hydrophilic bonding between hydroxylated silicon strips <i>via</i> hydrogen bonding [145].....	149
Figure 2.11	The preparation of fracture specimens for separating graphene that had been transferred to silicon: (a) A bare silicon strip and a graphene-coated one. (b) Epoxy was applied to the bare silicon strip. (c) The two strips were bonded together under uniform pressure. (d) The Si/epoxy/graphene/Si laminate was cured at $100\text{ }^{\circ}\text{C}$ .....	150
Figure 2.12	Outlines the steps that were taken to fabricate the laminate: (a) Copper foils ( $5 \times 5\text{ cm}$ ) with graphene on both sides were flattened on a silicon wafer. (b) Epoxy was applied over the entire surface of the first set of silicon strips. (c) Four to six epoxy-coated silicon strips were placed on the flattened foil and a uniform pressure was applied for one minute before the assembly was cured at $100\text{ }^{\circ}\text{C}$ for two hours. (d) The assembly was then cut between the silicon strips and another set of silicon strips partially coated with epoxy were prepared. (e) The two sets of strips were brought together under uniform pressure for one minute and the assembly was cured for two hours at $100\text{ }^{\circ}\text{C}$ to form a specimen with a blunt initial crack at in the region with no epoxy. (f) Bonding of aluminum loading tabs.....	151

Figure 2.13	Configuration of the Mode I fracture experiments: (a) The wedge test with IR-COI. The red solid line indicates various intermediate layers which are identified to the right side. (b) Double cantilever beam experiment using a hydraulic loading device. The blue solid line represents the layers shown to the right. ....	152
Figure 2.14	Ray diagram for crack opening interferometry. Rays reflected from the top and bottom crack surfaces interfere at P. ....	153
Figure 2.15	Verifying the IR-COI setup with three different configurations: (a) Newton's rings between a glass lens and a silicon strip. (b) Pure bending of a silicon strip and the associated hyperbolic fringe pattern. (c) An air wedge and comparisons of associated separations. ....	154
Figure 2.16	An IR image near a crack front and its intensity data: (a) A typical IR image near the crack front. (b) An improved image obtained by subtracting out the background signal. (c) Fit to the intensity profile from the subtracted image over the full field of view. (d) A close up of the intensity profile near the crack front and definition of the crack front as the intersection of the two tangents to the fitted intensity. ....	155
Figure 2.17	A schematic of the force-displacement response from a DCB test. The load drops following crack initiation. Several experiments can be conducted on one specimen by unloading and reloading it. ....	156
Figure 2.18	Cross sections of specimens used in the wedge tests. ....	157
Figure 2.19	The BOC Edwards vacuum system consists of a mechanical pump, turbo molecular pump, a wide range gauge and control units. The vacuum line is connected to the vacuum chamber where the fracture experiment is conducted. ....	158

Figure 2.20	The vacuum chamber with access to motor controls, IR-COI and vacuum port. ....	159
Figure 2.21	A cross section of the vacuum chamber. ....	160
Figure 2.22	A schematic of the carrier beam concept based on four-point bending of the carrier beam.....	161
Figure 2.23	The PZT and carrier beam characteristics illustrating the available force and displacement from the PZT under load [107]. ....	162
Figure 2.24	A schematic of DI water drop on a target substrate: the arrows indicate the three quantities in Young's equation. ....	163
Figure 2.25	Schematic of the cohesive zone near the tip of a crack and its interaction traction distribution.....	164
Figure 2.26	Two default traction-separation relations implemented in ABAQUS <sup>®</sup> , each with an initial linearly elastic response followed by (a) linear and (b) exponential softening. ....	165
Figure 3.1	XPS survey scan of CF <sub>3</sub> , COOH and NMe <sub>2</sub> SAMs on Si(111).....	166
Figure 3.2	A high resolution XPS scan of CF <sub>3</sub> SAMs for Fluorine 1s and Carbon 1s: (a) Fluorine 1s signal at 689 eV and (b) peaks associated with carbon bonds [160]. ....	167
Figure 3.3	A high-resolution XPS scan for NMe <sub>2</sub> and COOH SAMs for Carbon 1s and Nitrogen 1s bonding: (a) Carbon 1s bonding in C=O and CH <sub>2</sub> groups in a COOH SAM [160]. (b) Carbon 1s bonding in C-F, C=O, C-N, CH <sub>3</sub> and CH <sub>2</sub> groups in an NMe <sub>2</sub> SAM. (c) High-resolution scan for N 1s in an NMe <sub>2</sub> SAM.....	168
Figure 3.4	Contact angles between water and bare measurement corresponding to bare Si(111) as well as COOH and NMe <sub>2</sub> monolayers on Si (111).	169

Figure 3.5	A series of snapshots corresponding to various wedge insertions. The dark region on the left represents the bonded region. There are bright and dark fringes associated with the crack opening displacement. When $u_w$ was 5.0 $\mu\text{m}$ , the crack became unstable so that its front rapidly moved out of the field view. ....	170
Figure 3.6	Examples of intensity profiles from IR-COI with (a) background and (b) subtracted intensity profiles. The inset features the crack front region. ....	171
Figure 3.7	NCOD profiles for the (a) ambient and (b) vacuum environments.	172
Figure 3.8	The variation of the crack length with respect to wedge insertion.	173
Figure 3.9	Resistance curves for (a) ambient and (b) vacuum. ....	174
Figure 3.10	Examples of the variation of the J-integral with normal end-opening displacements under (a) ambient and (b) vacuum conditions. ....	175
Figure 3.11	The traction-separation relations from the wedge test under ambient and high vacuum. ....	176
Figure 3.12	A series of fringe patterns from a mixed-mode experiment under ambient conditions as the PZT actuator loaded and then unloaded the specimen. ....	177
Figure 3.13	Intensity data and fitting for the mixed-mode fracture experiment. (a) Raw intensity profiles averaged over the red dashed box, (b) subtracted intensity profiles, (c) smooth spline is fitting in order to define the location of the crack front and (d) smooth spline fitting of intensity data to determine the NCOD between fringes. ....	178
Figure 3.14	The typical NCOD plots from the mixed-mode experiment under (a) ambient and (b) high vacuum. ....	179



Figure 3.15	The variation of the J-integral under mixed-mode loading in terms of (a) crack extension and (b) normal end-opening displacement under both conditions.....	180
Figure 3.16	Traction-separation relations for COOH/NMe <sub>2</sub> interactions under ambient and high-vacuum conditions and mixed-mode loading. ....	181
Figure 3.17	XPS high-resolution scan for N1(s) on the fractured surfaces of specimens subjected to ambient and high vacuum. ....	182
Figure 3.18	Schematics of the fracture paths (dashed line) based on high resolution XPS scanning for (a) ambient and (b) high vacuum.....	183
Figure 4.1	Propagation of a bonding wave in wafer-to-wafer bonding [27]. (a) Wafer bonding was activated by tapping the top wafer, (b) spreading of the bonding wave and (c) complete bonding. ....	184
Figure 4.2	Infra-red images of the hydrophilic bonded-samples.: (a) Complete bonding and (b) the middle portion of the specimen was bonded leaving both ends separated.....	185
Figure 4.3	Infra-red images of the NCOD of the completely bonded (Fig. 4.2a) following (a) insertion and (b) removal of the wedge. Note the residual opening over 7.8 μm following removal. ....	186
Figure 4.4	A series of IR images as a wedge was inserted. The crack became unstable the wedge was inserted by 7.2 mm. The field of view is 4189×3130 μm with a resolution of 3.01 μm per pixel. ....	187
Figure 4.5	A series of intensity profiles associated with three different wedge-insertions $u_w$ and associated crack lengths $a$ . The red line is the best fit to the data. ....	188
Figure 4.6	NCOD profiles as a function of wedge insertion.....	189

Figure 4.7	Crack length as a function of wedge insertion for two well bonded specimens.....	190
Figure 4.8	Delamination resistance curves for all the specimens with hydrophilic bonding. ....	191
Figure 4.9	The variation of J-integral with end opening NCOD: (a) Case A for relatively strongly bonded specimens, (b) Case B for weaker bonding. ....	192
Figure 4.10	Traction-separation relations for hydrophilic bonding: (a) Case A. (b) Case B .....	193
Figure 4.11	Two different hydroxyl groups on silicon wafers [176]. (a) Type A bonding without any hydrogen bonding between the hydroxyl groups. (b) Type B bonding with hydrogen bonding (dashed line) between hydroxyl groups. ....	194
Figure 4.12	Topographical plot of 5×5 μm regions on a Si(111) surface. The overall roughness values in each case were (a) 0.255 nm and (b) 0.309 nm.	194
Figure 4.13	The surface topography of a silicon strip as seen by the Zygo interferometer and analyzed by MetroPro® software.....	195
Figure 4.14	A series of bonding surface profiles for three pairs of silicon strips. (a) Case A-1 in Figure 4.8, (b) Case B-4 in Figure 4.8 and (c) Case B-5 in Figure 4.8. ....	196
Figure 4.15	Opening displacements at the left and right ends after two silicon strips (Fig. 4.14a) were bonded. Open cracks at the (a) left and (b) right ends. ....	197
Figure 4.16	IR-COI images of bonded samples. (a) Case B-4, (b) Case B-5. ...	197

Figure 4.17	Comparison of the master traction-separation relation that was used in the finite element analyses and the data obtained from all specimens.	198
Figure 4.18	Predicting, based on the master traction-separation relation, the variation of the crack length with respect to wedge insertion for the well-bonded samples.....	199
Figure 4.19	Comparing the predicted resistance curves based on the master traction-separation relation with the measured ones for well-bonded samples.	200
Figure 4.20	Comparing the predicted and measured NCOD profiles for well-bonded samples. (a) Prior to steady-state growth ( $a = 6.987$ mm) and (b) at steady-state ( $a = 6.375$ mm) based on the master traction-separation relation. ....	201
Figure 4.21	Predicting, based on the damaged master traction-separation relation, the variation of the crack length with respect to wedge insertion for (a) case B-4 and (b) case B-5. ....	202
Figure 4.22	Comparing the predicted resistance curves based on the damaged master traction-separation relation with the measured ones for (a) case B-4 and (b) case B-5.....	203
Figure 4.23	Comparing the predicted and measured NCOD profiles for (a) case B-4 and (b) case B-5, based on damaged master traction-separation relations. ....	204
Figure 5.1	Raman spectra of graphene that had been wet-transferred to a Si(111) surface. The presence of the G and 2D-bands clearly indicates that graphene was successfully transferred to silicon. ....	205

Figure 5.2	Calibration of the contact angle measuring system with calibration blocks of (a) $39.6 \pm 1^\circ$ and (b) $90 \pm 1^\circ$ . The respective measured values were $39.9 \pm 0.25^\circ$ and $90.1 \pm 0.6^\circ$ . .....	206
Figure 5.3	Contact angle measurements using four different liquids on Si(111) substrates, graphene on silicon, HOPG, graphene/ on copper and PMMA on silicon. ....	206
Figure 5.4	The variation of the contact angle with (a) the number of graphene layers and probe liquid and (b) the liquid and several substrates. ...	207
Figure 5.5	Variation of the contact angle associated with surface aging of (a) graphene on silicon and (b) HOPG [197]. .....	208
Figure 6.1	AFM scanning of wet-transferred graphene on silicon: (a) The topography of wet-transferred graphene on silicon, (b) measurements of the RMS roughness over various regions, (c) the topography of torn, wet-transferred graphene on silicon and (d) measurements of the RMS roughness over various regions. ....	209
Figure 6.2	Optical transparency of the epoxy (EP30 from Master Bond Inc) particularly at 1050 nm. ....	210
Figure 6.3	Raman spectrum of epoxy on silicon. This epoxy has a peak at $1605 \text{ cm}^{-1}$ , which is close to the G band of the graphene. ....	211
Figure 6.4	Infra-red crack opening interferometry in the fracture experiments.	212
Figure 6.5	Defining the crack front and crack face separation from fringe patterns. ....	213

Figure 6.6	Characterization of the fracture surfaces: (a) Edge view schematic of graphene delamination from the lower silicon strip, (b) plan view schematic of the fracture surfaces of both silicon strips after complete separation, (c) low magnification SEM image of the fracture surfaces of both silicon strips, and (d) high magnification SEM image of the fracture surface of the lower silicon strip.....	214
Figure 6.7	Scratches in graphene due to wedge insertion: (a) AFM topology images of graphene on Si(111) in the region where the wedge was inserted and (b) height variations of graphene on Si(111); nominal values are listed in the legend.....	215
Figure 6.8	Characterization of the fracture surfaces: (a) Raman spectra of the fracture surface of the upper silicon strip at 7 different spots. (b) Raman spectra of the fracture surface of the lower silicon strip at 4 different spots. (c) Micro bubbles between graphene and epoxy on a 10 $\mu\text{m}$ by 10 $\mu\text{m}$ AFM scan of the fracture surface of the upper silicon strip. (d) Epoxy ligaments on a 50 $\mu\text{m}$ by 50 $\mu\text{m}$ AFM scan of the epoxy fracture surface of a silicon/epoxy/silicon specimen with no graphene.....	217
Figure 6.9	Variation of crack length with respect to wedge insertion. The initially linear response indicates that the crack was not growing as the wedge was inserted. Subsequent crack extension soon transitioned to steady state growth where each wedge insertion step produced the same amount of growth. Finite element solutions are shown as TSR1 and TSR2 as simulations of both tests 1 and 2 and test 3, respectively.....	218

Figure 6.10 Crack face separation during crack opening and growth. NCO profiles obtained by IR-COI as a function of crack length  $a$  as the wedge insertion progressed during test 3. Finite element solutions are shown as TSR2 for two steady state growth conditions. ....219

Figure 6.11 Delamination resistance behavior for graphene/silicon interactions. The resistance to fracture as represented by the J-integral initially rose steeply with small amounts of crack extension  $\Delta a$ . The resistance to crack growth eventually stabilized at the steady state toughness  $\Gamma_{ss}$  of the graphene/silicon interface. (a) Comparison of the resistance response with respect to data from tests 1 and 2 and a finite element solution using TSR 1. (b) Comparison of the resistance response with respect to data from test 3 with a finite element solution using TSR 2. ....220

Figure 6.12 High-resolution SEM images of wet-transferred graphene on Si(111): (a) Wrinkles, trapped residues and PMMA or copper residues and (b) other residues and non-uniform transfer of graphene. ....221

Figure 6.13 The variation of the J-integral with respect to the end opening displacement  $\delta_n^*$  (the inset defines the cohesive zone geometry and interactions). ....222

Figure 6.14 The traction-separation relations between wet-transferred graphene and silicon (the sketch identifies a typical shape of the traction-separation relation whose parameters are listed in Table 6.1). Traction-separation relations TSR1 and TSR2 were used in the finite element analyses of tests 1 & 2 and test3, respectively. ....223

Figure 6.15 Effect of the interaction range on delamination resistance curves. 224

- Figure 7.1 Schematics of the cross section of the specimen and experimental configuration are presented along with low and high resolution SEM images of the fracture surfaces: (a) Cross section and a specimen under load. The crack length  $a$  is defined as the distance from the crack front to the loading point. (b) Low resolution, stitched SEM images of graphene transferred to the epoxy. (c) High resolution SEM image of epoxy on silicon near the epoxy terminus after graphene transfer. (d) High resolution SEM of copper foil near the epoxy terminus after transfer. ....225
- Figure 7.2 High resolution SEM images of graphene transferred to epoxy and on copper following growth. (a) Following transfer, steps, ad-layers, wrinkles and epoxy islands or holes in the graphene can be seen on the epoxy fracture surface. Before transfer, (b) graphene wrinkles, copper oxide, grain boundaries and steps can be seen on the copper. (c) Another region contains notable defects (most likely holes) in addition to graphene wrinkles and copper steps. ....226
- Figure 7.3 Results of experiments at an applied separation rate of 254.0  $\mu\text{m/s}$ : (a) A schematic of delamination along the graphene/copper interface. (b) Force-displacement response of three experiments and associated simulations. (c) Raman spectra of graphene transferred on epoxy and pure epoxy. (d) Raman spectra of copper foil after mechanical transfer; the series of spots from 1 to 5 shows no graphene because it was transferred to the epoxy while spots 6 to 8 indicate the presence of graphene in the pre crack region where there was no epoxy. ....228

Figure 7.4	A schematic of the bimaterial corners formed at the terminus of the top epoxy layer.....	229
Figure 7.5	Raman spectra for graphene/epoxy (black), bare epoxy (red) and the subtracted response (blue).....	229
Figure 7.6	Raman maps of 100×100-μm regions of graphene on epoxy. (a) Intensity map of the G peak. (b) Intensity map of the 2D peak. (c) Map of the ratio of the intensities $I_{2D}/I_G$ of the 2D and G peaks. (d) Map of the range of the G peak location. (e) Map of the range of the 2D peak location.....	230
Figure 7.7	Variation of Raman spectra at 6 locations due to the topography of the epoxy fracture surface relative to the depth of field of the Raman microscope. Nonetheless, G and 2D peaks exist at every location, confirming the presence of graphene on epoxy. ....	231
Figure 7.8	Raman maps of 50×50-μm regions of graphene on epoxy. (a) Intensity map of the G peak. (b) Intensity map of the 2D peak. (c) Map of the ratio of the intensities $I_{2D}/I_G$ of the 2D and G peaks. (d) Map of the range of the G peak location. (e) Map of the range of the 2D peak location.....	232
Figure 7.9	Raman maps of 50×50-μm regions of graphene on epoxy. (a) Intensity map of the G peak. (b) Intensity map of the 2D peak. (c) Map of the ratio of the intensities $I_{2D}/I_G$ of the 2D and G peaks. (d) Map of the range of the G peak location. (e) Map of the range of the 2D peak location.....	233



Figure 7.10	Raman maps over 100×100- $\mu\text{m}$ regions of the copper fracture surface following delamination. (a) Intensity map of the G peak. (b) Intensity map of the 2D peak. The essentially zero values indicate that there was no graphene on the copper .....	234
Figure 7.11	Distribution of Raman 2D peak locations from spectra obtained from graphene on copper following growth and the shift of the Raman 2D peaks from spectra obtained from graphene on epoxy following delamination.....	235
Figure 7.12:	Electrical measurement of (a) Resistance vs. length and (b) Ohmic response during TLM experiments. (c) Results from four-point measurement. ....	236
Figure 7.13	Results of experiments at an applied separation rate of 25.4 $\mu\text{m/s}$ : (a) A schematic of delamination along the graphene/epoxy interface. (b) Force-displacement response of an experiment and associated simulations. (c) Raman spectra of ten spots on the epoxy with no graphene on it. (d) Raman spectra of copper foil after separation; the series of spots from 1 to 9 confirm the presence of graphene because it was not transferred to the epoxy. ....	238
Figure 7.14	Raman maps over 100×100 $\mu\text{m}$ regions on the epoxy fracture surface. (a) Intensity map of the epoxy peak at approximately 1600 $\text{cm}^{-1}$ . (b) Intensity map of the 2D peak. ....	239
Figure 7.15	Raman maps over 100×100 $\mu\text{m}$ regions on the epoxy fracture surface. (a) Intensity map of the epoxy peak at approximately 1600 $\text{cm}^{-1}$ . (b) Intensity map of the 2D peak. ....	239

Figure 7.16 Raman maps over 100×100µm regions on the copper fracture surface.  
(a) Intensity map of the G peak. (b) Intensity map of the 2D peak. (c)  
Map of the ratio of the intensities ( $I_{2D} / I_G$ ) of the 2D and G peaks. (d)  
Map of the range of the G peak location. (e) Map of the range of the 2D  
peak location. ....240

Figure 7.17 Raman spectra and low resolution SEM images were prepared to track  
the transfer of graphene at intermediate loading rates: (a) Raman spectra  
of the epoxy fracture surface following experiments at 42.3, 84.6 and  
169.3 µm/s. (b) Low resolution SEM image of the epoxy fracture  
surface following an experiment at 42.3 µm/s which shows small  
patches of graphene transferred to the epoxy. (c) Low resolution SEM  
image of the epoxy fracture surface following experiments at 84.6 µm/s  
which again shows small patches of graphene. (d) More continuous  
transfer of graphene (5×5.4 mm) was achieved at a loading rate of 169.3  
µm/s. ....241

Figure 7.18 A summary of delamination modes: (a) delamination along the  
graphene/copper interface at 254 µm/s. (b) Delamination along the  
graphene/epoxy interface at 25.4 µm/s. (c) Onset of case 3 via the  
formation of a blister below the epoxy terminus on the bottom side the  
copper. (d) Case 3-1, where the blister arrested and delamination  
continued at one of the interfaces above the copper. (e) Case 3-2 where  
the blister continued to grow along one of the interfaces below the  
copper foil. ....242

Figure 7.19	Schematic of Mode I fracture experiment in Si/epoxy/Si specimen and its fracture toughness in terms of load rate: (a) Double cantilever beam fracture experiment and (b) resistance response; the J-integration with respect to the crack propagation $\Delta a$ .	243
Figure 7.20	The stress-strain curves of annealed copper foils for 0.5 /s and 1.5 /s loading rates. The yield strength of all four copper foils is $23.3\pm 3.5$ MPa	244
Figure 7.21	Uniaxial tension test at room temperature: (a) An epoxy tensile specimen and (b) the stress-strain curve at two different loading rates: 2 /s and 12 /s.	245
Figure 7.22	The decomposition of the J-integral with respect to the work of plasticity for the graphene/copper interface.	246
Figure 7.23	The decomposition of the J-integral with respect to the work of plasticity for the epoxy/graphene interface.	247
Figure 7.24	The delamination resistance curve for the graphene/copper interface.	248
Figure 7.25	The delamination resistance curve of the epoxy/graphene interface.	249
Figure 7.26	Variety of features on copper foil. (a) Before graphene growth, (b) after graphene growth, (c) grains, steps and graphene wrinkles on copper foil and (d) high-resolution image observation at the junction of three copper grains.	250
Figure 7.27	(a) An AFM scan over a $25\times 25$ $\mu\text{m}$ region of graphene on copper foil with a copper oxide trace growing through the graphene. (b) The topography profiles taken along each of the colored lines bring out steps and rolling marks in the foil.	251

Figure 7.28 AFM scans prior to and following transfer of graphene: (a) The initial state of graphene on copper foil following deposition. The RMS roughness was 11.4 nm. (b) Copper without graphene after transfer had an RMS roughness of 12.3 nm. (c) The RMS roughness of the graphene-coated epoxy surface was 7.35 nm. (d) The RMS roughness of epoxy without graphene was 11.3 nm. (e) Profiles indicate that the wavelength of the surface roughness was quite similar in all cases.....252

Figure 7.29 Scans of 1×1.3-mm regions graphene on epoxy obtained with a Veeco Optical Profilometer. The overall RMS roughness of each region is noted on each image.....253

Figure 7.30 A higher resolution image of the surface topology of graphene on epoxy obtained with a Veeco Optical Profilometer.....254

## **Chapter 1 Introduction**

Since Richard Feynman gave his famous address “There is Room at the Bottom” at the annual meeting of the American Physical Society at the California Institute of Technology [1], nanotechnology is becoming a fundamental and essential aspect of modern life. One of the ramifications of dealing with materials and structures at smaller scales is that surface forces become dominant. This can be seen in microelectromechanical systems (MEMS), wafer bonding and the integration of graphene into useful devices and composite materials. The objective of this dissertation is to characterize, from a continuum mechanics perspective, the interactions between:

- a) Self-assembled monolayers (SAMs), which are used to modify surface interactions between components in MEMS devices,
- b) hydroxylated silicon surfaces in wafer bonding of microelectronics components
- c) and graphene and its growth on target substrates.

The expectation is that such an approach can be used to tailor interactions for specific objectives, perform reliability estimates and develop novel nano-manufacturing processes, all in a quantitative manner. This introduction provides some context to each of the three applications just mentioned as well as the basis for the continuum approach to be used to quantify the interactions that are encountered.

### **1.1 SELF-ASSEMBLED MONOLAYERS**

The ordered molecular monolayer formed on an active surface is known as a self-assembled monolayer. Their well-ordered forms and unique chemical structures on substrates allow surface interactions to be controlled [2, 3].

### **1.1.1 General Structure and Deposition**

A schematic (Fig. 1.1) of a SAM with its characteristic tilting angle and highly ordered, dense packing on a silicon substrate briefly identifies its three major components. Each SAM consists of a head group, a backbone group, and a functional group. The head group forms covalent bonds between the head group and substrate, thereby anchoring it to the substrate [4]. SAMs are able to maintain stable bonding on substrates through their covalent bonding (or chemisorption) on interfaces [2]. The backbone group, which is made up of alkyl chains, bridges the head group with the functional group. The van der Waals interactions between the alkyl chains are responsible for the highly ordered-dense packing of SAMs [2]. The functional groups can be used to control the degree of hydrophilic or hydrophobic response of surfaces (Fig. 1.2) as well as the degree of adhesion between functional groups and other surfaces.

SAMs can usually be grown on gold, silicon or silicon oxide substrates using various deposition techniques depending on the substrate [2]. For example, a highly ordered thiol group on an Au(111) surface can be formed by dipping (for approximately one hour) clean gold substrates in an alkanethiol solution at room temperature [5]. In contrast to gold, the formation of SAMs on either silicon or silicon oxide calls for multiple deposition processes [5, 6] including chemical vapor deposition (CVD), thermal and solution deposition, and UV-deposition. These processes can be combined to produce a wide range of functional groups [2, 5].

### **1.1.2 Detection of SAMs**

When SAMs are synthesized, imperfections such as voids, clustering and multi-layers may occur. Experience has shown that a series of diagnostics such as X-ray Photoelectron Spectroscopy (XPS), Atomic Force Microscopy (AFM) and Ellipsometry are required to verify that uniform SAMs have been formed.

XPS is a quantitative analytical spectroscopy that can detect the elemental composition and chemical and electronic states that exist near the surface of materials [7]. Therefore, XPS is ideally suited to analyzing SAM-terminated surfaces. The uniformity of SAMs can be confirmed by AFM [8], as the roughness of SAMs should follow the roughness of the substrate. Therefore, a critical step prior to deposition is to prepare a smooth substrate. Any changes in roughness following deposition can be used to detect clustering [8].

The final step in verifying that a monolayer has been formed is to use ellipsometry to estimate the thickness of SAMs [8]. A fundamental principle in the ellipsometry is that both the amplitude and the phase of the reflected light are changed by the thickness and material properties of thin films [9]. To evaluate the thickness of films, one can quantify changes in polarization in the incident light. Ellipsometry requires the indices of refraction of the materials to be known; although such information is generally unavailable for SAMs, it is still possible to detect the formation of multilayer *via* the Cauchy or Sellmeier relationship [10].

### **1.1.2 Self-Assembled Monolayers for Friction Control**

Several researchers have reported that SAMs can function as friction-reducing layers on substrates. Xiao *et al.* [11] saw how the friction force depended on the chain length of SAMs. In their study, friction forces between SAM-functionalized surfaces were measured with a custom AFM system coupled with a quadrant photodiode detector. It was seen that the profile of the friction signal from SAMs with short backbone groups less than 8 alkyl-chains in length were similar in shape and magnitude over the range of applied loads that was considered. However, as the chain length increased, the magnitude of the frictional force was significantly smaller than that of either short-chain

SAMs or the bare substrate. By considering SAMs terminated by methyl and trifluoromethyl groups, Kim *et al.* [12] observed that the chemical composition and structure of the functional group could alter the frictional force by a factor of three. Moreover, Masuko *et al.* [13] also reported on the chain length, functional group and temperature dependence of tribological properties. Hild *et al.* [14] also found that octadecyl trichlorosilane (OTS) and fluoro-decyl-trichloro-silane (FDTS) could have an effect on the tribological behavior of silicon surfaces. According to that report, the friction force decreased due to the presence of the SAMs on Si(100) as it has been verified by several researchers. A similar study was conducted by Cui *et al.* [15] with a lateral force microscope (LFM). Poly-amino-amine (PAMAM) dendrimers were deposited on silicon, PAMAM/C18, and PAMAM/HTTS SAMs to measure friction forces and coefficients. The results supported the idea that the functional group and chain length control tribological properties. More details of the tribological behavior of surfaces coated with SAMs that can be achieved are described in a review paper by Carpick *et al.* [16].

### **1.1.3 Self-Assembled Monolayers for Adhesion Control**

SAMs may be used to enhance the adhesion energy of interfaces as molecular level glues. Zhuk *et al.* [17] measured the fracture toughness between thin epoxy films and SAMs on Au/Ti/Si substrates. Their experiments showed that the fracture toughness between epoxy film and SAMs increased as the ratio of COOH/CH<sub>3</sub> functional groups increased. Moreover, it was observed that the rate increase of the fracture toughness was faster than the rate increase in the work of adhesion. This can be attributed to the variety of dissipation mechanisms that can be present during separation as opposed to approach, particularly if the strength of SAMs is larger than yield strength of epoxy. Tsukruk *et al.*



[18] reported that the functional group of SAMs could increase adhesion energy of silicon. It was found that the presence of epoxysilane SAMs on the surface of silicon increased the adhesion force between the tip of a scanning probe microscope and epoxysilane SAMs over that of bare silicon. Burns *et al.* [19] measured the adhesion energy of several SAMs with an interfacial force microscope (IFM) controlling normal and lateral loads. In their experiments, the IFM sensor pad was terminated by  $\text{CF}_3(\text{CF}_2)_5(\text{CH}_2)_2\text{Si}(\text{Cl})_3$ ,  $\text{CH}_3(\text{CH}_2)_{11}\text{SH}$ , or  $\text{COOH}-(\text{CH}_2)_{11}\text{SH}$  SAMs and a 3 mm-long glass fiber whose tip radius was less than 100 nm was brought into contact. The contact area between the tip and SAMs was estimated by the John-Kendal-Roberts (JKR) [20, 21] contact model, which allowed the adhesive interactions between surfaces to be estimated by single asperity contact. Gandhi *et al.* [22] measured the fracture energy of the interface between copper and silicon oxide without and with SAMs. The fracture energy was increased by the SAMs. Moreover, annealing the SAMs at high temperature further increased the fracture energy due to chemical interactions between silicon oxide and the SAMs.

Mello *et al.* [23] used binary SAMs to control the adhesion between sapphire and epoxy and measured the associated interaction strength and range or traction-separation relation. It was found that, although the adhesion energy increased with increasing shear component, this was not due to plastic dissipation in the epoxy as had been noted by Swadener *et al.* [24, 25] for the glass/epoxy interface with no SAMs. Instead, it was found that peak strength of the interaction was lower than the yield strength of the epoxy, which led to the conclusion that the intrinsic toughness of the SAM-mediated interface was itself dependent on mode-mix.

## 1.2 WAFER BONDING

Silicon wafer to wafer bonding technology, alternatively termed fusion bonding or wafer bonding, has been widely used in the semiconductor industry for several decades to develop silicon on insulator (SOI), three-dimensional packaging for microelectronics and MEM devices. Generally speaking, wafer bonding can be summarized as bonding two separate wafers without or with adhesive agents between the wafers. Three types of wafer bonding are common: direct bonding, anodic bonding and intermediate-layer bonding [26-28]

Direct bonding is a scheme for joining two separate wafers without any adhesive agent. Nonetheless more effective bonding can be obtained by functionalizing the silicon surfaces, making them hydrophilic or hydrophobic. Despite such surface treatments, the adhesion energy between two wafers tends to be low so that it may be necessary to heat (or anneal) the assembly in order to improve the bond-strength by activating chemical interactions between the surfaces. Such interactions may be reversible or irreversible depending on the annealing temperature. Anodic bonding uses an applied electric field in addition to temperature to join the wafers, which are usually glass and silicon. The processing temperature ranges between 200 °C and approximately 500 °C [26]. Intermediate-layer bonding makes use of thin gold film, solders, and soft metal films as the intermediate layer with suitable temperatures and compression forces to activate bonding. Generally speaking, the whole process is similar to cold welding but it is necessary to heat the wafers and intermediate layers in order to improve the quality of the bonding.

No matter which bonding technique is used, it is necessary to control the flatness, smoothness, and cleanliness of the wafers for successful bonding. Flatness of a wafer is defined by the variation of the surface from an ideally flat surface as a reference. As a

result, the flatness of a wafer can be evaluated by the difference between the highest and lowest points on the wafer. A critical flatness is defined as the largest variation in flatness that will still allow for successful bonding [28]. The smoothness of wafer is another parameter that is a more local measure of surface topology. It is often described by the root mean square (RMS) roughness of wafers [28]. Contamination can be present in a number of ways and must be minimized for successful bonding. The contaminants can be categorized as particles, organic contaminants and ionic contaminants [28]. There are various sources of organic contaminants such as airborne hydrocarbon, organic debris, etc. The presence of any organic contaminants may result in weak or non-uniform bonding along the interface. Ionic contaminants are not so critical for initial bonding. But it is known that the presence of ionic contaminants may cause variations in electrical properties [28].

For wafer bonding, prime grade, mirror-polished silicon wafers exhibiting flatness values from 1 to 3  $\mu\text{m}$  and RMS roughness values less than 0.5 nm [28] are common standards. The silicon wafers are chemically cleaned with several cleaning processes such as dipping in RCA1 solution (also known as SC1 or standard cleaning 1; a 1:1:5 mixture of  $\text{NH}_4\text{OH}:\text{H}_2\text{O}_2:\text{H}_2\text{O}$ ) followed by rinsing in deionized (DI) water and dipping again in an RCA2 solution (a 1:1:5 mixture of  $\text{HCl}:\text{H}_2\text{O}_2:\text{H}_2\text{O}$ ) followed by DI rinsing to remove any RCA2 residues. The role of the RCA1 treatment is to remove organic contaminants. The RCA2 treatment not only removes ionic particles but also produces a hydroxylated (OH) surface. Due to the complexity of these processes an alternative is to dip silicon wafers in a piranha solution, which is 1:3 a mixture of hydrogen peroxide and sulfuric acid. No matter which cleaning process is used, the silicon surfaces are terminated by hydroxyl groups. In the current work, piranha solution was used for hydrophilic wafer bonding under ambient conditions. Once the two treated wafers are brought into contact

and tapped at their center, hydrophilic or hydrophobic bonding is initiated and propagates uniformly until the entire wafer is bonded; the propagation of the bonding front is known as the bonding wave. This initial bonding is relatively weak and the strength of the bonding can subsequently be increased by heating or annealing the assembly.

The fracture toughness or adhesion energy of wafer bonds with and without annealing has been explored for some time. Bengtsson *et al.* [29], Rieutord *et al.* [30], and Navarro *et al.* [31] studied the propagation of bonding wave and developed mathematical models to explain key parameters of the phenomenon. Bengtsson [29] pointed out that the speed of the bonding wave was controlled more by the thickness of the wafers than their diameter. Rieutord [30] explained the propagation of the bonding wave was due to a coupling between the bonding energy and the viscous flow of air in the gap between the wafers. Navarro [31] suggested more complicated models that coupled plate theory with the Reynold equation for trapped water between wafers. This approach allowed the transient deformation of the wafers during bonding to be modeled.

The strength of adhesion has been evaluated by fracture experiments such as the wedge experiment or four point bending delamination [27, 32]. Martini *et al.* [32] reported that the fracture toughness (or adhesion energy) of hydrophilically bonded silicon wafers, delaminated under mode I conditions varied from  $100 \text{ mJ/m}^2$  without annealing to  $1.5 \text{ J/m}^2$  with annealing. The increased toughness was due to the activation of chemical bonds between the silicon wafers at high temperatures. More details were reported by Tong *et al.* [33], who measured the variation of the fracture toughness of hydrophically or hydrophobically bonded silicon wafers at various annealing temperatures of ambient and vacuum bonded wafers. His experiments revealed that vacuum bonded silicon wafers were tougher. It is possible that a decrease in the amount of trapped air at the interface under vacuum improved the ability of silanol bonds to

polymerize. The relationship between the fracture toughness and roughness was examined by Miki and Spearing [34] by controlling the roughness of the silicon wafers. Basically, the silicon wafers were roughened by dipping them in an etching solution before bonding and the fracture energy was measured in wedge tests. RMS roughness values up to a few nanometers were considered and the toughness decreased with increasing roughness over this range.

In related work, Bengtsson [29] found that the propagation of the bonding wave was controlled by the thickness, rather than the diameter, of the wafer. This was confirmed in subsequent work [35] where the effects of bow and etching patterns were modeled using the virtual crack closure technique. Predictions of the bonded area of wafers as a function of shape and boundary conditions were also explored [36] using the virtual crack closure technique. Moreover, Cole *et al.* [37] examined the interaction between water molecules and silicon in molecular dynamics simulations (MD) through the development of classical interaction potentials. Based on hydrophilic conditions, the calculated surface free energies associated with amorphous silica and native oxide were  $90 \text{ mJ/m}^2$  and  $97 \text{ mJ/m}^2$ , respectively. Additionally, the resulting normal force-separation profiles associated with amorphous silica had repulsive and adhesive forces over several nanometers.

### **1.3 GRAPHENE**

One of the fundamental chemical elements, carbon has the atomic number of 6. On the periodic table, carbon is defined as a nonmetallic and tetravalent element—the state of atoms having four electrons capable of covalent bonding. The best-known allotropes of carbon are graphite, diamond, and amorphous carbon. Graphite, the most

stable form of carbon allotropes under ambient conditions [38], is a layered material arranged in a honeycomb lattice with a 0.142 nm carbon-to-carbon bond and an equilibrium spacing of 0.335 nm between layers [39]. Diamond is another variation of carbon, defined by a diamond lattice having a face-centered cubic crystal structure. Even though diamond is not as stable as graphite, the conversion from diamond to graphite under ambient conditions, rarely occurs [40]. Diamond is the hardest material and has the highest thermal conductivity of any bulk material. Amorphous carbon is a material without any explicit crystalline structure resulting from reactive carbon [41]; it is possible for negligibly small scale ordered forms to exist in highly localized domains. It is also possible for ordered forms of carbon to exist as carbon nanotubes or as Bucky balls. Finally, graphene is a two-dimensional atomic carbon membrane one atom layer thick with  $sp^2$  bonding in the plane, transparent and stronger than any other materials [42-46]. In 1859, Brodie [45] reported graphite oxide or graphitic acid in highly lamellar structures. This came from treating graphite with a mixture of potassium chlorate and nitric acid [47]. Since May's report of the experimental discovery of graphene [46], thousands of groups have researched the synthesis, electrical, mechanical, and optical properties of graphene.

### **1.2.1 Creating Graphene**

In 2004, graphene layers exfoliated from graphite were transferred onto  $SiO_2$  by a process called the scotch tape technique [42], which can separate monolayer graphene from bulk graphite because the interaction between layers is governed by relatively weak van der Waals forces. By repeatedly applying and peeling the scotch tape to fresh silicon substrates, graphene flakes can be transferred to the  $SiO_2$  surface as monolayers or multilayers.

To obtain larger areas of graphene, Li *et al.* [48] developed CVD deposition of graphene in 2009. This was a breakthrough in the graphene field because it allowed graphene to be synthesized in an easily scalable manner. Pure copper foil (99.8% copper) without any copper oxide layers or anti-corrosion layers was used as the seed layer. In addition, Lee *et al.* and Tao *et al.* [49, 50] reported on the direct growth of graphene on silicon substrates. A thin layer of copper film ( $\sim 500$  nm) was grown on thermally grown SiO<sub>2</sub> using an e-beam process in order to provide the base for graphene deposition by CVD. Other metals, such as nickel and platinum have been considered as seed layers [51, 52] as well as silicon nitride [53].

### **1.2.2 Electrical Properties**

Since Novoselov *et al.* [42] showed that the temperature independence of the electron mobility in graphene was as high as  $10,000 \text{ cm}^2/\text{Vs}$ , papers by Novoselov *et al.* and Zhang *et al.* [43, 44] presented the unique electrical properties of graphene. Novoselov *et al.* [43] reported that the Schrödinger equation does not govern graphene, which is governed instead by Dirac's equation. This means that the electron mass near the Dirac points becomes massless, so the charge carrier in graphene is called the massless Dirac fermion. Zhang *et al.* [44] observed that the half-integer, quantum-Hall effect in graphene caused different transport phenomena, which are not observed in typical two-dimensional materials. These unique electrical properties make graphene a unique and powerful two-dimensional atomic layer material.

### **1.2.3 Mechanical Properties**

The mechanical properties are also superior to any other material. Lee *et al.* [54] reported that exfoliated graphene (or pristine graphene) has Young's modulus of 1 TPa and a strength of 130 GPa; both properties were obtained from nanoindentation

experiments on free standing films using a AFM as the indenter. Although such values are clearly exceptional, there was a concern that the corresponding properties of graphene grown by CVD would be significantly lower due its polycrystalline nature [55]. However, Lee *et al.* [56] proved that the Young's modulus of CVD-grown graphene was identical to the that of pristine graphene and the fracture strength of CVD-grown graphene was only 15% lower than that of pristine graphene because of the existence of grain boundaries in CVD-grown graphene membrane.

The adhesion energy of graphene flakes to silicon was reported by Zong *et al.* [57], Koenig *et al.* [58] and Boddeti *et al.* [59]. Their measurements represented the adhesion energy between exfoliated graphene and thermally grown (~300 nm thick) SiO<sub>2</sub> on Si(100). Zong *et al.* [57] determined the adhesion energy to be  $151 \pm 28$  mJ/m<sup>2</sup> by draping graphene over nanoparticles. Koenig *et al.* [58] designed a micro blister test and measured  $450 \pm 20$  mJ/m<sup>2</sup> for the monolayer graphene on SiO<sub>2</sub> and  $310 \pm 30$  mJ/m<sup>2</sup> for multi-layers graphene on SiO<sub>2</sub>. Boddeti *et al.* [59] carried out similar same blister experiments with exfoliated graphene on SiO<sub>2</sub>. An average adhesion energy of graphene was 240 mJ/m<sup>2</sup>, which was lower than  $450 \pm 20$  mJ/m<sup>2</sup> reported by Koenig [58]. Larger scale blister tests by Cao *et al.* [60] were used to determine the adhesion energy between CVD grown graphene that had been transferred to copper plate, yielding similar level of the adhesion energy.

Recently, Yoon *et al.* [61] measured  $720 \pm 70$  mJ/m<sup>2</sup> as the adhesion energy between CVD-grown graphene and copper films using a mechanical peeling process. Moreover, Das *et al.* [62] used a nano-scratch experiment for as-grown graphene on copper and nickel substrate, yielding an adhesion energy of 12.75 J/m<sup>2</sup> and 72.70 J/m<sup>2</sup> for the graphene/copper and the graphene/nickel interfaces, respectively. The same nano-scratch experiments by Das *et al.* [63] were repeated for graphene that was wet-



transferred to SiO<sub>x</sub>/Si substrates, resulting in the adhesion energy of 2.978 J/m<sup>2</sup>, 10.09 J/m<sup>2</sup>, and 20.64 J/m<sup>2</sup> for as-transferred graphene to SiO<sub>x</sub>/Si, rapid thermal annealed graphene, and vacuum annealed graphene.

The possibility of using graphene as a micro lubricant of was considered by Li *et al.* [64], Lee *et al.* [65] and Kim *et al.* [66]. Their research indicated that monolayer graphene with its low surface energy is an effective material for reducing the friction force and adhesion pull-off force. Furthermore, the friction force decreased as the number of graphene layers increased. This result was explained by observing that the graphene puckered in an out-of-plane mode in front of the probe tip [64].

#### **1.2.4 Optical Behavior and Chemical Resistance**

Graphene is a two-dimensional, one-atomic layer thick nano-material with an equilibrium thickness of 0.335 nm [39]. Nonetheless graphene is unique in that it is visible on thermally grown SiO<sub>2</sub> when its thickness is 280 nm to 350 nm [67]. Another optical property of monolayer graphene is its uniform absorbance  $\pi\alpha = 2.3\%$  [68]. In addition, graphene is almost transparent to infrared [61]. Such optical properties result from graphene's unique electronic structure known as massless Dirac fermions [42-44].

Graphene may also play a key role as a protective or chemically resistant material. Studies in 2008 proved that graphene is chemically impermeable to standard gas so that trapped gas in a graphene/substrate interface can pressurize a graphene membrane [69, 70]. These studies proved the potential of graphene as nano or micro-scale filters. Graphene's role as an anti-oxidation film on metal substrates was reported by Chen *et al.* [71]. Their experiments demonstrated that the metal layers terminating in a graphene monolayer showed excellent oxidation resistance even after four hours heating at 200 °C in air.

### 1.2.5 Transfer of Graphene

Dry transfer of graphene has been an integral part of its history from the earliest days when scotch tape was first used to exfoliate graphene from graphite [72]. This approach produces relatively small flakes with single or multiple layers. Chemical vapor deposition of graphene on thin ( $\sim 35 \mu\text{m}$ ) large area copper foils [73-75], and related metal foils such as commercially available Cu-Ni foils [76], produces large area graphene, up to meters in the in-plane dimension [77]. Graphene has also been grown on copper film ( $\sim 1 \mu\text{m}$  thick) [50] that has been deposited on silicon wafers.

No matter which approach to the deposition of large area graphene is taken, the same problem remains: transferring the graphene to its destination substrate for the myriad of applications that are currently being considered. Some applications may require intermediate carrier films to be used, so several contact and separation events can be expected. In most cases, the adhesive interactions that are involved in contact and separation are assumed to be van der Waals in nature, but the details could vary significantly depending on the contact pair and environmental effects [78]. The strongest interactions may be between graphene and its seed metal; interactions between graphene and target substrates are expected to be weaker but may be modified by surface functionalization. The effort that is featured here relates to the most challenging interface at this stage in our development; removing graphene from its seed copper foil, which is an attractive substrate for roll-to-roll nano-manufacturing processes. Doubts about being able to meet this dry transfer challenge have led to so called “wet transfer” where the seed copper foil is etched away [79] or an electrochemical process [80] that generates bubbles at the graphene/copper foil interface and separates the graphene from the foil. Yoon *et al.* [61] were the first to demonstrate that graphene could be mechanically separated from its seed copper layer. In that work, the copper film had been deposited on

silicon oxide prior to CVD of graphene. A second silicon strip was bonded to the graphene with an epoxy. The two silicon strips were peeled apart and, for applied displacement rates above 5.0  $\mu\text{m/s}$ , it was shown that delamination occurred along the graphene/seed copper interface, transferring a graphene monolayer onto the epoxy.

#### 1.4 TRACTION-SEPARATION RELATIONS

When the stress field near a crack front is estimated by linear elastic fracture mechanics (LEFM), the infinite stresses predicted at the crack front are unreasonable given the finite stress-strain response of materials. Dugdale in 1960 [81] and Barenblatt in 1962 [82] suggested that crack faces be separated into two regions: the main portion, which is free of tractions and the region near the crack front which is subject to tractions (or cohesive stresses) that tend to bring the crack faces together. In the Dugdale model, the cohesive stresses were taken to be the yield strength of the material. The Barenblatt model was motivated by brittle materials and it was assumed that the size of the process zone was constant, independent of crack driving force and small compared to other dimensions. Since then, cohesive zone modeling has developed significantly, mainly because it does not require the presence of a preexisting flaw to model crack initiation and growth.

An early example of a more general implementation of cohesive zone modeling is the prediction of crack growth in concrete [83]. In such homogeneous bodies, the crack path is not known *a priori*, as opposed to interfacial crack growth. Knauss [84] analyzed the growth of interfacial crack growth in a bonded double cantilever specimen where the damaged material ahead of the crack was modeled by softening behavior in the cohesive zone. Suggestions for extracting the form of the traction-separation relation from beam deformations were also made. Needleman [85] adopted the cohesive zone modeling to

simulate the interaction of rigid inclusion and ductile material. Numerous simulations with cohesive zone modeling can be reviewed in various applications [86-95]

The modeling crack growth *via* cohesive zone modeling depends on the identification of parameters that describe variation of the strength of interfacial interactions as a function of separation. Various forms of commonly used traction-separation relations are shown in Figure 1.4. The simplest is the constant traction (Fig. 1.4a) up to a critical separation or crack opening displacement [81] due to Dugdale. More general forms (Fig. 1.4b) of the traction-separation relation rely on the formulation of an interface potential; as examples, consider the cubic or exponential softening suggested by Needleman [85, 96]. The trapezoidal and the bi-linear forms (Fig. 1.4c-d) exhibit linear responses prior to damage initiation. The trapezoidal form maintains a constant traction followed by the linear softening [97]. On the other hand, only linear softening is defined beyond the damage initiation point in the bi-linear form [98]. In general, the key parameters of any traction-separation relation are the stiffness of elastic response, the damage initiation point which may be specified by strength or displacement, and the critical interaction range that may be specified by total fracture energy or critical displacement.

Parameter identification for traction-separation relations is usually accomplished in two ways. The first is the so-called direct approach in which the crack opening displacement at the origin of the original crack front is measured and the corresponding energy release rates are known.[99-108]. Then, by taking the derivative of the energy release rate with respect to the opening displacement, the traction-separation relation can be obtained. The advantage of the direct method is that the traction-separation relation can be measured in a relatively direct manner. However, this approach may be affected by the resolution of the measurement scheme, both in identifying the crack front location

and the normal crack opening displacements: The second approach is iterative method deciding key parameters of the traction-separation relation are varied parametrically until the solutions converge with measured quantities such as the load-displacement response, crack extension and crack opening displacements [24, 106, 109]. If the direct approach does not have sufficient resolution in measuring opening displacement at the crack front, the two approaches can be combined to determine the form of the traction-separation relation at separations below the resolution in opening displacements. [110].

## 1.5 RESEARCH SCOPE

In this dissertation, the traction-separation relations of several atomic interactions are measured and supplemented by numerical simulations. The atomic interactions considered here are SAM/SAM interactions, hydrophilic interactions as well as interactions between graphene and seed copper graphene and epoxy and graphene and silicon. In general, nano indentation experiments directly yield the force-displacement response, which can be considered to be a primitive or convoluted form of the traction-separation relation. Wang *et al.* [8] measured the force profiles of tungsten probes indenting OTS SAMs on silicon using an interfacial force microscope (IFM) and went on to determine, *via* a combined atomistic and continuum model, the parameters associated with a bilinear traction separation as the continuum representation of the interactions between tungsten and OTS SAMs. Similar measurements have been made by Binggeli *et al.* [111, 112] and Thomas *et al.* [113], but neither were supplemented by analyses that extracted the traction-separation relations associated with the interactions that were being considered.

In the current study, fracture experiments coupled with IR-COI were used to examine the interactions listed above. Among the advantages of IR-COI are that it allows

direct observation of the location of crack front and the normal crack opening displacements to within 17 nm. As a result, it has been possible not only to measure the adhesion energy of the interactions but also to determine their strength and range. The dissertation is organized as follows.

Chapter 2 describes the details of sample preparation including cleaning, functionalization of silicon and growth of graphene into fracture specimens. All the surface diagnostics including XPS, AFM, ellipsometry and Raman spectroscopy are summarized, as well as the experimental procedures associated with wedge tests, crack opening interferometry, double cantilever beam tests and contact angle measurements. All the common components are presented in this chapter; specific details or variants are described in the subsequent relevant chapters.

Chapter 3 is assigned to examining SAM/SAM interactions between carboxyl and diamine functional groups under mode I and mixed-mode loading conditions in controlled environments. For the mixed-mode fracture experiment, a new loading device based on a carrier beam concept was developed to measure traction-separation relations under ambient and high vacuum conditions. This allowed the traction-separation relation and adhesive energy associated with carboxyl and diamine to be compared with those determined in mode I condition. Chapter 4 is devoted to understanding the nature of hydrophilic bonding under ambient conditions. Even though certain aspects of this topic have been extensively studied, the strength and range of the associated interactions had yet to be considered. Chapter 5 lays the foundation for subsequent Chapters on graphene interactions by focusing on the surface free energy of graphene and highly ordered pyrolytic graphite (HOPG) *via* contact angle measurements. The contact angles of several liquids on graphene and HOPG were measured in order to determine their surface free energy. In Chapter 6, interactions between graphene that had been wet-transferred to

silicon are measured *via* wedge tests and associated modeling. This hybrid approach completed the partial description of the traction-separation relations that was available to experiment. Chapter 7 presents a mechanical approach to the selective transfer of graphene from its seed layer based on the rate dependence of the interface between a polymer backing layer and graphene. This allowed the strength and range of interactions between graphene and seed copper and graphene and epoxy to be measured. In conclusion, Chapter 8 summarizes the results and suggests topics that might be addressed in the future.

## Chapter 2 Experimental Procedures

Various experiments have been conducted to examine the adhesive behavior associated with SAM/SAM interactions, hydrophilic bonding, and interactions between CVD-grown graphene and its seed copper layer as well as epoxy and silicon. A common feature of all the experiments is that the adhesive interactions were examined over relatively large spatial domains by making use of specimens that made use of laminated beam fracture specimens.

For the SAM/SAM interactions, silicon strips were functionalized with SAMs that were terminated with carboxyl and diamine end groups, brought into contact and then separated in mode I by wedge loading and under mixed-mode conditions using a carrier beam concept. All the experiments on hydrophilic bonding as well as those that involved graphene were conducted under nominally mode I conditions. For the experiments on hydrophilic bonding, silicon strips were hydroxylated, brought into contact under ambient conditions and then separated in wedge tests. Graphene that was grown on copper foil was sandwiched between two silicon strips using thin epoxy layers and then separated in a double cantilever beam fracture experiment in a universal loading device, thereby allowing the applied displacement rate to be controlled and selective transfer from the copper or epoxy to be effected. The interactions between silicon that had been transferred to silicon were examined by bonding a second silicon strip to the free surface of the graphene with the same epoxy and separating the specimens in a wedge test. In the wedge and mixed-mode fracture experiments, the normal crack opening displacements were measured using infrared crack opening interferometry. In all experiments, diagnostic tools such as Raman spectroscopy and scanning electron and atomic force microscopy were used to determine the delamination path. Finally contact angle measurements were



used to determine the work of adhesion of graphene deposited on silicon. The details of all these experiments are now presented.

## **2.1 SAMPLE PREPARATION**

In this doctoral work, all two-dimensional materials were deposited on the (111) surfaces of 5×40 mm silicon strips. The strips were diced from 100 mm wafers and cleaned in preparation for functionalization, deposition of graphene or lamination into sandwich structures.

### **2.1.1 Silicon Wafers**

Silicon is metalloid and tetravalent, which means that its atoms have four electrons available for covalent bonding. High purity, single crystal silicon wafers were selected as the substrate for all the experiments. The Si(111) surface was selected in order to present the smoothest surface and most dense atomic arrangement, diamond cubic crystal (Fig. 2.1) to the SAMs, graphene and epoxy. Both sides of the wafer were polished in order to make sure that the incident beam for crack opening interferometry was not scattered [114]. Moreover, the in-plane Young's modulus (169 GPa) in the (111) planes is the stiffest [108, 115, 116]. A dicing machine (Disco, DAD 321) was used to prepare 5×40 mm silicon strips for all the fracture experiments. The contact angle experiments required 10×10 mm chips.

#### ***Silicon Surface Preparation***

Generally speaking, the quality of this research rests on the quality of the silicon surfaces for several reasons: First, organic residues on the silicon surface prevent SAMs or graphene from having proper atomic interactions with silicon. Second, particularly for fabricating defect-free SAMs on Si(111) surfaces, the RMS roughness of the Si(111) surfaces should be less than 0.5 nm. Finally, in order to ensure that the contacting

surfaces can approach sufficiently close to properly interact, SAM clustering and the waviness of the contacting surfaces should be minimized. [28].

The first step in preparing the silicon strips following dicing was to remove any debris. This was accomplished by dipping each silicon strip in an ultrasonic bath filled with de-ionized (DI) water [108] for 30 minutes. The next step was to remove any organic residues from the Si(111) using a piranha solution, a mixture of hydrogen peroxide ( $\text{H}_2\text{O}_2$ , 50 %, Thermo Fisher Scientific Inc.) and sulfuric acid ( $\text{H}_2\text{SO}_4$ , 95%, Thermo Fisher Scientific Inc.). To prepare the piranha solution, 5 mL of hydrogen peroxide was poured into a glass beaker, followed by 15 mL of sulfuric acid. Each silicon strip was individually immersed in the piranha solution for 30 minutes. The characteristic feature of the piranha solution is that the solution will attack the organic materials on the native  $\text{SiO}_2$  layer and leave the hydroxyl-terminated  $\text{SiO}_2$  ( $\text{SiO}_2\text{-OH}$ ) surface, with hydrophilic qualities. The silicon strips were then rinsed with DI water to remove any residue of the piranha solution. Finally, each silicon strip was blown with dry  $\text{N}_2$  gas [114].

The piranha solution was the only step required for producing silicon strips for hydrophilic bonding and graphene transfer. The SAM/SAM study required an additional ammonium fluoride ( $\text{NH}_4\text{F}$ , 98%, ACROS Organics<sup>TM</sup>) treatment in preparation for depositing SAMs. When  $\text{SiO}_2\text{-OH}$  surfaces are etched by  $\text{NH}_4\text{F}$ , the native  $\text{SiO}_2$  layer is removed and replaced by a hydrogen-terminated silicon surface ( $\text{Si-H}$ ) [117, 118]. Hydrofluoric acid (HF) is also commonly used [117, 119] but  $\text{NH}_4\text{F}$  was preferred in this study chosen for safety reasons [114] and better control of surface roughness [117, 118, 120]. Etching with hydrofluoric acid forms a microscopically rough surface [118] with a mixture of monohydride, dihydride, or trihydride-terminated surfaces (Fig. 2.2b) [121]. On the other hand, an ammonium fluoride treatment only produces monohydride-

terminated surfaces. Neither treatment produces monohydride-terminated surfaces on Si(100) surfaces (Fig 2.2a). The solution was prepared by mixing 12 g of  $\text{NH}_4\text{F}$  powder in 18 mL of DI water [114] in a plastic bottle. It should be noted that only plastic bottles can be used with ammonium fluoride [114]. The best exposure time of the silicon strips to ammonium fluoride was from three to five minutes, which yielded (Fig. 2.3) an RMS roughness of approximately  $0.4 \pm 0.05$  nm [114, 118]. Longer exposure leads to increased roughness [122] and four minutes was chosen as the optimal etching time for this study.

The hydrogen-terminated Si(111) surfaces were rinsed with de-gassed DI water de-oxygenated with Argon gas. This minimizes the formation of chemically-fresh silicon oxide ( $\text{SiO}_x$ ) reacting with dissolved oxygen in DI water. To dry out Si(111) strips completely, the glass tube was evacuated and filled with inert gas (either  $\text{N}_2$  or Ar) to keep the hydrogen-terminated surface from decomposing and becoming contaminated [114].

### **2.1.2 Deposition of Self-assembled Monolayers<sup>1</sup>**

In order to study molecular level bonding *via* SAMs, two different SAMs, 10-undecylenic acid (COOH) and 10-undecylenic N,N'-dimethylamino ethyl amide (NMe2), shown schematically in Figures 2.4b-c, were considered. The process commenced with the deposition (Fig. 2.4a) of 10-undecylenic trifluoroethyl ester SAM ( $\text{CF}_3$ -SAMs) on the Si(111) surfaces of silicon strips. The trifluoroethyl ester moiety in the  $\text{CF}_3$ -SAMs was converted to undecylenic acid for COOH-SAMs or N,N'-dimethylamino ethyl amide for NMe2 SAMs. The presence of the fluorine in  $\text{CF}_3$ -SAMs is a highly useful ingredient as

---

<sup>1</sup> The deposition of SAMs was fully supported by Dr. Abbas Hassan and Dr. Krische of UT Austin and Dr. Oliver Seitz and Dr. Chabal of the UT Dallas. The author thanks them for their support and assistance in this work.

a diagnostic element because the fluorine cannot be found in ambient conditions [114]. The details of the functionalization now follow with reference to Figure 2.5.

To obtain CF<sub>3</sub>-terminated SAMs on Si(111) surfaces, 1 mL of 2,2,2-trifluoroethyl undec-10-enoate was poured onto mono-hydride-terminated Si(111) surfaces in a glass tube in a nitrogen environment. The solution and silicon pieces were heated to 200 °C for two hours. The functionalized Si(111) strip was then rinsed with pentane, methanol and dichloromethane, respectively. This process results in a Si(CH<sub>2</sub>)<sub>10</sub>(CO)O(CH<sub>2</sub>CF<sub>3</sub>) structure with covalent bonding between silicon and carbon atoms, followed by a 10-group alkyl chain and terminated with the functional group, O(CH<sub>2</sub>CF<sub>3</sub>). The molecular structure of CF<sub>3</sub> SAMs on a silicon substrate [114] appears in Figure 2.4a.

COOH SAMs (Fig. 2.4b) were obtained by substituting the trifluoroethyl ester in the CF<sub>3</sub> SAMs, with the COOH acid moiety. First, silicon strips terminated with CF<sub>3</sub> SAMs in a nitrogen atmosphere were added to 0.25 M potassium t-butoxid (t-BuOK) in dimethyl sulfoxide (DMSO). After the mixture was allowed to stand at room temperature for three minutes, the strips were rinsed with DI water and then soaked in a 0.1 M HCl solution for one minute. The strips were then rinsed with a mixture of DI water and methanol. After deposition, the strips were placed in a clean test tube, dried under a vacuum and stored in an N<sub>2</sub> atmosphere [114].

SAMs with a diamine functional group (Fig. 2.4c) could also be obtained by converting the trifluoroethyl ester of the CF<sub>3</sub> SAMs. First, CF<sub>3</sub>-terminated strips were placed in 1 mL of freshly distilled N,N'-dimethylamino ethyl amide and sonicated at room temperature for 100 minutes. Then, the silicon strip was rinsed three times with methanol and cleaned after each rinse with dichloromethane (DCM). Once deposition was complete, each silicon strip was placed in a clean test tube, dried under vacuum and stored in an N<sub>2</sub> atmosphere [114].

### 2.1.3 Growth of Graphene on Copper and its Wet-transfer to Silicon

Large-scale polycrystalline graphene was synthesized on 2×2 inch copper foil in a low pressure CVD deposition system [123]. Once the growth was complete, graphene was transferred *via* a wet-transfer process, to the Si(111) surfaces of silicon strips [48, 124].

Prior to the deposition of graphene on copper foils, it is necessary to treat the surface of the copper foil (Cu foil, 99.8 %, Alfa Aesar No. 13382, CAS 7440-50-8). First, the surface of the copper foil may have a layer of chromium oxide for anticorrosive protection [125]. In addition, the RMS roughness of the copper foil formed by the cold-rolling process (Fig. 7.26a) is too rough to be suitable for uniform graphene growth [125]. To obtain the smoothest possible pure copper foil, either electro-polishing the copper-foil [125, 126] or chemically etching it [127] will remove the chromium and reduce the rolling marks.

For this study, the copper foils were dipped in acetic acid ( $C_2H_4O_2$ ) for several hours to remove the chromium layer and copper oxide. This was complemented by a hydrochloric acid (HCl) etch [125, 126]. The treated copper foil was annealed at 1030 °C with two sccm (standard cubic centimeters per minute) hydrogen for approximately an hour. This was followed by a ten-minute exposure to five sccm of methane ( $CH_4$ ) and two sccm of hydrogen ( $H_2$ ) [123]. The graphene-coated copper foil was then gradually cooled to room temperature, ready for further processing for the dry transfer experiments or for the wet transfer of graphene to silicon in order to examine graphene/silicon interactions.

The wet transfer of graphene to silicon begins (Fig. 2.6) by depositing PMMA on the graphene as an intermediate backing layer while the copper foil is etched away [110]. A PMMA solution (20mg/mL) was spin coated on the graphene and cured under ambient

conditions. It took several hours to completely etch away the copper foil with an iron (III) nitrate solution (0.05g/mL in water; Fig. 2.6a). The remaining PMMA/graphene bilayer was transferred to a distilled water bath to rinse off the etchant. The bilayer was then scooped up by a silicon strip (Fig. 2.6b) with the graphene side facing the silicon. When one transfers the PMMA/graphene to silicon strips, small gaps between the PMMA/graphene and the silicon surface may form. This poor contact can cause wrinkles and cracks to form in the graphene when the PMMA backing is removed. In order to overcome the potential defects associated with improper contact, samples were heated to 130~150 °C ( $T_g \sim 120$  °C) which caused the PMMA backing to relax and conform more closely to the Si(111) surface. After curing, the PMMA layer was removed in an acetone bath (Fig. 2.6c) and any residue was thermally decomposed at 400 °C with an Ar/H<sub>2</sub> flow (Fig. 2.6d) [79, 127, 128]. Once the PMMA was completely removed, the transfer of graphene to the silicon strip was complete (Fig. 2.6e) [110].

## **2.2 THIN FILM DIAGNOSTICS**

A variety of surface analysis tools was required to determine the quality of the deposited SAMs and graphene films. They were also used to determine the composition of the delamination surfaces once the fracture tests had been completed.

### **2.2.1 X-ray Photoelectron Spectroscopy<sup>2</sup>**

X-ray photoelectron spectroscopy (XPS) is a tool determining the surface chemistry of a material. This includes the elemental composition, chemical state, and electronic state of the surface elements [7]. The X-rays irradiate the target surface while simultaneously measuring the kinetic energy of the material and the number of electrons

---

<sup>2</sup> The author appreciates support from Undergraduate Research Assistants Boris Doynov and Adam Christopherson.

ejected as deep as 10 nm from the surface [114]. The best performance is achieved in ultra-high vacuum (UHV,  $P \sim 10^{-9}$  Torr). A Kratos X-ray Photoelectron Spectrometer - Axis Ultra DLD, with a depth resolution of 2 to 8 nm, was used to determine and help optimize the quality of the SAMs following each step of their deposition. Figure 2.7 is a survey scan of a  $\text{CF}_3$  SAM and brings out the presence of carbon, fluorine, silicon, and oxygen. XPS was also used to determine where the COOH and NMe<sub>2</sub> SAMs broke after they had been brought into contact and then separated.

### 2.2.2 Atomic Force Microscopy<sup>3</sup>

The atomic force microscope (AFM) is a high-resolution scanning probe microscope that allows the topographical features of a surface to be examined [129]. The Agilent 5500 AFM is capable of characterizing the topology of a surface to a resolution of 0.5 Å, with features ranging up to 7 μm in height over a scan area of up to 100× 100 μm.

The tapping, as opposed to the contact mode, was more useful for tracking the topological features of all the surfaces considered in this study (SAMs on silicon, graphene on copper and graphene on epoxy) because it causes less damage. [2, 114]. Frictional force measurements in the contact mode have been useful for detecting graphene because its low surface-free energy results in very low friction forces [65, 66]. However, the scanning area is more limited in this approach, so it was not adopted for this study. All the silicon probes (Budget Sensors Inc.) used in this study were coated with an aluminum reflex coating to enhance sensitivity. They had a resonant frequency of 300 kHz and a spring constant of 40 N/m. An AFM scan of a 5×5 μm bare Si(111) surface after cleaning is shown in Figure 2.8; its RMS roughness was 0.264 nm.

---

<sup>3</sup> Specially thanks to Daniel E. Sarceno, Undergraduate Research Assistant, and Dr. R. Piner, Research Associate for their valuable support with AFM analysis.

### 2.2.3 Ellipsometry

Ellipsometry is an optical measurement tool that measures the amplitude difference,  $\psi$  and phase difference,  $\Delta$  from polarized light that is reflected from ultra-thin films [9, 114, 130]. These measurements can be used, in conjunction with some analysis, to estimate the film thickness. The advantage of the ellipsometry is its speed and accuracy [114]. A J.A. Wollam M2000 spectroscopic ellipsometer was used to measure the thickness of the SAMs used in this study. Porter *et al.* [131], Wang *et al.* [8] and Lee *et al.* [132] all used the ellipsometry to measure the thickness of SAMs on silicon substrates. Their measurements compared well with theoretical expectations.

### 2.2.4 Raman Spectroscopy

Ever since scientists began studying carbon, Raman spectroscopy has been widely used to investigate the structural and electronic properties of graphite and graphene [133-137]. Raman spectroscopy reveals a range of information such as the G-peak associated with the in-plane vibration mode of carbon  $sp^2$  bonding, the 2D-peak corresponding to the stacking order, as well as the D-peak, which is linked to damage to the graphene sheet. The G-peak in the Raman spectrum of graphene is a doubly degenerate (TO and LO) phonon mode ( $E_{2g}$  symmetry) of the Brillouin zone center [138]. Because the 2D-peak is sensitive to the stacking order of multiple layers, it can be used to determine the thickness of graphene, as well as its electronic structure [133, 139]. In addition, the D-peak is associated with phonon branches, which makes it useful for detecting damage in graphene sheets [133].

In this study a Raman spectrometer (Witec Alpha 300 micro-Raman confocal microscope,  $\lambda = 488$  nm) was used to check for the presence of graphene following its deposition on copper or silicon as well as on delamination surfaces. If graphene is present on a Si(111) surface, the G- and 2D-peaks should appear (Fig. 2.9) at approximately 1583



$\text{cm}^{-1}$  and  $2693 \text{ cm}^{-1}$ . These values can be affected multi-layers of graphene, residual stresses, and substrate effects [133, 134, 137, 139-144]. A silicon peak at  $1450 \text{ cm}^{-1}$ , associated with a higher vibration mode of silicon can also be observed.

### 2.3 FRACTURE SAMPLES

In order to understand the interactions between SAMs with COOH and NMe<sub>2</sub> end groups, hydroxylated silicon surfaces and graphene and silicon and graphene and copper or epoxy, four different types of sandwich specimens were prepared for the fracture experiments. The first type consisted of silicon strips terminated by SAMs with COOH and NMe<sub>2</sub> end groups that were brought into contact to make Si/COOH/NMe<sub>2</sub>/Si sandwiches. The interactions between the two functional groups are depicted in Figure 2.10a, as the possibility of ionic bonding. The second type of specimen was formed by bringing two hydroxylated silicon strips into contact to form Si/OH/H<sub>2</sub>O/OH/Si sandwiches. In semiconductor engineering, this is known as either hydrophilic bonding or wafer-to-wafer bonding [145, 146]. The possibility of several hydrogen bonding interactions appear in Fig. 2.10b as links between the hydroxyl groups with water molecules as well as hydrogen bonding between water molecules themselves. The third sandwich specimen consisted of graphene that had been transferred to silicon strips. The free graphene surface was bonded to a second silicon strip using an epoxy to form a Si/epoxy/graphene/Si laminate (Fig. 2.11). Because the bond between the epoxy and silicon was expected to be stronger, this scheme had the potential to separate the graphene from the silicon in a controlled manner. The last type of specimen consists of graphene-coated copper foil sandwiched between silicon strips with thin epoxy bond layers (Fig. 2.12). This will be used to obtain selective delamination between graphene

and copper or graphene and epoxy, as well as determining the adhesive interactions for each interface.

## **2.4 FRACTURE EXPERIMENTS**

This section describes the experiments that were used to delaminate the sandwich specimens just described in 2.3. Nominally mode I experiments were conducted with wedge (Fig. 2.13a) and double cantilever beam configurations (Fig. 2.13b). The former allowed the normal crack opening displacements (NCOD) to be measured with infrared crack opening interferometry (IR-COI), while the latter provided a larger range of applied displacement rates.

### **2.4.1 Wedge Tests**

Wedge tests were used to determine the interactions between COOH and NMe<sub>2</sub> SAMs, hydroxylated silicon strips and graphene that had been transferred to silicon. The test can be relatively easily augmented with the IR-COI making it possible to observe in real-time crack initiation and NCOD near a crack front. An IR microscope (Olympus-BH2-UMA) with a 2.5 $\times$  objective lens (M. Plan APO 2.5 $\times$ , Seiwa Optical America Inc.) was incorporated in the experiment as shown in Figure 2.13a. An IR camera (Lumenera Corporation, Infinity 3) with 1392 $\times$ 1040 pixels was used to record the interference fringes.

The wedge tests were conducted by inserting a 25  $\mu$ m-thick razor blade between the silicon strips of each of the sandwich specimens. It was manually driven in 0.2-mm loading steps, which were applied within 10 seconds and followed by a hold time of 20 seconds. During the 30 seconds associated with each load step, the interference fringes near the crack front were recorded every second using the time-lapse feature of the IR-camera.

### ***Infrared Crack Opening Interferometry***

A brief outline of IR-COI [147, 148] follows with a ray diagram (Fig. 2.14) that ascertains how interference can arise when monochromatic beams are reflected from the crack faces. Assuming that the opposing surfaces, A and B, are tilted at an angle  $\phi$  to one another and the gap between the two surfaces is filled with a medium with a refractive index  $n_2$ . Two different beams, SDP and SABCP, which are incident at point D on surface A and point B on surface B, respectively, are considered. Since the optical path length through several media is equal to the sum of the optical path-length in each medium, defined by  $n \cdot L$ , where,  $n$  is the refractive index of the medium and  $L$  is the path length in the medium. As a result, difference of the optical path length  $\delta_0$  between SABCP and SDP is

$$\delta_0 = [n_1(SA + CP) + n_2(AB + BC) - n_1(SD + DP)] \quad (2.1)$$

In addition, the distance AC is negligible compared to  $SD$  and  $DP$ , and then

$$n_1SD \approx n_1SA + n_2AE \quad (2.2)$$

$$n_1DP \approx n_1CP + n_2FC \quad (2.3)$$

By combining Equations (2.1), (2.2), and (2.3), Equation (2.1) can be simplified to

$$\delta_0 = n_2(EB + BF) = 2n_2\delta_n \cos \gamma \quad (2.4)$$

where  $\gamma$  is the angle of the incident ray on surface B and  $h$  is the vertical distance or separation distance between the two surfaces. Furthermore, the reflected light at point B results in retardation or a phase change of  $\lambda/2$  so that the total optical path difference between path SABCP and path SDP arriving at point P (interference point) is given by

$$\delta_0 = 2n_2\delta_n \cos \gamma + \lambda/2 \quad (2.5)$$

In addition, the destructive interference (dark fringes) occurs for

$$\delta_n = \frac{n\lambda}{2n_2 \cos \gamma}, \quad n = 0, 1, 2, 3, \dots \quad (2.6)$$

The constructive fringe (bright fringe) is represented by

$$\delta_n = \frac{(2n-1)\lambda}{4n_2 \cos \gamma}, \quad n = 1, 2, 3, \dots \quad (2.7)$$

Therefore, the NCOD for any gap filled with air ( $n_2 = 1.000293$ ) and normal incidence ( $\gamma \sim 0$ ) is represented by

$$\delta_n = \frac{n\lambda}{2}, \quad n = 0, 1, 2, 3, \dots \quad (2.8)$$

$$\delta_n = \frac{(2n-1)\lambda}{4}, \quad n = 1, 2, 3, \dots \quad (2.9)$$

By combining Equation (2.8) for the dark fringes and Equation (2.9) for the bright fringes, the whole displacement field can be assessed with a resolution of  $\lambda/4$ . In addition, measuring the light intensity between peaks and valleys allows the resolution in NCOD to be improved [24, 107, 108, 149]. Thus, the NCOD between fringes can be obtained by measuring the intensity  $I$  in

$$\frac{I}{I_{pp}} = \frac{1}{2} \left[ \pm 1 \mp \cos \left( \frac{4\pi |\delta_n|}{\lambda} \right) \right] \quad (2.10)$$

where  $I_{pp}$  is the peak-to-peak amplitude between the two fringes. The wavelength of light used here was  $1040 \pm 15$  nm, yielding a resolution of  $\lambda/4 = 260 \pm 4$  nm when bright and dark fringes were used. The resolution increased to 17 nm when intensity measurements were used to obtain the NCOD.

In order to verify the scheme just outlined for crack between silicon strips, three different experiments were. The first experiment was to observe Newton's rings which formed when a silicon strip was placed on a glass lens (Fig. 2.15a). The radius of the lens was estimated through

$$R = \frac{r_m^2}{\frac{2n+1}{2} \lambda} \quad (2.11)$$

where  $R$  is the radius of the lens,  $r_m$  is the location of each fringe from the center of the Newton's rings, and the index  $n = 0, 1, 2, 3, \dots$  is for the bright fringes and  $n = 0.5, 1.5, 2.5, 3.5, \dots$  is for the dark fringes. The spatial calibration factor for the  $2.5\times$  objective lens was  $2.638 \mu\text{m}/\text{pixel}$ . Using Equation (2.11), the radius of the lens was  $28.9 \pm 1.4 \text{ mm}$ , which compared well with the  $29.1\text{-mm}$  radius of the lens.

In the second case, a silicon strip was placed on a strip in four-point bending (Fig. 2.15b) and the anticlastic bending gave rise to the hyperbolic fringe pattern. The radius of curvature, measured using Equation (2.11), was  $182.2 \pm 1.3 \text{ mm}$ , which compared well with  $181 \text{ mm}$  predicted by simple beam theory. In addition, Poisson's ratio was extracted from the angle of inclination  $\theta$  of the hyperbolic fringes *via*

$$\nu = \frac{1}{\tan^2 \theta} \quad (2.12)$$

The measured value of Poisson's ratio was  $0.242$ , well within the range  $0.23$  to  $0.25$  [115, 116, 150-152] that has been reported for silicon.

The third experiment was to measure the gap between a silicon strip and an optical flat (Fig. 2.15c). The silicon strip was offset from the optical flat by a silicon chip at the right end so that the strip made an angle  $\theta$  with the flat. The fringes near the left end of the strip were used to determine the separation between the strip and the optical flat. The main objective of this experiment was to check the validity of Equation (2.10) between the line of contact of the strip and the first few fringes.

The thickness of the silicon chip was  $281.2 \mu\text{m}$  and the unsupported length  $L$  of the silicon strip was  $20.7 \text{ mm}$ . A perfectly flat strip yields an expected wedge angle of  $0.776^\circ$  for the straight line plotted in Figure 2.15c. The separation obtained from intensity measurements (Eq. 2.10) and fringes (Eq. 2.8-9) deviated from the straight line. In case the variation was due to a lack of flatness of the bottom surface of the silicon strip, its

surface profile was measured in a Zygo Optical Profilometer. The red error bars associated with these measurements were assigned to the  $\pm 50$  nm maximum roughness of the optical flat. It can be seen that Zygo profile was in excellent agreement with the IR-COI measurements near the contact line. The two measurements did deviate between the second and third fringes. This turned out to be due slight deviations between the intensity data and the fit to it in this region. Generally it was found that the fit to the intensity data was always excellent within the first fringe, so Equation 2.10 was only used for obtaining NCOD there and fringes were used further away.

### ***Mode I Wedge Fracture Experiments***

Figure 2.16a is a typical image of the crack front region where the darker region is still bonded and the fringes indicate the open part of the crack. The intensity in the bonded region was not uniform, which suggested that there was a background signal which should be subtracted out before making intensity measurements. The modified image (Fig. 2.16b) from subtracting out the background intensity resulted in a much more uniform intensity in the bonded region which made locating the crack front location a lot easier. Horizontal intensity profiles were extracted using ImageJ 1.47v (developed by the National Institutes of Health) and smoothed by a spline-fitting scheme that provided the best fit to any intensity plot (Fig. 2.16c). The location of the crack front was determined by the intersection (Fig. 2.16d) of the two straight lines that are the tangents to the fitted data near the crack front [107]. This crack front was taken to be the position of the first zero-dark fringe so that other peaks and valleys in the intensity plot corresponded to the location of the bright and dark fringes. Equations (2.8), (2.9) and (2.10) were used to convert all the intensity data to the NCOD values.

We define the crack length  $a$  by the distance between the crack front and the shoulder of the wedge (Fig. 2.13). This was made up of the initial crack length  $a_0$ , the amount of wedge insertion  $u_w$  and any crack growth  $\Delta a$  as

$$a = a_0 + \Delta a - u_w \quad (2.13)$$

where  $a_0$  is the original crack length associated with the distance between the initial crack front and the shoulder of the wedge,  $\Delta a$  is the distance from the location of new crack front to the location of the initial crack front.

To evaluate the adhesion energy or the fracture toughness, we calculated the J-integral corresponding to the measured crack length  $a$  in the fracture specimen. Based on simple beam theory, the J-integral under a wedge load is given by

$$J = \frac{3E_{si}h^3h_w^2}{16a^4} \quad (2.14)$$

where  $E_{si}$  is the in-plane Young's modulus for Si(111),  $h$  is the thickness of the silicon strip and  $h_w$  is the thickness of a razor blade. In the experiments conducted here, the crack lengths were such that  $a \gg 20h$ , which is sufficient for simple beam theory [106, 108]. For specimens that contained an epoxy layer, Equation (2.14) had to be modified to

$$J = \frac{3E_{si}h^3(h_w - h_e)^2}{16a^4} \quad (2.15)$$

where  $h_e$  was the thickness of the epoxy.

#### 2.4.2 Double Cantilever Beam Test

This configuration (Fig. 2.13b) was used delaminate graphene from copper foil or epoxy, where the rate of loading turned out to be key. The silicon strips on the outer surfaces of the laminate, which consisted of a symmetric layup of silicon, epoxy, graphene and copper, were bonded to aluminum tabs. These were attached to a servo

hydraulic loading device capable of providing a wider range of applied displacement rates. The reaction force was measured *via* a 10-lb load cell (LCHD-10, Omega Inc.) and it and the applied displacements were recorded *via* a user-defined data acquisition program. The upper epoxy layer terminated a short distance from the tabs and provided a rather blunt crack as the initial crack. This made using the peak load at initiation (Fig. 2.17) to determine toughness suspect, and the specimens were therefore quickly unloaded to produce much sharper initial cracks for subsequent loading and unloading cycles.

The load-displacement response was used to determine the adhesion energy as well as the strength and range of the interactions between delaminating surfaces. The simple beam theory expression for load-displacement response is

$$P = \frac{E_{Si}bh^3\Delta}{8a^3} \quad (2.16)$$

where  $P$  and  $\Delta$  are the applied load and displacement,  $E_{Si}$  is the in-plane Young's modulus of silicon (169 GPa),  $b$  is the width of the specimen,  $h$  is the thickness of each silicon strip and  $a$  is the crack length, measured from the loading point to the crack front. If there is no sub-critical crack growth prior to the critical force corresponding to steady state crack growth, Equation (2.16) should predict the initial slope of the load-displacement response. The corresponding value of the J-integral is given by

$$J = \frac{12a^2P^2}{E_{Si}b^2h^3} \quad (2.17)$$

Once the applied load reaches the critical load for steady state growth, the descending portion of the load-displacement response can be obtained by combining both Equations (2.16) and (2.17) to yield

$$P^2\Delta = \frac{E_{Si}^{1/2}b^2h^{3/2}}{\sqrt{27}}\Gamma_{ss}^{3/2}, \quad (2.18)$$



where  $\Gamma_{ss}$  is the steady state toughness or adhesion energy of the interaction.

### 2.4.3 Mixed-Mode Fracture

The only specimens to be separated under mixed-mode conditions were the silicon/COOH/NMe<sub>2</sub>/silicon specimens. An additional requirement for these samples was to be able test them in high vacuum, in order to remove as much water from the interface as possible while the specimens were being loaded. The three major components of the system are: a vacuum pump (Fig. 2.19), a vacuum chamber (Fig. 2.20), and a four-point bending loading device (Fig. 2.22), actuated by the piezoelectric actuator (PZT, P-216. 8SV PI Inc.) (Fig. 2.21).

The vacuum pump system (Fig. 2.19) consists of four major parts: a mechanical pump (A724-01-903), a turbo molecular pump (EXT 70H 24V), the control unit (TIC) and a wide range gage (WRG). The oil-free mechanical pump is able to reach up to  $\sim 10^{-1}$  Torr. To achieve higher vacuum levels, a turbo molecular pump (EXT-70H-24V) was attached to the mechanical pump, which extended the capability to an ultra-high vacuum ( $\sim 10^{-9}$  Torr). These two pumps were controlled by a TIC unit, which can be operated by the front input panel on the pump or by the TIC software installed in a PC. The WRG between the flexible bellows and the turbo molecular pump read the total pressure of the vacuum system.

The vacuum chamber contains a PZT actuator at the center of the chamber (Fig. 2.21) and has a three way cross as shown in Figure 2.20. The left one in Figure 2.20 was connected to a vacuum pump, and the one on the bottom of Figure 2.20 shows two feedthroughs corresponding to the PZT in/out and power source. The last one shown in

Figure 2.20 is a dead-end. The top of the vacuum chamber is covered by sapphire glass, which allows specimens to be observed with the IR-microscope.

The setup of the PZT actuator is described in Figure 2.21. As was explained in the previous session, the PZT actuator is mounted at the center of the chamber. The loading device consists of three major parts: the PZT actuator, a rigid block, and a carrier beam crossing above the rigid block.

The loading device consists of a PZT actuator which is used to apply a four-point bending load to a carrier beam. The PZT (P-216.8SV) with a UVH option and a ball tip (P-176.B16) is capable of operating at  $10^{-6}$  torr and, if necessary, 176 °C. To minimize or remove the transmission of a bending moment through the PZT, it is necessary to have a ball tip at the contact point between the PZT and the loading fixture. The PZT was bolted to the base of the chamber and its displacement was controlled by a control unit (E-509.S1 and E-517.11). The maximum operational voltage of the PZT is 1000 V, and it has 120- $\mu\text{m}$  travel range at zero load, which drops linearly to zero at 4500 N, as shown in Figure 2.23. The load and displacement ranges are controlled by the operational voltage [107]. The load and displacement ranges that can be applied to a structural element are modulated by its stiffness as can be seen for various carrier beams thicknesses. Selecting a 4 mm-thick carrier beam, the maximum travel distance (Fig. 2.23) is 110  $\mu\text{m}$ .

The PZT actuator applied the load to the carrier beam (Fig. 2.21) through its ball tip making contact with a very stiff block that then applied the load to the two bottom contact points of the carrier beam. The bottom surface of Si/COOH/NMe<sub>2</sub>/Si specimens was bonded to the carrier beam with super-glue so as to maintain a uniform and sufficiently strong bond between the specimen and the carrier beam. The free-body diagram (Fig. 2.22) shows how a uniform bending moment  $M = PL$  is applied to the

carrier beam. The load  $P$  is half of the total applied load and  $L$  is the distance between outer constraint point and the inner loading point.

If the crack length is much longer than the thickness of the silicon strips, the energy release rate of this loading configuration is given by

$$J = \frac{216E_s^2 I^2 \Delta^2}{L^2 E_{Si} (3N - 4L)^2 b^2} \left[ \frac{1}{h_1^3} - \frac{1}{(h_1 + h_2)^3} \right] \quad (2.19)$$

where  $E_{Si}$  is the in-plane Young's modulus (169 GPa),  $E_s$  is Young's modulus of the steel carrier beam (210 GPa),  $N$  is the distance (80 mm) between the left and right constraints  $L$  is the moment arm (9.5 mm),  $I$  is the moment of inertia associated with the carrier beam,  $h_1$  is the total thickness of the carrier beam and lower silicon strip attached on the carrier beam,  $h_2$  is the thickness of the upper silicon beam ( 250  $\mu\text{m}$  ), and  $\Delta$  is the displacement applied by the PZT. Equation (2.19), which reflects displacement control, was obtained by modifying Hutchinson and Suo's [153] expression

$$J = \frac{6P^2 L^2}{Eb^2} \left[ \frac{1}{h_1^3} - \frac{1}{(h_1 + h_2)^3} \right] \quad (2.20)$$

for load control.

## 2.5 CONTACT ANGLE MEASUREMENT

When a liquid drop is in equilibrium with the surface on which it rests, its surface makes a characteristic angle with the surface, known as the contact angle (Fig.2.24). This reflects equilibrium between adhesion and cohesion forces [154]. The former are due to the interaction between the liquid and the solid. The cohesion force is the attraction between molecules within the liquid and limits the amount that the liquid can spread. If the equilibrium contact angle  $\theta$  is less than  $90^\circ$ , then the solid surface is defined as being hydrophilic. Such surfaces have relatively high surface energies and tend to be more

adhesive in nature and promote wetting. Contact angles, greater than 90°, are considered to be hydrophobic, with lower surface energies, adhesiveness and wettability.

Solid (S), liquid (L) and vapor (V) phases are identified in Figure 2.24 in the vicinity of a water drop on a surface. Also identified are the interfacial energies between each phase. These are designated  $\gamma_{SV}$  for the interfacial energy between solid and vapor (called the surface free energy),  $\gamma_{SL}$  for the interfacial energy between solid and liquid (called the solid/liquid interfacial energy) and  $\gamma_{LV}$  for the interfacial energy between liquid and vapor (called the surface tension), respectively and are related by static equilibrium or Young's equation by

$$\gamma_{SV} = \gamma_{SL} + \gamma_{LV} \cos \theta. \quad (2.21)$$

The work of adhesion between a solid and a liquid is defined as the work required to separate the liquid from the solid and is given by

$$W_a = \gamma_{LV} + \gamma_{SV} - \gamma_{SL}. \quad (2.22)$$

It can also be obtained from the surface tension of the liquid by combining Young's equation with Equation (2.22) [154-156]. Thus

$$W_a = \gamma_{LV} (1 + \cos \theta). \quad (2.23)$$

Similarly, the work of cohesion is defined as the required work to separate the liquid into two separate liquids so that

$$W_c = 2\gamma_{LV}. \quad (2.24)$$

Fowkes [157] assumed that the components (dispersive, polar, hydrogen, acid-base) of the surface energy are additive so that

$$\gamma_{SV} = \gamma_{SV}^d + \gamma_{SV}^p + \gamma_{SV}^h + \gamma_{SV}^{ab} \quad (2.25)$$

where  $\gamma_{SV}^d$ ,  $\gamma_{SV}^p$ ,  $\gamma_{SV}^h$ , and  $\gamma_{SV}^{ab}$  are the dispersive, polar, hydrogen and acid-base components of the surface free energy. The second assumption was that the work of adhesion of each component of the surface energy was given by

$$W^d = 2\sqrt{\gamma_{LV}^d \gamma_{SV}^d} \quad (2.26)$$

$$W^p = 2\sqrt{\gamma_{LV}^p \gamma_{SV}^p} \quad (2.27)$$

$$W^h = 2\sqrt{\gamma_{LV}^h \gamma_{SV}^h} \quad (2.28)$$

As a result, if two surfaces have dispersive and polar interactions, then the work of adhesion can be described by the extended Fowkes equation [155] so that

$$W_a = W^d + W^p, \quad (2.29)$$

which can be extended to

$$W_a = \gamma_{LV} (1 + \cos \theta) = 2\sqrt{\gamma_{LV}^d \gamma_{SV}^d} + 2\sqrt{\gamma_{LV}^p \gamma_{SV}^p} \quad (2.30)$$

by coupling Equations (2.29), (2.23), (2.26) and (2.27). This suggests that the dispersive and polar components,  $\gamma_{SV}^d$ , and  $\gamma_{SV}^p$ , of the surface energy of a solid can be obtained by conducting contact angle experiments with two different liquids, if the dispersive and polar components of their surface tensions are known. Common liquids in this experiment are diiodomethane as an apolar liquid (L1) and DI water as a polar liquid (L2), whose surface tensions are summarized in Table 2.1. This, along with the measured contact angles, provides two equations,

$$\gamma_{SV}^d = \frac{1}{4} \gamma_{LV1}^d (1 + \cos \theta_{LV1})^2 \quad (2.31)$$

$$\gamma_{LV2} (1 + \cos \theta_{LV2}) = 2\sqrt{\gamma_{SV}^d \gamma_{LV2}^d} + 2\sqrt{\gamma_{SV}^p \gamma_{LV2}^p} \quad (2.32)$$

for the unknown components  $\gamma_{SV}^d$  and  $\gamma_{SV}^p$  of the surface energy of the solid.

Van Oss *et al.* [158] indicated that, in general, three liquids are required to determine the surface energy of solids. This is based on the decomposition of the surface energy into a Lifshitz-van der Waals component that includes the dispersion (London), orientation (Keesom) and induction (Debye) interactions in the condensed state (the same as Fowkes' dispersion energy) and a polar component. The polar or Lewis acid-base or electron-acceptor/electron donor interactions are intrinsically asymmetrical and thus non-

additive. Thus, if  $\gamma^+$  and  $\gamma^-$  are designated as electron-acceptor and electron-donor components of the acid/base interaction, Young's equation (2.30) is modified [158] as follows

$$W_a = \gamma_{LV} (1 + \cos \theta) = 2\sqrt{\gamma_{LV}^d \gamma_{SV}^d} + 2\sqrt{\gamma_{LV}^+ \gamma_{SV}^-} + 2\sqrt{\gamma_{LV}^- \gamma_{SV}^+} \quad (2.33)$$

In order to measure each component of the surface energy in Equation (3.23) it is necessary to measure the contact angle with three different liquids. Commonly, an apolar liquid (L1) and two polar liquids (L2 & L3) are used [158] so diiodomethane, water, and glycerol, respectively were chosen for this work. Thus

$$\gamma_{SV}^d = \frac{1}{4} \gamma_{LV1}^d (1 + \cos \theta_{LV1})^2 \quad (2.38)$$

$$\gamma_{LV2} (1 + \cos \theta_{LV2}) = 2\sqrt{\gamma_{SV}^d \gamma_{LV2}^d} + 2\sqrt{\gamma_{SV}^+ \gamma_{LV2}^-} + 2\sqrt{\gamma_{SV}^- \gamma_{LV2}^+} \quad (2.39)$$

$$\gamma_{LV3} (1 + \cos \theta_{LV3}) = 2\sqrt{\gamma_{SV}^d \gamma_{LV3}^d} + 2\sqrt{\gamma_{SV}^+ \gamma_{LV3}^-} + 2\sqrt{\gamma_{SV}^- \gamma_{LV3}^+} \quad (2.40)$$

The three equations (3.28), (3.29), and (3.30) with the measured contact angles  $\theta_{LV1}, \theta_{LV2}, \theta_{LV3}$  and known properties of all three liquids can be solved for the components  $\gamma_{SV}^d$ ,  $\gamma_{SV}^+$ , and  $\gamma_{SV}^-$  of the surface energy of the solid phase.

## 2.5 TRACTION SEPARATION RELATIONS

The traction-separation relations representing the interactions between COOH and NMe2 SAMs, hydroxylated silicon surfaces and graphene and copper, graphene and epoxy and graphene and silicon were determined directly [97, 102, 104] or by an iterative, inverse approach [106, 159]. In the case of interactions between hydroxylated silicon surfaces, a combination of the two approaches was used.

The direct approach relies on the path independence of the J-integral and measurements of the NCOD at the end of the cohesive zone, or the end-opening

displacement, (Fig. 2.25). The J-integral from a local contour surrounding the cohesive zone under mode I conditions is

$$J = \int_0^{\delta_n^*} \sigma(\delta_n) d\delta_n \quad (2.41)$$

where  $\sigma$  is the normal traction acting on the crack faces in the cohesive zone, and  $\sigma(\delta_n)$  is the normal traction-separation relation that must be determined. By taking the derivative of Equation (2.41) with respect to  $\delta_n^*$ , the traction-separation relation is

$$\sigma(\delta_n) = \frac{\partial J}{\partial \delta_n^*} \quad (2.42)$$

In view of the path independence of the J-integral, the measured values of the J-integral in Equation (2.42) were obtained by making use of Equation (2.14) or (2.15) and  $\delta_n^*$  was obtained from NCOD profiles. [107].

The direct, indirect, and hybrid approaches made use of cohesive zone modeling modules in the finite element code ABAQUS<sup>®</sup>. The three different approaches implemented there are the so-called tabular, bilinear and exponential forms (Fig. 2.26). The tabular form was more suitable to the hydrophilic bonding problem (Chapter 4) because portions of the traction-separation relations could be measured using the direct approach. The exponential form was used in the investigation of interactions between graphene and silicon (Chapter 6), mainly because the measured resistance curves were informative. The bilinear form was used for modeling interactions between graphene and copper and graphene and epoxy (Chapter 7), where there were fewer local measurements to compare solutions with and the shape of the traction-separation relation was less revealing. At the same time, using all three options provided a richer understanding of the parameter identification process.

As a cracked body is loaded, the cohesive zone (Fig. 2.25) begins to develop ( $c$  increases) without any change in the open crack length  $a$ . In this regime, the traction

and separation are increasing elastically with the initial stiffness ( $K$ ). Damage initiates when the maximum strength  $\sigma_0$  is reached at an end opening  $\delta_n^0$ . A damage parameter ( $0 \leq D \leq 1$ ) is then introduced in order to track the evolution of damage in the cohesive zone. Generally speaking, the evolution of damage (Fig. 2.26) is defined as the ratio of the traction in the softening regime to the traction, at the same separation, had there been no damage. That is

$$D = 1 - \frac{\sigma_d(\delta)}{\sigma_u(\delta)}, \quad (2.43)$$

where  $\sigma_d(\delta)$  reflects the damaged response,  $\sigma_u(\delta)$  is the elastic response  $\sigma_u(\delta) = K\delta$  and  $K$  is the stiffness of the elastic response. The form given in Equation (2.43) is useful when the tabular form is being used. The equivalent analytical forms for the bilinear (Fig. 2.26a) and the exponential (Fig. 2.26b) forms are, respectively

$$D = \frac{\delta_n^c(\delta - \delta_n^0)}{\delta(\delta_n^c - \delta_n^0)} \quad (2.44)$$

and

$$D = 1 - \frac{\delta_n^0}{\delta} \left[ 1 - \frac{1 - \exp\left(-\alpha \frac{\delta - \delta_n^0}{\delta_n^c - \delta_n^0}\right)}{1 - \exp(-\alpha)} \right], \quad (2.45)$$

where  $\delta$  is the separation distance,  $\delta_n^0$  is the separation distance for damage initiation,  $\delta_n^c$  is the critical separation distance, and  $\alpha$  reflects the strength of the decay of the tractions during the evolution of damage.

In all cases, when  $\delta = \delta_n^c$ , the traction  $\sigma_d(\delta) = 0$ , and  $D = 1$  and the material at that location is fully damaged. The damage process is irreversible so that if there is any unloading prior to complete damage, the damage parameter ( $D$ ) remains constant and



stress decreases linearly with a slope of  $(1-D)K$  during unloading. Subsequent reloading occurs elastically and follows the same slope until the damaged response of the traction-separation relation is rejoined and damage evolution proceeds. If there is combined loading such as normal and shear loads along interface, the opening displacement should be effective displacement denoted by

$$\delta = \sqrt{\delta_n^2 + \delta_s^2 + \delta_{ts}^2} \quad (2.46)$$

where  $\delta_n$  is the separation distance normal to the fracture surface,  $\delta_s$  is the separation distance for shear direction, and  $\delta_{ts}$  is the separation distance for transverse shear direction. In the current work, Mode I fracture was simulated for hydrophilic interaction, graphene/silicon interactions, graphene/copper and graphene/epoxy interaction in Chapter4, 6 and 7.

## Chapter 3 Interactions between Self-Assembled Monolayers<sup>4</sup>

Molecular interactions between COOH and NMe<sub>2</sub> SAMs were explored *via* fracture mechanics concepts. This required high quality SAMs to be deposited over relatively large spatial domains. A significant effort was made using a combination of XPS, AFM, ellipsometry and contact angle measurements to ensure that monolayers of each SAM were deposited on silicon strips prior to bringing the functionalized surfaces together. The silicon strips were then separated in Mode I and mixed-mode fracture experiments under ambient and high vacuum conditions and the locus of fracture was determined *via* XPS of the fracture surfaces.

### 3.1 SAM DIAGNOSTICS

This section provides the details of the XPS, AFM, ellipsometry and contact angle measurements of the SAMs prior to bonding.

#### 3.1.1 XPS

XPS was used to determine the chemical composition of the functionalized silicon strips following each step in the deposition of the SAMs. Survey scans were used to identify all the elements on the surface and high resolution scans were used to focus on specific components of the monolayers. [160].

The survey scans of Si(CH<sub>2</sub>)<sub>10</sub>(CO)(CH<sub>2</sub>)(CF<sub>3</sub>), Si(CH<sub>2</sub>)<sub>10</sub>(CO)OH, and Si(CH<sub>2</sub>)<sub>10</sub>(CO)(NH)(CH<sub>2</sub>)<sub>2</sub>NMe<sub>2</sub> SAMs are shown in Figure 3.1. As expected, silicon, oxygen and carbon signals were present in each one. Fluorine was present in the CF<sub>3</sub> SAMs (Fig. 3.1, black line) as indicated by the peak at 689 eV. Because fluorine does not exist in air, its appearance in the survey scan confirmed that the deposition of CF<sub>3</sub>-SAMs

---

<sup>4</sup> The contents in this chapter were published in Experimental Mechanics: K.M. Liechti, S.R. Na, M. Wakamatsu, O. Seitz and Y. Chabal "A High Vacuum Fracture Facility for Molecular Interactions," Experimental Mechanics, vol. 53, pp. 231-241, 2013/02/01 2013.

was successful. At the same time, the fluorine peak was absent from the spectra obtained from the COOH and NMe2 SAMs (blue and red lines, respectively). It was concluded that the trifluoroethyl ester moiety in the CF<sub>3</sub> SAMs was converted to a COOH functional group and dimethylamino ethyl amide moieties, respectively. Further evidence that the CF<sub>3</sub> SAMs were properly transformed to dimethylamino ethyl amide moieties (NMe2) was the existence of the nitrogen peak at 400 eV. High resolution scans are now considered for each of the SAMs.

High resolution scans for any fluorine and carbon 1s peaks in the CF<sub>3</sub> SAM are shown in Figure 3.2. The fluorine peak was clearly present at 689.2 eV (Fig. 3.2a). The presence of the carbon 1s peaks could be seen (Fig. 3.2b) in the alkyl chain (CH<sub>2</sub>)<sub>10</sub> at 285.2 eV, CH<sub>2</sub> group at 288.4 eV, C=O at 290 eV, and CF<sub>3</sub> at 293.7 eV. The carbon 1s peak in the COOH SAMs is shown in Figure 3.3a with two main peaks: (CH<sub>2</sub>)<sub>10</sub> at 285.4 eV and C=O double bonding at 290.1 eV, respectively. There were no signals indicating CH<sub>2</sub> and CF<sub>3</sub> in COOH SAMs. The absence of C-F bonds verified that the trifluoroethyl ester moiety was converted to the acid moiety. The NMe2 SAMs had a (CH<sub>2</sub>)<sub>10</sub> peak at 285.75 eV, a CH<sub>3</sub> peak at 287 eV, a C-N peak at 288.6 eV, a C=O peak at 290 eV and a C-F peak at 293.8 eV (Fig. 3.3b). The existence of C-F single bonding at 293.8 eV indicates that a negligible amount of fluorine, undetected in the survey scan, could be seen. This suggests that the conversion from CF<sub>3</sub> to NMe2-terminated SAMs was not quite complete. The high resolution XPS scan for the N 1s peak (Fig. 3.3c) brought out the C-N-C single bonding at 401 eV, which was not present in the CF<sub>3</sub> and COOH SAMs. The conclusion from all the scans was that the proper elements were present in each SAM, which is the first step towards realizing the presence of monolayers.

### 3.1.2 AFM

Once the chemical composition of each SAM was verified by the XPS survey scan and high-resolution scans, the RMS roughness of each SAM was measured as a measure of uniformity. AFM was able to identify defects such as islands, voids and clusters, which all gave rise to RMS roughness values that were greater than 0.5 nm over the scanned area. The tapping mode was employed in all cases in order to diminish the potential for damage.

The scans were conducted over regions that were  $6\times 6$  and  $0.6\times 0.6$   $\mu\text{m}$ . Since there is a greater probability of encountering defects over larger areas, consistency in the RMS roughness is another indicator of monolayer formation. The values of the roughness for bare silicon and the three SAMs are shown in Table 3.1. The RMS values for bare silicon were 0.306 nm and 0.206 nm over the  $6\times 6$  and  $0.6\times 0.6$   $\mu\text{m}$  regions, respectively. The RMS roughness values of the SAMs were consistent with those of bare Si(111) surfaces. The largest deviation in RMS roughness between the large and smaller area scans occurred for the  $\text{CH}_3$  SAMs at 0.512 nm vs. 0.289 nm. Thus it was concluded that the deposition scheme was giving rise to uniform films. Because the films were so uniform it was not possible to measure their thickness by scanning over voids or islands and it was left to ellipsometry to establish the presence of monolayers.

### 3.1.3 Ellipsometry

The thickness of monolayers can be theoretically estimated by accounting for the bonding lengths between each atom pair. The expected values, which did not account for the characteristic tilt of each SAM, are shown in Table 2.2 and range from 2.238, to 2.204 and 2.57 nm for the  $\text{CF}_3$ ,  $\text{COOH}$  and  $\text{NMe}_2$  terminated SAMs, respectively. The measured values were 2.21 nm, 1.94 nm, and 2.46 nm. There is some uncertainty in the refractive index in each case, which is required for the model to determine thickness.

Nonetheless the level of uncertainty was not enough to influence the conclusion that monolayers were formed in each case.

### 3.1.4 Contact Angles

The combination of XPS, AFM, and ellipsometry confirmed that the SAMs had been deposited as monolayers. Contact angle measurements are not as discriminating as three measurements just cited, but they do provide an indication as to the hydrophilic or hydrophobic nature of the functionalized surface. The COOH SAMs have both C=O double bonding and C-OH single bonding within the functional group. This suggests that they could be hydrophilic because of the presence of negatively charged hydroxyl groups (OH), which are strongly hydrophilic. The functional group of the NMe<sub>2</sub> SAMs contains hydrophobic CH<sub>3</sub> groups, so these SAMs were expected to be more hydrophobic. Godawat *et al.* [161] studied the wettability of a wide range of molecules (CF<sub>3</sub>, CH<sub>3</sub>, OH, CONH<sub>2</sub>, etc.) based on extensive molecular dynamics simulations. The CH<sub>3</sub> group was indeed hydrophobic, but the CONH<sub>2</sub> group was more hydrophilic due to the presence of nitrogen. Thus it might be expected that NMe<sub>2</sub> SAMs would be more hydrophobic than COOH SAMs.

The contact angles of oxidized Si(111) surfaces as well as those functionalized by SAMs terminated by COOH and NMe<sub>2</sub> groups were measured over 60-second intervals (Fig. 3.4). The contact angles decreased slightly over this time period and were almost static at the end with values of 44, 56 and 65° for Si(111), COOH SAMs and NMe<sub>2</sub> SAMs, respectively. According to the definition of hydrophilicity ( $\theta < 90^\circ$ ), all surfaces were hydrophilic. However, the NMe<sub>2</sub> SAMs were more hydrophobic as expected from Gadawat's work [161].

### 3.1.5 Fabrication of Si/COOH/NMe<sub>2</sub>/Si Laminates

Silicon strips (45×5 mm) were coated with COOH and NMe<sub>2</sub> SAMs and brought into contact in the presence of DI water. The primary bonding between the two surfaces was expected to be ionic [114]. The COOH SAMs are negatively charged whereas NMe<sub>2</sub> SAMs are positively charged. A schematic of the ionic bonding is depicted in Figure 2.10a. In addition, it is possible that hydrogen bonding, which forms electromagnetic attractive interactions between hydrogen atoms and highly electro-negative ones such as oxygen, fluorine and nitrogen [162] would occur.

If the two surfaces are brought into contact under ambient or vacuum conditions, no bonding occurs. Preliminary trials established that an active medium is needed for the ionic bonding associated with proton transfer and the hydrogen bonding resulting from attractive electromagnetic interactions. In this study, the bonding was obtained *via* DI water. Each COOH-terminated silicon strip was completely covered by one droplet of fresh-DI water by virtue of its hydrophilic nature. An NMe<sub>2</sub>-terminated silicon strip was then placed on top of the first strip and bonding was activated by gently squeezing the strips together. The resulting Si/COOH/NMe<sub>2</sub>/Si laminate was cured for one day under ambient conditions, in order to obtain maximum bonding strength. In addition, some ambient-cured specimens were subjected to high vacuum ( $\sim 3 \times 10^{-7}$  Torr) for one day, so as to compare the interactions between strips that were cured under the two conditions.

### 3.2 MODE I FRACTURE

Wedge tests were conducted on the ambient and vacuum-cured Si/COOH/NMe<sub>2</sub>/Si laminates. The NCOD near the crack front were recorded at each loading step and were used to extract the traction-separation relations that represented the interactions between the COOH and NMe<sub>2</sub> SAMs, XPS was then used to examine the fracture surfaces so as to define the fracture path.

During an experiment, a 25- $\mu\text{m}$  thick metal shim was gradually driven (Fig. 2.13a) between the silicon strips. A series of fringes that were obtained during one such experiment are shown in Figure 3.5. The applied wedge displacement is shown at the top of each image, whose field view was  $1.5 \times 1.2$  mm. On the right side of each image, there are a series of fringes corresponding to the crack opening displacement. As the wedge was driven further from right to left, the density of the fringes first increased. Gradual movement of the crack front to the left followed and growth ended with an unstable jump out of the field of view at a wedge insertion  $u_w$  of 5.0 mm. The intensity profiles taken along the center of six of the images are shown in Figure 3.6a. They all had the same intensity in the bonded region and the increase in the density of the fringes can be seen as the wedge was inserted. The background signal was removed by subtraction (Fig. 3.6b) and this made it easier to locate the crack front (see insert) [107].

The NCOD profiles associated with each intensity plot are presented in Figures 3.7a,b for ambient and vacuum-cured specimens. The crack front remained stationary as the wedge was first inserted, but then its subsequent growth could be tracked, along with the NCOD, prior to the unstable jump that ended the test. The crack length data from the intensity profiles was combined with the wedge insertion measurements to obtain the variation in crack length with wedge insertion (Fig. 3.8) for several ambient and vacuum-cured specimens. The response was initially linear as the wedge was inserted without any crack growth. In two of the ambient-cured specimens, there was a gradual transition to steady state behavior, which is marked by a flat or zero slope response, where the crack extension matched each wedge insertion. In the other cases, there was no extended period of steady state growth and the cracks jumped prior to arrest with a concomitant drop in energy available for fracture.

The relatively high resolution of the crack length measurements combined with Eq. (2.14) allowed delamination resistance curves (Fig. 3.9) to be obtained for this relatively brittle interface. For the ambient-cured specimens (Fig. 3.9a), the lack of crack growth, defined by the resolution in crack extension measurements, gave rise to a vertical rise in the J-integral up to  $20 \sim 40 \text{ mJ/m}^2$ . After this, about 30-40  $\mu\text{m}$  of stable crack growth was observed with a relatively small increase in the J-integral. This phase was followed by a steeper increase in the J-integral to about  $60 \sim 100 \text{ mJ/m}^2$ . The increase in J-integral leveled off thereafter, providing a measure of the steady state adhesion energy,  $\Gamma_{ss}$  ( $110\text{-}157 \text{ mJ/m}^2$ ) prior to the onset of unstable growth, marked by the last data point in each case. A somewhat similar pattern of growth was observed for the two tests on vacuum-cured samples (Fig. 3.9b). The initial rise or pop-in values of the J-integral were about  $20 \text{ mJ/m}^2$  higher and the steady state adhesion energy ranged from 125 to 147  $\text{mJ/m}^2$ . Thus it appears that the vacuum cure did not really change the adhesion energy of the interaction.

In preparation for determining the traction-separation relations, the variation in the J-integral with the end opening displacement,  $\delta_n^*$  was obtained from the NCOD profiles and Eq. (2.14). The trends (Fig. 3. 10) bear some resemblance to the resistance curves with an initially steep rise in resistance to delamination followed by a gradual transition to steady state and then unstable growth. A central difference scheme was used to differentiate the data in accordance with Eq. (2.42). The resulting traction-separation relations (Fig. 3.11) displayed a notable difference between the ambient and vacuum-cured conditions. The maximum strength (4.7-5.7 MPa) was much higher under vacuum and occurred at separations of 26-33 nm. The corresponding values under ambient conditions were 1.5-2.2 MPa and 54 nm. The interaction range was about the same in both cases at approximately 120 nm, but the area under the steep rise and fall of the



traction-separation relations under vacuum was about the same as that encountered by the broader response under ambient, making the adhesion energies quite similar.

### **3.3 MIXED MODE FRACTURE**

In this case, the Si/COOH/NMe<sub>2</sub>/Si sandwich specimens were bonded with a very thin layer of cyanoacrylate adhesive (super glue) to a stainless steel carrier beam that was loaded in four-point bending under ambient or high vacuum (Fig. 2.21) conditions. A piezoelectric actuator provided displacement-controlled loading of the carrier beam.

A series of images of fringe patterns associated with the applied displacement levels under ambient conditions appear in Figure 3.12. The level of the applied displacement was noted in each image, whose field view was about  $3.7 \times 2.8$  mm. There are several fringes to the right side of each image and the arrangement of fringes moves, as the displacement increases, towards the crack front on the left. Some stable growth can be seen up to an applied displacement of 50  $\mu$ m, at which point the crack jumped forward and arrested. The specimen was fully unloaded but the crack front did not return to the original location.

In order to obtain the NCOD profiles at each recorded interval, the intensity of the given fringes was obtained by averaging all the intensities taken along pixel rows within the red box shown in Figure 3.12. The averaged intensity profiles for several applied displacement levels appear in Figure 3.13a. The background signal was subtracted out in order to better define the crack front. As a result and as shown in Figure 3.13b, the signal to noise ratio ahead of the crack front was significantly reduced and made it easier to determine the location of the crack front as illustrated in Figure 3.13c, where the location of the crack front was defined by the intersection of the straight lines that represented the intensity near the crack front. The error in locating the crack front was chosen to be the

distance between the points of tangency (Fig. 3.13c). The NCOD were obtained as a function of distance from the crack front by using the same smooth-fitting spline scheme to fit the subtracted intensity profile shown in Figure 3.13d in conjunction with Eq. (2.8-10). The raw and subtracted intensity profiles are presented in Figure 3.13d for comparison.

A series of NCOD profiles are shown as a function of the applied displacement under ambient (Fig. 3.14a) and high vacuum (Fig. 3.14b) conditions. The vacuum level was typically ( $3 \times 10^{-7}$  Torr). There was usually some initial opening prior to the application of the load due to slight differences in flatness between the silicon strips and the carrier beam. The amount of crack growth under ambient conditions was slightly greater than under high vacuum.

With the relatively high resolution of the crack front provided by IR-COI, it was possible to track the variation of J-integral with the crack extension, shown in Figure 3.15a, under ambient and high vacuum conditions. Once the loads were applied, in both cases, crack growth increments of about 20  $\mu\text{m}$  were detected almost immediately. In addition, the increase in J-integral values up to approximately 400  $\text{mJ/m}^2$  was nearly the same in all tests. Thereafter, the high-vacuum sample exhibited more resistance to growth without the extended period of steady state growth that was apparent under ambient. At the fracture mode-mix of  $50^\circ$  provided by this specimen fast fracture occurred at 1.4 and 1.7  $\text{J/m}^2$  for the ambient and high vacuum samples. This was an order of magnitude higher than the pure mode I adhesion energy.

In preparation for obtaining the traction-separation relations under mixed-mode loading, the variation of the J-integral with the normal end-opening displacement  $\delta_n^*$  is shown in Figure 3.15b. The rise in the J-integral for initial values of  $\delta_n^*$  was again more dominant in the high-vacuum samples. The traction-separation relations associated with

ambient and high vacuum conditions were determined by applying Equation (2.23) applying a central difference scheme to the raw data (Fig. 3.15b). The resulting traction-separation relations are shown in Figure 3.16. The maximum strength in the high-vacuum condition was significantly higher (34 ~ 37 MPa) than the ambient one (10~13 MPa). The corresponding crack opening displacements were 51 nm and 82 nm for the ambient condition and 48 nm and 60 nm for the high-vacuum conditions, respectively. In addition, the initial stiffness of the high vacuum cured specimens was greater than that of the ambient-cured specimens. Both sets of interactions had relatively long tails to them, making it difficult in each case to determine the critical crack openings. The critical opening displacement for both cases appeared to be in the 400-nm range.

### 3.4 FRACTURE SURFACE ANALYSIS

In an attempt to understand the mechanisms underlying the measured traction-separation relations obtained for each condition, each fracture surface was scanned with high-resolution XPS. Because this technique identifies chemical species present on surfaces, there is the potential to determine the weak link in the COOH/NMe<sub>2</sub> interactions as the surfaces were brought together and then separated.

High-resolution XPS scans of the ambient-cured specimen were conducted on the surfaces of the silicon strips that had been functionalized with COOH and NMe<sub>2</sub> SAMs (Fig. 3.17); these will be designated as the COOH and NMe<sub>2</sub> fracture surfaces in the discussion that follows in spite of the fact that their surface chemistry might have changed. The scans on the COOH surfaces of specimens that had been exposed to ambient showed no signs of nitrogen in either C-N-C or C-N-O bonding at 401.2 and 403.3 eV, respectively. Nitrogen was present in C-N-C bonding on the NMe<sub>2</sub> surface of specimens exposed to ambient conditions, but there was only slight evidence of C-N-O

bonding in a relatively weak peak. This suggests (Fig 3.18a) that the weak link between the SAMs under ambient conditions was the ionic and or hydrogen bonding between the functional groups.

The situation just described switched dramatically when the fracture surfaces of specimens that were subjected to high vacuum were examined. First the NMe<sub>2</sub> surface had two equally prominent peaks corresponding to C-N-C and C-N-O bonding. The mechanism for the latter is unknown at this time. There was also evidence of nitrogen in C-N-C on the COOH surface, which had none prior to bonding. The presence of such bonding suggests that bond breaking occurred somewhere along the alky chain of the COOH SAM. The presence of nitrogen on both fracture surfaces suggests a wavy fracture surface (Fig. 3. 18b) with bond breaks sometimes occurring in the COOH SAM and sometimes in the NMe<sub>2</sub> SAM.

### **3.5 DISCUSSION**

The differences in the adhesion energy and traction-separation relations under mode I and mixed-mode conditions in specimens cured under ambient or high vacuum conditions raises a number of interesting questions. First, for a given mode-mix, the adhesion energies were approximately the same for samples bonded and broken in either ambient or vacuum environments. Nonetheless, the traction-separation relations were quite different. The effect of mode-mix on the adhesion energy was marked by a tenfold increase in adhesion energy, irrespective of the bonding and separation environment. In the past, it has been noted that the introduction of shear stresses increased the adhesion energy of glass/epoxy interfaces [163] due to increases in the viscoplastic dissipation in the epoxy [24, 25, 149]. In these cases the intrinsic toughness of the interfaces and the associated traction-separation relations were independent of fracture mode-mix. Asperity

locking [164] has also been suggested as a shear toughening mechanism. In both cases, the toughening mechanism can be viewed as being extrinsic to the interface. However, when SAMs were used to link sapphire to epoxy [23], the intrinsic toughness of the interface increased with mode-mix with no plastic dissipation in the epoxy. The SAM lowered the maximum strength of the interaction below the yield strength of the epoxy at all mode-mixes. In the current case, only SAMs were present and the intrinsic toughness can be viewed as being mode-mix dependent. Thinking about SAMs being loaded in tension or shear, it is certainly possible that more configuration changes are possible in shear with *cis*↔*trans* switching [165], for example, and these may dissipate energy. Zhang *et al.* [166] and Wang *et al.* [167] have studied the deformation of the SAMs on a rigid substrate under applied shear displacement. Their MD simulations revealed that atomic stick-slip behavior between SAMs is governed by the relative motion of the functional group as well as jumping of the head group from its original location to an adjacent one. Such mechanisms may also be at play during mixed-mode fracture between SAMs.

Going beyond adhesion energies to the details of the traction-separation relations, the initial stiffness and maximum strength of the specimens that were subjected to high vacuum were approximately twice the values encountered for ambient conditioning. The first thought might be that high vacuum was removing molecular levels of water and allowing more intimate interactions to occur. However, XPS evidence of C-N-O bonding in addition to the expected C-N-C bonding in the NMe<sub>2</sub> head group suggests that vacuum also triggered a chemical reaction with potentially stronger interactions. Although high vacuum led to higher strength, the loss of strength following damage initiation was more dramatic and the broader response (lower stiffness coupled with gentler decay) under ambient conditions led to adhesion energies that were quite similar for both conditions.

The maximum strengths of 5 and 40 MPa encountered under vacuum conditions for mode I and mixed-mode conditions, respectively, are lower than the greater than 100 MPa expected for ionic or hydrogen bonding. This may be due to the 20-nm resolution of the IR-COI employed in this study, which would be unable to resolve higher strengths if they were indeed present. This issue was taken up in Chapters 4 and 5 in dealing with hydrophilic bonding and graphene silicon interactions, respectively.

Finally, the question still remains as to the precise nature of the bonding that was actually encountered as the COOH and NMe<sub>2</sub> SAMs were brought into contact. In addition to the expected ionic and hydrogen bonding interactions, there was evidence of chemical bonding. Such additional complexity may be resolved by Attenuated Total Reflectance Fourier Transform Infrared (ATR-FTIR) Spectroscopy [168, 169] which can be used to determine the nature of interactions between functionalized silicon surfaces and detect any evidence of trapped water in the bonded state *in situ*. The results of such investigations could then be compared with XPS and other studies of the fracture surfaces in order to obtain a more complete picture of bond formation and breakage.

## Chapter 4 Hydrophilic Bonding between Silicon Strips

Wafer bonding technology, which often bonds two separate wafers without additional adhesive agents between wafers has been a cornerstone of the semi-conductor industry [27, 28] because it allows for effective interconnection of stacked three-dimensional wafer structures. The understanding of the chemistry of wafer bonding is quite mature [27-29, 33-36, 145, 146, 170-176] and fracture mechanics approaches have been used [27, 28, 36, 175, 176] to determine the toughness associated with various processing steps such as ambient curing, annealing, plasma treatments, etc. As a result, room temperature hydrophilic bonding seemed to provide a natural vehicle for strengthening and validating some of the observations that were made in the previous chapter regarding interactions between SAMs. The strength and interaction range associated with ambient hydrophilic bonding have been examined *via* MD simulations [37], where interaction potentials were developed to determine the molecular interactions between water and hydroxylated silicon or native silicon oxide. The MD simulations captured the repulsive and adhesive forces in terms of separation distances which had ranges of several nano meters as the water coverage or relative humidity was varied. Nonetheless, such interactions have not been characterized at the continuum level *via* traction-separation relations, thereby further motivating the current study.

### 4.1 SAMPLE PREPARATION

Figure 4.1 illustrates how hydrophilic bonding of silicon wafers occurs [27]. Once the two treated wafers are brought into contact and tapped at their center, hydrophilic bonding initiates and propagates uniformly until the entire wafer is bonded; the propagation of the bonding front is known as the bonding wave. This initial bonding can subsequently be strengthened by heating or annealing the assembly. Christiansen *et al.*

and Tong *et al.* [28, 33] reported that the fracture toughness of hydrophilic bonding below 100 °C was less than 300 mJ/m<sup>2</sup>. From 100 °C to 200 °C, the bonding energy increased rapidly to approximately 1200 mJ/m<sup>2</sup> and remained constant up to 800 °C. Below 100 °C, the main bonding mechanism is hydrogen bonding. Covalent bonding between silicon and oxygen and the formation of hydrogen gas molecules is dominant at higher temperatures. The range of values reported reflects a number of possible chemical reactions between silicon, oxygen and hydrogen, which are now described in more detail.

The schematic shown in Figure 2.10b depicts the situation that first arises when hydroxyl terminated silicon surfaces are brought together in the presence of water molecules. The main interaction at this stage is reversible hydrogen bonding between oxygen and hydrogen atoms. Once heat is applied, the interactions become covalent through the polymerization reaction [28]



which is a reversible process below 400 °C [28, 176]. However, above 400 °C, the water molecules produced during polymerization can diffuse through bulk silicon to form silicon oxide and release hydrogen gas through the reaction



In this process, the fracture toughness increases by a factor of six over the value at the initial bonding state. In the current work, hydrophilic bonding under ambient conditions is explored in order to understand the role of water molecules between contacting silicon surfaces. Thus hydrogen bonding is expected.

In this work, the initial step in preparing the silicon surfaces for bonding was to remove any contaminants. This was followed by a piranha (a mixture of 5ml of H<sub>2</sub>O<sub>2</sub> and 15 ml of H<sub>2</sub>SO<sub>4</sub>) treatment, which results in OH<sup>-</sup> termination of the wafer surface. The presence of these hydroxyl groups on silicon wafers gives rise to very strong hydrophilic



behavior or very small contact angles. The second step was to activate the bonding by bringing two hydroxyl terminated silicon strips into contact. However, in order to obtain more effective bonding, it was necessary to apply a drop of DI water to one strip before bringing the second one into contact. Finally, bonded samples were cured for one day under ambient conditions.

The extent of bonding between the silicon strips was detected by the IR microscope. A panoramic view of a nearly fully bonded sample, using images that were taken by the 2.5× objective lens over the 5×45 mm extent of the silicon strips is shown in Figure 4.2a. Only three small regions, highlighted by red dashed lines showed any signs of separation. Another example is presented in Figure 4.2b, where there was a fully bonded region in the middle of sample (not shown) and unbonded regions at both ends of the sample. The separation at the end of the 12mm-long crack on the left was approximately 11µm, while the 5.34 mm crack on the right had a separation of 3.12 µm.

Despite the presence of initial edge cracks in some samples, it was necessary to lengthen the cracks and produce well-aligned crack fronts by inserting a rigid wedge by a small amount and then removing it. The fringe patterns corresponding to such an insertion and withdrawal are shown in Figures 4.3a and 4.3b. The residual opening displacement is indicated in Figure 4.3b by the number on each fringe.

## **4.2 MODE I WEDGE EXPERIMENTS**

Quite a number of hydrophilic-bonded silicon samples were examined under ambient conditions of 24°C and 72 % relative humidity (RH). In order to calculate the adhesion energy and the traction-separation relations associated with the bonding interactions, the wedge tests described in Chapter 2 (Fig. 2.13) were conducted, coupled with IR-COI. The razor blade was re-inserted and the IR camera, located above the

original crack front, recorded the NCOD and the propagation of the crack at each wedge insertion. These quantities were used to extract the traction-separation relation associated with hydrophilic bonding under ambient conditions.

#### 4.2.1 Results

A 33- $\mu\text{m}$  thick razor blade was inserted in a series of 0.2-mm steps (Figure 2.13a), which were each held for 30 seconds. Figure 4.4 shows a series of fringes with the applied wedge insertion at the top of each image. The field view of each image is 4.189 $\times$ 3.130 mm with a spatial resolution of 3.01 $\pm$ 0.03  $\mu\text{m}$  per pixel. The dark area on each IR image represents the bonded-region. The separated region appears as a series of bright and dark fringes resulting from the interference of the reflected IR beams from the crack surfaces. As the wedge was inserted, the NCOD initially increased without any movement of the crack front. The first discernible growth occurred at about 1.6 mm of wedge insertion. Steady state growth occurred at about 4.8 mm and the crack jumped and arrested when the wedge insertion reached a value of 7.2 mm (final image, Fig. 4.4). The razor blade was then completely removed to terminate the experiment.

The intensity plots from three of the images in Figure 4.4 are shown in Figure 4.5. They all exhibited the same background signal over the bonded region. The intensity variations resulting from the fringes in the cracked region can be seen clearly. Comparing the intensity patterns for wedge insertions of 0 and 2.0 mm, it can be seen that the crack opened further but did not propagate. Determination of the crack front location followed the procedure established in Chapter 2.4.2. The increment in crack length ( $\Delta a$ ) at a wedge insertion of 4.8 mm can be observed from the change in the location of the origin of the intensity variation from the background signal. The same fitting procedure (Chapter 2.4.2) was used to obtain the NCOD from the intensity data [107].

The NCOD corresponding to each fringe pattern (Fig. 4.4) are plotted in Figure 4.6. The NCOD at each dark and bright fringe were obtained from Equations (2.8) and (2.9), respectively. The higher resolution NCOD were obtained from the intensity measurements between fringes (Eq. 2.10). The NCOD profiles bring out the initial increase in crack face separation without growth and the subsequent propagation of the crack to steady state. The location  $r = 0$  marks the location of the initial crack front and subsequent growth was used to plot the change in crack length with wedge insertion (Fig, 4.7). The linear portion of the response corresponded to wedge insertion without crack growth. This was followed by a gradual transition to steady state growth, where each increment in wedge insertion produced the same increment in crack length.

The data in Figure 4.7 was converted to fracture resistance curves using Equation 2.14 to determine the J-integral as a function the crack extension (Fig. 4.8). The data was divided into two sets for subsequent discussion: Case A corresponds to specimens with a steady state toughness  $\Gamma_{ss} = 329 \pm 12 \text{ mJ/m}^2$ , which was noticeably higher than that of the remaining specimens (Case B), whose toughness varied from  $90 \text{ mJ/m}^2$  to  $237 \text{ mJ/m}^2$ . Generally speaking, initial portion of the two sets of the resistance curves were similar for J-integral values up to  $42 \text{ mJ/m}^2$ . For Case A, the J-integral continued to increase steeply up to  $250 \text{ mJ/m}^2$ , at which point there was a more gradual transition to steady state growth, which was defined as the average value ( $329 \pm 12 \text{ mJ/m}^2$ ) of the J-integral for  $500 < \Delta a < 1000 \text{ }\mu\text{m}$  from both samples. The response beyond this amount crack extension exhibited signs of slip-stick behavior with a rise to  $308 \pm 5 \text{ mJ/m}^2$ , but this portion of the response was ignored. In addition to lower steady state toughness, the specimens in Case B exhibited more irregular patterns of growth. Some specimens displayed stick-slip behavior, which seemed to be absent from those with the lowest steady state toughness.

All of the silicon strips that were used in this work made contact over their (111) surfaces which were functionalized with OH<sup>-</sup> groups from the piranha solution. It appeared that the distribution of the functionalization was very uniform based on the uniform wetting over entire surface from a single drop of deionized water. The next potential level of imperfection in the surface arises from the roughness. However, the roughness issue may be ruled out here because the RMS roughness of the silicon strips was less than 0.3 nm (Figure 2.8 and Figure 4.12), which, as will be seen shortly, are a factor approximately 1000 times less than the measured range of the hydrophilic interactions. Other possible reasons for the range of steady state adhesion energy observed in Figure 4.8 could be due to the local waviness of each of the contacting surfaces, which will be discussed in Section 4.3.

As was indicated in Chapter 2, traction-separation relations for each sample were obtained by taking the derivative of J-integral versus crack tip opening displacement  $\delta_n^*$  data. Such data is shown in Figure 4.9 for Cases A and B, the study obtained the variation of the J-integral with respect to the crack tip opening displacement. The shapes of these curves were very similar to the shapes of the resistance curves. The traction-separation relations obtained by applying Equation 2.23 and a central differential scheme to the data (Fig. 4.9) are shown in Figure 4.10. The two traction-separation relations obtained for the samples in Case A (Fig. 4.10a) exhibited the same maximum adhesive strength of 12.5 MPa. The location of the maximum strengths appears to be shifted from 28 nm to 40 nm for Cases A2 and A1, respectively. The strength then decayed exponentially in an approximately similar fashion as the opening displacement increased. The two traction-separation relations differed in their initial rise to the maximum strength, a point which will be discussed in conjunction with the results obtained from the modeling.

The traction-separation relations for the samples in Case B (Fig. 4.10b) exhibited more variability. As will be discussed later, this may be due to differences in their initial bonding state, brought about by less intimate contact of the silicon surfaces.

### 4.3 SURFACE ANALYSIS

Potential reasons for the range of toughness values exhibited in the previous section are now explored. The differences may have chemical or physical origins.

From a chemical point of a view, hydroxyl ( $\text{OH}^-$ )-terminated samples can be achieved by dipping silicon strips in a piranha solution. As indicated above, non-uniform termination of the surface by hydroxyl groups is unlikely to occur. However, an analysis [176] of the surface concentration of the hydroxyl groups revealed that silicon wafers were covered with an average of  $4.6 \pm 0.2$   $\text{OH}^-$  groups per  $1 \text{ nm}^2$ . However, within such regions,  $1.4 \pm 0.1$  groups were single-paired while the remainder were double-paired (Fig. 4.11). The single-paired groups (Fig. 4.11a) do not have any hydrogen bonding as opposed to the double-paired ones, which do [176]. Nonetheless, the entire surface was entirely wet when a drop of DI water was applied to the treated surface, which is a characteristic of termination by hydroxyl groups, whether or not they are single-paired.

The topography of the surfaces of the silicon strips was analyzed with AFM and interferometry (Zygo Inc.). AFM was used to define the local RMS roughness over  $5 \times 5 \text{ }\mu\text{m}$  regions because its resolution ( $\sim 0.05 \text{ nm}$ ) is more precise than the resolution of the Zygo interferometry. However, due to limitations of the scanning range of AFM ( $100 \times 100 \text{ }\mu\text{m}$ ), a Zygo interferometer equipped with a He:Ne laser with a wavelength  $\lambda = 632 \text{ nm}$  was used to examine the flatness of the  $5 \times 40\text{-mm}$  surfaces of the silicon strips. Both measurements were made before the silicon strips were treated in the piranha solution.

AFM images of two  $5 \times 5$ - $\mu\text{m}$  regions on the Si(111) surface of a silicon strip are shown in Figures 4.12a and b. The respective RMS roughness was 0.255 nm and 0.309 nm. These values are typical for surfaces that have been prepared by chemical-mechanical polishing (CMP), a mirror polishing process that renders the surface to be atomically smooth. In the schematic (Fig. 2.10) of hydrophilic bonding, the length of the hydrogen bonds is 0.276 nm, which is on the order of the RMS roughness. In addition, there are likely to be several water molecules between the surfaces, so bonding of the silicon strips is likely.

The silicon wafers used in the study were mirror-polished so that it was possible for interference to occur in the Zygo interferometer. Once the fringe data was recorded, the analysis software MetroPro<sup>®</sup> converted the fringe data into surface topography data (Figure 4.13). The surface profiles of the contacting surfaces that made up samples A-1, B-4 and B-5 are shown in Figures 4.14a-c. The height variation of each surface was less than  $\pm 2 \mu\text{m}$ , which was much larger than the RMS roughness values noted above. Thus the height variation, or lack of flatness of the contacting surfaces could contribute to variations in the effective strength of the bonding from region to region as the bonding was accomplished in a spontaneous manner (similar to Fig. 4.1) without the addition of any clamping force.

Recall that the toughness of sample A-1 was approximately  $341 \pm 4 \text{ mJ/m}^2$ . The bonded surfaces both had quadratic profiles (Fig. 4.14a) prior to activation of bonding. In addition, neither of the surfaces exhibited additional high-frequency content such as can be seen in Cases B-4 and B-5 (Figs. 4.14b and c). The high-frequency content, which may have been caused by variations induced by wafer slicing and polishing, reduced the toughness values in these samples to 192 and  $87 \text{ J/m}^2$  for samples B-4 and B-5, respectively.

The residual separation of the contacting surfaces following bonding was obtained by IR-COI. The stitched images of the unbonded regions of sample A-1 are shown in Figure 4.15. The central 28-mm region (not shown) was fully bonded as indicated by a lack of fringes. The unbonded region on the left was 11.7 mm long, whereas the one on the right was only 4.91 mm long. This was consistent with the smaller initial opening on the right. Interestingly though, the opening at both ends following bonding was larger than before it. At the left end, the separation was approximately 11  $\mu\text{m}$ . It was 3.12  $\mu\text{m}$  at the right end.

The stitched-IR images of sample B-4 following bonding is shown in Figure 4.16a. Its central bonded area was similar in area to the previous one but the unbonded regions were more irregular. The bright region near the top-left corner indicates that the separation was approximately 262.5 nm due to the absence of any dark fringes. Similarly, incomplete bonding was apparent near the right end of the specimen. In this case, there were two regions that were clearly separated. Between them were two regions of full contact and a region with smaller opening. Looking at Figure 4.14b, it can be seen that the bonded state was consistent with the initial shapes of the contact surfaces.

There were several regions of incomplete bonding in sample B-5 (Fig. 4.16b). There was a small separated region near the bottom left corner of the sample, a larger one ( $\sim 780$  nm high) in the middle and the largest separation ( $\sim 2.3$   $\mu\text{m}$ ) near the top right corner. There were other smaller isolated regions that were just separated; some of them had little black dots in the middle, which suggests that particles were trapped [177]. Such a degree of non-uniform bonding was again consistent with the much more irregular initial state of the bonded surfaces of this sample (Fig, 4.14c).

Thus is reasonable to conclude that the noted variation in the fracture toughness between samples stemmed from imperfections in the flatness of the silicon surfaces

associated with the wafer fabrication process. Similar effects on fracture toughness have been reported by Miki *et al.* [34], who found that increasing the roughness of the contact surfaces *via* etching decreased the toughness.

#### 4.4 COHESIVE ZONE MODELING

The traction-separation relations that were obtained by taking the derivative of the J-integral with respect to the measured end opening displacement  $\delta_n^*$  were shown in Figure 4.10. A range of responses were noted there, which, based on the discussion regarding the effect of flatness on the bonded state, were most likely caused by high frequency undulations in the contacting surfaces. To examine this point further, cohesive zone modeling of the wedge tests was conducted using ABAQUS. The silicon strips were modeled as being linearly elastic and isotropic with the properties listed in Table 4.1. The traction-separation relations from sample A-1 and A-2 were approximated by the traction-separation relation shown in Figure 4.17a. This reference traction-separation relation captured the initial elastic response, the maximum strength and the decay of the measured traction-separation relation using the tabular input format of ABAQUS (see Table 4.2 for specific values). This approach ignored the initial stiffening that was seen in the measured traction-separation relation, because separations were close to the resolution of IR-COI in this regime. Nonetheless, the area underneath the traction-separation relations was selected to reflect the average steady state toughness ( $329 \pm 12 \text{ mJ/m}^2$ ) of the samples A-1 and A-2. The reason that the tabular formulation was selected instead of the bilinear or exponential decay formulations was that neither of those approaches captured the measured traction-separation relation as effectively. The softening part of the reference traction-separation relation was compared (Fig. 4.17b) to the softening part of the traction separation relations (Fig. 4.10) obtained from all the



samples. The reference traction-separation relation captured the initial steeply decaying portions of the measured traction-separation relations very well. Below 2 MPa, the measured traction-separation relations exhibited more scatter but were reasonably well represented by the reference one. Thus the reference traction-separation relation may represent the interactions for a well-bonded interface and the lower strengths attributed to the poorly bonded may be due to the initial damage state caused by differing degrees of curvature mismatch. This point is now considered in more detail by comparing the crack length vs. wedge insertion, resistance curves and NCOD profiles for the samples whose traction-separation relations appear in Figure 4.17.

The wedge tests conducted on samples A-1 and A-2 were simulated by accounting for the silicon thickness, initial crack length and wedge thickness in each case. The solutions for crack length vs. wedge insertion, resistance curves, and NCOD profiles were compared with the data that has already been provided in Figures 4.7, 4.8 and 4.6, respectively. The solutions for the crack length as a function of the wedge insertion are shown in Figure 4.18. The crack lengths from the solutions were defined by the location where the normal cohesive traction began to develop. This definition is slightly different from the visible crack length which carries with it the 20-nm uncertainty in NCOD. The difference between these two definitions is small, as can be seen in the figure, and nearly corresponds to the length of the cohesive zone. The solution captured the gradual transition to steady state delamination. This transition is controlled by the form of the softening or damaged portion of the traction-separation relation. For example, bilinear traction-separation relations result in a very sharp transition (discontinuity in slope) to steady state (see Chapter 6). The form of the decaying portion of the traction-separation relation does not capture the stick slip behavior that was observed in Case A-1.

The corresponding resistance curves are shown in Figure 4.19. The solution captured the gradual rise in toughness prior to steady state that was observed in the data. The gradual rise in toughness was again controlled by the damaged response as will be discussed in Chapter 6. The steady state toughness of  $329 \pm 12 \text{ mJ/m}^2$  had been selected as an average of the data and this was reflected in the solution.

The final step in the verification process was to compare solutions for the NCOD with the data. Snapshots of NCOD profiles for a nearly developed cohesive zone (Fig. 4.20a) and at steady state (Fig. 4.20b) for crack lengths of 6.987 and 6.375 mm, respectively. In both cases, the finite element solutions were in excellent agreement at each fringe point (discrete data points at increments of  $\lambda/4=0.260 \text{ nm}$ ). The main discrepancy in the NCOD existed near the crack front for NCOD within the first bright fringe as shown by the inserts to each figure. The measured NCOD were consistently higher in this region.

To simulate the poorly bonded interfaces noted in cases Case B-4 and B-5, the decaying portion of the reference traction-separation-relation was maintained (Fig. 4.21). However, in order to simulate damage or poor bonding, the stiffness of the rising portions of the traction-separation relations was reduced so that the maximum strength on the reference traction-separation relation provided the measured adhesion energy for each case. The solutions for the crack length vs. wedge insertion (Fig. 4.22a and b) were compared with the measurements and yielded slightly longer crack lengths. As discussed above, this was due to the definition of crack length and the development of cohesive zones. Note that the cohesive zones were longer here than in cases A-1 and A-2, so the difference is more noticeable. Nonetheless, the overall responses were in good agreement. The solutions for the resistance curves (Fig 4.23a and b) were also in excellent agreement over the range of crack extension. The last step in the verification

was to compare the NCOD during steady-state growth (Fig. 4.22a and b). The solutions for the NCOD were in good agreement with the data beyond the first bright fringe ( $\lambda/4=0.2625$  nm). Once again, the solution for the NCOD was consistently lower than the data closer to the crack front.

The reason for this discrepancy response is not clear at this time but could be due to hydration forces [178] or chemisorption of oxygen in the silicon [179-181]. Hydration forces would add a repulsive component to the traction-separation relations with an interaction range of several nanometers and repulsive tractions of at least 100 MPa [37, 178]. If such repulsive forces were added to the traction-separation relations used here, the NCOD near the crack front would be closer to the measured values. Chemisorption into Si(111) surfaces leads compressive in-plane residual stresses [179-181]. If these were acting near the crack in the current experiment, they could also conceivably lead to larger NCOD in that region. Interestingly, the same study found that chemisorption into Si(100) surfaces leads to tensile in-plane stresses, which should have the opposite effect. This suggests an interesting series of parallel experiments, which are beyond the scope of the current study. The same applies to analyses with traction-separation relations with a repulsive component.

The simulated and measured responses just presented in Figures 4.18-4.20 indicate that the traction-separation relation used in the simulation reflects the nature of the adhesive interactions between hydroxylated silicon strips in the presence of deionized water. The maximum strength, range and adhesion energy of the interaction were 12 MPa, 350 nm and  $325 \text{ mJ/m}^2$ , respectively. Although the adhesion energy is commensurate with Van der Waals interactions, the strength and range are not. Electrostatic interactions are typically within 1 nm [182], which also rules them out. The presence of water has been considered by Pallares *et al.* [183], Binggeli *et al.* [111, 112]

and Wang *et al.* [184]. However the interaction ranges noted in these studies were much shorter than the ones measured here.

Pallares *et al.* [183] measured the length of condensed water near crack tips in pure silica glass specimens using AFM to scan one of the specimen surfaces that was intersected by the crack faces. The scanned surface of the double cleavage drilled compression (DCDC) specimen was polished to an RMS roughness of 0.25 nm. Once a crack was initiated, the crack tip region was scanned with AFM in phase contrast mode in order to detect the presence of condensed water between the crack faces. Cracks in silica glass were filled with condensed water to crack openings of  $5 \pm 0.7$  nm. A Dugdale model was then used to obtain an interaction strength of  $36 \pm 5$  MPa. The difference between these values and the corresponding values in the traction-separation relations obtained here may be due to differences in the surfaces as water condensation on the surface of recently cleaved glass may differ from that associated with piranha-treated silicon surfaces.

In Binggeli's experiments, a force microscope equipped with a tungsten indenter having a 100-nm tip radius. Force-displacement responses (or force profiles) between the tip and hydrophilic native silicon oxide of Si(100) surfaces at various relative humidity levels were measured. At 97% RH, the interaction ranges were approximately 7 and 15 nm for approach and withdrawal, respectively [111]. The interaction ranges were within 5 nm for both approach and withdrawal when the relative humidity was reduced to nominally zero. This does not rule out the presence of monolayer water on the surfaces of the tungsten and silicon or the possibility of retarded Van der Waals interactions. Similar measurements was conducted by Wang between tungsten tips and octadecyltrichlorosilane (OTS) SAMs on Si(100) using an interfacial force microscope (IFM) with tip radii that ranged from 100 nm to 200 nm. There were several common

observations: hysteresis between responses during approach and withdrawal and very short interaction ranges. The interaction range for approach was always shorter than that associated with withdrawal, indicating that water gathered around the tip during contact and the separation range was longer due to the thinning of the capillary bridge. Nonetheless, the interaction ranges were much shorter than the 350 nm measured here.

In 2005 and 2006, two different studies by Weeks *et al.* [185] and Sirghi *et al.* [186] reported on water menisci trapped between AFM tips and substrate. Observing water condensation between AFM tips in contact with silicon in environmental SEM (ESEM), Weeks demonstrated that the height of water menisci increased to 1.2  $\mu\text{m}$  with increasing humidity. In addition, the variation in the meniscus height during condensation and evaporation was hysteretic. For a given humidity level, the meniscus height during condensation was much lower than during evaporation. It might be inferred that water layers formed at the beginning of condensation may be chemically adsorbed on the solid surfaces, which would result in different responses during condensation and evaporation.

Sirghi [186] evaluated the interaction range between hydrophilic AFM tips on glass at 15 %RH. Differences in the entire force profiles between sharp ( $<50$  nm) and blunt ( $\sim 400$  nm) tips were noted. This culminated in pull-off distances for sharper tips that were approximately 15 nm, compared to 130 nm for the blunt tips. When the force-displacement response associated with AFM pull-off experiments was simulated with the Young-Laplace difference equation under volume constant constraint there was good agreement with the data over the entire separation range. On the other hand, when the constant curvature condition was enforced, the force profile was only valid for small separations. An even more interesting aspect of the experiments was that the pull-off distance increased with the length of time the tip was in contact with the glass surface. For example, when the contact time was 2 s instead of 5 ms, the pull-off distance for the

blunt tip was doubled at approximately 250 nm. This situation was simulated by increasing the initial volume of the meniscus to reflect an increase in volume with increasing contact time. In the current study, two hydroxylated silicon strips with large initial curvatures were bonded in the presence of deionized water for one day under ambient conditions. If this led to a relatively large volume of trapped water, then Sirghi's observations suggest that this in conjunction with the large radii of curvature were responsible for ultra-long interaction ranges observed here. In principle, the Sirghi's analysis could be extended to the wedge test configuration as a way of predicting the traction-separation relation that was used to analyze the wedge tests. This is beyond the scope of the current work. Nonetheless, such an approach to modeling the observed traction-separation relations is much more promising than the atomistic model presented by Cole *et al.* [37] that developed force fields for oxidized silicon surfaces in order to model hydrophilic bonding in the presence of small amounts of water. In that case, the maximum strength of the interactions were 150 MPa and were decreased by the presence of water. The interaction ranges were very short and slightly increased by the presence of water. Adhesion energies ranged from 80 to 120 mJ/m<sup>2</sup>.

The values of adhesion energy associated with hydrophilic bonding under ambient conditions that are available in the literature [33, 34, 187, 188] have ranged from 20 to 260 mJ/m<sup>2</sup>. There are several possible explanations for this range of adhesion energies associated with hydrophilic bonding. The adhesion energy in [34] ranged from 80 to 20 mJ/m<sup>2</sup> for surfaces that were subjected to the RCA cleaning process<sup>5</sup> and then subjected to buffered oxide etch (BOE)<sup>6</sup> treatments for increasing exposure times in order to roughen the surfaces. Bäcklund *et al.* [187] used a number of surface treatments,

---

<sup>5</sup> RCA clean is a standard set of wafer cleaning steps.

<sup>6</sup> The BOE solution is a mixture of ammonium fluoride and hydrofluoric acid.

including the RCA process, to control their wettability. For surfaces with contact angles ranging from 5-9°, adhesion energy was 140-160 mJ/m<sup>2</sup>. The adhesion energies in [34, 187] were obtained from fracture or separation experiments. On the other hand, Legtenberg *et al.* [188] used beam contact experiments to obtain adhesion energies that ranged from 240 to 260 mJ/m<sup>2</sup> for surfaces that were treated with nitric acid. The initial curvatures were not measured in any of these experiments. Based on the results obtained in the current study, where a range of adhesion energies was obtained for the same surface treatments but with differing degrees of curvature mismatch, it is also possible that this could have also contributed to the range of adhesion energies that have been previously reported.

#### 4.5 CONCLUSIONS

The traction-separation relations and adhesion energy associated with interactions between hydrophilic Si(111) surfaces were investigated from fracture experiments coupled with measurements of crack opening displacements and cohesive zone modeling. The curvature and roughness of the surfaces of the silicon strips prior to bonding was established by interferometry and AFM. The latter confirmed that the RMS roughness was uniform and less than 0.5 nm in all cases. The interferometry measurements indicated that the surfaces of silicon strips had different curvatures that were modulated by varying degrees of waviness. The height variation of the surfaces over their 40-mm length varied from 0.5 to 1.5 μm. When contact between the bonded surfaces was fully conformable, the steady state adhesion energy was 329±12 mJ/m<sup>2</sup>. The mismatch in the waviness of other samples caused the adhesion energy to vary from 90 to 250 mJ/m<sup>2</sup> from specimen to specimen.

The traction-separation relations associated with the various degrees of adhesion were first determined from measurements of the J-integral and NCOD as a function of wedge insertion. Because the measured traction-separation relations essentially incorporated a range of initial damage due to the aforementioned curvature and waviness mismatches between contacting surfaces, these measured traction-separation relations formed the basis of a reference traction-separation relation that was used in the cohesive zone modeling that followed. Finite element solutions based on this reference provided crack growth responses, delamination resistance curves and far-field NCOD profiles that were in excellent agreement with measurements. This supported the hypothesis that the range of adhesion energies that was encountered was indeed associated with varying degrees of contact between the mating surfaces.

The master traction-separation relation had a maximum strength of 12 MPa and an interaction range of 350 nm. These are unlikely to be associated with Van der Waals, or hydrogen bonding. Instead the most likely mechanisms are DLVO forces and capillary bridging, possibly modulated by surface waviness. Another issue to be resolved is the fact the measured near-tip NCOD were larger than those predicted on the basis of the master traction-separation relation. This difference may be due to repulsive hydration forces or highly localized residual stress states due to chemisorption.



## Chapter 5 Surface Energy of Graphene

This experiment measured the static contact angle of graphene on various substrates in order to determine the wetting properties of graphene as well as the surface energy. One wetting property of interest included the possibility of wet transparency [189] where the substrate on which the graphene has been deposited has no effect on the contact angle between the graphene and the drop. The second issue that was considered was the effect of the number of layers graphene beneath the surface on the contact angle [189, 190]. In previous studies [191, 192], the wetting properties of graphene on Si(100) surfaces with 300 nm thermally grown oxide layers were considered. In this work, bare Si(111) surfaces covered with a native oxide layer approximately 2 nm thick were considered because of the inherent smoothness of the Si(111) surface. Contact angle measurements were made on wet-transferred monolayer graphene on Si(111) and as-grown graphene on copper foil. The surfaces of bare Si(111), highly ordered pyrolytic graphite (HOPG) and poly(methylmethacrylate) (PMMA) on Si(111) were considered as controls. All samples were tested in a 1000-class clean room. The contact angle measurements were used to determine the surface energy of each of the surfaces based on the three-liquid method [193, 194].

### 5.1 MEASUREMENT OF THE CONTACT ANGLE.

To measure the surface energy, contact angle measurements were made with two polar liquids (water and glycerin) and two non-polar liquids (toluene and diiodomethane): the acid and base components of polar interactions as well as the dispersive components of the surface energy are summarized in Table 2.2. Each target surface was placed beneath a 10 mL syringe filled with one of the liquids. Approximately  $39 \pm 1$   $\mu\text{L}$  drops were applied by an automated motor system synchronized with a real-time recording

system. Images of drops forming on target substrates were recorded by a camera capable of taking images at intervals ranging from a second to an hour. The software supplied by the manufacturer of the contact angle goniometer was used to analyze the contact angle between the substrate and liquid. Snapshots of the drops of all four liquids on all five substrates are shown in Figure 5.2. The mean values of the associated contact angles are summarized in each snapshot. The average contact angle was obtained from at least 100 readings taken every second during steady state contact in each experiment and at least three experiments per substrate/liquid pair.

### **5.1.1 Cleaning and Sample Preparation**

Contact angle measurements are very sensitive to surface treatments because the atomic interactions between the drop and target surface control the contact angle. Therefore, it is essential to prepare high quality surfaces.

In this study, bare Si(111) surfaces (1×1 cm) were ultrasonically cleaned in a DI water bath for 30 minutes, followed by 10 minutes in a piranha solution and rinsed in DI water. Once this was complete, the silicon was blown dry with N<sub>2</sub> gas [195, 196]. This treatment was the same that was used to prepare silicon for the wet transfer of graphene.

Fabricating wet-transferred graphene on Si(111) was more complicated. Prior to transferring graphene film to Si(111), the silicon was cleaned in the piranha solution as indicated above. Then, CVD-grown graphene was wet-transferred to Si(111) surface using the process [99, 124] outlined in Figure 2.6. The quality of the transferred-graphene was confirmed by the Raman spectra in Figure 5.1, due to the presence of G and 2D bands as well as the absence of the D-band corresponding to the graphene membrane. The peaks below 1600 cm<sup>-1</sup> are silicon peaks as previously discussed in reference to Figure 2.9.

The samples with graphene on copper were prepared by CVD of graphene on copper foil (Section 2.1). Because the copper foil had to be wrapped around a 5-cm diameter quartz tube during deposition, it was flattened for the contact angle measurements by cutting it into 2×2 cm patches and bonding it to 1×1 cm silicon chips.

PMMA/Si samples were prepared by coating the silicon surface with a PMMA solution (C9, MicroChem. Inc.), which was spin-coated on the surface at 3000 rpm for 30 seconds and dried in ambient conditions. The spin-coating process resulted in PMMA films that were a few microns thick.

HOPG consists of AB-stacked graphene. When its surface is exposed to air it may be contaminated by airborne hydrocarbons [197] as well as residues from previous measurements. As a result, it was necessary to prepare fresh HOPG surfaces for each measurement. Fresh surfaces were prepared by attaching Scotch<sup>®</sup> tape (3M Inc.) to the existing surface and gently peeling off several layers of HOPG.

### **5.1.2 Calibration of the Contact Angle Goniometer**

Prior to the contact angle measurement, the camera and the image analysis software were calibrated with two reference pieces of aluminum (Fig. 5.2) that had been machined to mimic contact angles of  $39.6\pm 1^\circ$ , and  $90\pm 1^\circ$ . The calibration (Fig. 5.2) yielded values  $39.9\pm 0.25^\circ$  and  $90.1\pm 0.6^\circ$  for the two pieces. Thus the system error was within  $\pm 1\%$  error of the manufacturer's standard.

## **5.2 SUBSTRATE EFFECT**

The potential for wet transparency of graphene on silicon and copper was considered here. As indicated above, the silicon was pretreated with ethanol or piranha solutions prior to the application of graphene.

### 5.2.1 Silicon

Water almost completely wet ( $2.7\pm 0.7^\circ$ ) the piranha-treated bare Si(111) (Fig. 5.3) in the 1000 class clean room environment. Rafiee *et al.* [189] reported values of  $32.6^\circ$  and  $20.2^\circ$  for piranha-treated bare silicon and glass, respectively. However both substrates were dried with methane as opposed to nitrogen. The ideal contact angle of piranha-treated glass or silicon surfaces should be close to zero due to the OH<sup>-</sup> termination that it produces. However, the resulting hydrophilicity could have been modified by the methane drying treatment due to its reaction with the hydroxyl groups on the piranha-treated bare silicon surfaces. Drying with nitrogen gas is unlikely to have such an effect due to its inert nature.

In the same environment, the contact angle of a DI water droplet on graphene/Si increased to  $72.2\pm 0.2^\circ$  due to the presence of the graphene film. This was much larger than the baseline of  $2.7\pm 0.7^\circ$  for the piranha-treated bare silicon and implies a much more hydrophobic response. This difference contradicts the claim of wet transparency of graphene that was made by Rafiee *et al.* [189] who claimed that, when graphene was transferred to silicon, there was no difference in the contact-angle of DI water and the substrate with and without graphene. On the other hand, Shih *et al.* [191] contended that the wet transparency of graphene is not universal. They reported that the wet transparency of graphene is only likely to be observed when the contact angle between water and the bare substrate ranges from  $30^\circ$  to  $90^\circ$ . Thus it should be noted that the contact angle between water and silicon in [189] was within this range.

When a second polar liquid, glycerin, was used in this work (Fig. 5.3), the contact angle for glycerin on piranha-treated Si(111) was  $14.3\pm 1.7^\circ$ . This results from its chemical structure, consisting of three hydroxyl groups resulting in high solubility in water. When the glycerin was dropped on a graphene-coated silicon surface, the contact

angle increased to  $52.7\pm 1.1^\circ$ . Thus, no wetting transparency was observed for either of these polar liquids.

Toluene was considered as the apolar liquid for the three liquid method. When toluene was dropped (Fig. 5.3) on piranha-treated silicon and graphene on silicon surfaces, the toluene spread very quickly to its stationary contact angle and then started to evaporate. This made the measurements relatively difficult, given the temporal resolution of the camera. The contact angles for the piranha-treated silicon and graphene-coated silicon were  $7.0\pm 1.9^\circ$  and  $8.6\pm 1.8^\circ$  respectively. Within the resolution of the contact angle measurements, these values are quite similar, so toluene may exhibit wet transparency for graphene on silicon.

Diiodomethane was used to check the surface energy of piranha-treated silicon that was determined using water, glycerin and toluene. The contact angle of diiodomethane on silicon was  $40.7\pm 1.0^\circ$ .

### **5.2.2 Copper**

Unfortunately, a baseline for contact angles on pure copper cannot be determined because of the presence of the native copper oxide and anti-corrosion coatings on copper foil (Section 2.1.3). It should be noted that neither of these exist on the copper surface following the exposure to  $1000^\circ\text{C}$  in a hydrogen environment, which is the final phase prior to the introduction of methane and the subsequent growth of graphene on copper that is free of any contaminants. Moreover, graphene grown on copper foil is chemically impermeable to gas [69-71]. Therefore the assumption that the interface between copper and graphene is free of any oxide layer following deposition is valid. For such copper surfaces, Schrader [198] reported a super hydrophilic response ( $0^\circ$ ) between oxygen-free water and copper. This was an extremely demanding experiment in ultra-high vacuum, so

their measurements were adopted as the baseline for the current work. When a droplet of water interacted with graphene on copper, it exhibited a value of  $73.5\pm 0.2^\circ$ , close to the value of  $72.2\pm 0.2^\circ$  for graphene on silicon reported above. Thus, based on these measurements, graphene can be considered to be a “surface neutralizer”.

This is in contrast to the findings of Rafiee *et al.* [189] who claimed that graphene on copper was also transparent to water. It was reported that the contact angles were  $85.9^\circ$  for bare copper and  $86.2^\circ$  for single layer of graphene on copper. However, his measurement of the contact angle of water on bare copper was masked by the native oxide layer and contaminants. Thus, it is unlikely that the claim of wet transparency was justified in this case. Note that the measurement of the contact angle of graphene on copper in the current work was approximately  $13^\circ$  less than Rafiee's observation. This difference can be justified by a recent report [199], showing that airborne hydrocarbons on graphene or graphite made the surfaces much more hydrophobic. For example, when the water contact angle was measured on fresh graphene on copper, the value of the contact angle was less than  $50^\circ$ . As the exposure time to air was increased, the contact angle rapidly increased and saturated at approximately  $82^\circ$ .

As indicated above, contact angle experiments on pure copper have to be conducted in ultra-high vacuum in order to avoid oxidation issues. Although glycerin is a fairly commonly used polar liquid, there is no contact angle data for glycerin on pure copper. Nonetheless, very low contact angles ( $<10.0^\circ$ ) are expected because glycerin is also a polar liquid. When glycerin was dropped on graphene-coated copper, its contact angle was  $65.0\pm 3.0^\circ$ . Thus, assuming that the contact angle of glycerin and copper free of native oxide are very small, there are no signs of wet transparency of copper with respect to glycerin. Again, in contrast to the findings reported in [189], the conclusion of this

study is that graphene was not transparent to silicon or copper with either of the polar liquids (water and glycerin) that were considered here.

It was seen that graphene could be transparent to silicon in the presence toluene, so this apolar liquid was again considered for copper. Unfortunately, it spread much too quickly for the temporal resolution of the camera and no data could be obtained on the transparency of graphene on copper. The difference in the spreading speed of toluene on silicon and copper is interesting and may also suggest some transparency of graphene to apolar liquids.

Another interesting aspect of the contact angles of glycerin on graphene on silicon and copper was their difference: When glycerin was dropped on graphene-coated copper, its contact angle was  $65.0 \pm 3.0^\circ$ , noticeably higher value than the value of  $52.7 \pm 1.1^\circ$  for graphene-coated silicon. One possible explanation of this is that, when graphene is transferred to silicon, it could be damaged (Fig. 6.7) and thereby expose the drops to both graphene and bare silicon, which should reduce the contact angle. It has been shown [192] that damaged graphene pins the receding liquid.

### **5.3 LAYER EFFECT**

In the previous section, the substrate effect was explored with four liquids on bare silicon, graphene on silicon and as-grown graphene on copper foil. In this section, the effect of the number of layers of graphene on the contact angle with respect to the two polar and apolar liquids that were considered above. In order to study the layer effect of graphene, it is necessary that multiple layers of graphene be carefully prepared on silicon and copper. However, after many attempts, this idea was abandoned and the limit case of HOPG was considered due to the fact that it naturally consists of a large number of stacked graphene layers.

The contact angle of water droplets on HOPG surfaces exhibited very strong hydrophobic behavior with a contact angle of  $94.6\pm 0.6^\circ$  (Fig. 5.3). This was the same value that had been determined in previous studies [189, 190, 192, 199] with more than three layers of graphene on silicon, copper and glass. The measured value is much higher than the values of  $72.2\pm 0.2^\circ$  and  $73.5\pm 0.2^\circ$  respectively for graphene on silicon and copper. The same trend was observed when glycerin was dropped on HOPG: The contact angle was  $85.8\pm 0.9^\circ$  for HOPG vs.  $52.7\pm 1.1^\circ$  and  $65\pm 0.2^\circ$  for graphene on silicon and copper, respectively. This indicates that contact angle of water and glycerin on graphene was affected by the number of layers (Fig. 5.4a), because the HOPG consists of stacked graphene, usually with A-B stacking.

Toluene was also considered as the apolar liquid for this portion of the study. The contact angle was  $15.5\pm 0.3^\circ$ . Toluene on HOPG exhibited an increase of 50% compared to graphene on silicon. Thus the effect of the number of layers of graphene was repeated with the apolar liquid, toluene.

#### **5.4 CONTAMINATION OF GRAPHENE**

Whenever surface properties of graphene or HOPG have been considered, it is generally accepted that HOPG has a very strong hydrophobic response to water and that the surface of graphene should respond similarly. Recently, Li *et al.* [199] and Kozbial *et al.* [197] examined the effect of exposing graphene and graphite, respectively, to ambient environments for as long as 1 and 7 days, respectively. They both found that fresh graphene and HOPG could be characterized as a hydrophilic surfaces. However the response of both surfaces became gradually more hydrophobic with exposure time. Chemi-absorption by the airborne hydrocarbons on the exposed surfaces of graphene or HOPG was cited as the cause of reconstruction of the exposed surfaces [197, 199]. This



idea was supported by the observation that contaminated surfaces of graphene or HOPG could be returned to hydrophilic surfaces following the thermal treatment which is usually used to remove PMMA residues from graphene following wet transfer from copper (Fig. 2.6d).

To confirm such contamination issues, the current study compared (Fig. 5.5a) the contact angle between water and graphene on silicon that had been aged for three days and then re-annealed at 400 °C for 2 hours in argon and hydrogen environments (Fig. 2.6d). The second contact angle measurement was made within minutes of this treatment. The contact angle was  $68.8 \pm 1.1^\circ$  for aged graphene on silicon, which was about  $4^\circ$  less than earlier measurements, possibly due to different exposure times. Nonetheless the contact angle of water on re-annealed graphene on silicon was noticeably smaller at  $53.5 \pm 1.0^\circ$ . This is a promising observation because it implies that surface of graphene can be re-constructed.

A similar study was conducted on fresh and one-day aged HOPG samples. Fresh surfaces were prepared by peeling HOPG with Scotch<sup>®</sup> tape. Once the contact angle with water was measured, the measured surface was peeled off and the fresh surface was exposed to ambient conditions for one day. Fresh samples had contact angles of  $83.8 \pm 0.6^\circ$  and this was increased by the one-day exposure to  $94.6 \pm 0.7^\circ$ . These two measurements were good agreement with the series of results (Fig. 5.5b) reported by Kozbal *et al.* [197].

## 5.5 PMMA ON SILICON

When CVD-grown graphene is transferred to target substrates, the PMMA backing layer is often removed by dipping in acetone and annealing in an argon and hydrogen environment [79, 110, 127]. Nonetheless, the question remains as to whether

there is any significant PMMA residue in bulk or in the form of ultra-thin films or islands. If such residues still exist [200, 201] following the wet-transfer of graphene to silicon, contact angles may be affected. In order to address this issue, bulk PMMA (10  $\mu\text{m}$ ) was spin-coated on Si(111) surfaces and the contact angle with water and glycerin was measured. For water, this resulted in a contact angle of  $73.1\pm 0.5^\circ$ , which was very similar to the  $72.2\pm 0.2^\circ$  for graphene on silicon and  $73.4\pm 0.2^\circ$  for graphene on copper (Fig. 5.3). When glycerin was dropped on PMMA, the contact angle was  $63.4\pm 0.7^\circ$  (Fig. 5.3), which was noticeably larger than the  $52.7\pm 1.2^\circ$  for graphene on silicon. The significance of this finding awaits the determination of the surface energies of graphene in the various configurations that have been explored.

## 5.6 SURFACE ENERGY OF GRAPHENE

The surface free energy of the Si(111), graphene on silicon and HOPG surfaces was calculated using the three-liquid method (Eq. 2.38, 2.39, 2.40). However, due to the lack of contact angle data from apolar liquids on graphene-coated copper and PMMA (Sections 5.4 and 5.5), the two-liquid method (Eq. 2.30, 2.31 and 2.32) was used instead.

The surface free energy of silicon (Table 5.1) was  $62.4\pm 1.4 \text{ mJ/m}^2$ , which is close to the surface free energy of water ( $73.1 \text{ mJ/m}^2$ ). This value was the same as was measured in [202] and may be explained by the presence of very thin layers of water on hydrophilic silicon wafers [203]. In the current work, piranha-treatment of the silicon resulted in silicon surfaces that were terminated with hydroxyl groups, thereby resulting in a strongly hydrophilic surface. As a result, it is fair to assume that ultra-thin water films were present on the silicon prior to adding water droplets for the contact angle measurement. Thus the droplets were essentially interacting with ultra-thin water film instead of bare silicon. Thus it is not surprising that the surface free energy of  $62.4\pm 1.4$

$\text{mJ/m}^2$  just determined is close to that of water, or  $73.1 \text{ mJ/m}^2$ . When diiodomethane instead of toluene was taken to calculate the surface free energy of piranha-treated silicon, the surface free energy was  $62.3 \pm 0.9 \text{ mJ/m}^2$ , thereby providing a good consistency check on the three-liquid method.

The surface free energies of graphene on silicon, graphene on copper and HOPG (Table 5.1) were  $36 \pm 0.1$ ,  $33.9 \pm 0.5 \text{ mJ/m}^2$  and  $27.6 \pm 2.3$ , respectively. The values for graphene on silicon and HOPG were obtained using the three liquid method, whereas only two liquids were used for the graphene on copper. These are quite consistent results and indicate that graphene effectively neutralized any interactions from the substrate beneath it. There have been relatively few measurements of the surface free energy of graphene, but Wang *et al.* [194] claimed that the surface free energies of graphene on silicon and natural graphite were  $46.7 \text{ mJ/m}^2$  and  $54.8 \text{ mJ/m}^2$ , respectively. These values were obtained by making use of Neumann's method [194, 204, 205] coupled with an equation of state. However, five liquids were used and all contact angles were reported so the surface free energies were recalculated here for comparison, using contact angle data from water, glycerin and diiodomethane. The surface free energy for graphene on silicon and natural graphite became  $42.3$  and  $49.3 \text{ mJ/m}^2$ , which are slightly lower than the values obtained by Neuman's method. No matter which approach is used to analyses Wang's data, the values of surface free energy obtained by Wang *et al.* are significantly larger than those obtained here. For graphene on silicon, the difference may be attributed to the fact that Wang's data was obtained from graphene that had been chemically exfoliated from graphite. The flakes obtained in this way are relatively small and potentially rougher than CVD grown graphene. Increasing roughness results in an effective free surface energy, which is lower than the intrinsic value [206], so roughness effects do not seem to be an explanation. For case of graphite, it is not clear what was

meant by natural graphite and whether or not it is different from the HOPG that was used here. In addition, airborne hydrocarbons tend to increase surface free energies, so this may have contributed to the higher values, particularly because the values obtained in the current study were obtained from freshly exposed surfaces and should not have suffered much contamination.

Li *et al.* [199] found that the surface free energies of extremely fresh graphene on copper foil and HOPG were 85 mJ/m<sup>2</sup> and 125 mJ/m<sup>2</sup>, respectively. These values were obtained from the expression

$$\gamma_{sv} = \gamma_{sv}^d = \frac{\left(\gamma_{H_2O} (1 + \cos \theta_{H_2O})\right)^2}{4\gamma_{H_2O}^d} \quad (5.1)$$

where  $\gamma_s$  is the total surface free energy,  $\gamma_{sv}^d$  is the dispersive surface free energy,  $\gamma_{H_2O}$  is the surface free energy of water (73.1 mJ/m<sup>2</sup>) and  $\gamma_{H_2O}^d$  is the dispersive energy of water (22.1 mJ/m<sup>2</sup>). Equation (5.1) is a simplified version of Eq. 2.30 based on the assuming that the polar surface energy of graphene is negligible, which is not the case (Table 5.1). However, the polar component of the surface free energy of graphene on silicon that was measured here was 11.6 mJ/m<sup>2</sup>, which, combined with dispersive component of 24.4 mJ/m<sup>2</sup>, yielded a surface free energy of 36 mJ/m<sup>2</sup>. When Li's data was supplemented by the data in Figure 5.3 for glycerin, the surface free energy of graphene on silicon was reduced from 85 mJ/m<sup>2</sup> to 66.8 mJ/m<sup>2</sup>. Based on this result, Li's result for HOPG should have been lower than 125 mJ/m<sup>2</sup>, but it was not possible to recalculate it here due to insufficient data.

During the preparation of this manuscript some very recent work on the surface free energy of graphene-coated copper by Kozbial *et al.* [207] came to light. Four liquids and three different models for the surface free energy were considered in examining the effect of exposure time up to 24 hours. The value of the surface energy corresponding to

the exposure time considered here was  $45.6 \text{ mJ/m}^2$ , which is somewhat higher than the  $33.9 \text{ mJ/m}^2$  that was measured here. This difference could be due to the materials (glass or polymer) used for the containers in which samples are stored. Furthermore, these values are all much lower than the  $90 \text{ mJ/m}^2$  [190] that have been obtained from molecular dynamics simulations, which simulate contaminant free environments, but may have shortcomings of their own.

The surface free energies of graphene and silicon were used to determine the thermodynamic work of adhesion between them from Eqn. (2.37). It turned out to be  $95.5 \text{ mJ/m}^2$ , which is much lower than the adhesion energy between silicon and graphene that has been determined in separation. Zong *et al.* reported  $151 \pm 28 \text{ mJ/m}^2$  for the adhesion energy of graphene that was draped over nano particles on silicon oxide surfaces. This value is closer than any other measurements to the thermodynamic work of adhesion because it essentially reflects an equilibrium condition during approach, rather than separation. In separation or fracture experiments, values of  $450 \pm 20 \text{ mJ/m}^2$  [58] and  $240 \text{ mJ/m}^2$  [59] were obtained for exfoliated graphene on thermally grown silicon oxide. The case of graphene that had been wet-transferred to Si(111) and then peeled off will be discussed in Chapter 6.

## 5.7 CONCLUSIONS

Contact angle measurements with two polar liquids and an apolar liquid were conducted to determine the surface free energy of graphene-coated silicon and copper as well as HOPG.

There has been a lot of interest in the effect of various liquids and substrates on the contact angles associated with graphene, which have led to concepts such as wet transparency in the literature. In many cases only one liquid was considered, so that the

surface free energy could not be computed, except in some special cases. The surface free energy is a much more quantitative measure of surface effects than contact angles. The surface free energies of graphene-coated silicon and copper and HOPG were  $36\pm 0.1$ ,  $33.9\pm 0.5$  mJ/m<sup>2</sup> and  $27.6\pm 2.3$ , respectively. Thus, on the basis of surface free energy, graphene acted as a "surface neutralizer" on silicon, copper and HOPG in the sense that the substrates did not affect the surface free energy of graphene, the thinnest possible material.

## Chapter 6 Interactions between Graphene and Silicon<sup>7</sup>

The wet-transfer of graphene grown by chemical vapor deposition (CVD) has been the standard procedure for transferring graphene to any substrate. However, the nature of the interactions between large area graphene and target substrates is unknown. In this Chapter, we determine and examine the strength and range of the adhesive interactions as well as the adhesion energy between wet-transferred, CVD grown graphene and the native oxide surface of silicon substrates. Traction-separation relations, which are the continuum representation of such interactions, were obtained by coupling interferometry measurements of the separation between the graphene and silicon with fracture mechanics concepts and analyses.

Measurements of the adhesion energy of graphene transferred to silicon has been reported by Zong *et al.* [208] and Bunch *et al.* [58, 209]. Each group measured the adhesion energy between exfoliated graphene flakes and thermally grown silicon oxide (280 nm) on Si(100). By draping graphene over nano-particles deposited on the substrate, Zong *et al.* [208] obtained the adhesion energy at  $151 \pm 28$  mJ/m<sup>2</sup>. Bunch's group used micro-blister tests to arrive at values ranging from  $450 \pm 20$  mJ/m<sup>2</sup> [58] to 240 mJ/m<sup>2</sup> [209]. At larger scales, blister tests have also been used to determine the adhesion energy between CVD-grown graphene that had been transferred to copper, yielding similar levels of adhesion energy [60].

Van der Waals (vdW) interactions have been considered, theoretically, as the dominant mechanism for the adhesive interactions between graphene and silicon. Using a semi-empirical density functional theory (DFT) approach (DFT-D2) with vdW

---

<sup>7</sup> The contents in this chapter were published in ACS Nano: S. R. Na, J. W. Suk, R. S. Ruoff, R. Huang, and K. M. Liechti, "Ultra Long-Range Interactions between Large Area Graphene and Silicon," *ACS nano*, vol. 8, pp. 11234-11242, 2014.

corrections, Fan *et al.* [210] obtained an adhesion energy of 235 mJ/m<sup>2</sup> for graphene on a reconstructed crystalline SiO<sub>2</sub> surface. Other DFT calculations with more sophisticated vdW corrections have predicted higher adhesion energy for the same interface (~349 mJ/m<sup>2</sup>) [211]. Based on classical force field calculations, the adhesion energy due to vdW interactions between graphene and amorphous silica was found to vary from 149 to 250 mJ/m<sup>2</sup> [212]. In addition to the adhesion energy, the strength and range of vdW interactions have also been predicted, typically with higher strengths (> 100 MPa) and shorter ranges (< 10 nm) than the traction-separation relations that were obtained here. Although the theoretical predictions of the adhesion energy due to vdW interactions compare closely with the reported measurements, what are yet to be measured are the more revealing traction-separation relations associated with the interactions between wet-transferred CVD-grown graphene and the native oxide layer (2 nm) on Si(111) surfaces.

## 6.1 WEDGE EXPERIMENTS

Sample preparation involved a number of steps, including the characterization of the state of surfaces at each step along the way. Diagnostics included Raman spectroscopy, SEM and AFM as outlined in a number of subsections prior to delineating the steps involved in the wedge tests themselves.

Agilent 5500 Atomic Force Microscope (AFM) was used to verify the quality of the bare silicon prior to the wet-transfer process. The AFM scans were conducted on 5×5 μm regions. The topography of the bare silicon was shown in Figures 2.8, 4.12a and 4.12b. The RMS roughness of each region covered by the figures was 0.264, 0.255 and 0.309nm respectively, which indicates that the surfaces of bare silicon prior to wet transfer of graphene were very smooth.



Figure 2.6 outlines the procedure for the wet-transfer of graphene that was grown on copper foil to silicon strips [110]. Initially, a PMMA solution (20mg/mL) was spin-coated on the graphene and cured under ambient conditions. The copper foil was etched for several hours with an iron (III) nitrate solution (0.05g/mL in water; Fig. 2.6a) for complete removal. The remaining PMMA/graphene film was transferred to a distilled water bath to rinse off the etchant. The PMMA/graphene composite was then scooped up by a silicon strip (Fig. 2.6b) with the graphene side facing the silicon. This step may result in small gaps between the graphene and the silicon surface. Such poor contact can cause wrinkles and cracks to form in the graphene when the PMMA backing is removed. In order to overcome such defects, the samples were heated to 130~150 °C ( $T_g \sim 120$  °C), causing the PMMA backing to creep and conform more closely to the Si(111) surface. After curing, the PMMA layer was removed in an acetone bath (Fig. 2.6c) and any residue was thermally decomposed at 400 °C with an Ar/H<sub>2</sub> flow (Fig. 2.6d) [79, 127, 128]. An example of successfully wet-transferred graphene on silicon appears in Figure 2.6e [110].

Once the graphene was transferred to the silicon strips (Fig. 2.6), its presence was verified, at several locations, by Raman microscopy (Witec Alpha 300 micro-Raman confocal microscope,  $\lambda = 488$  nm). The Raman spectrum (Fig. 2.9), exhibited two major peaks at 1583 cm<sup>-1</sup> and 2698 cm<sup>-1</sup>, respectively associated with the G and 2D bands of monolayer graphene on Si(111). The intensity ratio of the 2D band to the G band was 2.8 and the FWHM (full width half maximum) of the 2D band was  $\sim 35.9$  cm<sup>-1</sup>, indicating that this wet transfer process had indeed deposited monolayer graphene on the silicon strips [133]. Another interesting feature of the Raman spectra is the peak at 1450 cm<sup>-1</sup>, which is associated with Si<sup>3TO</sup> [142] and means that the silicon beneath the  $\sim 2$  nm-thick

oxide layer was being detected. This peak was apparent in bare silicon samples as well as the graphene-coated silicon surfaces following the wet transfer.

The AFM scan in Figure 6.1 shows many common characteristics of graphene that was transferred to silicon. There were graphene wrinkles, graphene bubbles and trapped copper residue that was not completely etched away when PMMA/graphene/copper foil was in the iron (III) nitrate solution. These features also demonstrate that graphene was successfully transferred to the silicon. The overall RMS roughness was approximately 5.3 nm (Fig. 6.1b); however, the RMS roughness where trapped-copper residues were not present ranged from 0.9 nm to 1.3 nm. Figure 6.1c also shows an AFM scan of graphene bubbles and graphene that had curled up following a tear. Copper residues could not be seen in Figure 6.1c, but torn graphene, where the bare silicon is highlighted by the white dashed lines in Figure 6.1c, curled up. The overall RMS roughness over these features was approximately 4.9 nm (Fig. 6.7d); however, the RSM roughness outside both the bare silicon region and the curled graphene varied from 0.46 nm to 2.05 nm.

The next step in the fabrication was to bond the graphene to a second silicon strip using an epoxy. Crack opening interferometry relies on the IR transparency of all materials in the optical path. Here, we attach transparency data (Fig. 6.2) for the epoxy. This epoxy has a relatively broad response in the I.R range. In particular, the transparency at the  $1050\pm 10$  nm wavelength of the light source is almost 100%.

It was also necessary to determine the Raman characteristics of the epoxy as a control in anticipation of obtaining Raman spectra of graphene on epoxy. We prepared epoxy/silicon samples to examine the Raman response (Fig. 6.3) of the epoxy on silicon. It can be seen that the response exhibits a major peak at  $1605\text{ cm}^{-1}$  similar to the G band of graphene near  $1590\text{ cm}^{-1}$  and indicates that one major bonding in epoxy at  $1605\text{ cm}^{-1}$  is

similar to the  $sp^2$  bonding in graphene. It should be noted that this epoxy has no peak at  $2670\text{ cm}^{-1}$  (2D), which is a measure of graphene stacking.

The epoxy (EP30, Master Bond Inc.) was prepared by mixing the resin and hardener in a 4:1 ratio by weight. The mixture of the resin and hardener was degassed in a vacuum jar to remove trapped bubbles formed during the reaction and the mixing process. In order to fabricate the sandwich specimens (Si/epoxy/graphene/Si) in Figure 2.11, some epoxy was added to one end of the bare silicon strip, allowed to spread through gravity, and then further extended with a spatula to about 40% of the length of the silicon strip (Fig. 2.11b). The silicon strip with the graphene layer was then brought into contact with the strip partially covered by epoxy and compressed with a weight (17 g) to spread the epoxy over about 75% the specimen length (Fig. 2.11c). The specimen was then cured for two hours (vendor's recommendation) at  $100\text{ }^\circ\text{C}$  to enhance the bonding strength of the silicon/epoxy and epoxy/graphene interfaces (Fig. 2.11d) [110].

The resulting silicon/graphene/epoxy/silicon laminates were separated *via* wedge tests. These tests are reminiscent of Obreimoff's classic cleavage experiments on mica [213]. The tests were conducted using a screw-driven wedge that was inserted or withdrawn under displacement control, as shown schematically in Figure 6.4 [106, 108]. The left end of the specimen was clamped in order to provide a vertical reference state for easier focusing of the IR microscope and to react to the axial load applied by the wedge. The thickness of the silicon strips and epoxy were  $h$  and  $h_e$ , respectively. The wedge, with thickness  $h_w$ , was inserted from the right end by a displacement  $u_w$ , which was applied in 0.1 mm loading steps. The initial crack length  $a_0$  was measured from the epoxy terminus to the shoulder of the wedge. The subsequent crack extension  $\Delta a$  due to wedge insertion was measured from the IR fringe patterns (Fig. 6.5). At any particular time, the measured crack length was obtained from  $a = a_0 + \Delta a - u_w$ .

The initial crack in Figure 6.5 was produced by the limited spreading (~75%) of the epoxy along the silicon strip, resulting in essentially blunt cracks with sometimes irregular fronts (red dashed line) at the termination of the epoxy. As a result, it was necessary to insert the wedge until a small amount of growth,  $\Delta a$ , occurred. It was then withdrawn, leaving a sharp crack with a more regular crack front (blue dashed line), which was taken to be the redefined initial crack length  $a_0$ .

To begin the experiment, the wedge was reinserted with 0.1-mm steps applied for 10 seconds followed by a hold time of 20 seconds. During this 30-second period, interference data near the crack front were recorded every second using the time-lapse feature of the IR camera. Intensity profiles along a line perpendicular to the crack front were extracted from the interference fringes using image processing software. This data was then used to determine the separation of the crack faces by Equations (2.8), (2.9), and (2.10), commonly referred to as the normal crack opening displacements (NCOD) [106, 107, 214].

## 6.2 FRACTURE SURFACE CHARACTERIZATION

The fringes (Fig. 6.5) obtained IR-COI indicate that the fracture surfaces were smooth and flat enough to cause interference. This suggests that delamination occurred along either the graphene/silicon, graphene/epoxy, or epoxy/silicon interfaces or cohesively within the epoxy layer. Branching between some of these interfaces is also possible. A combination of SEM, AFM, and Raman spectroscopy were applied to both fracture surfaces of each specimen in order to determine the fracture path.

Figure 6.6a offers a schematic side view of the specimen under wedge loading in which it was assumed that the graphene/silicon interface delaminated, initiating near the termination of the epoxy layer above and leaving behind graphene on the lower silicon

strip (designated LSi) in the region where there was no epoxy on the upper strip (USi). If this was indeed the case, then the graphene that had been transferred to the lower silicon strip must have been transferred to the epoxy on the upper silicon strip. The corresponding plan view of this scenario is shown in Figure 6.6b, where the locations examined later in Raman spectroscopy are identified by seven red and four blue spots on USi and LSi, respectively. Relatively low magnification SEM images of the fracture surfaces of the upper and lower strips are shown in Figure 6.6c. On the left part, the wavy epoxy terminus on USi clearly identifies the boundary between graphene on the epoxy surface and bare silicon. The darker region indicates that there was no charging of the epoxy surface due to the presence of graphene. The grey region corresponds to the bare silicon. The image on the right in Figure 6.6c is of the surface of LSi, where the boundary between graphene on silicon and bare silicon is apparent but not as clearly as before. In addition, straight line features indicate that the graphene was scratched off the silicon by the wedge in places. The region enclosed by the orange box in Figure 6.6c is magnified by 100 $\times$  in Figure 6.6d, where the boundary between silicon with and without graphene is clearly visible. Furthermore, the dark lines on the graphene correspond to wrinkles and the hexagonal dark islands may be ad-layers of graphene.

An Agilent 5500 Atomic Force Microscope (AFM) was used to measure the surface topography of the fracture surface of the lower silicon strip (LSi), in the region where graphene remained on the silicon surface due to the absence of epoxy. Parts of this region came into contact with the wedge, which as it was inserted and removed, left behind three scratches (Fig. 6.7a) on the graphene. Further validating this interpretation are the wrinkles and add layers observable in the graphene, shown in Figure 6.6d. Three different lines (1, 2, & 3 in Fig. 6.7a) were selected in order to monitor the height profiles of the graphene inside and outside of the scratches (Fig. 6.7b). The transition from the

bottom of the scratch, presumably the silicon surface, to the top of the graphene layer can be easily discerned. Close to the edges of the scratches are large jumps in the height profile due to curls and burrs. Far away from the scratches, the height profiles were reasonably constant. The difference in height from the silicon to the upper surface of the graphene is suggested by the dashed lines and the values at the three locations are noted in Figure 6.7b. The expected thickness of the graphene is 0.335 nm, so it can be seen that the values obtained here were larger, probably because the graphene was lifted from the silicon surface in this disturbed region.

To confirm that the graphene was indeed removed from the silicon, several spots were interrogated with Raman spectroscopy. Each spot was separated by approximately 1 mm (Fig. 6.6b). The results for the seven spots on the fracture surface of the upper strip (USi) are shown in Figure 6.8a, where they are compared with the background signal of a pure epoxy layer. (The Raman spectra for bare silicon and epoxy appear in Figures 2.9 and 6.3, respectively.) The seven spots in Figure 6.8a all contained the graphene 2D band at  $2700\text{ cm}^{-1}$ , while the G bands of graphene were obscured by the background signal of the epoxy. Raman spectroscopy was also conducted (Fig. 6.8b) on the fracture surface of the lower strip (LSi) at the four spots identified in Figure 6.6b. A striking feature of all these spectra is that there were no signs of the G band or the 2D band. It can thus be concluded that graphene was removed from the lower silicon strip and successfully transferred to the epoxy surface on the upper silicon strip.

In previous interfacial fracture experiments between epoxy and silicon [108], AFM scans of the silicon and epoxy fracture surfaces identified dense ligament formation in regions where the epoxy had preferentially attached to the silicon. Also observed in previous studies of glass/epoxy interfaces has been ridge formation, reflecting a peculiar mechanism of interfacial crack propagation in these systems. Accordingly, as a control, a

wedge test was conducted on a silicon/epoxy/silicon laminate with the IR-transparent epoxy that was used in this study. Evidence of ligament formation and ridge formation on the epoxy surface was again evident (Fig. 6.8c)), albeit with a much lower density of ligaments.

The AFM scan of the fracture surface of USi is shown in Figure 6.8d, where it can be seen that there was no ligament or ridge formation at all. This was yet another indication that the graphene had been transferred to the epoxy. The features that did appear on the otherwise smooth graphene surface were bubbles rising as much as 150 nm above the surrounding surface. These bubbles may suggest that the graphene was not completely attached to the epoxy, though further study of this phenomenon is required. The overall RMS roughness over a  $7 \times 10 \mu\text{m}$  region removed from the large bubbles was 9.7 nm. Smooth regions away from bubbles had RMS roughness values ranging from 0.4 to 0.7 nm.

### **6.3 TRACTION-SEPARATION RELATIONS FOR INTERACTIONS BETWEEN GRAPHENE AND SILICON**

Once the fracture path was confirmed, the interfacial fracture toughness or adhesion energy of graphene with respect to the Si(111) substrate was calculated using a simple beam theory approach. By tracking the J-integral as a function of the NCOI at the end of the cohesive zone, it was possible to determine the traction-separation relations for each specimen. This approach was only able to detect traction-separation relations for separations beyond the 20-nm resolution of the IR-COI. As a result, a nonlinear finite element analysis was used to complete the extraction of the traction-separation relations [101, 102, 106-108]

### ***Specimen Response***

Figure 6.9 shows a typical set of responses to the insertion of the wedge in three different samples. Each of the crack lengths noted in the figure was measured at the end of the 30-second interval for a given wedge position. It can be seen that, as the wedge was inserted without any crack growth, the responses were initially linear. The responses became nonlinear as the crack started to grow and soon achieved steady state in the sense that the crack length remained the same following each wedge insertion.

Shown in Figure 6.10 is a typical set of NCOD profiles measured by IR-COI for one of the specimens. A number of such profiles are shown as the wedge was inserted in order to capture the initial opening of the crack faces without growth, through initiation and subsequent steady state growth.

### ***Delamination Resistance Curves***

By measuring the crack length at any particular wedge insertion, Equation 2.15 allows the J-integral to be determined as a function of crack extension in order to obtain the adhesion resistance curve for the silicon/graphene interface. In the experiments that were conducted here, the crack lengths were such that  $a \gg 20h$ , which is sufficient for simple beam theory and transverse shear effects, could be neglected [106]

The results from the three different specimens (test 1 and 2 in Fig. 6.11a and test 3 in Fig. 6.11b) were quite consistent although specimen 3 exhibited a steeper increase in delamination resistance prior to some quite regular “stick-slip” behavior, which suggests that the adhesion between graphene and silicon may have been slightly different in this case.

In all cases, the J-integral grew steeply from zero to between 100 to 180 mJ/m<sup>2</sup> for small amounts of growth (< 3 μm), below the uncertainty in measurements of crack extension [107]. The rate of increase in the J-integral decreased with increasing crack



extension and eventually reached a plateau after crack extensions of 0.7 to 2 mm. The J-integral at the plateau was considered to be a steady state toughness  $\Gamma_{ss}$  at  $357 \pm 16$  mJ/m<sup>2</sup>. This was the average and standard deviation of all peak values once the plateau had been achieved in each specimen. This value is about 90 mJ/m<sup>2</sup> lower than previous results reported by Koenig *et al.* [58], but 120 mJ/m<sup>2</sup> higher than the value reported in [59]. It is unclear at this time whether or not this is a significant difference. However, in both reports [58, 59], the graphene was exfoliated from graphite and the silicon oxide layer was approximately 300 nm thick, grown on a Si(100) surface. In this study, the CVD-grown graphene was wet-transferred from its copper seed layer to the Si(111) with approximately 2 nm-thick native oxide layer with a root mean squared (RMS) roughness of less than 0.5 nm (Fig. 6.1). In addition, there may also have been differences in the nature of any liquid trapped between the graphene and silicon in each case when the graphene was wet-transferred to silicon substrate.

The presence of trapped copper residue and the number of cracks and wrinkles (Fig. 6.1 and Fig. 6.12) in the graphene may also differ from sample to sample and manifest in the slight differences noted here. The SEM images in Figure 6.12 display the worst examples of wet-transferred graphene on silicon, with evidence of residue on the surfaces in addition to the non-uniform surface morphology. Figure 6.12a shows high-resolution SEM images of wet-transferred graphene on Si(111), where wrinkles, copper and PMA residues, and trapped residue or voids remained. Figure 6.12b is another high-resolution image of a different spot where large and small residues were transferred with monolayer graphene. The large residues were fewer and randomly distributed whereas the smaller ones were aligned in patterns that might correspond to steps in the copper. It was not possible to determine the chemical composition of the residues with Energy-Dispersive X-ray spectroscopy (EDS) in the Quanta 650 SEM. This was due to the

abundance of silicon and the strength of its signal. Nonetheless these two SEM images certainly identified residues, which could in turn affect the adhesive interactions.

### ***Traction-Separation Relations***

The traction-separation relations associated with silicon/graphene interactions can be obtained by measuring the development of the J-integral with respect to  $\delta_n^*$ ; such data is shown (Fig. 6.13) for the same three samples. Similar to the resistance curves in Figure 6.11, there was a very steep rise in the value of the J-integral before the NCOD exceeded the resolution of the IR-COI. Subsequently, the J-integral increased gradually before reaching steady state.

The corresponding traction-separation relation (Fig. 6.14) was determined by applying Equation (2.23) to the data in Figure 6.13 using a central difference scheme. In each case, the traction-separation relations obtained in this way had very steep increases to the maximum value of the traction that could be measured given the resolution in NCOD. Note that this was not necessarily the actual maximum strength  $\sigma_0$  of the interaction at the associated separation  $\delta_n^0$  (insert to Fig.6.14).

The tractions then decayed to zero at  $\delta_n^c$ , the critical separation for fracture. The area under the traction-separation relation equals the steady state toughness  $\Gamma_{ss}$  (adhesion energy), while the strength and range of the interactions are characterized, respectively, by the maximum traction ( $\sigma_0$ ) and the critical separation ( $\delta_n^c$ ). The values of these parameters for each experiment are recorded in Table 6.1. The critical NCOD were the most difficult parameters to assign values to because of the long tails of the distributions and the levels of uncertainty in the measurements.

Looking at Figure 6.14, it can be seen that the measured traction-separation relations obtained from the first two samples were quite similar. The initial stiffness,

measured strength and the critical NCOD from the third sample were all noticeably lower. From Table 6.1, the measured strengths for samples 1 and 2 were between 1.95 and 2.42 MPa at associated NCOD  $\delta_n^0$  of 19.84 and 25.9 nm. The values of  $\delta_n^c$  were estimated to be 820 and 530 nm, respectively for specimens 1 and 2. While the value of the adhesion energy (366 and 377 mJ/m<sup>2</sup>) compares closely with predictions for vdW interactions [211], the range of the interactions are much longer than vdW. Hence, the present results challenge the current understanding that vdW interactions are the dominant mechanism for the adhesive interactions between graphene and silicon. The interaction ranges for electrostatic interactions between graphene and silicon are in the nanometer range [182] thereby ruling them out as a potential mechanism for the interactions measured here. A likely mechanism for the observed long-range interactions may be capillary effects, although the interaction range for capillary forces due to water menisci is typically less than 5 nm [183], [21] on smooth surfaces. One factor that might explain the noted differences is the roughness of the silicon substrate and how well graphene can conform. The combined effects of surface roughness and capillary forces could in principle extend the interactions to longer ranges but reduce the magnitude of tractions. The RMS roughness of the Si(111) surface considered in this study is less than 0.5 nm (Fig. 2.8 and 4.12), which is much less than the range of RMS roughness (2.6 to 10.3 nm) that was considered by DelRio *et al.* [215] for vdW interactions between polysilicon surfaces. Capillary effects were also considered [216, 217] over the same range of roughness. In both cases, the roughness effect brought the interaction range into registration with the values measured here. However, the adhesion energies were much lower ( $\sim\mu\text{J}/\text{m}^2$ ) and no information on traction levels was provided.

## 6.4 ANALYSIS

The 20-nm resolution limit of the IR-COI measurements meant that interactions over smaller separations could not be measured. Nonetheless, the measurements at larger separations formed the basis of reference traction-separation relations that accounted for smaller separations. These were incorporated in finite element analyses of the experiments and were adjusted based on other data from the experiments.

The linearly elastic behavior of the silicon was accounted using an in-plane Young's modulus for Si(111) of 169 GPa and a Poisson's ratio of 0.2. The linearly elastic behavior of the epoxy was initially accounted for with a modulus of 3 GPa and a Poisson's ratio 0.4. However, the computation times were extremely long and convergence was often difficult and the resulting separations were within 5.6% of calculations that ignored the presence of the epoxy. Consequently, the results that are presented here were obtained from solutions that neglected the epoxy layer. The analyses also accounted for interactions between the graphene and silicon through traction-separation relations (insert Fig. 6.14) that had the form

$$\sigma = K_n \delta_n H(\delta_n^0 - \delta_n) + \left( \sigma_0 \left( 1 - \frac{1}{1 - e^{-\alpha}} \right) + \frac{\sigma_0}{1 - e^{-\alpha}} e^{-\alpha \left( \frac{\delta_n - \delta_n^0}{\delta_n^c - \delta_n^0} \right)} \right) H(\delta_n - \delta_n^0) \quad (6.1)$$

where  $\delta_n$  is the separation of the crack surfaces at any location,  $K_n$  governs the elastic portion of the interaction, the parameter  $\alpha$  governs the decay of the interaction and  $H$  is the Heaviside step function. This form is the so-called exponential decay traction-separation relation, which was the better of two options available in ABAQUS.

Two traction-separation relations (Table 6.2) were considered in the analysis. One (TSR1) matched the measured traction-separation relations from tests 1 and 2 while TSR2 corresponded to the traction-separation relation from test 3. While these traction-separation relations matched the measurements in the range where they could be

measured (Fig. 6.14), they both continued the interactions closer to zero separation. The maximum strength for TSR1 was 24 MPa at 2 nm with  $\alpha = 0.25$  and a cut-off separation of 150 nm for an adhesion energy of  $357 \text{ mJ/m}^2$ . The corresponding parameters for TSR2 were 8 MPa, 2 nm, 5.5, 250 nm and  $360 \text{ mJ/m}^2$ . TSR1, which was constrained by Equation 2.22, matched the measured traction-separation relations quite well from 20-70 nm but did not capture the long tail. The fit between TSR2 and the data from test 3 was excellent over the entire range of measurements. The finite element solutions for the variation of crack length with respect to wedge insertion (Fig. 6.9), crack opening displacements (Fig. 6.10) and resistance curves (Fig. 6.11) were all compared with measurements.

In Figure 6.9, it can be seen that the solution that made use of TSR1 was in good agreement with the data from test 1, but not test 2. This was because the adhesion energy of  $357 \text{ mJ/m}^2$ , which was selected for TRS1 as the average of all steady-state adhesion values, was close to the adhesion energy that was measured in test 1. The agreement between the solution for TSR2 and the data from test 3 was excellent. It should also be noted that the transition from no growth to steady state growth is more gradual when the range of the interactions is longer.

The NCOD shown in Figure 6.10 were measured in test 3. The finite element solutions using obtained TSR2 for steady state growth are compared with data when the crack was 6.08 and 6.21 mm long. It can be seen that the agreement was quite good at locations behind the first fringe ( $\delta_n = 265.5 \text{ nm}$ ). However, the finite element solutions for the NCOD between the crack front and the first fringe were consistently lower than the measured values, which were obtained from the measured intensity between the crack front and first fringe. In view of the calibration given in Figure 2.15c and the confidence gained from it, the measured protrusion of the NCOD appears to be reasonable and an

explanation for it is required. The protrusion is most likely produced by repulsive forces very close to the crack front and hydration forces [156, 178] are certainly one possible mechanism.

The solution for the resistance curve with TSR1 (Fig. 6.11a) initially rose more steeply than the data but reached the steady state adhesion that was measured in test 1 for the reasons given earlier. The reason for the steeper rise was that TRS1 did not capture the more gradual decay of the measured traction-separation relations from tests 1 & 2. This point is brought out very well in Figure 6.11b, where the solution for TSR2 had the same gradual rise as the data and reached the adhesion energy of  $360 \text{ mJ/m}^2$ , which corresponded to the peaks of the measured stick-slip behavior.

Four different traction-separation relations with an adhesion energy of  $350 \sim 360 \text{ mJ/m}^2$  were used in a parametric study of the effect of the interaction range  $\delta_n^c$  on the shape of resistance curves (Fig. 6.15). As the interaction range of each traction-separation relation increased, the resistance curves approached the measured ones. If a vdW interaction with a maximum strength of 200 MPa and critical separation of 3 nm had been used as a traction-separation relation in the finite element analysis, it is clear that it would not match any of the measured portions of the traction-separation relations. Furthermore, the transition from no growth to steady state growth (Fig. 6.9) would have been very abrupt. Capillary interactions have been represented by a constant strength at 35 MPa for 5 nm [183] with an adhesion energy of  $175 \text{ mJ/m}^2$ . While such an interaction would still provide a sharp transition from no growth to steady state growth for the reason given above, the lower adhesion energy of capillary effects would cause the crack to grow at much longer crack lengths. The effect of either interaction on the NCOD would not be visible at the scales shown in Figure 6.10. The effect of longer interaction ranges is also apparent in the resistance curves (Fig. 6.11 and 6.15). For

example, the longer interaction range of TSR2 resulted in a more gradual rise in the J-integral prior to steady state growth. If a longer interaction range could have been incorporated in TSR1, it would have matched the more gradual rise in the J-integral prior to steady state growth that is apparent in the data. These observations support the claim that neither van der Waals nor capillary interactions, by themselves, were at play here.

The roughness of the graphene on silicon ranged from 0.4 to 5 nm due to defects such as wrinkles, trapped copper residues and torn graphene. This could affect the shape of the rising portion of the resistance curves (Fig. 6.11), the steady state toughness and the traction-separation relations. As a result, the long-range interactions that have been observed in this study are most likely reflections of the effect of roughness, which sets the stage for future investigations.

## **6.5 CONCLUSIONS**

A fracture mechanics approach was developed to determine the adhesion energy and traction-separation relations associated with the interactions between CVD grown graphene and silicon to which the graphene had been transferred using a wet transfer process. By bonding a second strip to the graphene surface with an epoxy and then peeling the silicon strips apart in a wedge test, interfacial crack growth between graphene and silicon was observed and analyzed. The crack length and NCOD were measured as a function of wedge insertion using IR-COI. This data was then coupled with fracture mechanics analyses to extract the adhesion energy, delamination resistance behavior and traction-separation relations associated with interactions between graphene and silicon.

The adhesion energy of  $357 \pm 16$  mJ/m<sup>2</sup> obtained in the present study was bounded by previously reported values for exfoliated graphene flakes, suggesting that the process of wet transferring polycrystalline CVD grown graphene on Si(111) over relatively large

areas has no adverse effects. Furthermore, it was in reasonable agreement with theoretical predictions for vdW forces between graphene and silicon, but probably for the wrong reasons. The range of interactions was beyond those usually attributed to retarded vdW interactions. The maximum strength that could be measured was most likely lower than the actual one because the resolution in the measurement of separation was not sufficient to capture it. This was brought out in subsequent continuum analyses with traction-separation relations which captured the measured interactions and extended them to smaller separations and higher tractions. The combinations of experiments and analysis described here should provide a basis for subsequent models of the nature of graphene/silicon interactions over relatively large spatial dimensions. Such developments will have to account for the effects roughness and humidity on long-range interactions. The approach developed here can be extended to other two-dimensional materials and substrates.



## Chapter 7 Selective Mechanical Transfer of Graphene<sup>8</sup>

As indicated in the introduction, transferring CVD grown graphene from its seed copper foil is currently achieved by etching away the copper [48, 66, 79, 99, 218] or electrochemically bubbling the graphene off the copper [80, 219]. Both are relatively slow processes. Yoon *et al.* [61] were the first to demonstrate that graphene could be mechanically separated from its seed copper layer. In that work, the copper film had been deposited on silicon oxide prior to CVD of graphene. A second silicon strip was bonded to the graphene with an epoxy. The two silicon strips were peeled apart and, for applied displacement rates above 5.0  $\mu\text{m/s}$ , it was shown that delamination occurred along the graphene/seed copper interface, transferring a graphene monolayer onto the epoxy. The adhesive energy of graphene grown on copper film was 720  $\text{mJ/m}^2$ . In this Chapter, it is demonstrated that graphene can be selectively removed from its seed copper foil or a polymer backing layer by peeling at different rates. The demonstration is supplemented by data and analyses that were used to extract the traction-separation relations for the interactions between graphene and copper and graphene and epoxy.

### 7.1 SELECTIVE TRANSFER

The approach for mechanically separating graphene from copper film on silicon introduced by Yoon *et al.* [61] is extended here to separating graphene from copper foil. The copper foil is quite thin so it was necessary to provide some reinforcement in order to delaminate the graphene from the seed copper. The reinforcement was in the form of two silicon strips which were bonded to each graphene surface of the graphene-coated copper foil.

---

<sup>8</sup> The contents in this chapter were published in ACS Nano: S. R. Na, J. W. Suk, L. Tao, D. Akinwande, R. S. Ruoff, R. Huang, *et al.*, "Selective Mechanical Transfer of Graphene from Seed Copper Foil Using Rate Effects," *ACS nano*, vol. 9, pp. 1325-1335, 2015.

### ***Sample Fabrication***

The graphene was grown using a CVD process [48, 79, 123, 124] on a 50×50 mm copper foil (35 μm thick) that had been formed into a thin tube for deposition purposes. The graphene-coated tube was then flattened on a silicon wafer (Fig. 2.12a). Several 5×40 mm silicon strips that were 295 μm thick were bonded to the flattened, graphene-coated copper foil (Fig. 2.12b) using an epoxy (EP30, Master Bond, Inc.). The cure followed manufacturer's recommendations at 100 °C for two hours. A second silicon strip was then bonded to the remaining graphene surface over 75% of its length (Fig. 2.12c-d) using the same epoxy and cure conditions. The resulting silicon/epoxy/graphene/copper/graphene/epoxy/silicon laminate was then tabbed at one end (Fig 2.12e) using aluminum tabs, which were connected to a servo-hydraulic loading device in preparation for a classical double cantilever beam fracture test [61, 220].

The ends of the upper and lower silicon strips were separated (Fig. 7.1a) under displacement control with rates ranging from 25.4 to 254.0 μm/s. The reactive load was measured by a 10 N load cell while the crack tip location was monitored by a camera. With many of the specimens, several load/unload/reload cycles could be conducted before each specimen was completely separated. Both fracture surfaces were then examined with Raman spectroscopy (WITec Alpha 300 micro-Raman confocal microscope ( $\lambda = 488$  nm) and scanning electron microscopy (SEM; FEI Quanta 650 ESEM) in order to determine the locus of delamination. The latter was particularly useful for mapping the full extent of any transfer of the graphene from its seed copper foil to the adjacent epoxy because the presence of any graphene on the epoxy prevented charging from occurring.

### ***Graphene/Copper Delamination***

The ends of the upper and lower silicon strips were separated (Fig. 7.1a) under displacement control with rates ranging from 25.4 to 254.0  $\mu\text{m/s}$ . As the stitched image in Figure 7.1b indicates, it was possible to obtain clean transfer of graphene over a  $16\times 5$  mm region starting from the epoxy terminus, when the applied displacement rate was 254.0  $\mu\text{m/s}$ . A more detailed view of the contrast that graphene provides is shown in Figure 7.1c at the epoxy terminus. The dark region is indicative of graphene on epoxy, while the grey region is the lower surface of the upper silicon strip that did not have any epoxy and consequently no graphene on it. An even higher magnification view of the corresponding region on the surface of the copper foil (Fig. 7.1d) reveals that graphene also provided contrast on copper. The mainly lighter region in the top portion of the figure is where the graphene was removed from the copper; some groups of lines corresponding to steps on the surface of the copper foil can be seen here. Note that some graphene (darker islands) was not removed from the copper, mainly near the epoxy terminus. On the other hand, the mainly darker region in the lower half, corresponding to the region where no epoxy had contacted the upper silicon strip or the graphene on the foil, shows that the graphene coverage was uniform in this region. The straight line features are wrinkles in the graphene and the small darker regions are ad-layers where additional graphene islands were grown on the monolayer graphene during growth.

A more detailed view of the graphene-coated surface of the epoxy is presented in Figure 7.2a. The steps and wrinkles that were observed on the bare copper surface were replicated by the relatively low viscosity epoxy. In addition, there were holes in the graphene which exposed bare epoxy as islands and led to local charging effects. The distribution of holes in the graphene was bimodal, with larger holes mainly within regions surrounded by wrinkles and much smaller ones along the wrinkles. The larger

holes in the graphene appear to have occurred during the transfer process as also indicated by the graphene patches left behind on the copper fracture surface (Fig. 7.1d). On other hand, the smaller holes in the graphene along the wrinkles may correspond to defects caused by wrinkling during growth. The initial state of the graphene on copper foil following deposition is captured in Figure 7.2b-c. The grain boundaries of the copper and steps within the copper grains are clearly visible (Fig. 7.2b). Wrinkles in the graphene following growth are again present and are accompanied by small dark spots along the wrinkles. Experience has shown that these spots are copper oxide that is formed by oxygen passing through very small defects induced by the wrinkles and oxidizing the bare copper beneath. Nonetheless, the coverage of the copper by the graphene was quite complete. There were no grain boundaries present in Figure 7.2c, because the image was taken inside a large copper grain. However some defects that were larger than the copper oxide spots appeared at some locations near the wrinkles. The conclusion from these images is that graphene was well-transferred to the epoxy, with a slightly higher defect count, particularly within regions surrounded by wrinkles. Nonetheless, as will be borne out later by Raman maps and electrical resistance measurements, these defects did not impair the overall quality of the graphene.

Based on the SEM micrographs just described, the fracture path at an applied displacement rate of 254.0  $\mu\text{m/s}$  is shown schematically in Figure 7.3a. The stress concentration provided by the bimaterial corner between the epoxy terminus and the graphene (Fig. 7.4) caused a crack to penetrate the graphene and then grow along the graphene/copper interface. The corresponding load-displacement response is shown in Figure 7.3b, where the first peak and load drop correspond to the initiation and growth of a fast crack from the bimaterial corner. The specimen was then unloaded, thereby arresting the crack and providing a sharp crack for the subsequent reloading. This time,

the onset of crack growth was followed by slower, more stable growth which transitioned to fast cracking prior to the next unloading for cycle 3, where the sequence was repeated.

While SEM micrographs of the graphene coated epoxy surface are indeed useful for determining the areal extent of graphene transfer, Raman spectroscopy (Fig. 7.3c) is required for determining the quality of the transferred graphene. Thirteen spots on approximately 1-mm centers along the graphene-coated epoxy surface were probed. All the Raman spectra exhibited G and 2D peaks at approximately 1600 and 2700  $\text{cm}^{-1}$ , respectively. The peak at approximately 1600  $\text{cm}^{-1}$  was made up of two peaks as can be seen in the decomposed spectrum (Fig. 7.5): the G peak for graphene at 1587  $\text{cm}^{-1}$  and a major peak at 1605  $\text{cm}^{-1}$  from the epoxy [99]. The graphene spectrum also exhibited the 2D peak at 2691  $\text{cm}^{-1}$ , thereby verifying the presence of the graphene on the epoxy. While the average intensity ratio  $I_{2D}/I_G$  was 1.89, indicating that monolayer graphene had indeed been grown on the copper foil. The average value of the intensity ratio  $I_{2D}/I_G$  for graphene in the decomposed spectrum was 1.3. Note the slight shifts in the G and 2D peaks on the epoxy and copper; taking the latter as a reference, it is possible that the shift that occurred upon transferring the graphene to the epoxy was due to residual stresses and substrate effects [133, 136]. There was a D band peak at 1353  $\text{cm}^{-1}$  for the 12th spot, which indicates that there was some damage to the graphene at this location. A set of 8 Raman spectra (Fig. 7.3d) was obtained from the opposite fracture surface. The first five had no G or 2D peaks, thereby confirming that the graphene had indeed been removed from that portion of the copper foil. The spots marked 6, 7 and 8 had G and 2D peaks at 1580 and 2709  $\text{cm}^{-1}$ , respectively, as they probed that part of the copper foil which had not been covered by epoxy.

The point wise Raman spectra were augmented by a series of Raman maps, which can verify the presence of the graphene over smaller but continuous domains. Raman

maps of 100×100 μm regions of graphene that had been transferred to epoxy over are shown in Figures 7.6 a-e for the intensity of G peak, 2D peak, the ratio of 2D and G peaks ( $I_{2D} / I_G$ ) and the peak distribution of the G and 2D peaks, respectively. Due to the topography of the epoxy layer, the intensity of the G and 2D peaks (Fig. 7.6a and b) varies and this data is presented in Figure 7.7. Nonetheless, the G and 2D peaks are still located at approximately 1598 cm<sup>-1</sup> and 2695 cm<sup>-1</sup> (Fig 7.6d and e), respectively. The ratio of the intensities of the 2D and G peaks are compared in Figure 7.6c. The ratio ranged from 0.23 to 1.2 which signifies the presence of continuous graphene on epoxy surface. Two other Raman maps of different 50×50 μm regions are shown in Figures 7.8, 7.9. They all confirmed the presence of graphene on epoxy surface. The ratios of the intensities of the 2D and G peaks are shown in Figure 7.8c and 7.9c and varied from 0.15 to 0.8 and from 0.43 to 0.93, respectively. Once the presence of transferred graphene on the epoxy was confirmed, the copper fracture surface, which should then be free of graphene, was mapped over 100×100 μm regions (Fig. 7.10). The intensities of both peaks were essentially zero.

The shift of 2D peaks due to graphene on epoxy relative to the location of the 2D peak following growth of the graphene was compared in Figure 7.11. Following growth, the 2D peak was usually located at 2709 cm<sup>-1</sup>. However, the 2D peak after delamination ranged from 2694 cm<sup>-1</sup> to 2697 cm<sup>-1</sup>. This shift of the 2D peak could be associated with the residual strain that accompanies any plastic deformation of the copper foil during delamination. It could also be associated with chemical doping by epoxy layer. In order to identify the dominant factor, tracking of the G band is required because the rate of change of the shifting of the G and 2D peaks of graphene is different for strain and doping effects [141, 221, 222]. However, it was not possible to discern any shifts in the G

peak of graphene due to the presence of a nearby epoxy peak. The maps confirmed the conclusions obtained by SEM and point wise Raman spectra.

As a final measure of the effective transfer of graphene from the seed copper to the epoxy, the sheet resistance of the graphene was measured using the transfer length method (TLM). The electrical behavior of the graphene after it had been transferred to the epoxy was measured on a Cascade® probe-station with an Agilent B1500 analyzer under ambient conditions. To characterize the contact resistance, 100- $\mu\text{m}$  wide channels that were 25, 100 and 200  $\mu\text{m}$  long were fabricated for TLM measurements. The corresponding resistances were  $1677\pm 162.9$ ,  $2225\pm 293.5$  and  $2693\pm 49.4$   $\Omega$ , respectively, giving a contact resistance ( $R_c=787.8$   $\Omega$ ) obtained by linear extrapolation as shown in Figure 7.12a-b. Moreover, the sheet resistance of the graphene film, measured by a four-point probe setup 20, was  $863.6$   $\Omega/\square$  (Fig. 7.12c). The sheet resistance was at the lower end of the range for graphene that had been transferred to PMMA using a conventional wet transfer process [219].

To our knowledge, this is the first time that large area, CVD grown graphene has been mechanically removed from its seed-copper foil and dry transferred to another substrate. Compared to wet transfer, the potential for speeding up graphene transfer in nano-manufacturing processes such as roll-to-roll transfer by such a mechanical approach is clear. An additional advantage is that the copper foil can potentially be recovered and recycled in the same roll-to-roll process [61].

### ***Graphene/Epoxy Delamination***

At an applied displacement rate of  $25.4$   $\mu\text{m/s}$ , the picture was quite different; the crack grew at the graphene/epoxy interface. As indicated in the schematic (Fig. 7.13a), the crack initiated at the bimaterial corner (Fig. 7.4) and propagated along the

graphene/epoxy interface without ever breaking the graphene monolayer itself. The corresponding load-displacement response is shown in Figure 7.13b. Only one loading cycle was applied, but there were clear signs of slow crack growth prior to the peak load, at which point the crack growth became faster with some indications of stick-slip behavior. There was no 2D peak in any of the 10 Raman spectra (Fig. 7.13c) that were taken on the epoxy side of the fracture surface. They all had peaks near  $1605\text{ cm}^{-1}$ , but these are attributable to the epoxy itself [110]. However both G and 2D peaks were present at  $1590$  and  $2710\text{ cm}^{-1}$ , respectively, in the 9 Raman spectra that were taken at a series of spots on the graphene-coated copper foil. The average value of the intensity ratio  $I_{2G}/I_G$  from the 9 spectra was 2.4, again indicating that monolayer graphene was present before and after delamination between the graphene and epoxy. The peaks were slightly shifted from those obtained from as-grown graphene on copper foil (Fig. 7.13d), again suggesting a residual stress in the graphene after delamination. This might have been due to plastic deformation in the copper foil as the crack front passed by a particular location, leaving behind residual strain in a plastic wake partly or entirely through the thickness of the copper foil. It is also possible that the orientation of copper grains and strains on graphene shifts Raman peaks [141, 221, 223]. However no such shifts were observed in Raman spectra that were obtained from graphene that had just been deposited on copper foil.

Raman maps of  $100\times 100\text{ }\mu\text{m}$  regions of the epoxy fracture surface are shown in Figures 7.14 and 7.15. The signal intensities near the G peak of graphene (Fig. 7.14a and 15a) were very high due to the epoxy peak nearby. However the intensity of the 2D peak (Fig. 7.14b and 15b) was essentially zero, confirming that there was no graphene on the epoxy fracture surface. The Raman maps of the copper fracture surface (Fig 7.16) and



particularly the intensity ratio (Fig. 7.16c), which varied from 1.3 to 4.8, confirmed the presence of monolayer graphene on copper.

### ***Other Delamination Modes***

The two scenarios presented so far were from applied displacement rates of 254.0 and 25.4  $\mu\text{m/s}$ . As indicated in Table 7.1, 35 experiments were conducted at the higher rate while 6 were conducted at the lower rate. Experiments were also conducted at intermediate rates of 42.3, 84.6, 127.0 and 169.3  $\mu\text{m/s}$ . These resulted in varying degrees of graphene transfer, with increasingly larger regions of graphene being transferred to the epoxy as the applied displacement rate was increased. This is demonstrated in Figure 7.17b-d, where SEM images of the fracture surfaces from experiments that were conducted at 42.3, 84.6 and 169.3  $\mu\text{m/s}$ , respectively are presented. At the lowest rate, three regions from the upper fracture surface are identified: bare silicon, graphene on epoxy and bare epoxy. The boundary between the bare silicon and graphene on epoxy is the epoxy terminus so there was indeed no graphene on the bare silicon. The contrast between the graphene/epoxy and bare epoxy regions above the terminus is clear, with the lack of charging due to the presence of graphene leading to the darker region. This is borne out by the Raman spectra from spots identified as G1 and E1 in Figure 7.17a. The spectrum from G1 had the G and 2D peaks with an average value of  $I_{2D}/I_G = 1.1$  for graphene, confirming the presence of graphene on epoxy and delamination at the graphene/copper interface. The spectrum from E1 only had the epoxy peak at 1605  $\text{cm}^{-1}$ ; thus in this region the delamination occurred at the graphene/epoxy interface. At 42.3  $\mu\text{m/s}$ , the patches of graphene on epoxy and bare epoxy were both about 3 $\times$ 3 mm. The situation at 84.6  $\mu\text{m/s}$  (Fig. 7.17c) was quite similar; the same three regions can be identified in the SEM image, the Raman spectra at the spots G2 and E2 had the same

features as those obtained at G1 and E1, and the patches of graphene on epoxy and bare epoxy are about the same size at 3×3 mm. At 169.3 μm/s, except for a very small patch of bare epoxy, it was a clean transfer of graphene to epoxy over the full width of the silicon strip and up to 5.4 mm from the epoxy terminus. The Raman spectra from the spots confirmed the presence of graphene on epoxy with average value of  $I_{2D} / I_G = 1.1$ .

### ***Identification of Delamination Modes***

The three major delamination modes observed in this study were designated case 1, case 2 and case 3. Case 1 (Fig. 7.18) was pure delamination along the graphene/copper interface and was dominant when the applied loading rate was 254 μm/s. Case 2, delamination along the epoxy/graphene interface, occurred when the applied displacement rate was reduced to 25.4 μm/s (Fig. 7.18b). Under this condition, graphene still remained on the copper foil. Case 3 occurred at all rates and always involved the formation of a blister below the copper foil (Fig. 7.17c), probably due to slightly lower adhesion, but its presence allowed subdivision into cases 3-1 (Fig. 7.17d) and 3-2 (Fig. 7.17e). Once a copper blister was formed, case 3-1 arose when delaminations could develop above the copper foil, which arrested further growth of the blister. Alternatively, it was possible for the blisters to grow below the copper without any further delamination growth above it; this was case 3-2. In both cases, graphene was transferred to epoxy, but there were regions where the graphene was continuous and others where it was only present as patches.

## **7.2 ANALYSIS**

The measured load-displacement responses associated with delamination along the graphene/copper (Fig. 7.3b) and graphene/epoxy (Fig. 7.13b) interfaces were used to determine the adhesion energy as well as the strength and range of the interactions

associated with each interface. The adhesion energy was first obtained from fracture mechanics concepts [224] using a simple beam analysis to determine the elastic energy available to separate the interfaces of interest. The strength and range of interactions were determined numerically using cohesive zone modeling concepts [96].

### ***Beam Theory Analysis***

The slope of the rising portion of the load-displacement response of the experiments at 254  $\mu\text{m/s}$ , where the copper graphene interface delaminated, was predicted by simple beam theory (Eq. 2.16) and matched the data in the first and subsequent load-unload cycles (Fig. 7.3b) using the measured crack length in each case and the other specimen dimensions and the Young's modulus of the silicon strips. The descending portion of the load-displacement response corresponds to the initiation and growth of the delamination along the graphene/copper interface and is governed in the simplest case by the adhesion energy  $\Gamma_{ss}$  and Equation 2.18. Values of 5 and 7  $\text{J/m}^2$  bounded the measured response in this regime.

These adhesion energy levels are much higher than the value  $720\pm 70 \text{ mJ/m}^2$  measured by Yoon *et al.* [61] for the graphene/copper film interface. They are also higher than value  $1.8 \text{ J/m}^2$  for an epoxy/silicon interface measured at very low separation rates [106], but lower than the fracture toughness of graphene itself at  $15.9 \text{ J/m}^2$  [225]. In separate control experiments on silicon/epoxy/silicon sandwich specimens, the adhesion energy of the epoxy/silicon interface was  $7.5\pm 0.2$  and  $11.1\pm 0.1 \text{ J/m}^2$  at loading rates of 84.6 and 254.0  $\mu\text{m/s}$ , respectively (Fig. 7.19). These values are higher than the bound of  $5\text{-}7 \text{ J/m}^2$  at 254.0  $\mu\text{m/s}$  for the graphene/copper foil interface, thereby explaining why delamination at the silicon/epoxy interface never occurred. The result also suggests that, at 254.0  $\mu\text{m/s}$ , the graphene/epoxy interface had higher adhesion energy. The question

then arises as to why the adhesion energy is so high. One possibility is that the copper foil and the epoxy were yielding with attendant energy dissipation during delamination growth, thereby adding to the intrinsic adhesion energy of the graphene/copper interface [24, 25].

The simple beam analysis of the experiment at 25.4  $\mu\text{m/s}$  captured (Fig. 7.13b) the initial stiffness of the measured response over this range of force and applied displacement. If delamination initiation is governed by the criterion,  $G = \Gamma_{ss}$ , the load-displacement response will continue to be linear until the associated load level, which can be computed from Equation (2.17), is attained; Thereafter, the response will follow Equation (2.18). This idealized scenario is depicted (Fig. 7.13b) by the two LEFM cases for adhesion energy levels of 3.0 and 3.6  $\text{J/m}^2$ , which bound the measured response in the descending portion of the load-displacement response. They are also about half of the toughness of the graphene/copper interface, which is consistent with the noted delamination paths. Just as the adhesion energy of the epoxy/silicon interface displayed a rate-dependence, so may the epoxy/graphene one with the likelihood of an adhesion energy that is greater than the 5-7  $\text{J/m}^2$ , that was determined for the graphene/copper interface at 254  $\mu\text{m/s}$ . Apparently, the simple criterion  $G = \Gamma_{ss}$  does not account for the gradual transition to steady state delamination that is reflected in the smooth change in slope of the measured response between 0.2 N and the maximum load; this should be captured by cohesive zone modeling.

### ***Cohesive Zone Modeling***

In order to address the gradual transition to steady state delamination and the possibility that plastic dissipation was largely contributing to the adhesion energies that were determined by simple beam theory analysis, a series of finite element analyses was

conducted that accounted for the elastic-plastic behavior of the epoxy and copper foil. The adhesive interactions of the relevant interfaces were also accounted for using traction-separation relations that were calibrated in an inverse manner on the basis of the load-displacement and adhesion resistance responses. The first step for the analysis was to obtain the stress-strain behavior of the copper foil and epoxy.

Due to the harsh graphene growth condition and high temperature annealing environment ( $\sim 1000$  °C), copper grains on the order of millimeters were formed after graphene growth. In the plastic deformation of polycrystalline materials, the grain boundaries play a very important role in the deformation process. Hall and Petch [226, 227] suggested the relation between the lower yield strength and grain size, could be given by

$$\sigma_y = \sigma_0 + kD^{-1/2} \quad (7.1)$$

where  $\sigma_y$  is the yield stress,  $\sigma_0$  is a fractional stress required to move dislocations,  $k$  is the strength coefficient, and  $D$  is the grain size. For copper,  $\sigma_0$  is 25.5 MPa and  $k$  is  $0.11 \text{ MN/m}^{3/2}$ , respectively [228]. Based on Equation (7.1), the estimated value of  $\sigma_y$  is approximately 29 MPa based on a grain size of 1mm (Fig. 7.1b-d) for the copper foil following deposition of graphene.

Uniaxial tension tests on the copper foil (Fig. 7.20) were conducted at strain rates of  $0.5 \text{ s}^{-1}$  and  $1.5 \text{ s}^{-1}$ . There was no obvious effect of strain rate on the yield strength, so the average yield strength from the tension tests was taken to be 23.3 MPa with a standard deviation 3.5 MPa. The yield strength of bulk, annealed copper is about 33 MPa. The lower value measured here suggests that grain size effects may be present due to the relatively large grains following annealing of the thin copper foil. As predicted by the classical Hall-Petch effect (Eq. 7.1), the yield strength was not only very low but also depends on the grain size.

Epoxy specimens with gage lengths of approximately 2 cm (Fig. 7.21a) were loaded in uniaxial tension at nominal strain rates of 2 /s and 12 /s. The properties obtained are summarized in Table 7.2. The initial responses (Fig. 7.21b) were the same, suggesting that the epoxy was in its glassy state with a Young's modulus of  $3.06 \pm 0.14$  GPa. The Poisson's ratio was not determined but a value of 0.35 was used in the analysis based on the reference [108]. There was a clear strain rate dependence to the response of the epoxy in the nonlinear regime. The responses departed from linearity above 30 and 35 MPa for strain rates of 2 and 12 /s, respectively. The corresponding maximum stress levels were 52 and 59 MPa.

These properties, as well as the elastic response of the silicon, were used in a cohesive zone modeling that accounted for the presence of the graphene in the sense that the strength  $\sigma_0$  and range  $\delta_n^c$  of the interactions between graphene and copper foil were modeled by a bilinear traction-separation relation. It should be noted that the graphene was not included as a bulk entity in the analysis as its contribution to axial and bending stiffness is relatively small because it is so thin. This approach allows the initiation and growth of cracks from pre-existing flaws [96] or bimaterial corners [229] to be modeled. Any plastic energy dissipation in the epoxy and copper foil associated with the delamination can be determined from the numerical solution [24, 25] and compared with the intrinsic adhesion energy,  $\Gamma_i$  of the graphene/copper interface, which is the area underneath the traction-separation relation. In the absence of any dissipation due to inelastic behavior,  $\Gamma_i = \Gamma_{ss}$ .

The parameters of the traction-separation relation for a particular interface have to be determined in some way. In principle, the interactions could be obtained from atomistic simulations [37]. In more complicated cases, the traction-separation relation is treated as a phenomenological entity in the same way as stress-strain relations are for

bulk materials and the parameters must be extracted by iterative [24, 25] or direct [101, 102, 108] methods. The former approach was selected for this work by conducting a parametric study, first varying  $\Gamma_i$  and then  $\sigma_0$  [108] until the numerical solutions converge to the measured load-displacement response; note that for any particular combination of these two parameters,  $\delta_n^c = 2\Gamma_i / \sigma_0$ , defining the range of the adhesive interactions.

The choice of parameters for the first load/unload cycle of the experiment at 254  $\mu\text{m/s}$ , where the graphene delaminated from the copper, is listed as TSR 1 in Figure 7.3b and Table 7.4, where the intrinsic adhesion energy was 6.0  $\text{J/m}^2$  and the strength and range of the interaction was 3.0 MPa and 4.0  $\mu\text{m}$ , respectively. The strength and range had to be modified to 0.5 MPa and 24.0  $\mu\text{m}$  (TSR 2) in order to capture the measured response in the second cycle. However no further adjustment was required to capture the third cycle.

The reason for the difference may be due to the fact that the crack initiated from a bimaterial corner in the first experiment and sharp interface cracks in the second and third experiments. In principle, the cohesive zone modeling approach should be able to handle both cases with one consistent set of parameters [229]. Nonetheless, it does appear that the parameters associated with TSR 2 should result in accurate modeling of delamination initiation and growth from sharp delaminations. No matter which set of parameters was employed, the strengths of the interactions were much lower than the yield strength of either the copper foil or the epoxy so that the amount of plastic dissipation obtained from the finite element solution was expected to be low.

The decomposition of the total adhesion energy into its intrinsic and plastic dissipation components is shown in Figure 7.22. At lower load levels, plastic deformation initiated at the bi-material corners. This mechanism of plastic dissipation remained

dominant and reached a maximum when delamination initiated and the plastic dissipation associated with the growth of a relatively sharp crack decreased. At this stage, the interface-delamination was the dominant dissipation mechanism and plastic deformation only accounted for about 7 % of the total fracture energy. It should be noted the latter component was entirely due to plastic deformation in the copper; there was never any dissipation in the epoxy layer due to its higher yield strength. Thus the value of  $6.0 \text{ J/m}^2$  stands as the intrinsic adhesion energy of the interface between graphene and its seed copper foil under the conditions that were employed here.

The same steps were taken to determine the adhesion energy, strength and range of the interactions between graphene and epoxy from the load-displacement response (Fig. 7.13b) measured at an applied displacement rate of  $25.4 \text{ } \mu\text{m/s}$ . Below  $0.2 \text{ N}$ , the measured response was linear, indicating that the delamination length in Equation (2.16) remained the same in this range and measurable delamination had yet to be detected. The gradual transition to steady state growth was captured by a traction-separation relation of the graphene/epoxy interface that was represented by an intrinsic adhesion energy of  $3.4 \text{ J/m}^2$ , which was bounded by adhesion energy levels of  $3.0$  and  $3.6 \text{ J/m}^2$  from the beam theory analysis. Two choices of the strength  $\sigma_0$  are plotted under the heading TSR in Figure 7.13b and associated parameters are listed in Table 7.4. The best fit to the measured response was provided by a strength of  $0.5 \text{ MPa}$  and an interaction range of  $13.6 \text{ } \mu\text{m}$ . The partitioning of energy dissipation for this case is shown in Figure 7.23. As indicated earlier, the steady state intrinsic adhesion energy was  $3.4 \pm 0.01 \text{ J/m}^2$  and, combined with a plastic dissipation in the copper of  $0.25 \text{ J/m}^2$ , gave rise to a total adhesion energy of  $3.66 \text{ J/m}^2$ . Thus energy dissipated in plastic deformation was less than about 6.6% of the total adhesion energy.



Delamination resistance curves were also obtained from the finite element solutions and compared with the measured ones. The crack extension data required for the latter were obtained from the measured compliance (Eq. 2.16) coupled with the fact that beam theory accounted so well for the initial specimen compliance. The J-integral was obtained from Equation 2.17 using the crack length obtained from Equation 2.16. The resistance curves from the finite element solution were obtained directly by tracking the evolution of the J-integral with crack extension.

The delamination resistance curves for the experiment at 254  $\mu\text{m/s}$ , where the graphene delaminated from the copper are shown in Figure 7.24. The J-integral increased sharply to about 2  $\text{J/m}^2$  without any resolvable crack growth. Subsequent growth came with a slightly less steep increase in the J-integral to approximately 5  $\text{J/m}^2$ . The rate of increase of the J-integral then slowed until unstable growth occurred, which was associated with the maximum value ( $6.299 \pm 0.06 \text{ J/m}^2$ ) of the J-integral. The resistance curves associated with the other two load-unload cycles both had similar characteristics. The finite element solutions compared reasonably well with the data in the initial rising portion. The linear softening of the traction-separation relations was unable capture the gradual transition to the peak resistance for the reasons explored in Chapter 4. The solution maintained the steady state resistance to delamination thereafter as the model did not capture any stick-slip or unstable growth.

The delamination resistance curves for the experiment at 25.4  $\mu\text{m/s}$ , where the graphene delaminated from the epoxy are shown in Figure 7.25. The solution and measured response were in good agreement up to the first peak in the data. Again, the resistance to delamination from the solution achieved steady state at  $3.66 \pm 0.01 \text{ J/m}^2$  as model did not have any mechanisms built in to account for the stick-slip behavior that was seen in the experiment.

### 7.3 DISCUSSION

All the steady state adhesion energy levels obtained were much higher than the value  $720\pm 70$  mJ/m<sup>2</sup> measured by Yoon *et al.* [61] for the graphene/copper film interface. They are also higher than value 1.8 J/m<sup>2</sup> for an epoxy/silicon interface measured at very low separation rates [106], but lower than the fracture toughness of graphene itself at 15.9 J/m<sup>2</sup> [225].

In the separate control experiments on silicon/epoxy/silicon sandwich specimens, the adhesion energy of the epoxy/silicon interface was  $7.5\pm 0.2$  and  $11.1\pm 0.1$  J/m<sup>2</sup> at loading rates of 84.6 and 254.0  $\mu\text{m/s}$ , respectively. These values are higher than the bound of 5-7 J/m<sup>2</sup> at 254.0  $\mu\text{m/s}$  for the adhesion energy of the graphene/copper interface, thereby explaining why delamination at the silicon/epoxy interface never occurred. The result also suggests that, at 254.0  $\mu\text{m/s}$ , the graphene/epoxy interface had a higher adhesion energy. Of course this could not be measured here due to preferential delamination at the graphene/copper interface.

The rate dependence of the adhesion energy of contact pairs has already been exploited for selective separation in transfer printing [230-233]. Given that the experiments in the present study were conducted at room temperature, well below the glass transition (100 °C) of this epoxy and the local strain rates near the delamination front are higher than the far field value, thereby shifting the epoxy even further into the glassy domain, it is unlikely that bulk viscoelastic effects were at play near the delamination front. It is also unlikely that the interactions between graphene and copper foil are rate dependent, at least in the quasi static regime being considered here. Accordingly, the noted switch in delamination from the graphene/copper interface to the graphene/epoxy interface may be attributed to rate dependence of the latter. This could be

due to the manner in which the epoxy cures near graphene, leaving a thin region often known as the interphase [234], whose properties differ from those of the bulk epoxy.

Prior to curing, the viscosity of the epoxy is low, so that it follows the morphology of the graphene grown on the copper foil. This leads to the possibility that surface roughness, in conjunction with an interphase layer, could contribute to the rate dependence of the interaction between graphene and epoxy.

Roughness effects may also help reconcile the difference in the  $720 \pm 70 \text{ mJ/m}^2$  adhesion energy of the graphene/copper film interface measured by Yoon *et al.* [61] and the  $6.0 \text{ J/m}^2$  measured here for the graphene/copper foil interface. The grains of the copper films were about  $10 \text{ }\mu\text{m}$  in lateral dimension, much smaller than those of the copper foil, and the overall root-mean-squared (RMS) roughness was on the order of  $20 \text{ nm}$  [235]. Due to the fact that the copper film was deposited on silicon, this was the only roughness scale. Copper foil has at least three roughness scales.

The morphology of graphene on copper foil following CVD is shown in Figure 7.26. The most obvious feature of the surface topography prior to deposition is the series of aligned scratches (Fig. 7.26a) induced by rolling (Fig. 7.26). Prior to deposition, the outer surface of the copper foil may be capped with a layer of copper oxide or coated with chromium oxide for protection from corrosion. However, these layers must be etched away with acetic acid before graphene can be grown on the copper foil. CVD takes place at  $\sim 1000^\circ\text{C}$ , followed by annealing to room temperature, a process which recrystallizes the copper foil. The rolling marks remain (Fig. 7.26b), albeit with a longer wavelength, but copper grains on the order of millimeters are also clearly visible. At higher magnification, it can be seen that each grain contains a series of steps whose alignment appears to be associated with the particular grain (Fig. 7.26c). Wrinkles in the graphene can also be detected along with occasional patches of copper oxide (Fig. 7.26d).

The latter must be revealing locations where there were holes or tears in the graphene as defect-free graphene is impervious to oxygen. An AFM tapping mode scan of a  $25 \times 25$   $\mu\text{m}$  region (Fig. 7.28) also reveals rolling marks (long wavelength undulations) and steps (short wavelength) and some copper oxide. The RMS roughness associated with the steps was  $11.4 \pm 1.3$  nm. The rolling marks had a peak to peak amplitude of about  $0.4$   $\mu\text{m}$ .

The roughness of the graphene on copper foil after deposition (Fig. 7.28a), bare copper foil (Fig. 7.28b) and graphene on epoxy (Fig. 7.28c) after separation along the graphene/copper interface and bare epoxy (Fig. 7.28d) after separation along the graphene/epoxy interface were measured by atomic force microscopy (AFM). These images all display step-like features, which appear to have very similar wavelengths ( $0.7$   $\mu\text{m}$ ) and peak to valley heights of about  $25$  nm (Fig. 7.28e). These features might be viewed as atomic steps in the copper foil, but the peak to peak variations in surface morphology would be much smaller than the  $25$  nm observed here, leading to the conclusion that the step-like features were formed at the high temperatures encountered in the CVD process and subsequent annealing. The RMS roughness of each surface noted in the figure caption were all quite similar at about  $10$  nm, confirming that both the graphene and epoxy and the fracture path conformed to the surface of the copper foil, even at this smallest roughness scale. The RMS roughness associated with the steps and other features such as the scratches (Fig. 7.26) produced during rolling of the foil and undulations associated with rumples in the foil associated with folding and unfolding it around the quartz cylinder (Fig. 2.12) were obtained over larger spatial domains on the epoxy fracture surface using a Veeco optical Profilometer.

Four images taken over  $1 \times 1.3$  mm regions of graphene on epoxy are shown in Figure 7.29 along with the associated overall RMS roughness noted in the top right hand corner of each image. The RMS roughness on this scale was much larger, ranging from

0.4 to 1.4  $\mu\text{m}$  and was made up of scratches and undulations. The flattest of the portions of the surface shown was the one in Figure 7.29a. The others had undulations along (Fig. 7.29b-c) and across (Fig. 7.29d) the scratches. The RMS roughness associated with scans in the rolling and transverse directions of each of the images are noted in Table 7.5. The RMS roughness values from the scans in Fig. 7.29a were quite similar at 0.444 and 0.391  $\mu\text{m}$ . This was the flattest portion of the surface, so these values appear to be associated with the roughness of the scratches. There was more variability between scans taken in the rolling and transverse directions in the other three images, which suggest that undulations were also present in each of the scans.

More details of graphene on epoxy are shown in Figure 7.30 taken by 100 $\times$  objective lens over a 48 $\times$ 63  $\mu\text{m}$  region. Replicated steps as well as rolling marks were quite apparent. The RMS roughness of the scratches was about 140 nm over a 48 $\times$ 63  $\mu\text{m}$  region while the RMS roughness of the undulations was about 775.9 $\pm$ 186 nm over 1 $\times$ 1.3 mm.

The graphene and epoxy were able to conform to all these varied angular features, meaning that delamination along the graphene/copper foil interface had to follow more complex paths compared to the simpler path for the copper film that was considered in Yoon *et al.* [61]. Such a range of angularity introduces local variations in fracture mode-mix and greater chances of interlocking of delamination surfaces, which could conceivably result in higher adhesion energies.

#### 7.4 CONCLUSIONS

It has been demonstrated that it is possible to mechanically separate CVD grown graphene from its copper foil seed layer by bonding the graphene-coated copper foil to silicon strips with an epoxy and then separating the silicon strips in a double cantilever

beam configuration at a high enough applied separation rate. For the conditions employed in this study, this had to be equal to or greater than 254.0  $\mu\text{m/s}$ . When the applied displacement rate was an order of magnitude lower, the graphene/epoxy interface delaminated. At intermediate rates, there was a mixture of the two modes. The delamination paths in all the experiments were diagnosed *via* a combination of Raman spectroscopy, scanning electron microscopy and atomic force microscopy.

This result has very important implications for nano manufacturing processes such as roll-to-roll transfer, where loading rates can be controlled so as to produce delamination at the desired interface. Although the silicon strips and epoxy that were used in this study to effect this selective delamination are not compatible with roll-to-roll devices, other materials that are compatible can be selected using the same fracture mechanics principles that were used to analyze the experiments here.

A fracture mechanics analysis of the load-displacement responses at the two extreme applied displacement rates was used to determine the adhesion energy as well as the strength and range of the interactions between graphene and copper and between graphene and epoxy. At 254.0  $\mu\text{m/s}$ , the intrinsic adhesion energy of the graphene/copper interface was 6  $\text{J/m}^2$  with a maximum strength and interaction range of 0.5 MPa and 24  $\mu\text{m}$ , respectively. The corresponding values of intrinsic adhesion energy, maximum strength and interaction range at 25.4  $\mu\text{m/s}$  were 3.4  $\text{J/m}^2$ , 0.5 MPa and 13.6  $\mu\text{m}$ , respectively, for the graphene/epoxy interface. These values of adhesion energy were surprisingly high and could have been due to significant contributions from plastic energy dissipation in the copper foil and epoxy layers. However, a detailed finite element analysis found very little dissipation in either layer due to the fact that their yield strengths were much higher than the maximum strength of the interfaces. Nonetheless, the underlying mechanisms for such high adhesion energy require further study.

The source of the rate dependence remains to be understood and doing so will allow much more definitive analyses of delamination scenarios for roll-to-roll manufacture. Nonetheless, it can be most likely narrowed down to a rate dependence of the graphene/epoxy interface, with an interphase layer of epoxy whose properties are different from those of the bulk epoxy due to the constraint applied by the graphene on the movement of the molecular chains of the epoxy near the graphene as the epoxy was cured. Another factor to be considered may be the multiple roughness scales of the copper foil.

## Chapter 8 Conclusions and Future Work

In the current work, fracture mechanics concepts and experiments were used to explore the molecular interactions between COOH and NMe<sub>2</sub>-terminated SAMs, hydroxylated Si(111) surfaces, graphene and seed copper, graphene and epoxy as well as graphene that had been transferred to Si(111) surfaces. The traction-separation relations associated with each of the interactions were determined in addition to the more commonly determined adhesion energies. They were extracted by so-called direct and indirect methods as well as a hybrid of the two, depending on the experiments that were conducted. The latter two approaches required finite element analyses that accounted for the behavior of each of the constituents as well as the interactions between them. In addition, the surface free energies of as-grown or transferred graphene, and silicon were investigated with static contact angle measurements using the two or three liquid methods. The results can be summarized as follows:

- (a) The interactions between SAMs with COOH and NMe<sub>2</sub> functional groups were examined in ambient and high vacuum environments under fracture mode-mixes of 0 and 50°. The adhesion energy was relatively insensitive to the environment under either mode-mix, but increased by a factor of ten at the higher mode-mix, possibly due to differences in chain/chain interactions under shear. On the other hand, the traction-separation relations for each of the four conditions were notably different. Vacuum raised the maximum strength of the interactions, ostensibly due to a reduction in the amount of water present and closer interactions. However, high vacuum also showed signs of inducing chemical reactions based on XPS analyses of fracture surfaces.



Future work in this area should address the formation of C-N-O bonding under high vacuum. Such additional complexity may be resolved by Attenuated Total Reflectance Fourier Transform Infrared (ATR-FTIR) Spectroscopy [168, 169] which can be used to determine the nature of interactions between functionalized silicon surfaces and detect any evidence of trapped water in the bonded state *in situ*. The results of such investigations could then be compared with XPS and other studies of the fracture surfaces in order to obtain a more complete picture of bond formation and breakage. It would also be informative to conduct MD analyses of deformation mechanisms in shear to see if the tenfold increase in adhesion energy could be accounted for.

(b) In examining the interactions between hydroxylated silicon surfaces, it became clear that they were affected by slight differences in the curvature of the mating surfaces. While the RMS roughness of all the surfaces considered was less than 0.5 nm, height variations over the 45 mm length of the silicon strips ranged from 0.5 to 1.5  $\mu\text{m}$ . These lowered the adhesion energy of the interactions in specimens with less conformal mating surfaces. This effect manifested clearly in the traction-separation relations of the interactions, where it appeared that one master traction-separation relation was able to represent all of the measured ones which had varying degrees of damage depending on the degree of waviness mismatch between the surfaces.

The master traction-separation relation had a maximum strength of 12 MPa and an interaction range of 350 nm. These are unlikely to be associated with van der Waals, or hydrogen bonding. Future work should focus on identifying other mechanisms such as DLVO forces and capillary bridging, possibly modulated by surface waviness. Another issue to be resolved is the fact the measured near-tip

NCOD were larger than those predicted on the basis of the master traction-separation relation. This difference may be due to repulsive hydration forces or highly localized residual stress states due to chemisorption.

(c) The adhesion energies of the interactions between large area, CVD grown graphene and silicon were similar to those that had been found for exfoliated graphene flakes. They were also commensurate with expectations from van der Waals forces. However, the strength and range of the interactions, which were extracted in a hybrid approach that extended the reach of direct measurements, were respectively smaller and longer than the values are attributed to van der Waals forces. In fact, it appears that neither van der Waals nor capillary interactions, by themselves, were at play here. The roughness of the graphene on silicon ranged from 0.4 to 5 nm due to defects such as wrinkles, trapped copper residues, and torn graphene so that the roughness may affect the traction-separation relations. As a result, the long-range interactions that have been observed in this study are most likely reflections of the effect of roughness, which sets the stage for future investigations.

The surface free energies of graphene and silicon were determined by contact angle methods and used to determine the thermodynamic work of adhesion between them. At  $95.5 \text{ mJ/m}^2$ , this was much lower than the adhesion energy between silicon and graphene that was determined in the wedge tests. Zong *et al.* reported  $151 \pm 28 \text{ mJ/m}^2$  for the adhesion energy of graphene that was draped over nano particles on silicon oxide surfaces. This value is closer than any other measurements to the thermodynamic work of adhesion because it essentially reflects an equilibrium condition during approach, rather than separation. Another outcome of the contact angle work was that the surface free energy of graphene

film was not influenced by the substrate below graphene films. This contradicts the conclusions of some earlier studies, which may have been confused by the ease with which graphene attracts airborne contaminants.

The most urgent emphasis for future work in this area should be on identifying the mechanisms that are contributing to the relatively long-range interactions. The most obvious starting point is the fact that the RMS roughness of the graphene on silicon was an order of magnitude higher than that of bare silicon due to wrinkles, ad-layers, etc.

(d) As expected, the highest adhesion energies (6 and 3.4 J/m<sup>2</sup>, respectively) were between graphene and its seed copper and graphene and epoxy. Based on control experiments with the silicon/epoxy interface and the fact that it was possible to select between graphene/copper and graphene/epoxy delamination based on loading rate, it appears that the graphene/epoxy interface may also be rate dependent. Because the epoxy is in its glassy state, the rate dependence may indeed be attributed to the interface. The strength of the interactions was on the order of few MPa, surprisingly low for the adhesion energies quoted above. This meant that yielding in the copper layer was minimal. The low strengths were made up for by long interaction ranges. These may be related to the three scales of roughness that were noted for the foil and the fact that graphene and epoxy both conformed to all of them during fabrication as well as in the process of separation. Future efforts in this area might be best directed towards understanding the rate dependence of graphene/polymer interfaces, so that it can be used to predict, in a highly quantitative manner, the possibility of selective mechanical transfer for any combination of materials, geometry and loading. This will in turn require rate dependent traction-separation relations to be measured. Another factor that can be

exploited in selective transfer is fracture mode-mix. Determining traction-separation relations in shear as well as tension will allow optimal peel angles in roll-to-roll transfer to be established, hopefully in conjunction with rate dependence. Another opportunity provided by understanding mode-mix effects is that they may be used to understand the role that surface roughness is playing in the high adhesion energies.

(e) The general feature of all the interactions that were measured in this study is that their strengths were lower and their ranges were longer than those associated with van der Waals or capillary forces acting on smooth surfaces. Although one estimate of electrostatic interactions between graphene and silicon [182] suggests that interaction ranges are about 1 nm, this claim may need to be considered further. Another factor to be considered is the contribution of roughness to all the interactions that were considered.

(f) The manner in which the various interactions were extracted provided a number of insights to extracting traction-separation relations. First, being able to measure NCOD near the crack front allows the normal component of a traction-separation relation to be extracted in a relatively direct manner under mode I fracture conditions. In some cases, IR-COI did not have sufficient resolution in NCOD to extract the traction-separation relations over their full range, in which case, inverse parameter fitting was implemented through cohesive zone modeling to complete the extraction. In cases where NCOD could not be measured, a fully indirect method for extracting traction-separation relations had to be implemented and reliance was placed on fitting parameters for traction-separation relations based on the global load-displacement response and the delamination resistance curves. The load-displacement response provided a reasonable measure of the

adhesion energy and the maximum strength, whereas the shape of the resistance curve sets the evolution of damage or the shape of the softening portion of the traction-separation relation.

## FIGURES

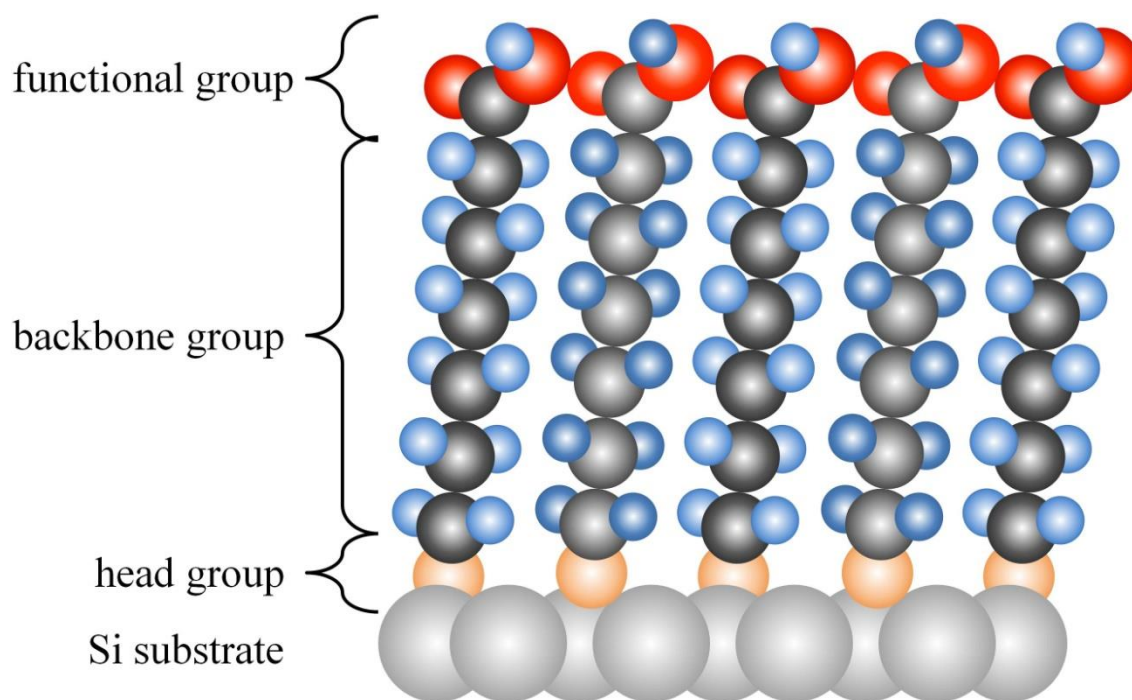


Figure 1.1 A schematic of a SAM on silicon showing the head group, backbone group, and functional group of each molecule. Red spheres represent oxygen atoms, blue hydrogen, black carbon, gray silicon, and orange covalent bonding between carbon and silicon.

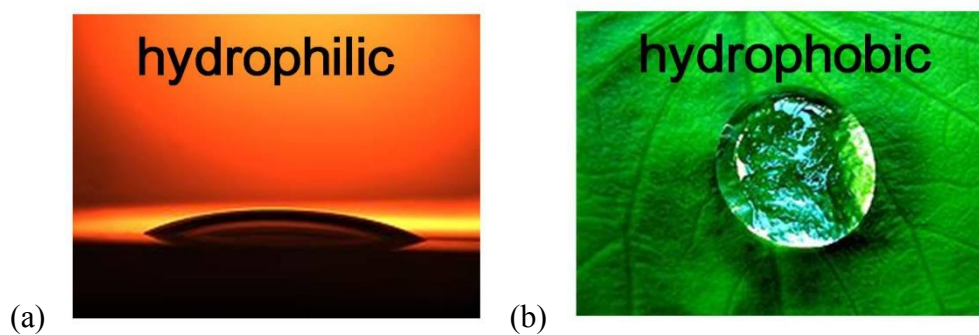


Figure 1.2 Water drops on (a) hydrophilic and (b) hydrophobic surfaces (ref. Wikipedia).

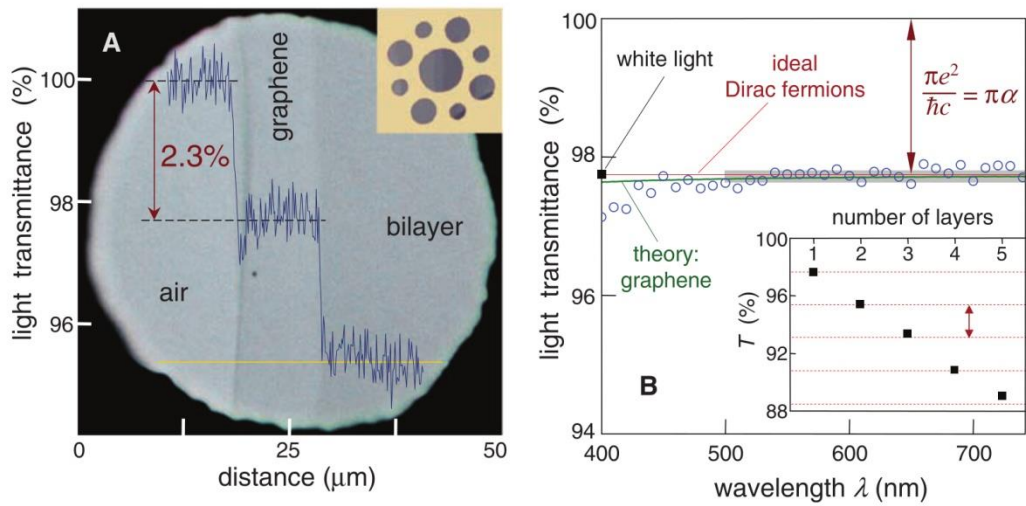


Figure 1.3 Transparency of both monolayer and bilayer graphene by Nair *et al.* [68]: (a) Optical observation of a 50 μm aperture covered by monolayer and bilayer graphene. (b) Transmittance spectrum of monolayer graphene in hollow symbols.

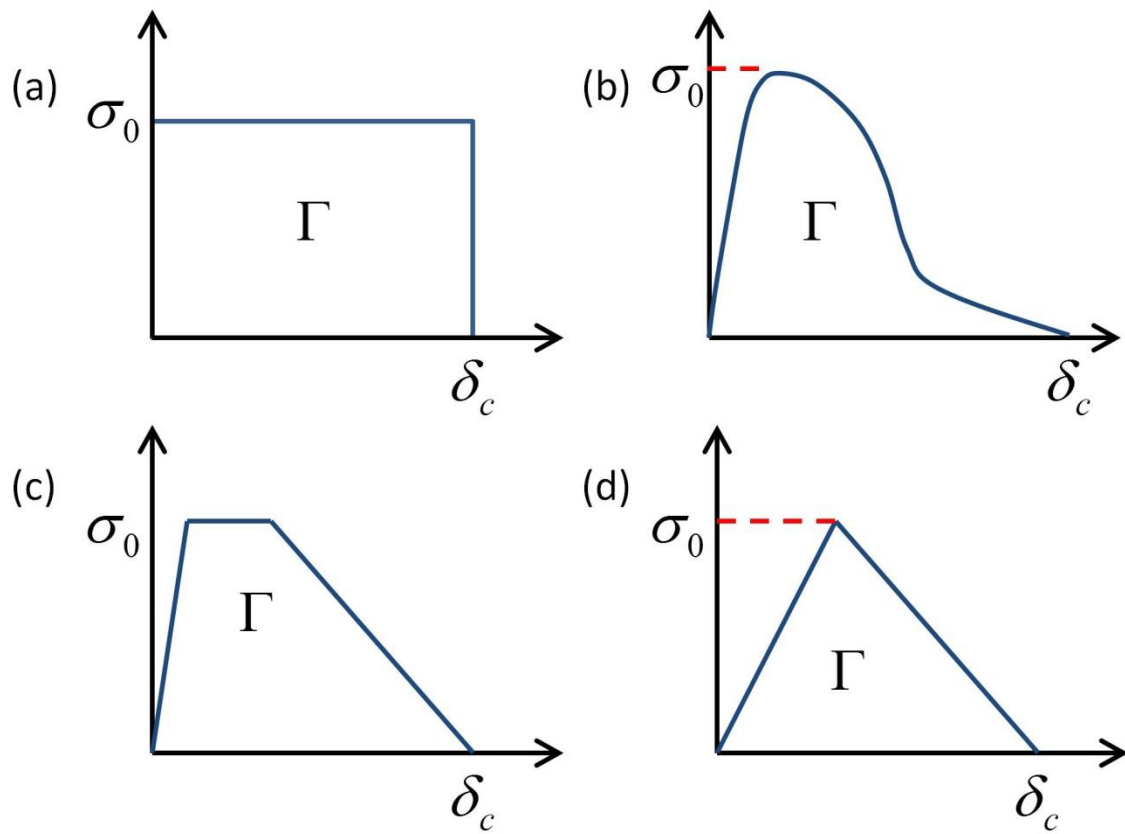


Figure 1.4 Various forms of the traction-separation relation: (a) Constant traction model suggested by Dugdale [81]. (b) Nonlinear relation by Needleman [96] (c) Trapezoidal shape suggested by Tvergaard *et al.* [97]. (d) Bilinear form by Geubelle *et al.* [98].



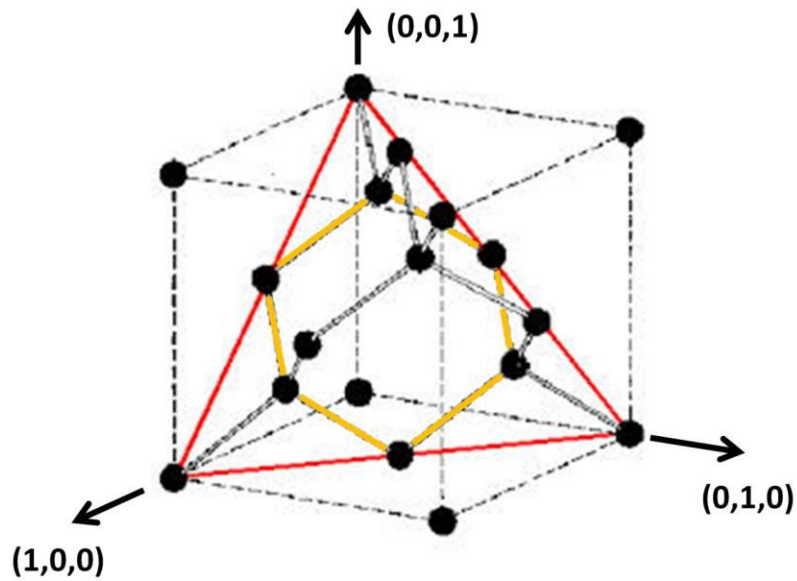


Figure 2.1 The crystal structure of silicon: Red solid lines present the Si(111) plane and yellow lines represent the unit cell associated with the diamond cubic structure on the [111] plane by Lilliestr le *et al.* [236].

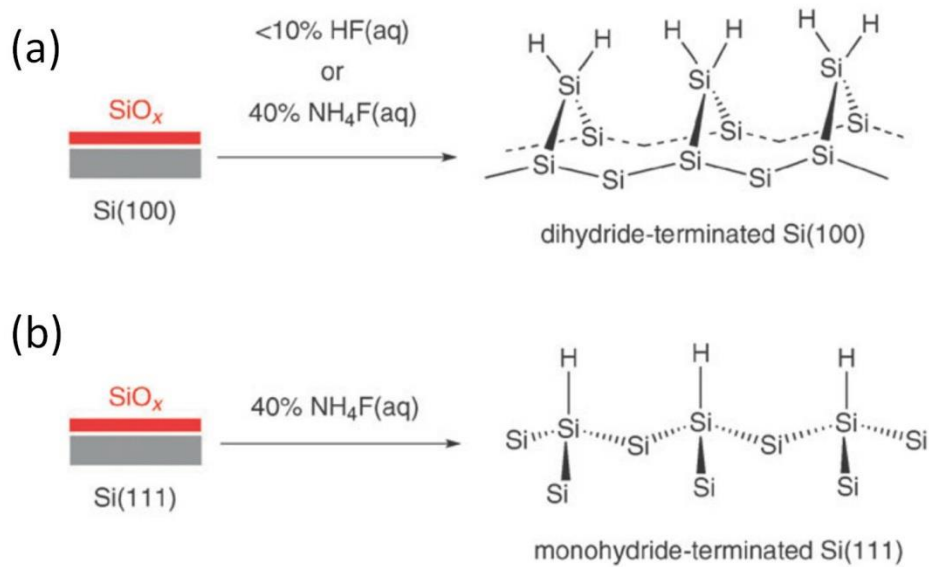


Figure 2.2 Termination of the hydrogen on various silicon surfaces by Ciampi *et al.* [120]: (a) Dihydride-termination on Si(100). (b) monohydride-termination on Si(111).

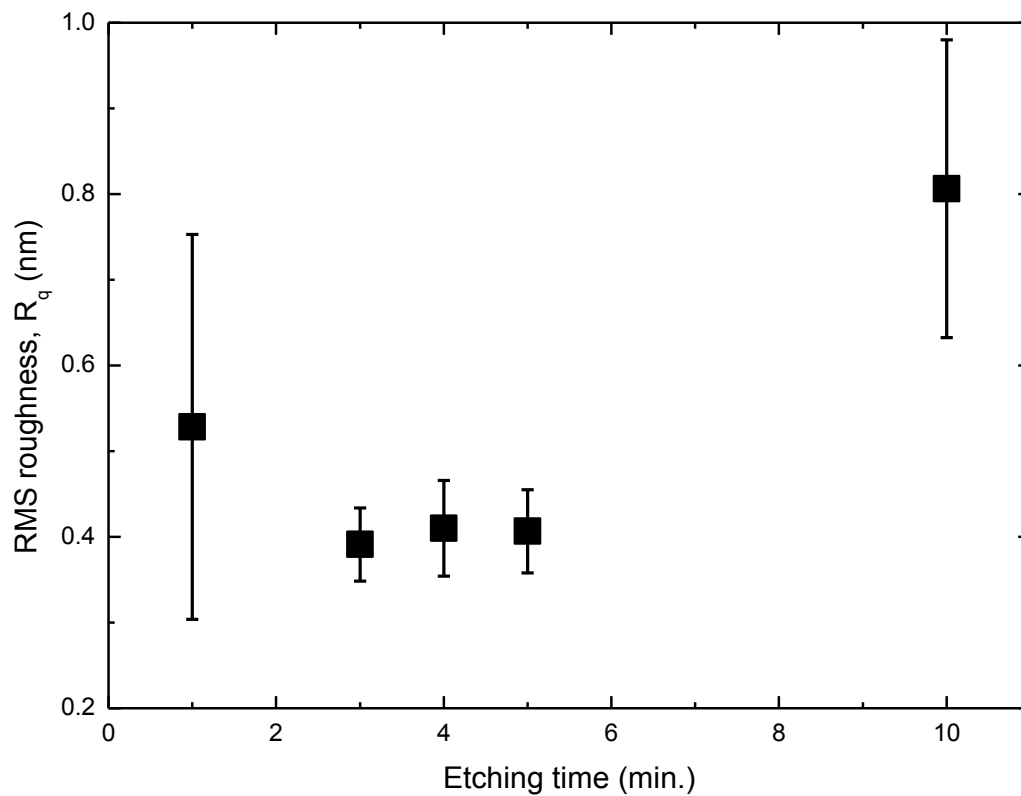


Figure 2.3 RMS roughness vs.  $\text{NH}_4\text{F}$  etching time. The Si(111) surfaces of silicon strips treated for 30 minutes in a piranha solution and then etched in ammonium fluoride solution for various etching times. The RMS roughness was measured by AFM. The optimum treatment was from three to five minutes, which yielded approximately 0.4 nm RMS roughness.

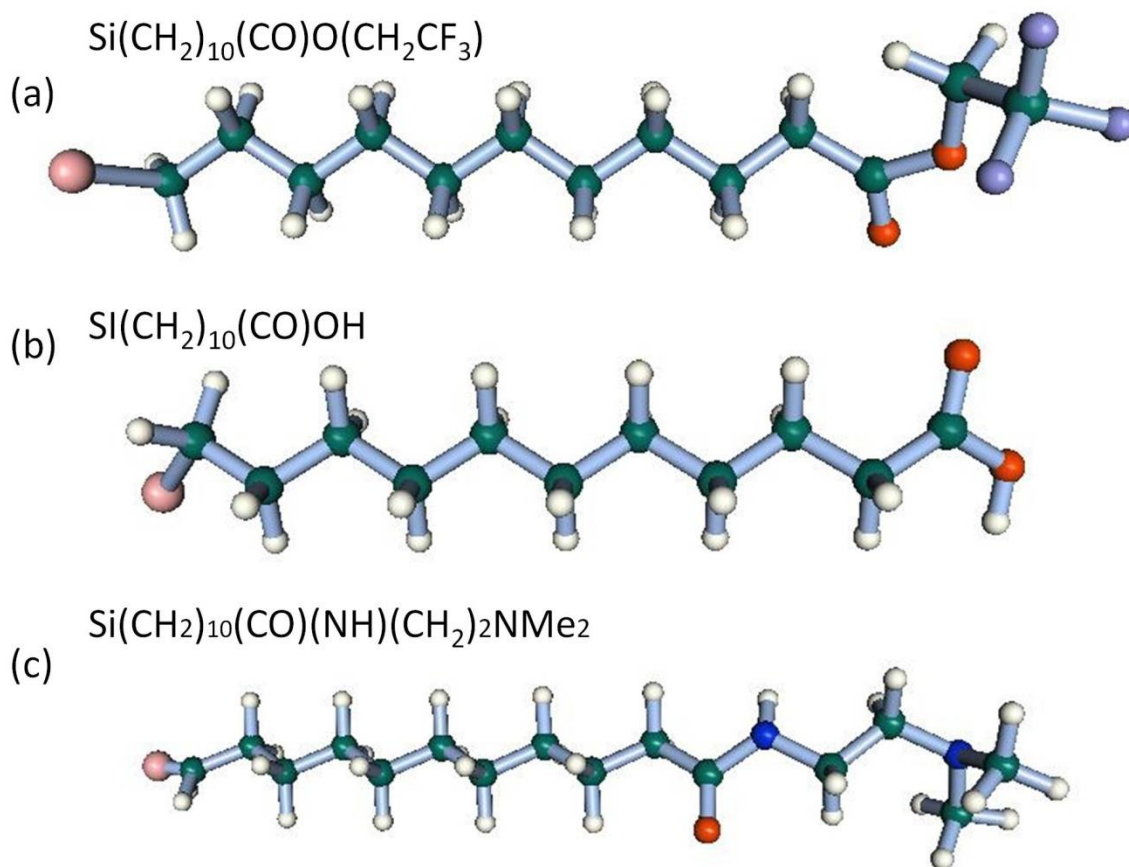


Figure 2.4 Schematics of the three SAMs considered in this work. Pink is for silicon, green for carbon, white for hydrogen, blue for nitrogen, and orange for oxygen from Wakamatsu [114]. (a) 10-undecylenic trifluoroethyl ester SAM (CF<sub>3</sub> SAM), (b) 10-undecylenic acid (COOH SAM), (c) 10-undecylenic N,N'-dimethylamino ethyl amide (NMe<sub>2</sub> SAM).

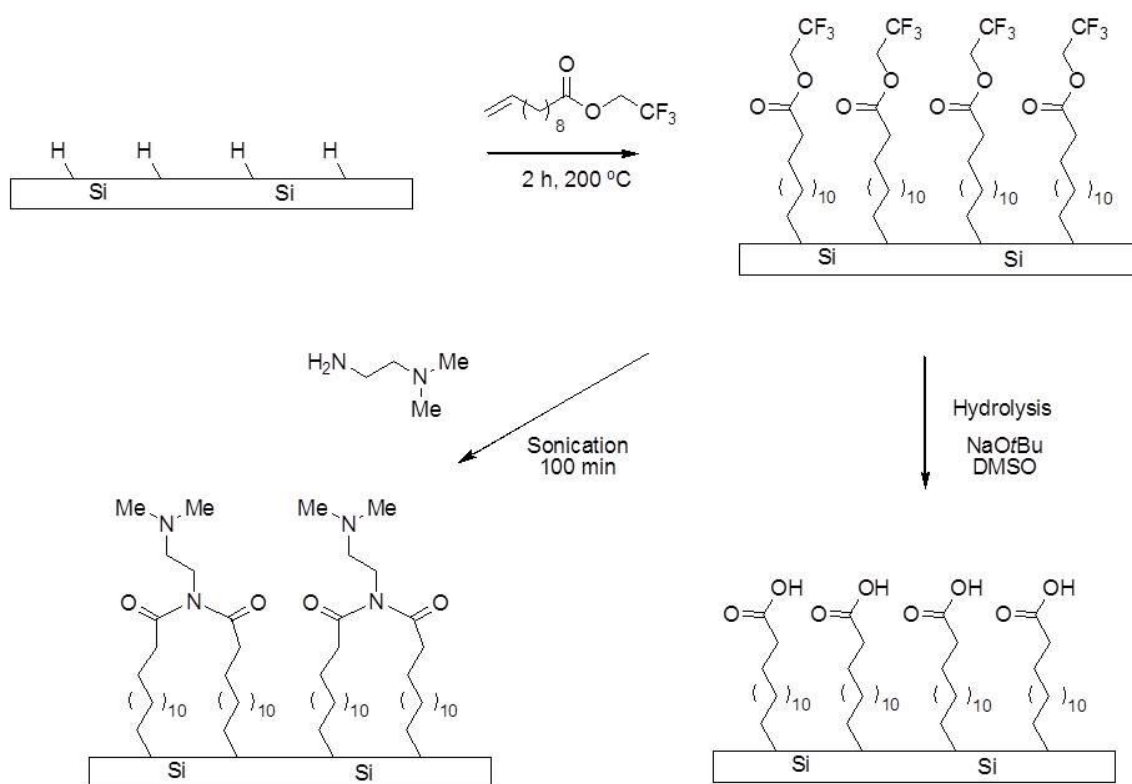


Figure 2.5 The schematic outlines the series of steps that were required to produce the COOH and NMe<sub>2</sub> SAMs on Si(111).

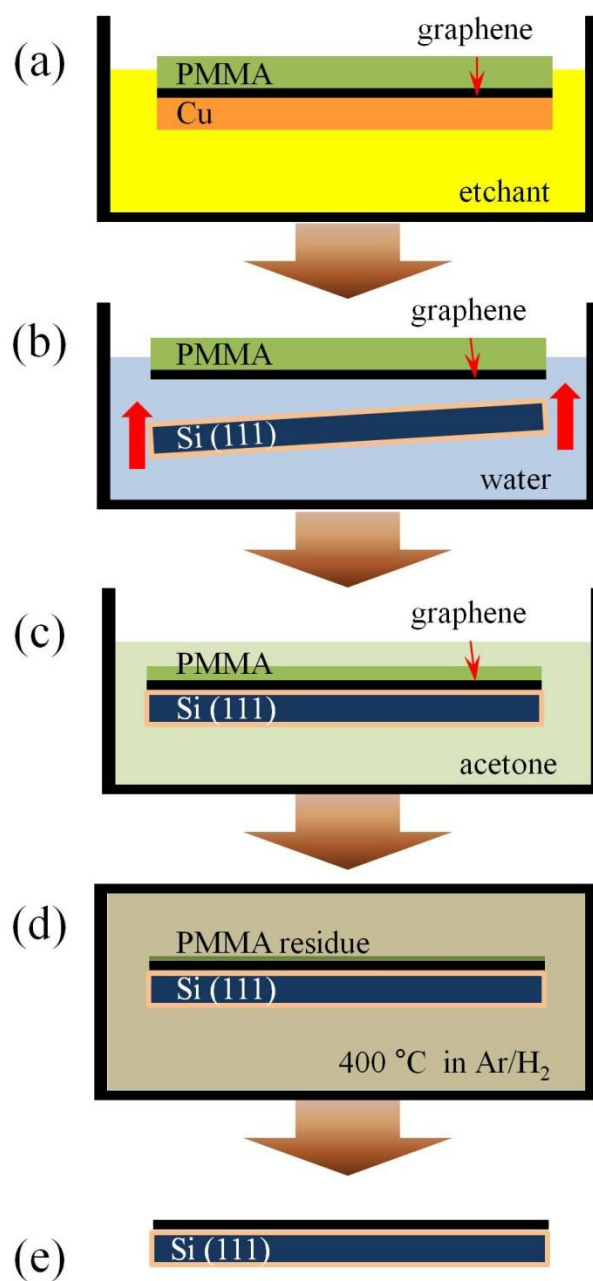


Figure 2.6 Wet transfer of graphene to the Si(111) surfaces of silicon strips: (a) Following the deposition of graphene on copper foil, PMMA is deposited on the graphene and the copper foil is then etched away leaving graphene with a PMMA backing. (b) The graphene/PMMA bilayer is scooped up by a silicon strip. (c) The PMMA layer was removed in an acetone bath. (d) The PMMA residue is evaporated at a high temperature in an inert gas (Ar/H<sub>2</sub>) chamber. (e) Graphene has been completely transferred to the silicon strip.

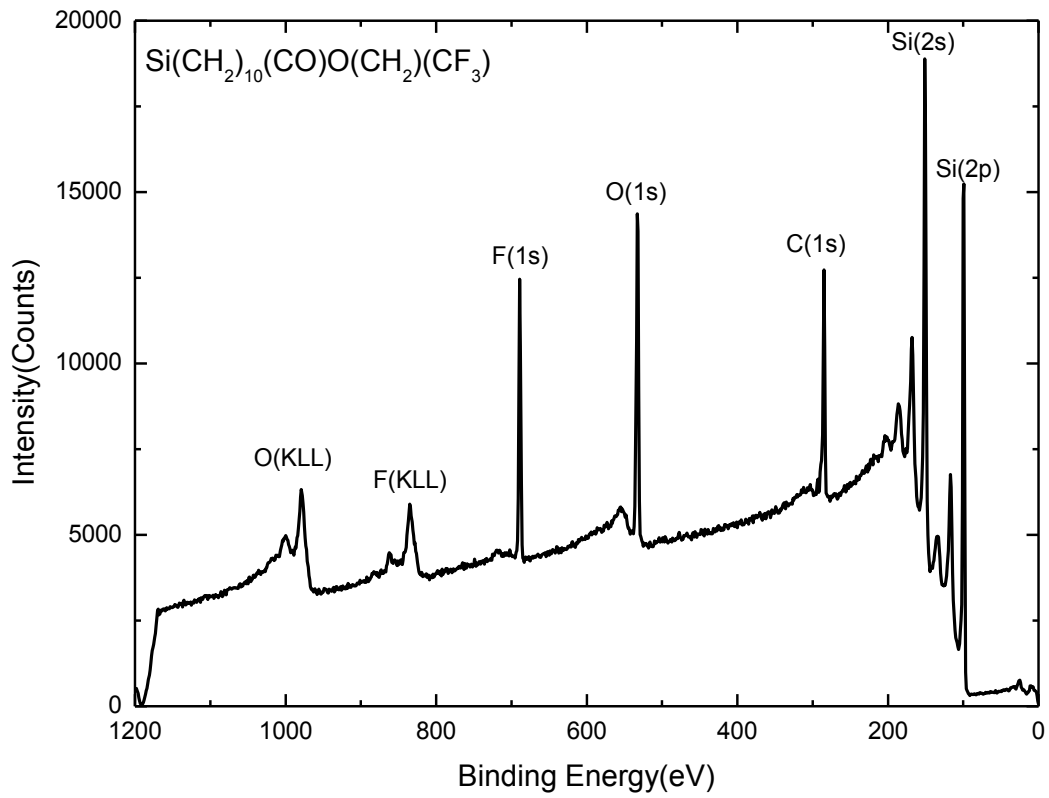


Figure 2.7 Example of an XPS survey scan on a  $\text{CF}_3$  SAM.

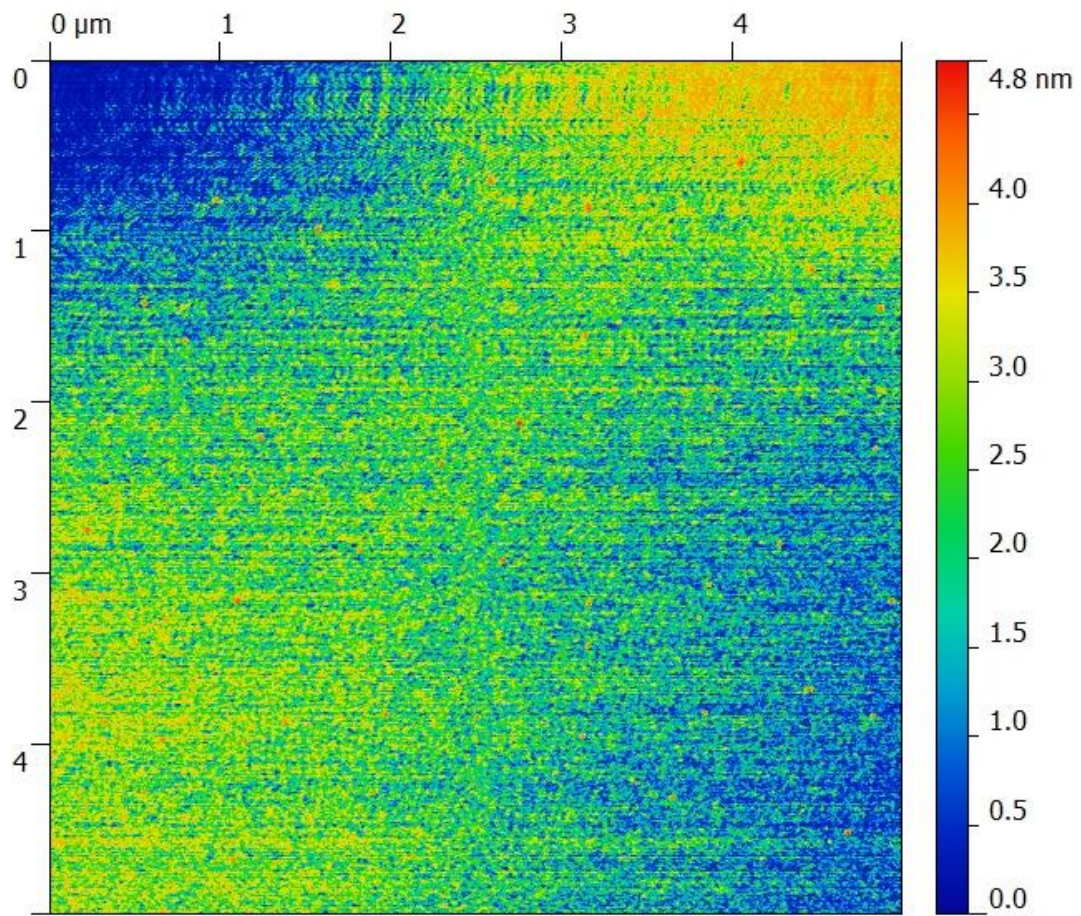


Figure 2.8 An AFM tapping mode scan on a silicon wafer. The overall RMS roughness was 0.264 nm.

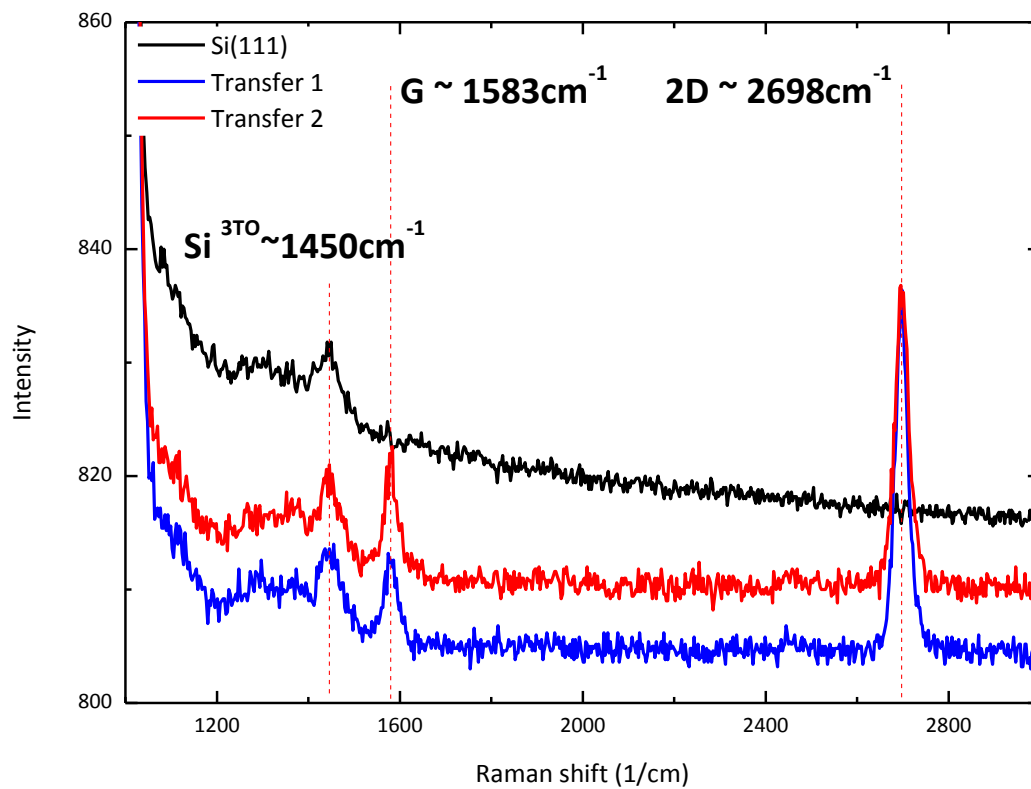


Figure 2.9 The Raman spectrum associated with CVD-grown graphene that was transferred to a silicon strip. The G and 2D peaks are clearly visible at  $1583\text{ cm}^{-1}$  and  $2693\text{ cm}^{-1}$ , respectively.



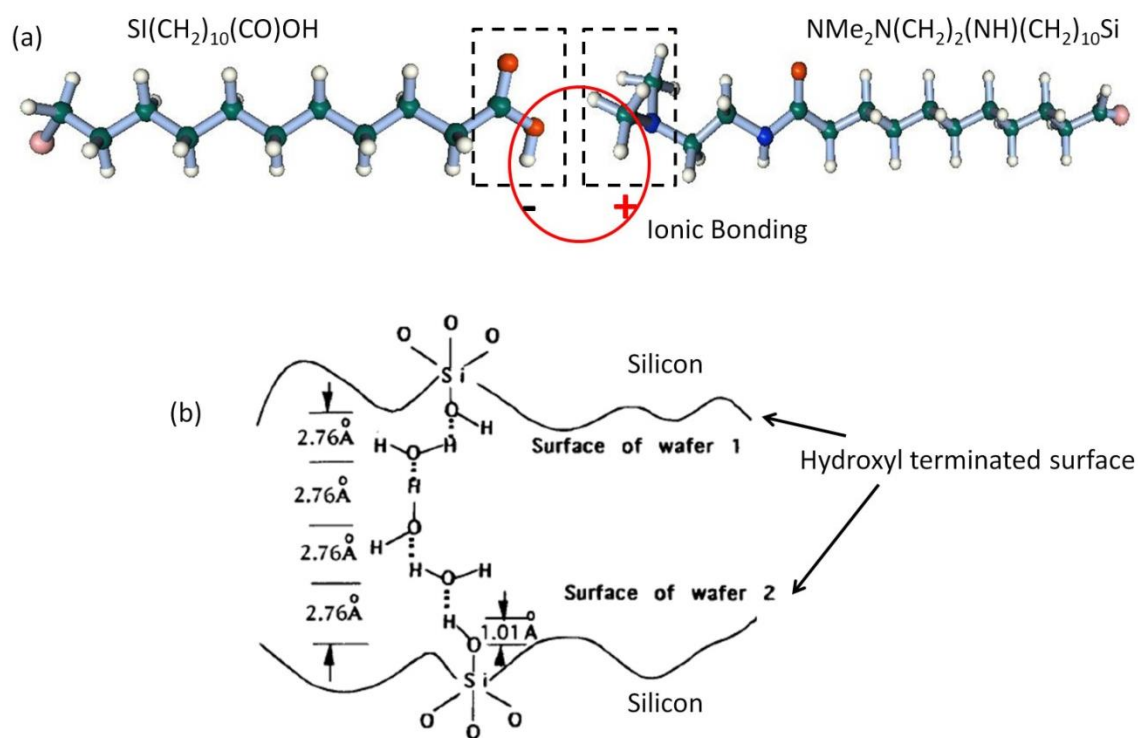


Figure 2.10 (a) A scenario for ionic bonding between COOH and NMe<sub>2</sub> SAMs [114].  
 (b) Hydrophilic bonding between hydroxylated silicon strips *via* hydrogen bonding [145].

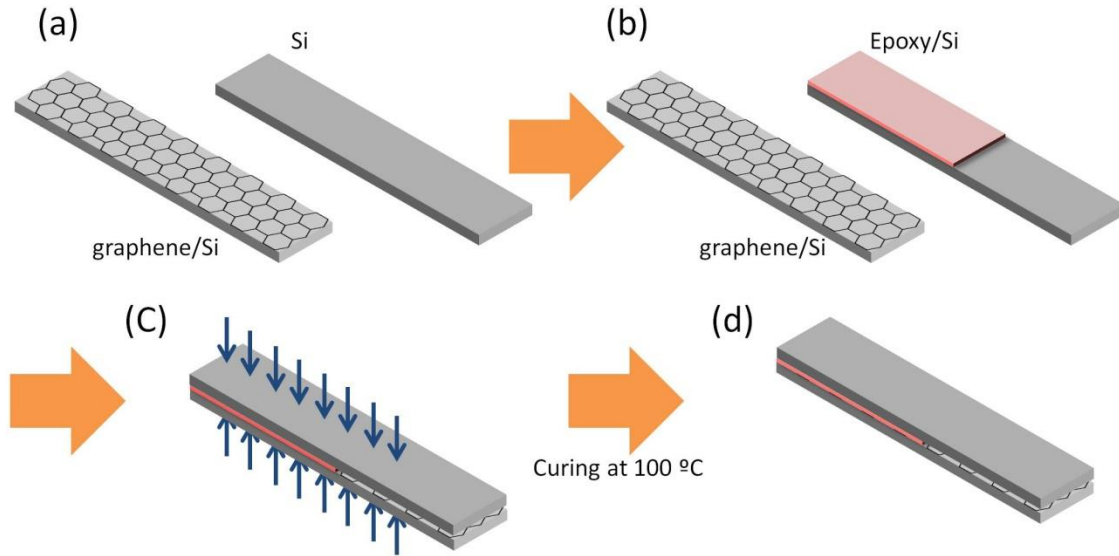


Figure 2.11 The preparation of fracture specimens for separating graphene that had been transferred to silicon: (a) A bare silicon strip and a graphene-coated one. (b) Epoxy was applied to the bare silicon strip. (c) The two strips were bonded together under uniform pressure. (d) The Si/epoxy/graphene/Si laminate was cured at 100 °C.

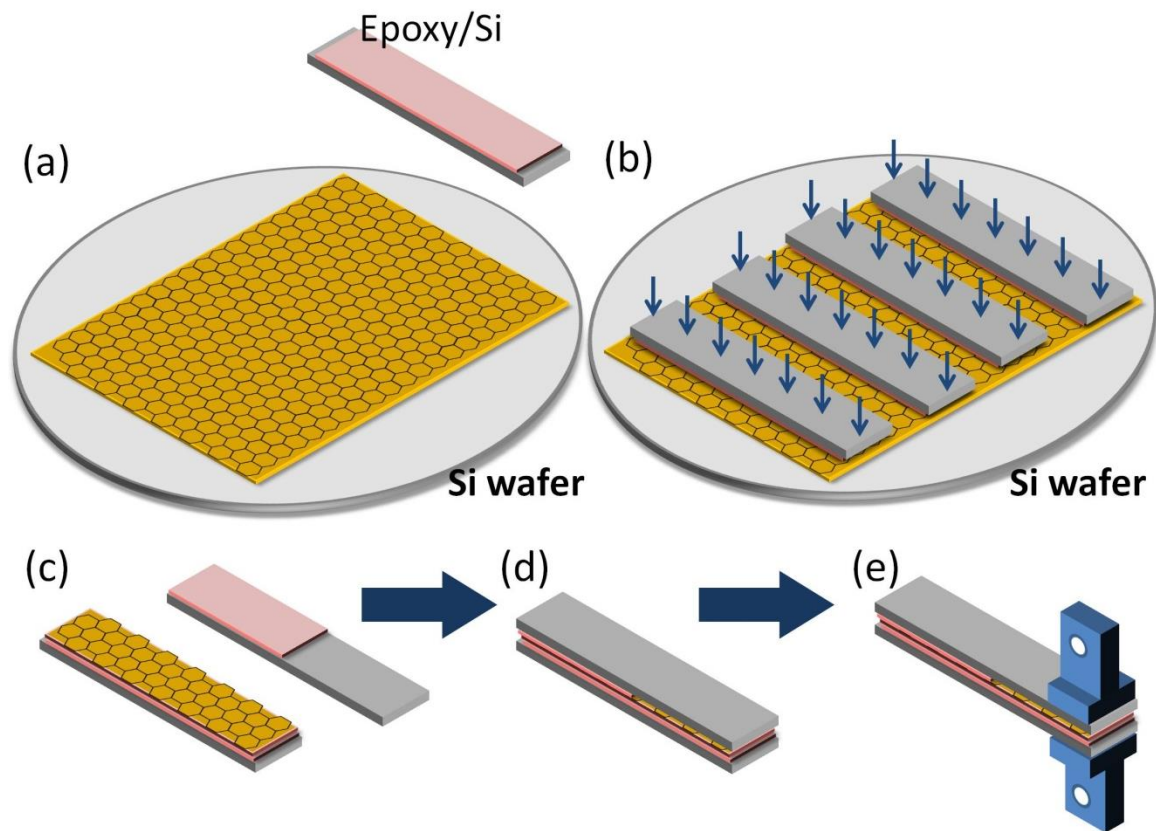


Figure 2.12 Outlines the steps that were taken to fabricate the laminate: (a) Copper foils ( $5 \times 5$  cm) with graphene on both sides were flattened on a silicon wafer. (b) Epoxy was applied over the entire surface of the first set of silicon strips. (c) Four to six epoxy-coated silicon strips were placed on the flattened foil and a uniform pressure was applied for one minute before the assembly was cured at  $100\text{ }^{\circ}\text{C}$  for two hours. (d) The assembly was then cut between the silicon strips and another set of silicon strips partially coated with epoxy were prepared. (e) The two sets of strips were brought together under uniform pressure for one minute and the assembly was cured for two hours at  $100\text{ }^{\circ}\text{C}$  to form a specimen with a blunt initial crack at in the region with no epoxy. (f) Bonding of aluminum loading tabs.

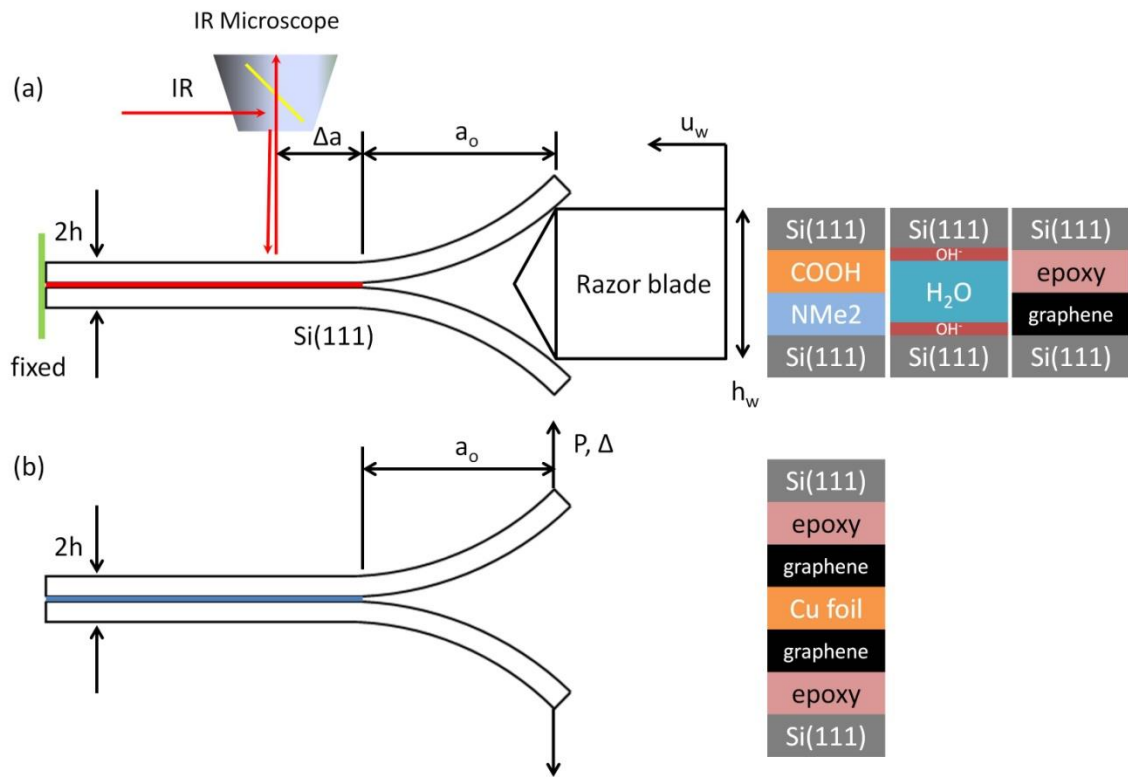


Figure 2.13 Configuration of the Mode I fracture experiments: (a) The wedge test with IR-COI. The red solid line indicates various intermediate layers which are identified to the right side. (b) Double cantilever beam experiment using a hydraulic loading device. The blue solid line represents the layers shown to the right.

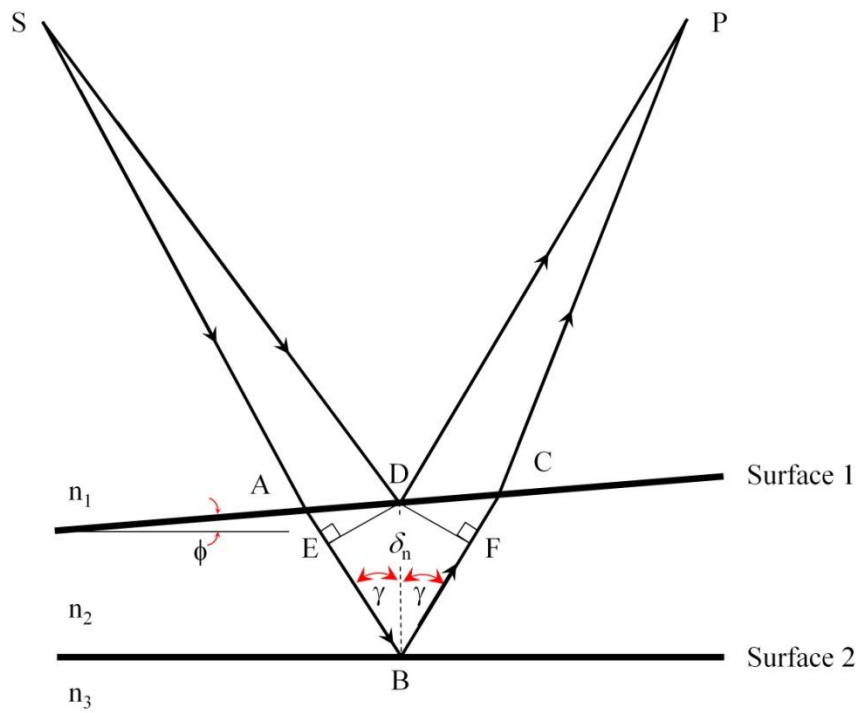


Figure 2.14 Ray diagram for crack opening interferometry. Rays reflected from the top and bottom crack surfaces interfere at P.

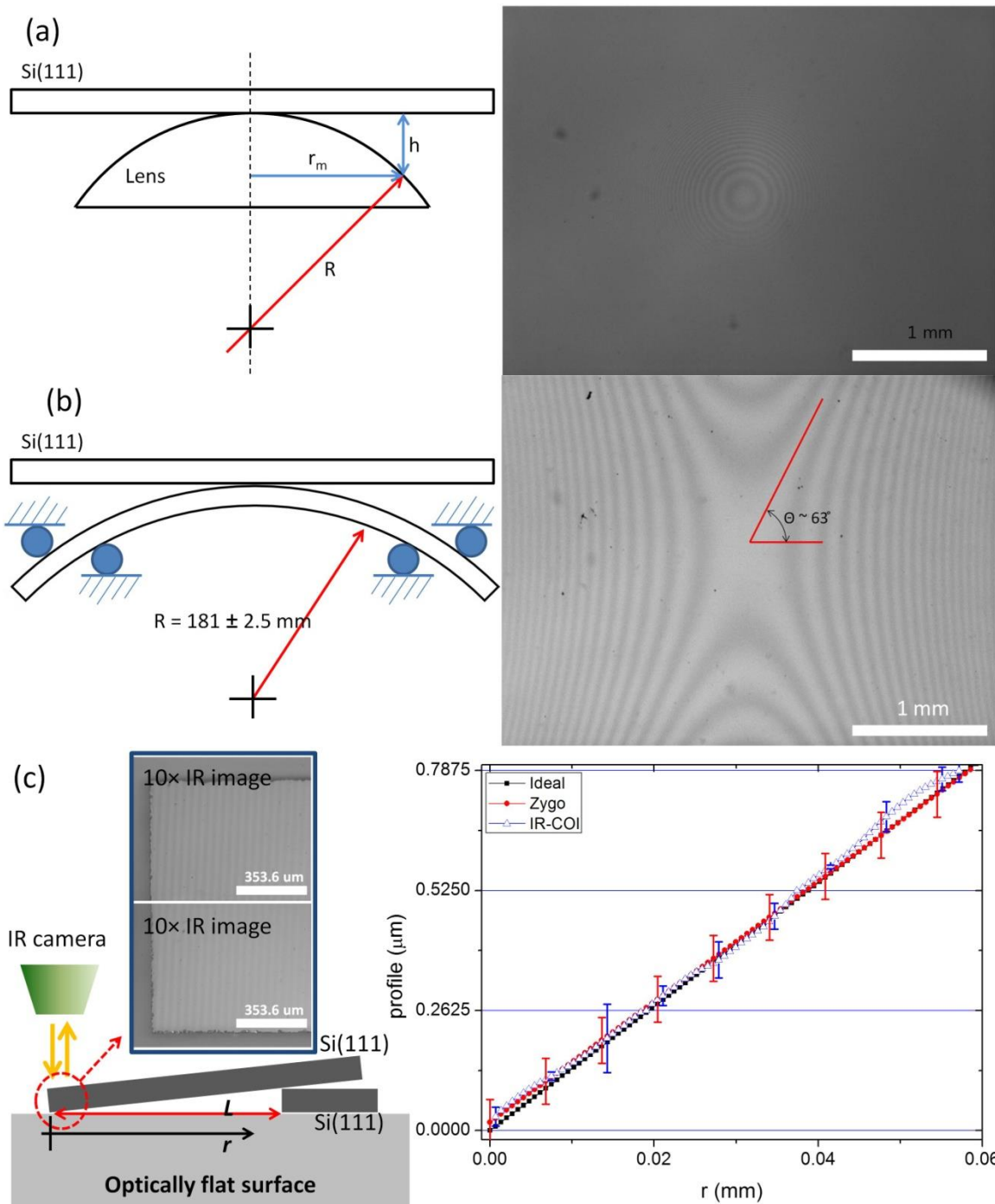


Figure 2.15 Verifying the IR-COI setup with three different configurations: (a) Newton's rings between a glass lens and a silicon strip. (b) Pure bending of a silicon strip and the associated hyperbolic fringe pattern. (c) An air wedge and comparisons of associated separations.

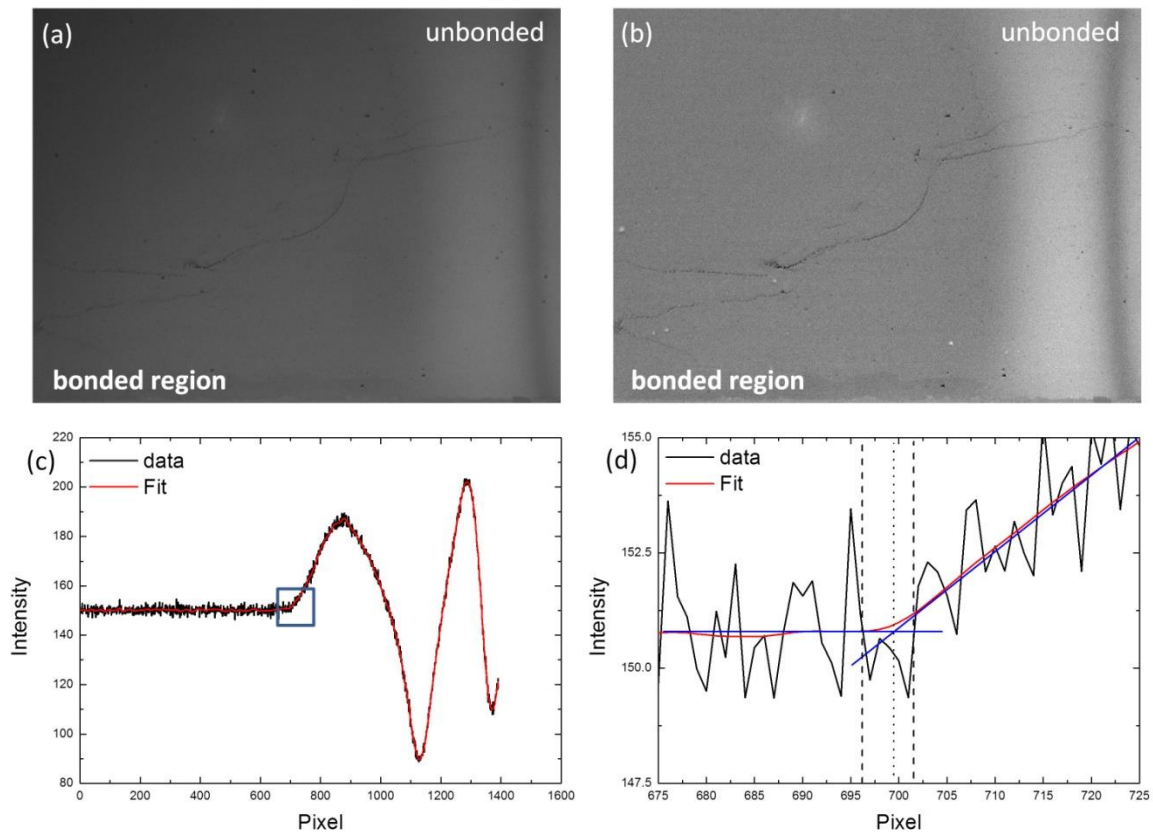


Figure 2.16 An IR image near a crack front and its intensity data: (a) A typical IR image near the crack front. (b) An improved image obtained by subtracting out the background signal. (c) Fit to the intensity profile from the subtracted image over the full field of view. (d) A close up of the intensity profile near the crack front and definition of the crack front as the intersection of the two tangents to the fitted intensity.

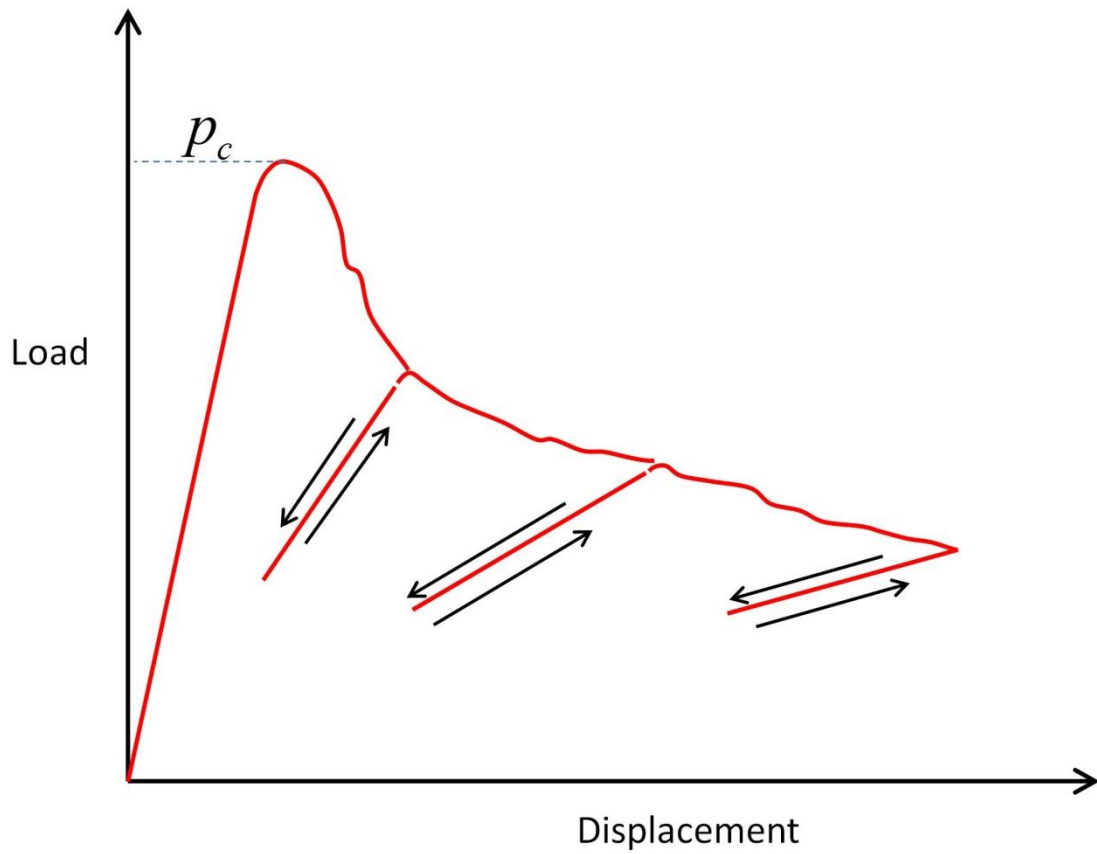


Figure 2.17 A schematic of the force-displacement response from a DCB test. The load drops following crack initiation. Several experiments can be conducted on one specimen by unloading and reloading it.



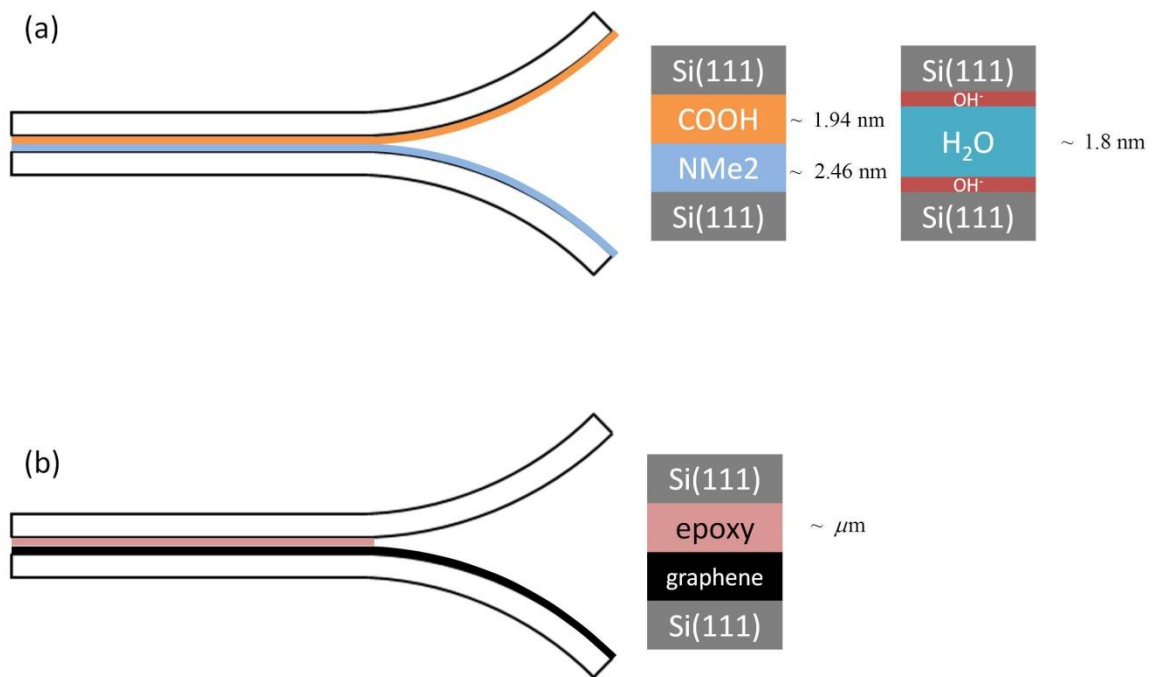


Figure 2.18 Cross sections of specimens used in the wedge tests.

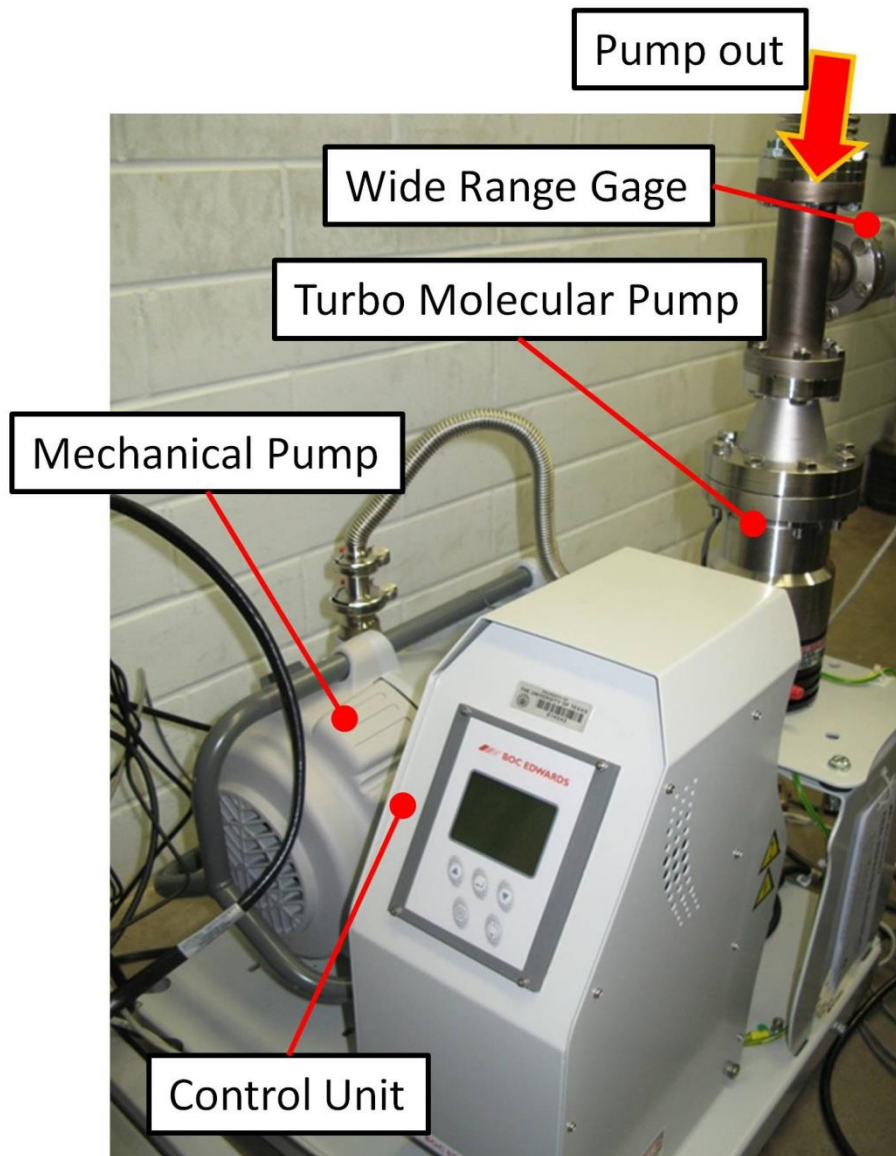


Figure 2.19 The BOC Edwards vacuum system consists of a mechanical pump, turbo molecular pump, a wide range gauge and control units. The vacuum line is connected to the vacuum chamber where the fracture experiment is be conducted.

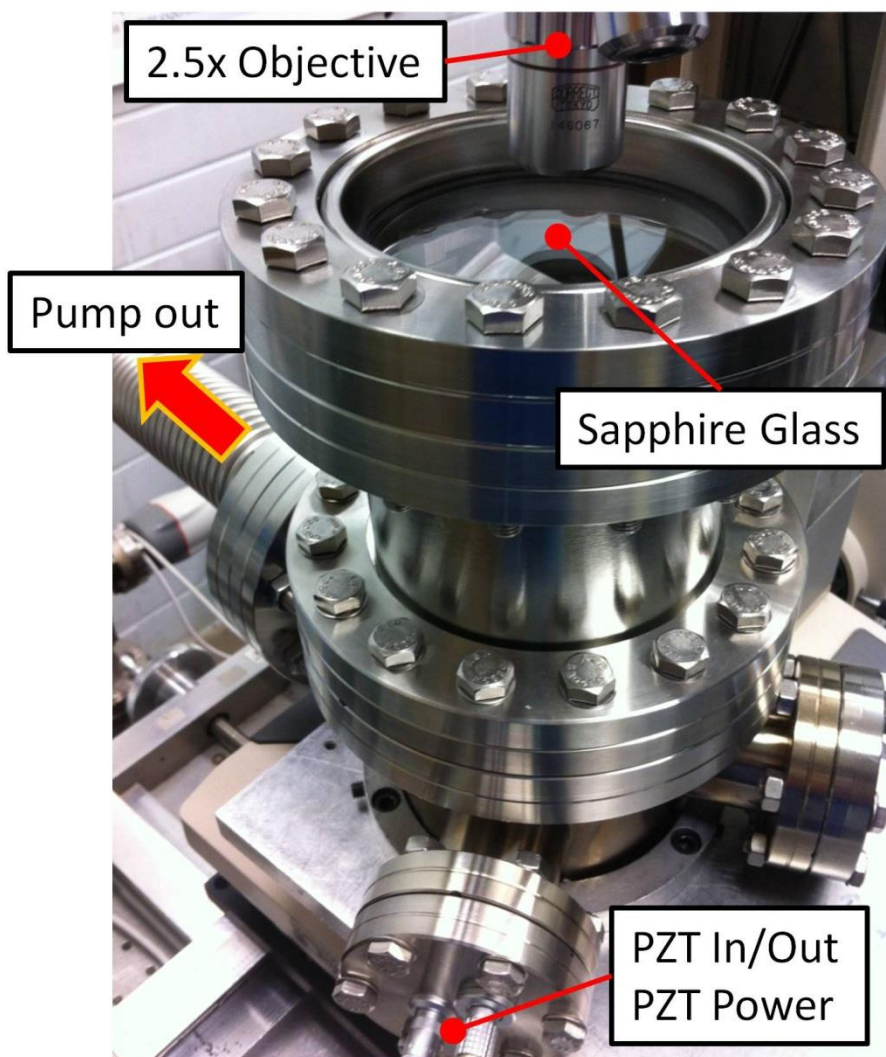


Figure 2.20 The vacuum chamber with access to motor controls, IR-COI and vacuum port.

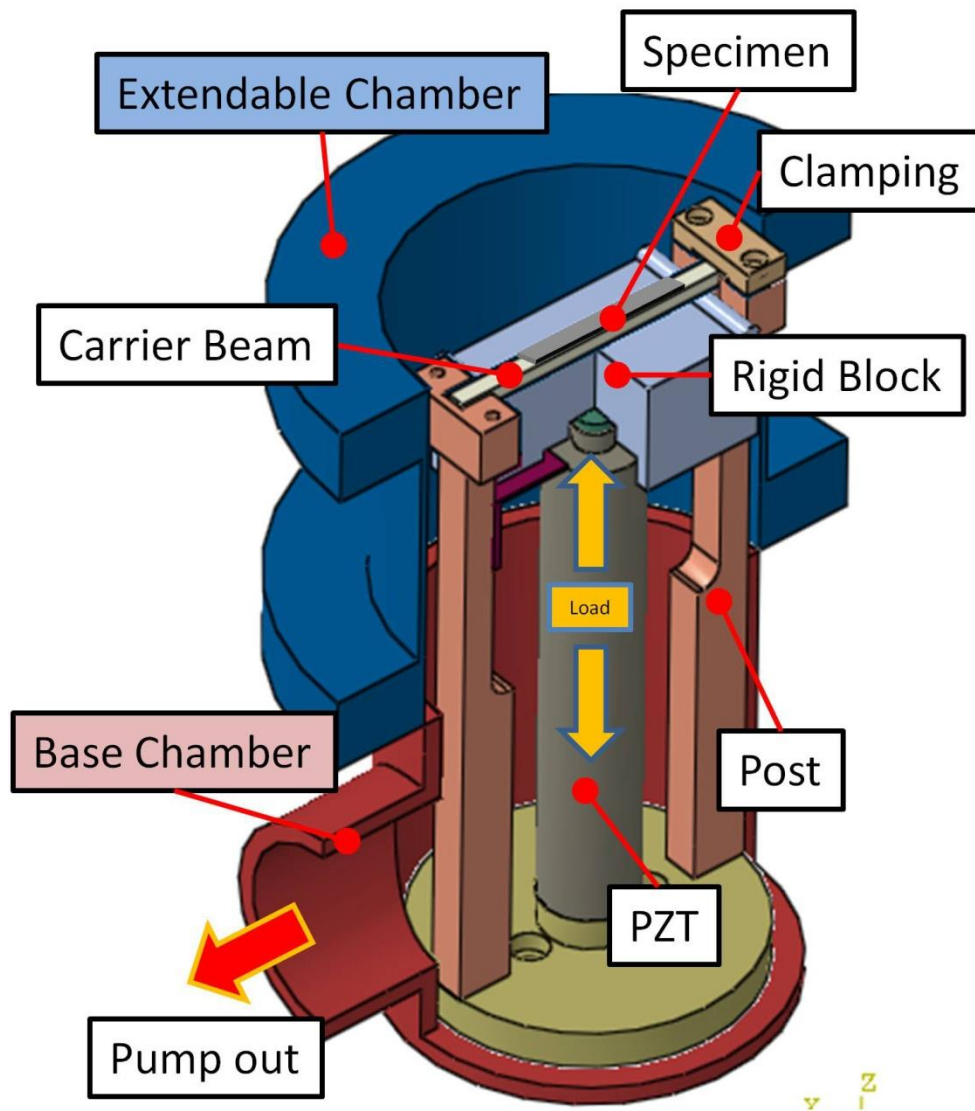


Figure 2.21 A cross section of the vacuum chamber.

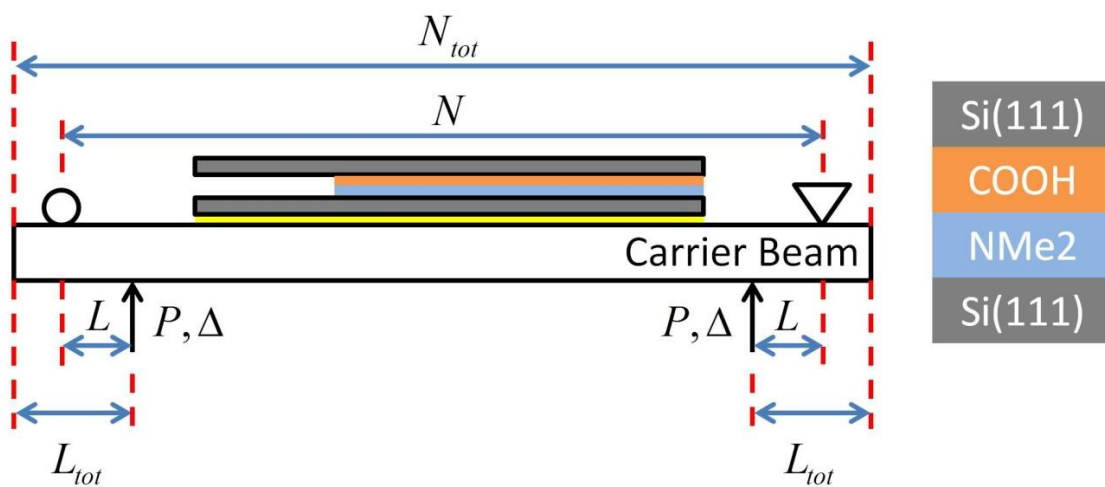


Figure 2.22 A schematic of the carrier beam concept based on four-point bending of the carrier beam.

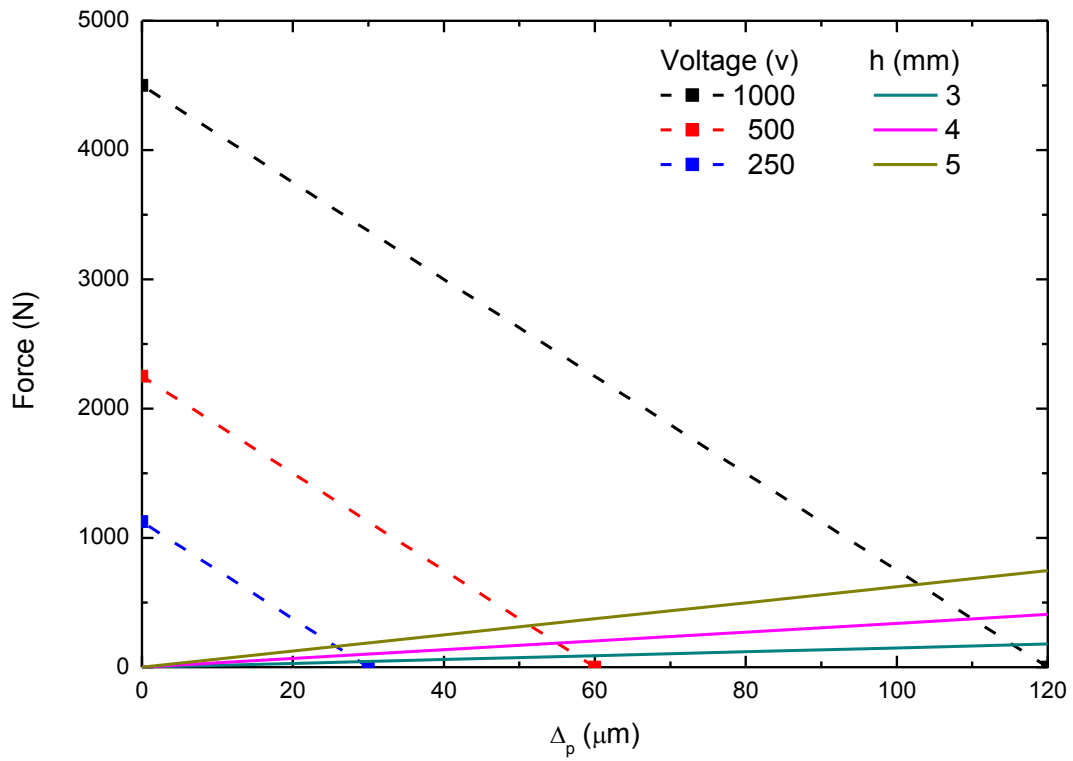


Figure 2.23 The PZT and carrier beam characteristics illustrating the available force and displacement from the PZT under load [107].

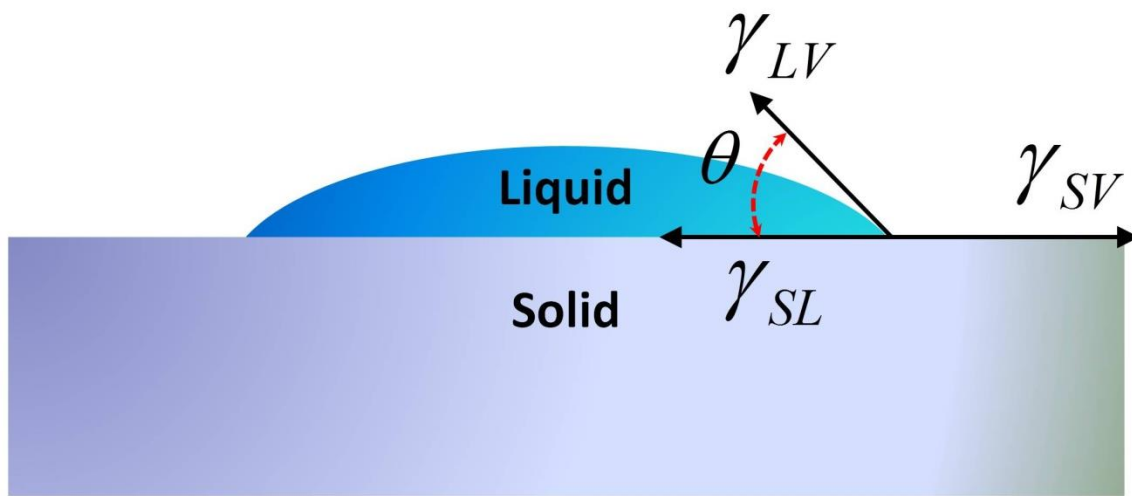


Figure 2.24 A schematic of DI water drop on a target substrate: the arrows indicate the three quantities in Young's equation.

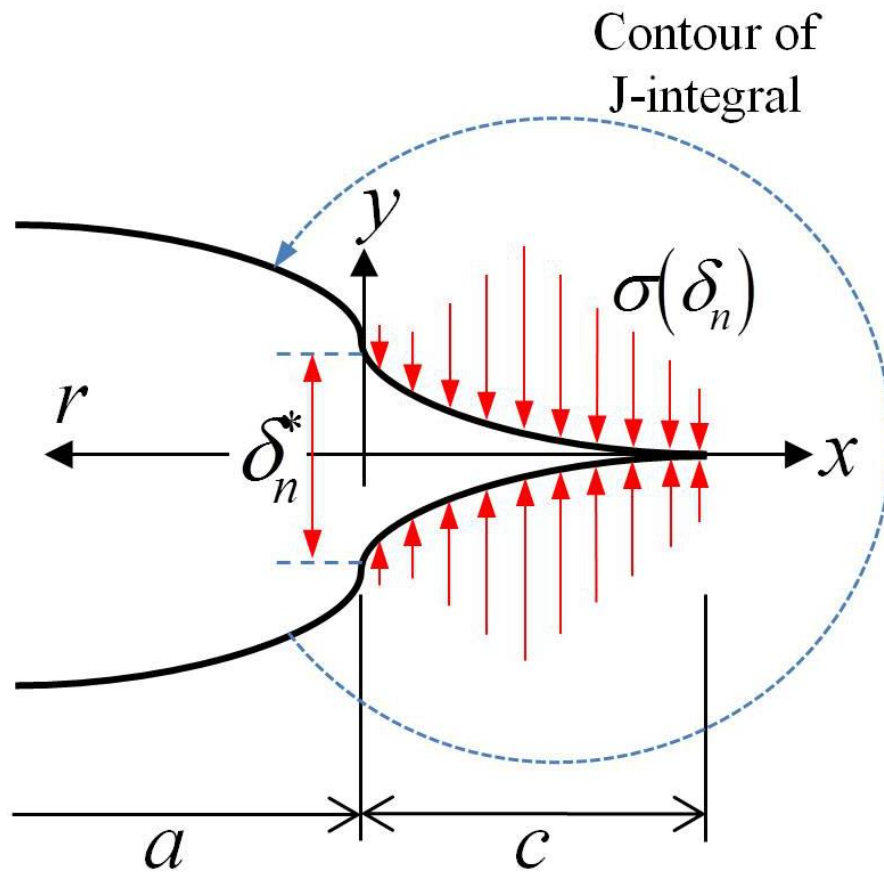


Figure 2.25 Schematic of the cohesive zone near the tip of a crack and its interaction traction distribution.



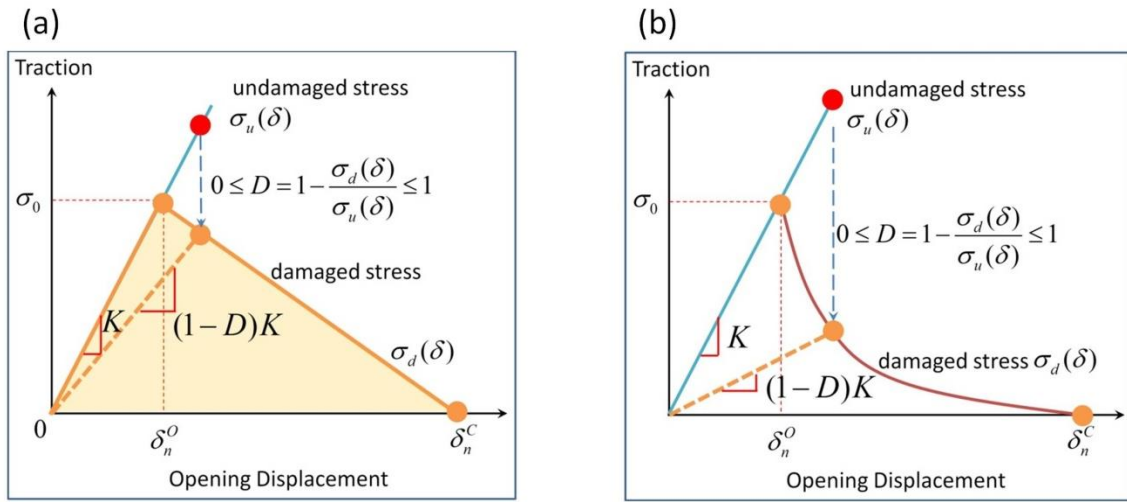


Figure 2.26 Two default traction-separation relations implemented in ABAQUS<sup>®</sup>, each with an initial linearly elastic response followed by (a) linear and (b) exponential softening.

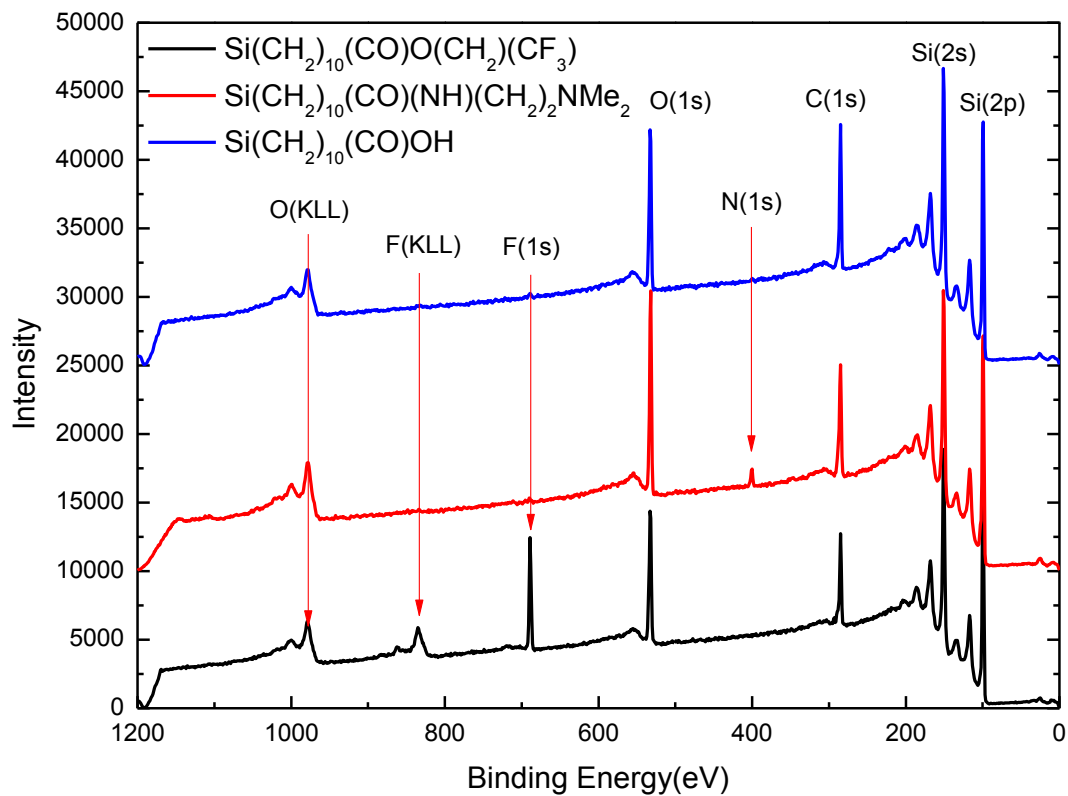


Figure 3.1 XPS survey scan of CF<sub>3</sub>, COOH and NMe<sub>2</sub> SAMs on Si(111).

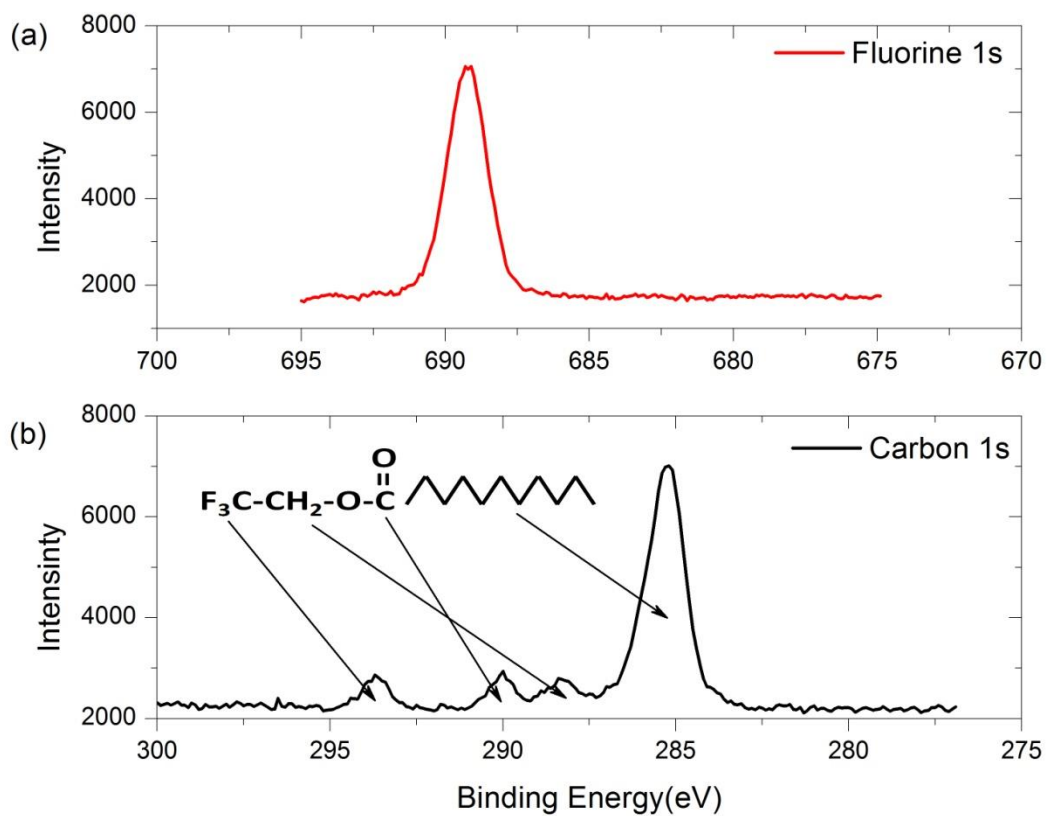


Figure 3.2 A high resolution XPS scan of  $\text{CF}_3$  SAMs for Fluorine 1s and Carbon 1s: (a) Fluorine 1s signal at 689 eV and (b) peaks associated with carbon bonds [160].

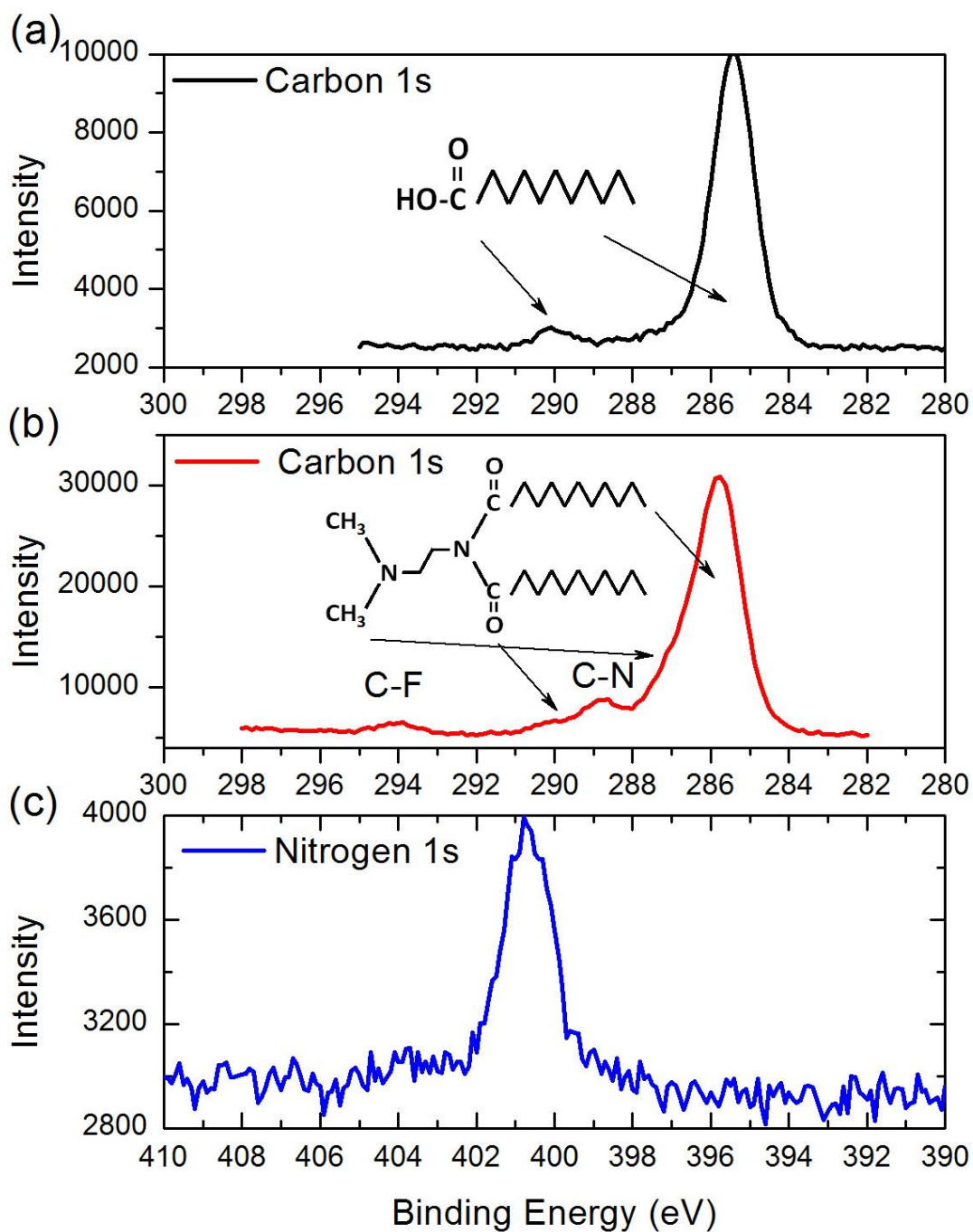


Figure 3.3 A high-resolution XPS scan for NMe<sub>2</sub> and COOH SAMs for Carbon 1s and Nitrogen 1s bonding: (a) Carbon 1s bonding in C=O and CH<sub>2</sub> groups in a COOH SAM [160]. (b) Carbon 1s bonding in C-F, C=O, C-N, CH<sub>3</sub> and CH<sub>2</sub> groups in an NMe<sub>2</sub> SAM. (c) High-resolution scan for N 1s in an NMe<sub>2</sub> SAM.

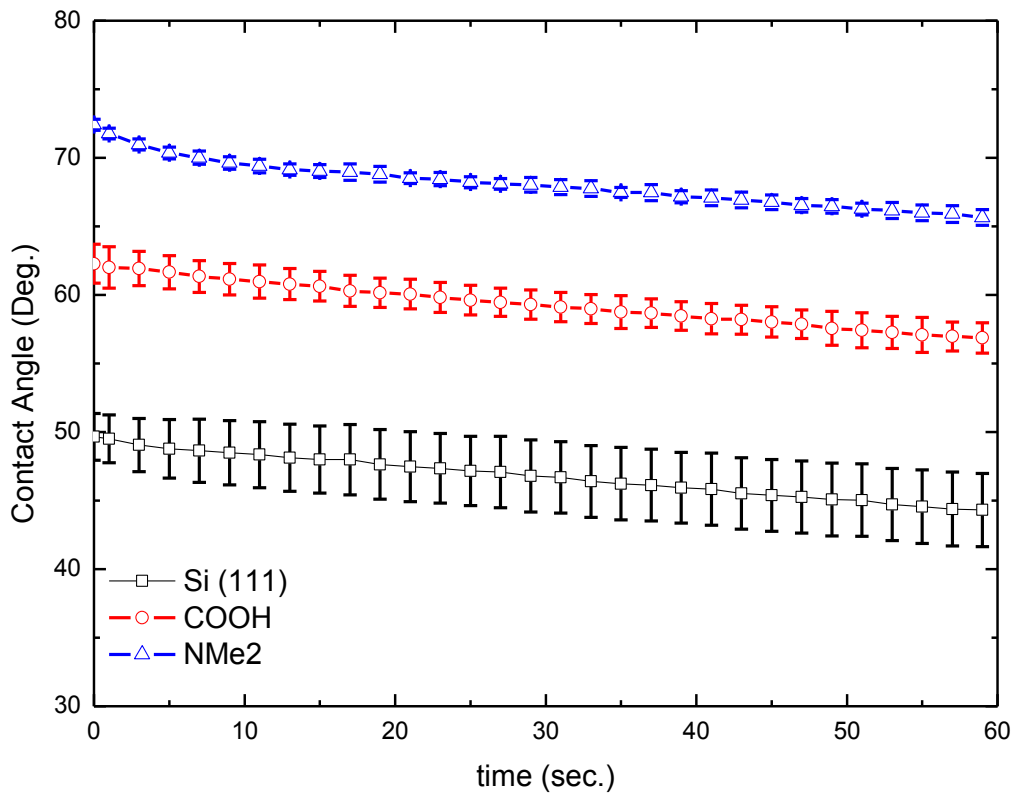


Figure 3.4 Contact angles between water and bare measurement corresponding to bare Si(111) as well as COOH and NMe2 monolayers on Si (111).

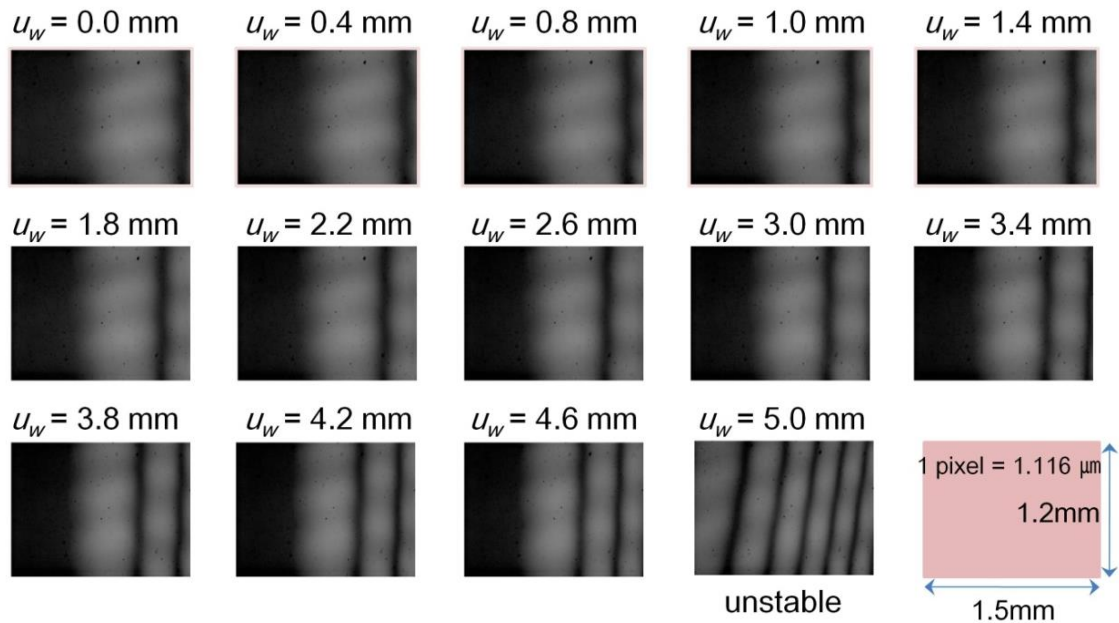


Figure 3.5 A series of snapshots corresponding to various wedge insertions. The dark region on the left represents the bonded region. There are bright and dark fringes associated with the crack opening displacement. When  $u_w$  was 5.0  $\mu\text{m}$ , the crack became unstable so that its front rapidly moved out of the field view.

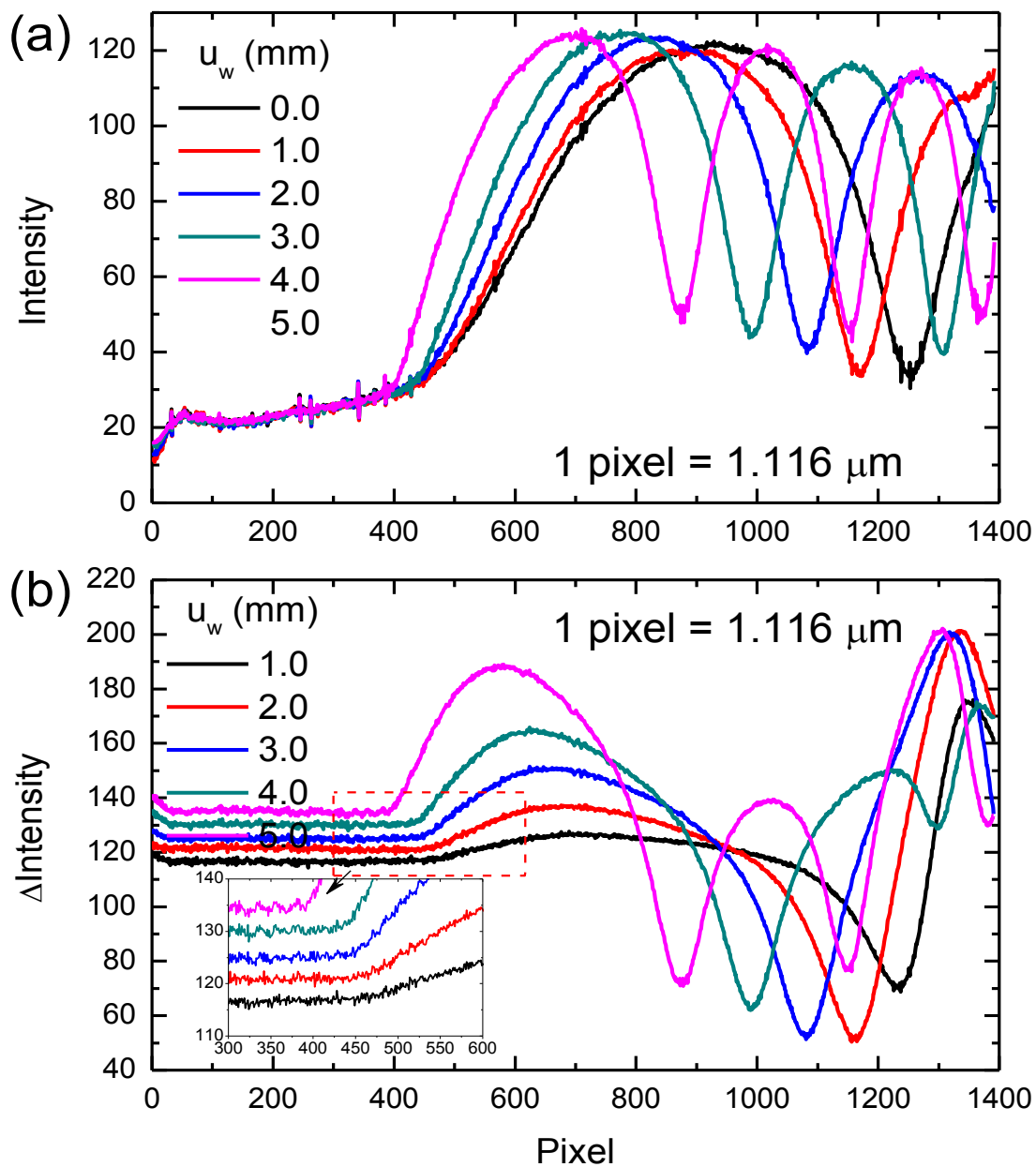


Figure 3.6 Examples of intensity profiles from IR-COI with (a) background and (b) subtracted intensity profiles. The inset features the crack front region.

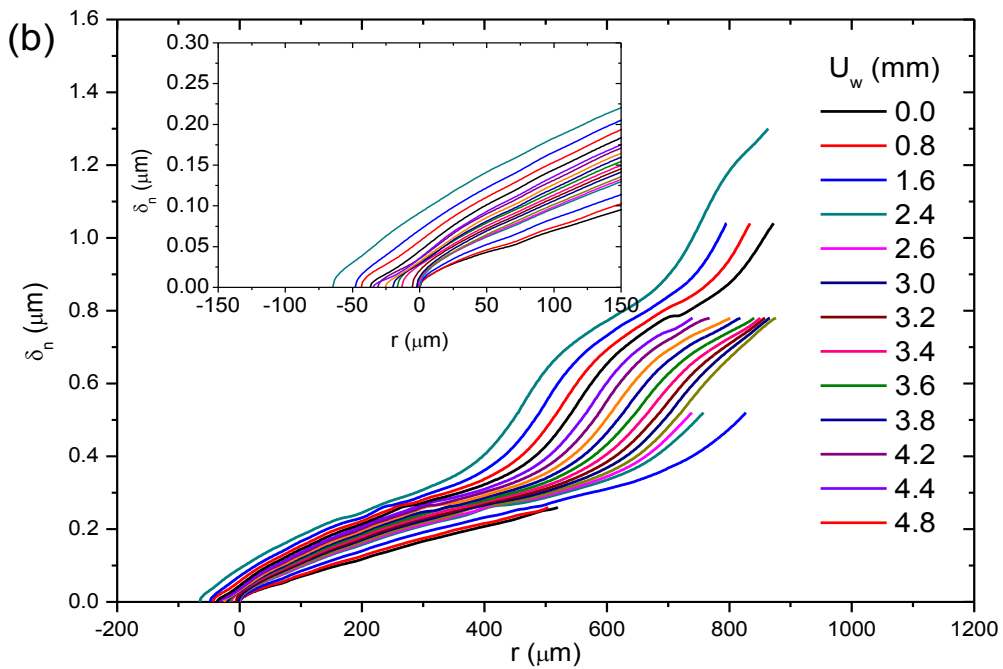
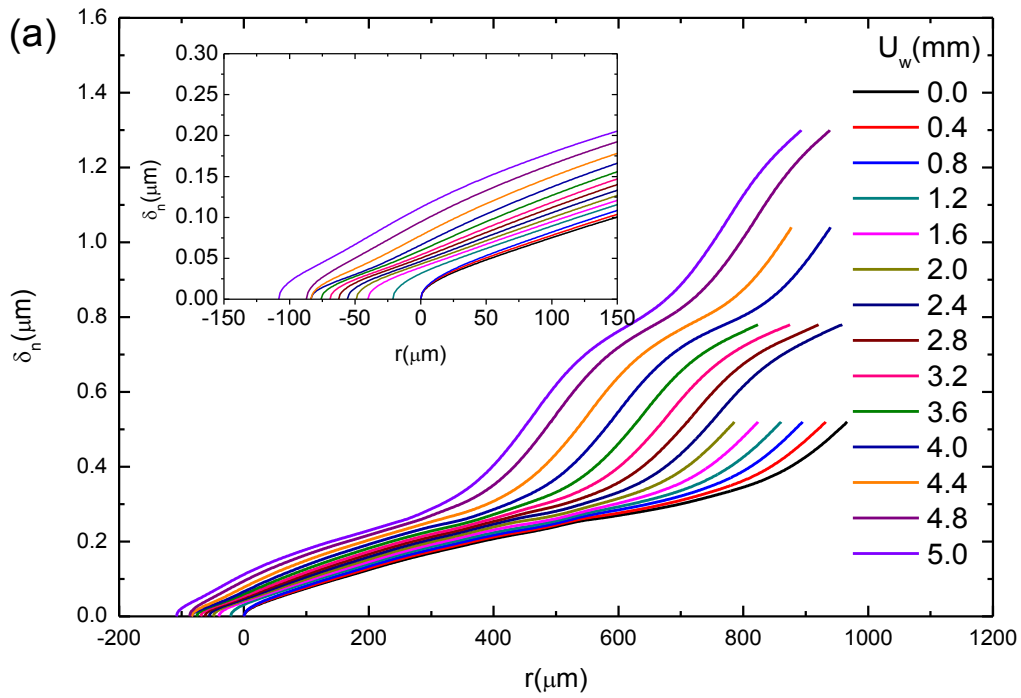


Figure 3.7 NCOD profiles for the (a) ambient and (b) vacuum environments.



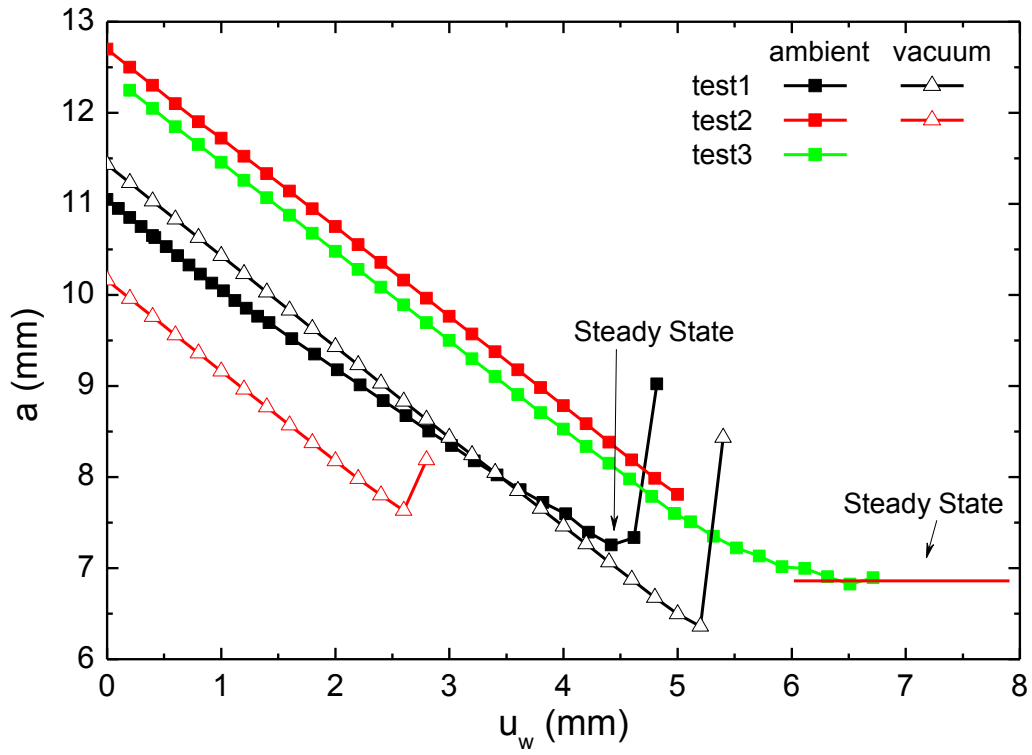


Figure 3.8 The variation of the crack length with respect to wedge insertion.

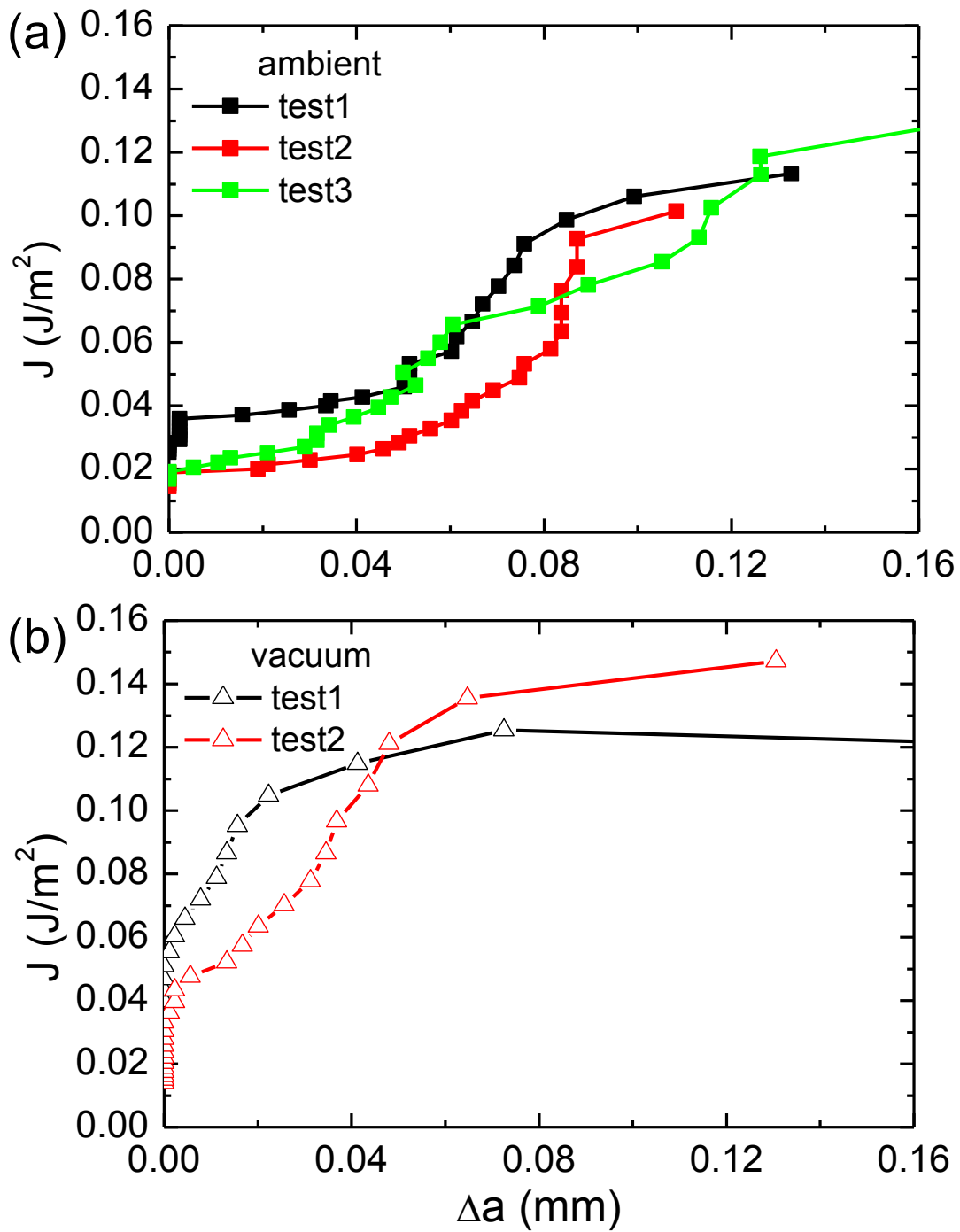


Figure 3.9 Resistance curves for (a) ambient and (b) vacuum.

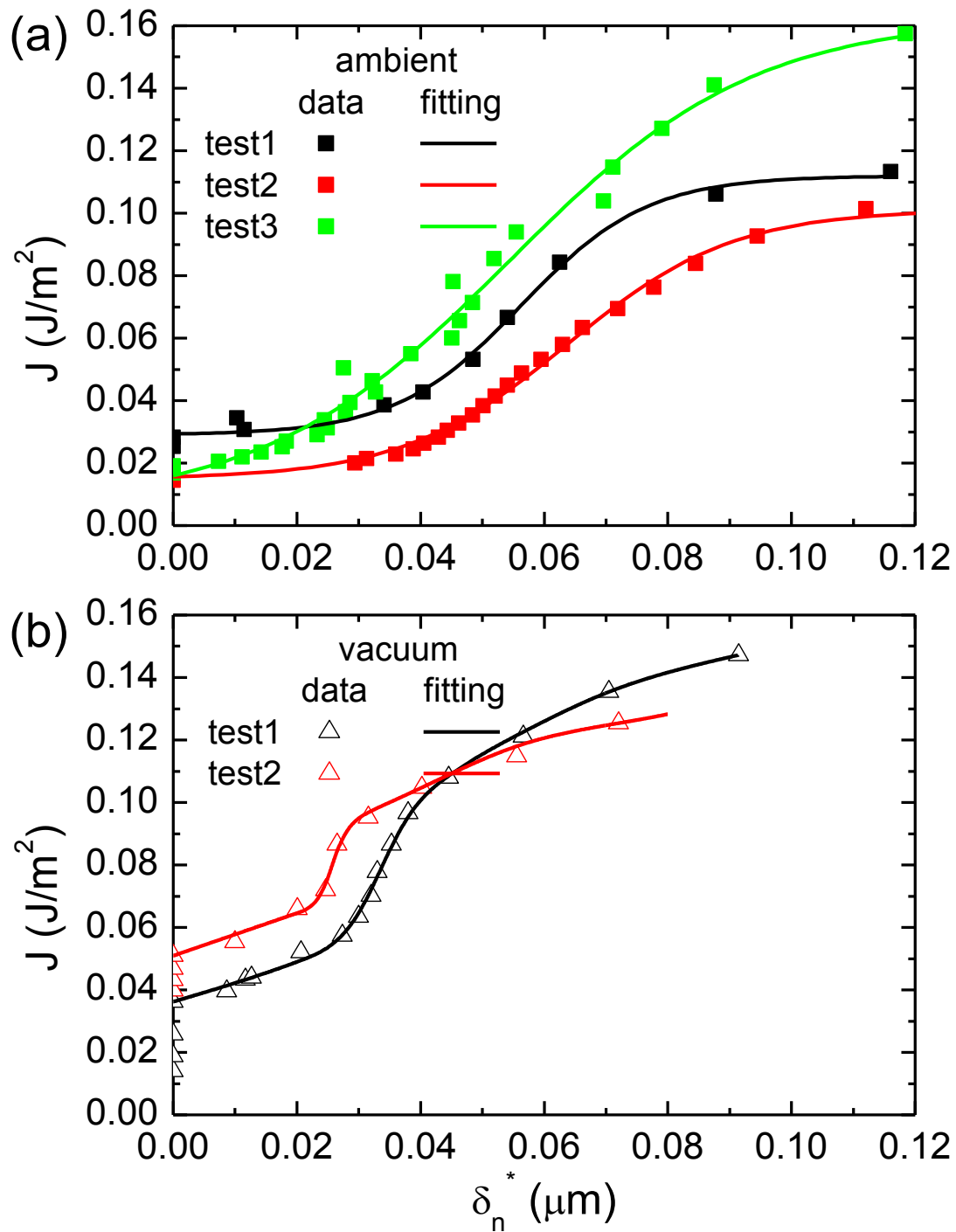


Figure 3.10 Examples of the variation of the J-integral with normal end-opening displacements under (a) ambient and (b) vacuum conditions.

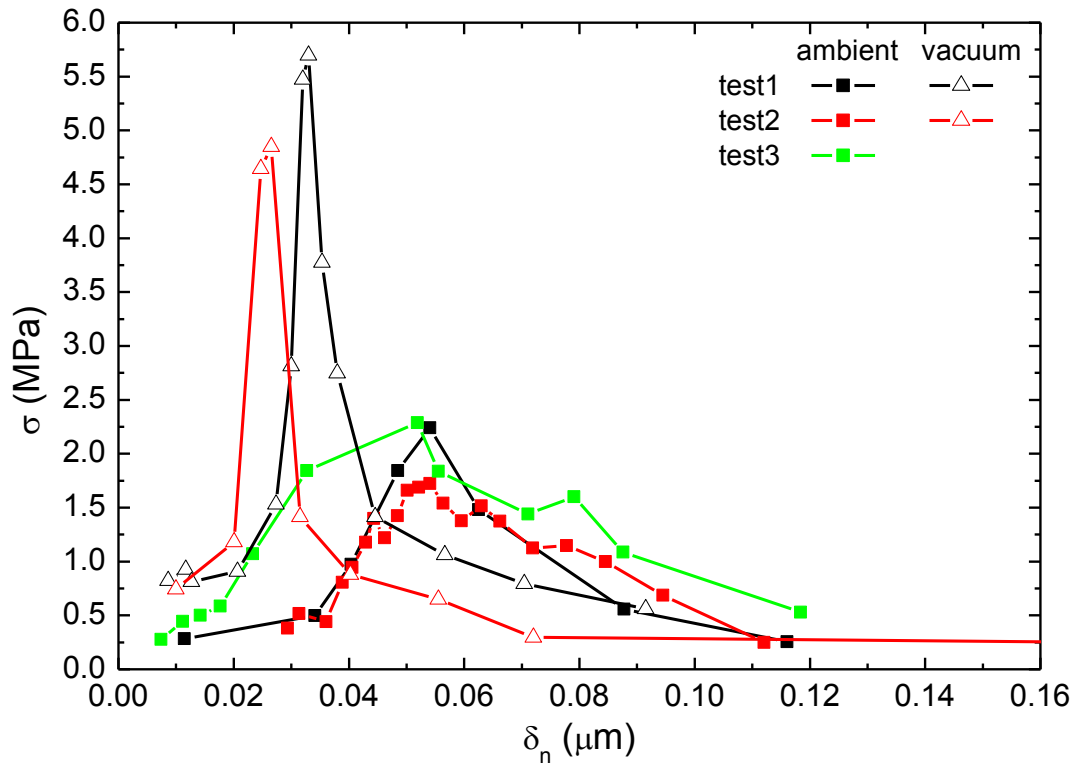


Figure 3.11 The traction-separation relations from the wedge test under ambient and high vacuum.

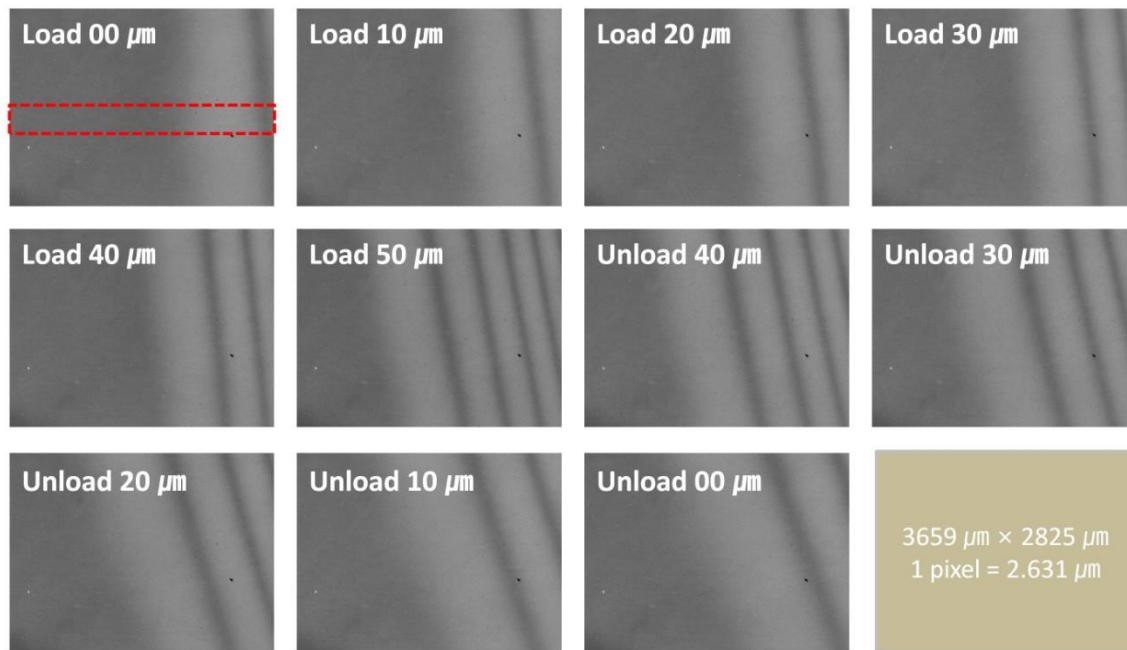


Figure 3.12 A series of fringe patterns from a mixed-mode experiment under ambient conditions as the PZT actuator loaded and then unloaded the specimen.

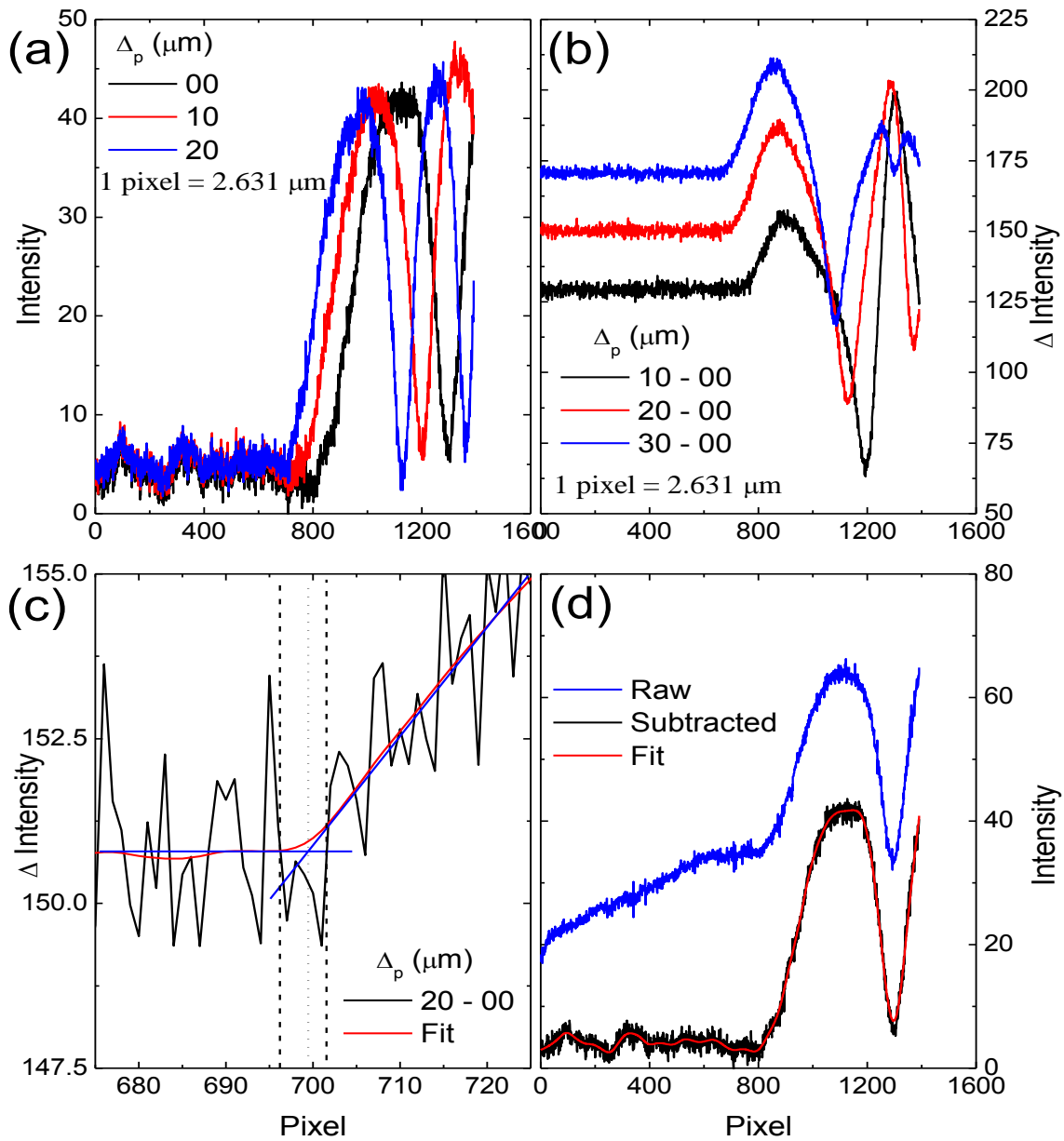


Figure 3.13 Intensity data and fitting for the mixed-mode fracture experiment. (a) Raw intensity profiles averaged over the red dashed box, (b) subtracted intensity profiles, (c) smooth spline is fitting in order to define the location of the crack front and (d) smooth spline fitting of intensity data to determine the NCOD between fringes.

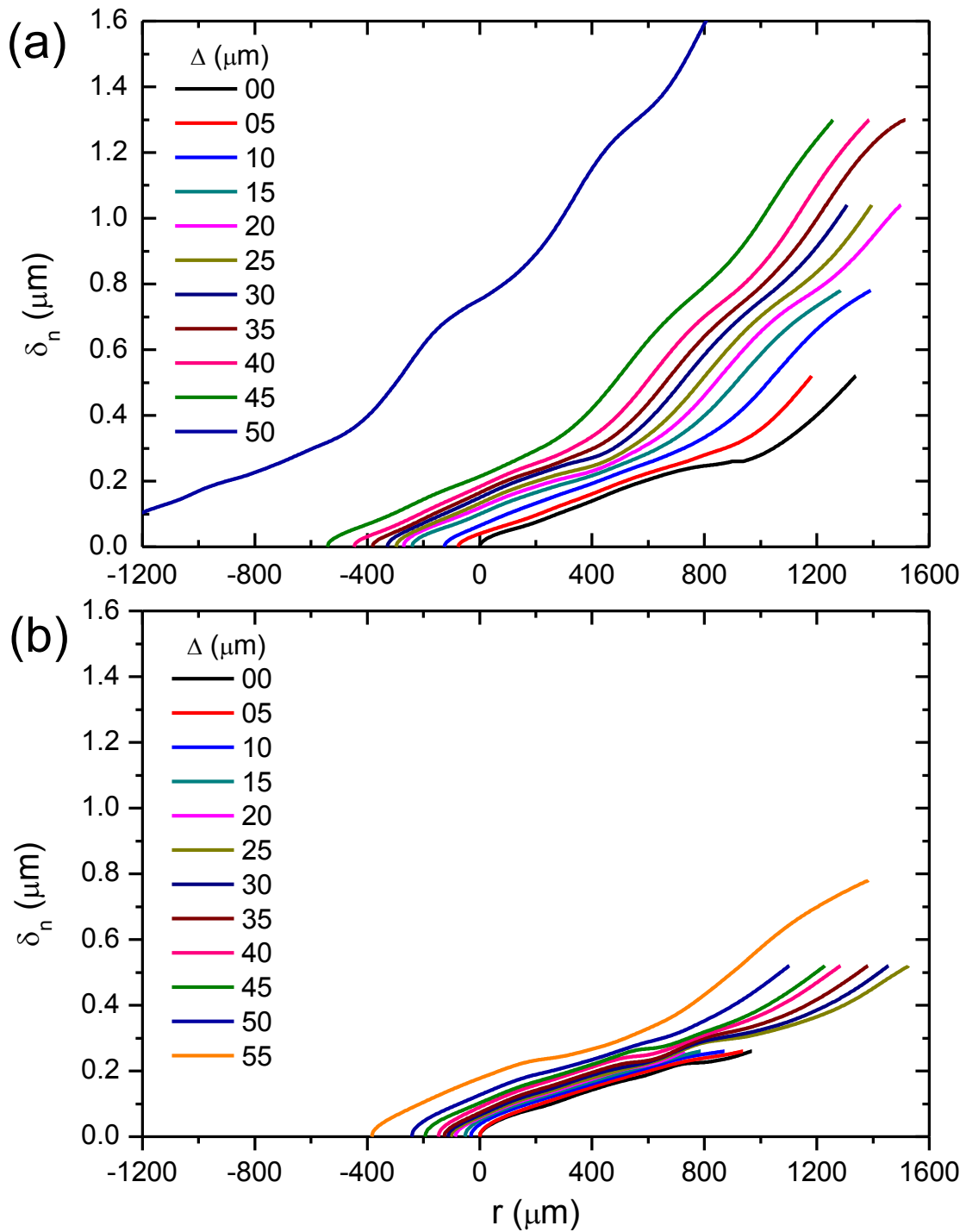


Figure 3.14 The typical NCOD plots from the mixed-mode experiment under (a) ambient and (b) high vacuum.

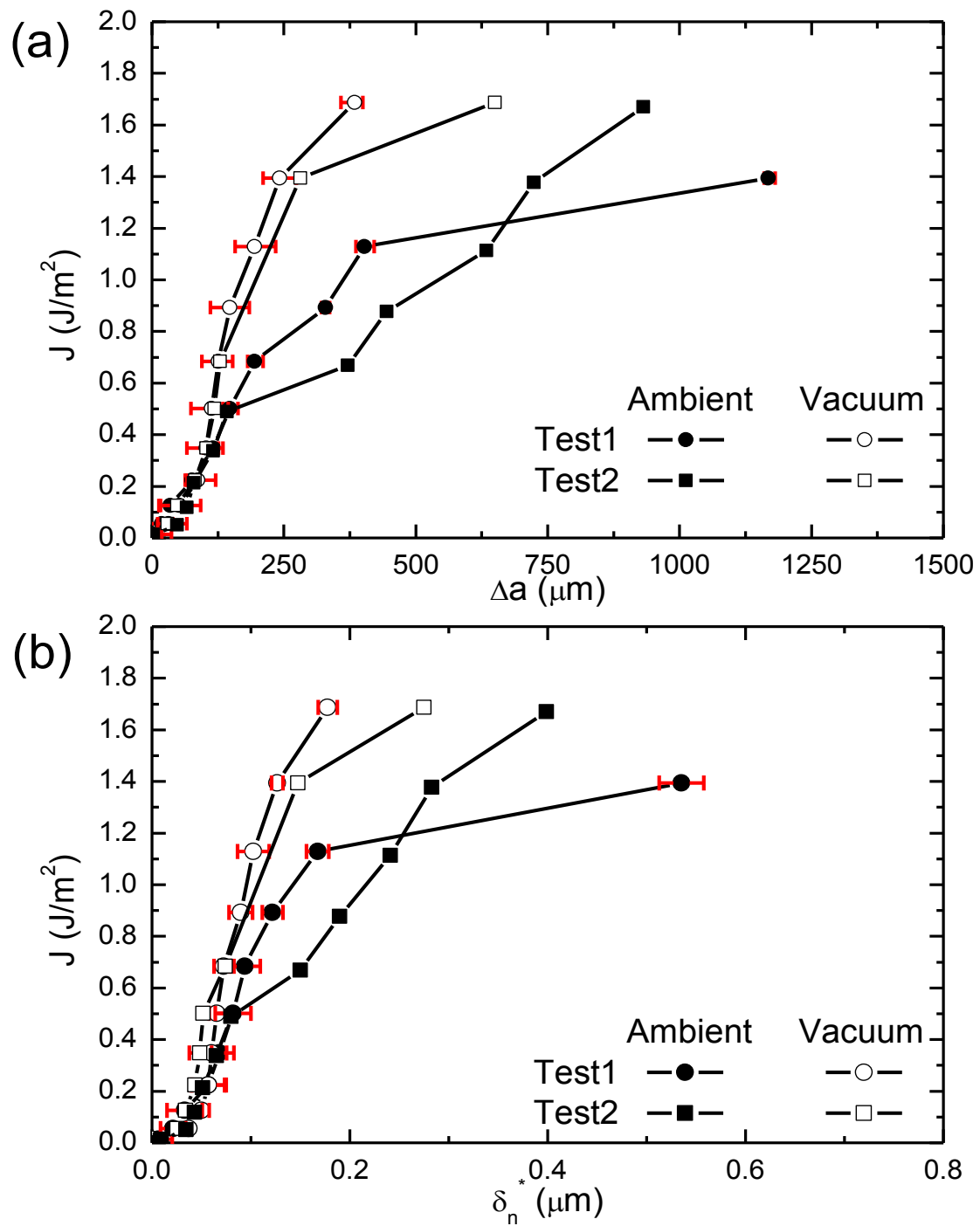


Figure 3.15 The variation of the J-integral under mixed-mode loading in terms of (a) crack extension and (b) normal end-opening displacement under both conditions.



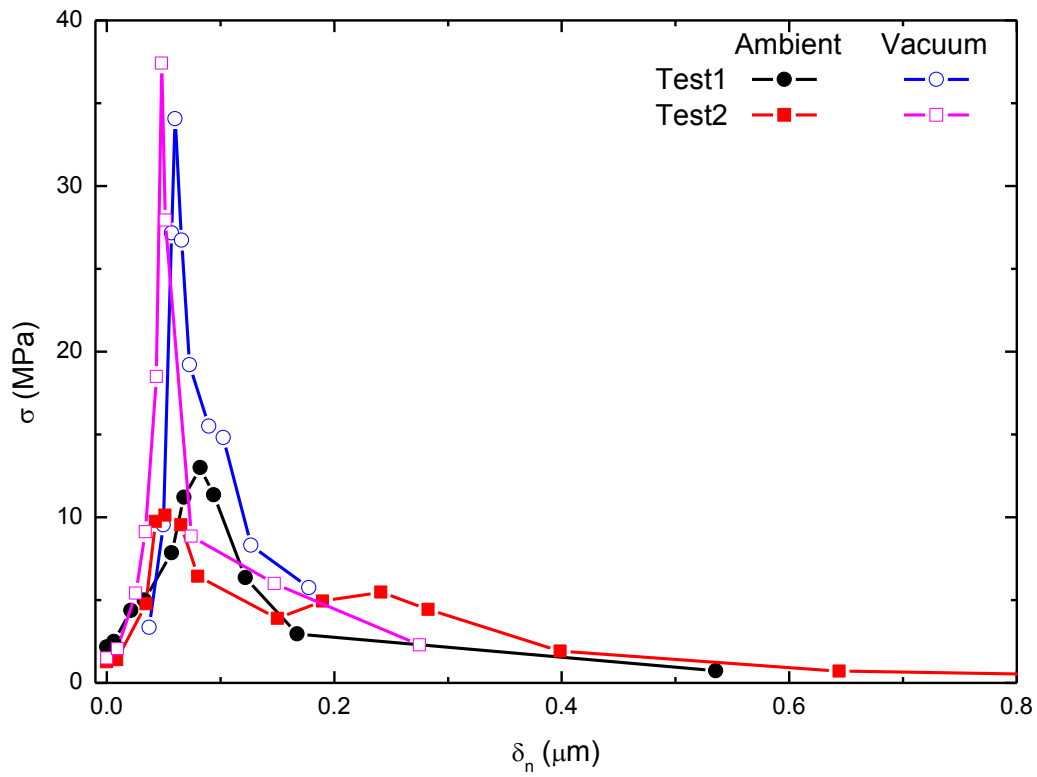


Figure 3.16 Traction-separation relations for COOH/NMe2 interactions under ambient and high-vacuum conditions and mixed-mode loading.

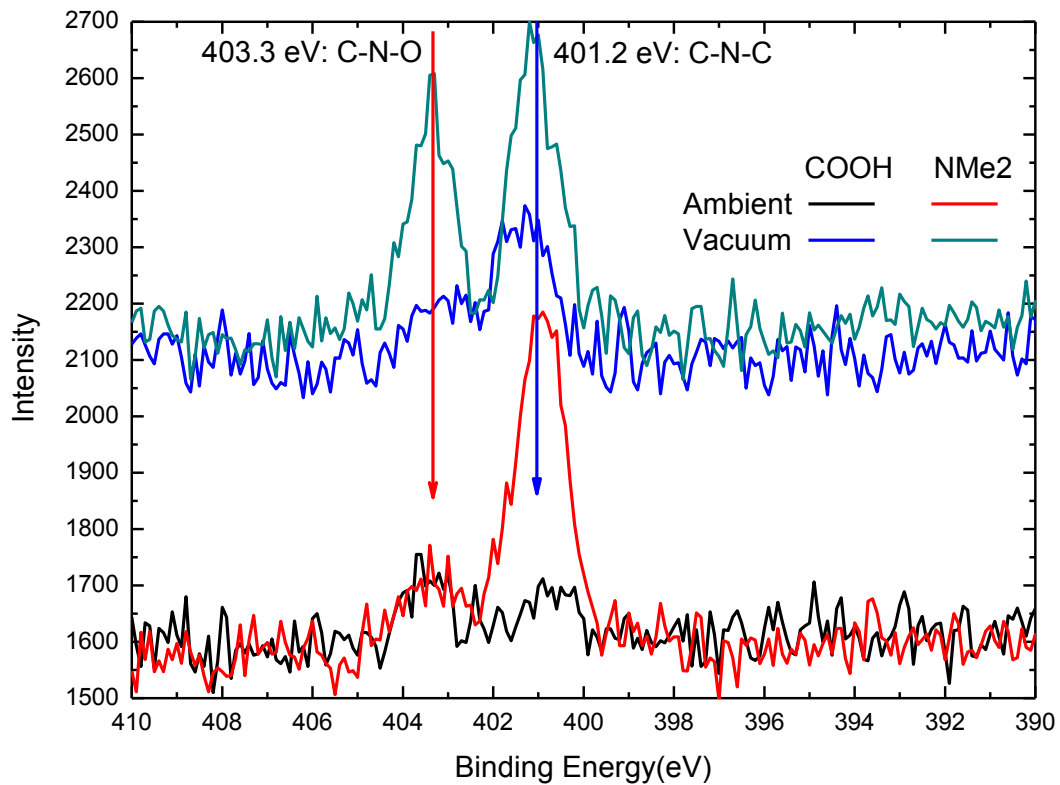


Figure 3.17 XPS high-resolution scan for N1(s) on the fractured surfaces of specimens subjected to ambient and high vacuum.

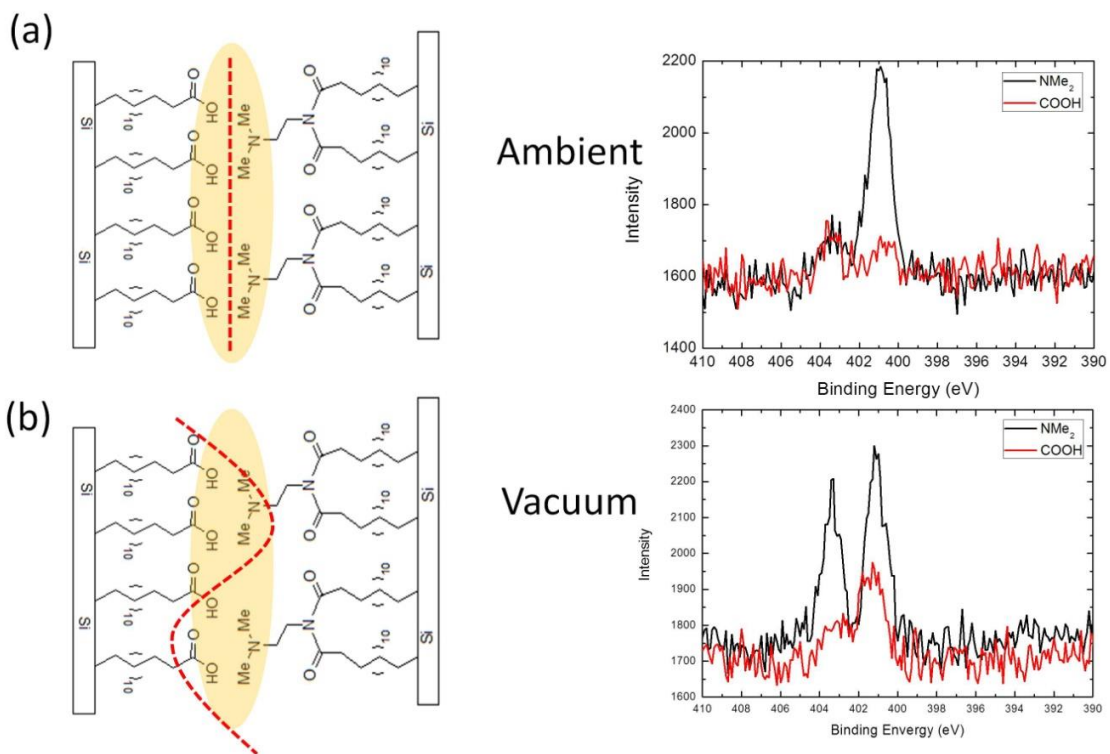


Figure 3.18 Schematics of the fracture paths (dashed line) based on high resolution XPS scanning for (a) ambient and (b) high vacuum.

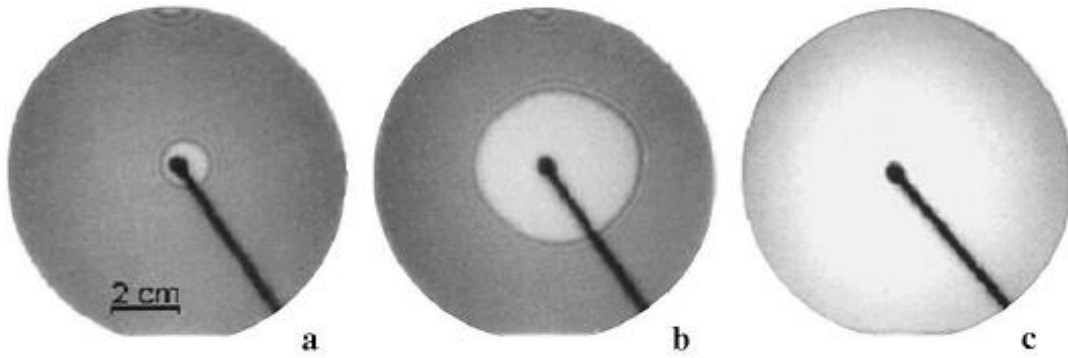
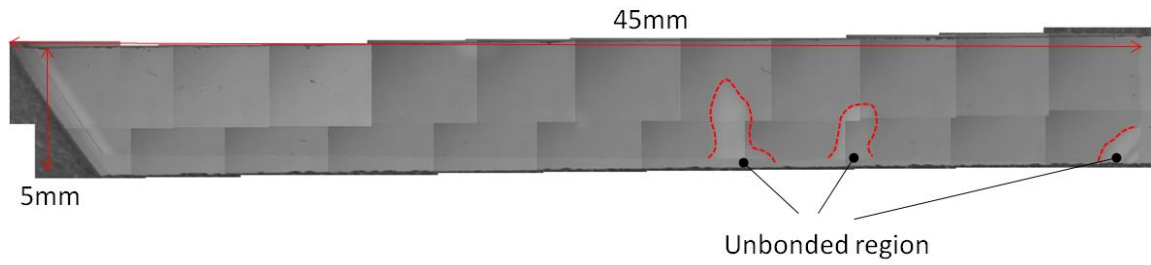


Figure 4.1 Propagation of a bonding wave in wafer-to-wafer bonding [27]. (a) Wafer bonding was activated by tapping the top wafer, (b) spreading of the bonding wave and (c) complete bonding.

(a) fully bonded case



(b) partially bonded case

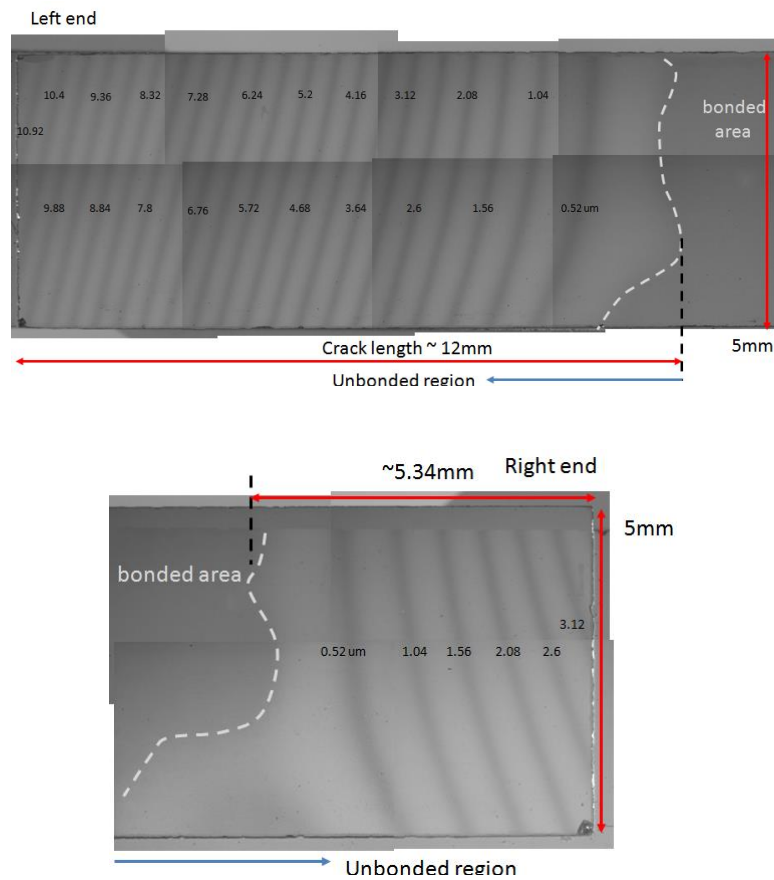
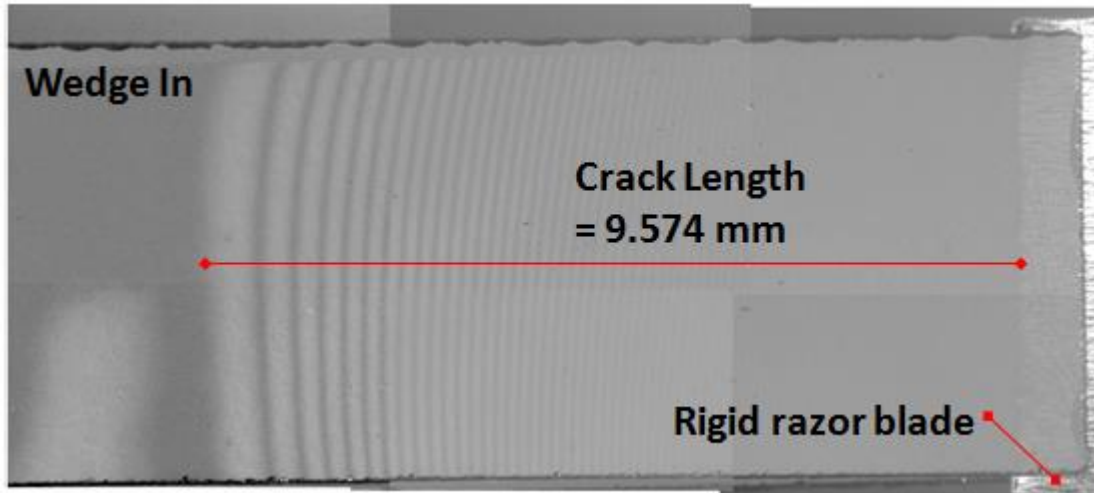


Figure 4.2 Infra-red images of the hydrophilic bonded-samples.: (a) Complete bonding and (b) the middle portion of the specimen was bonded leaving both ends separated.

(a)



(b)

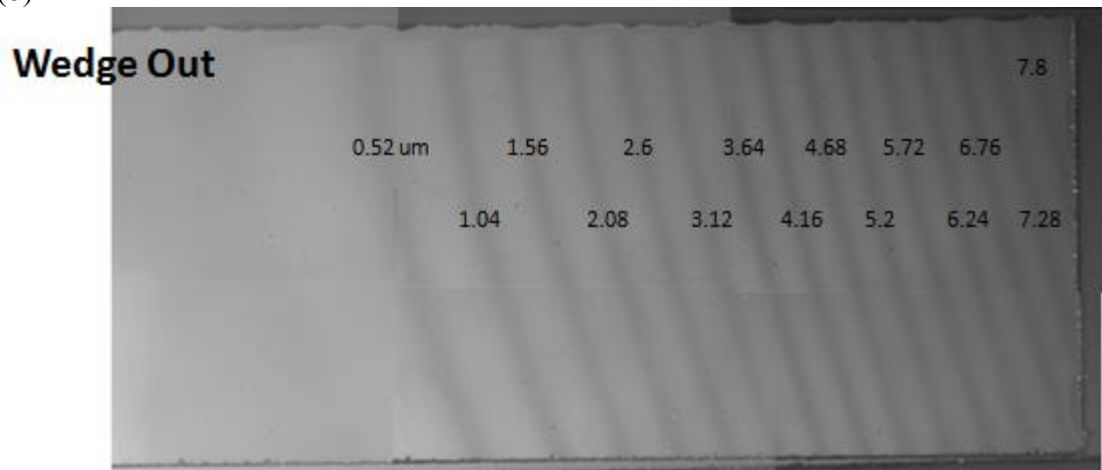


Figure 4.3 Infra-red images of the NCOD of the completely bonded (Fig. 4.2a) following (a) insertion and (b) removal of the wedge. Note the residual opening over 7.8  $\mu\text{m}$  following removal.

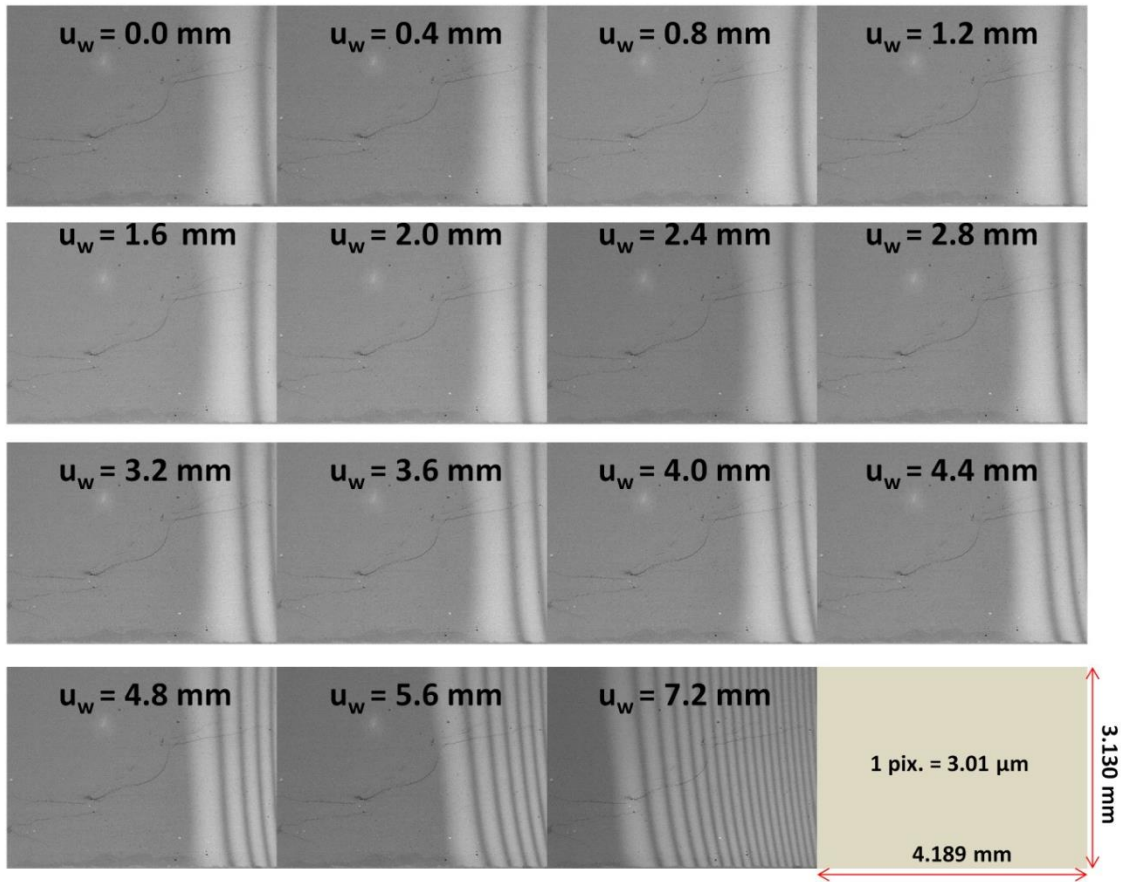


Figure 4.4 A series of IR images as a wedge was inserted. The crack became unstable the wedge was inserted by 7.2 mm. The field of view is 4189×3130 μm with a resolution of 3.01 μm per pixel.

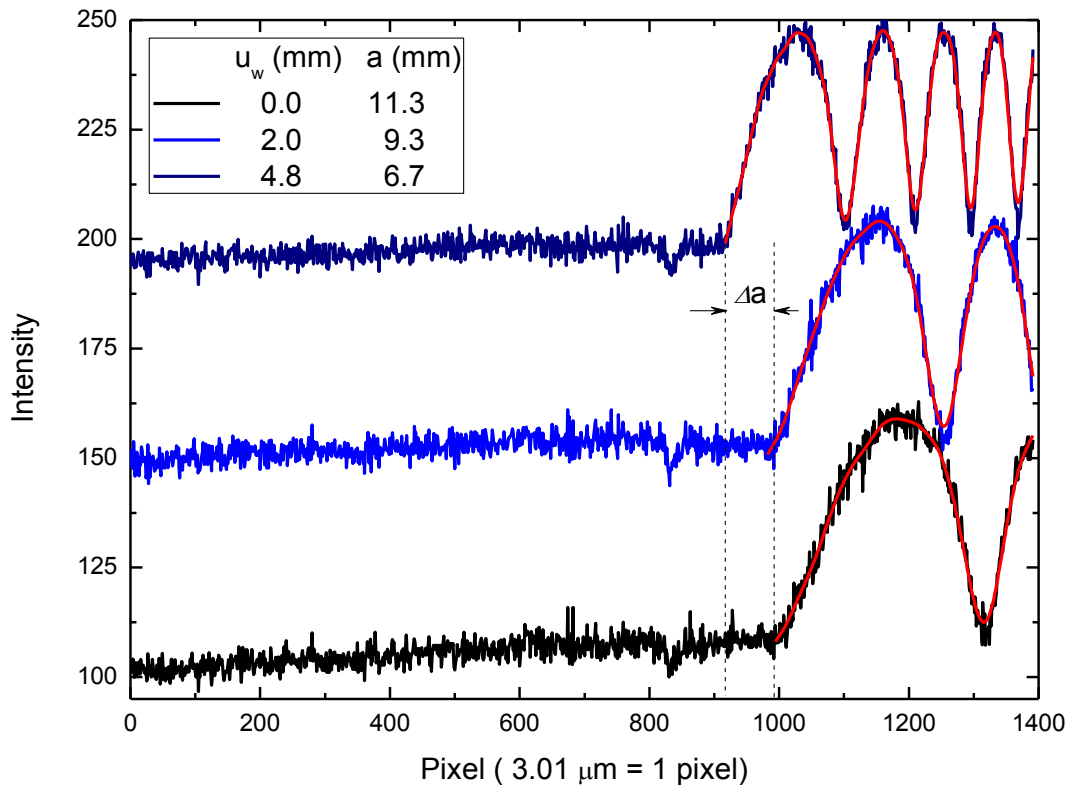


Figure 4.5 A series of intensity profiles associated with three different wedge-insertions  $u_w$  and associated crack lengths  $a$ . The red line is the best fit to the data.



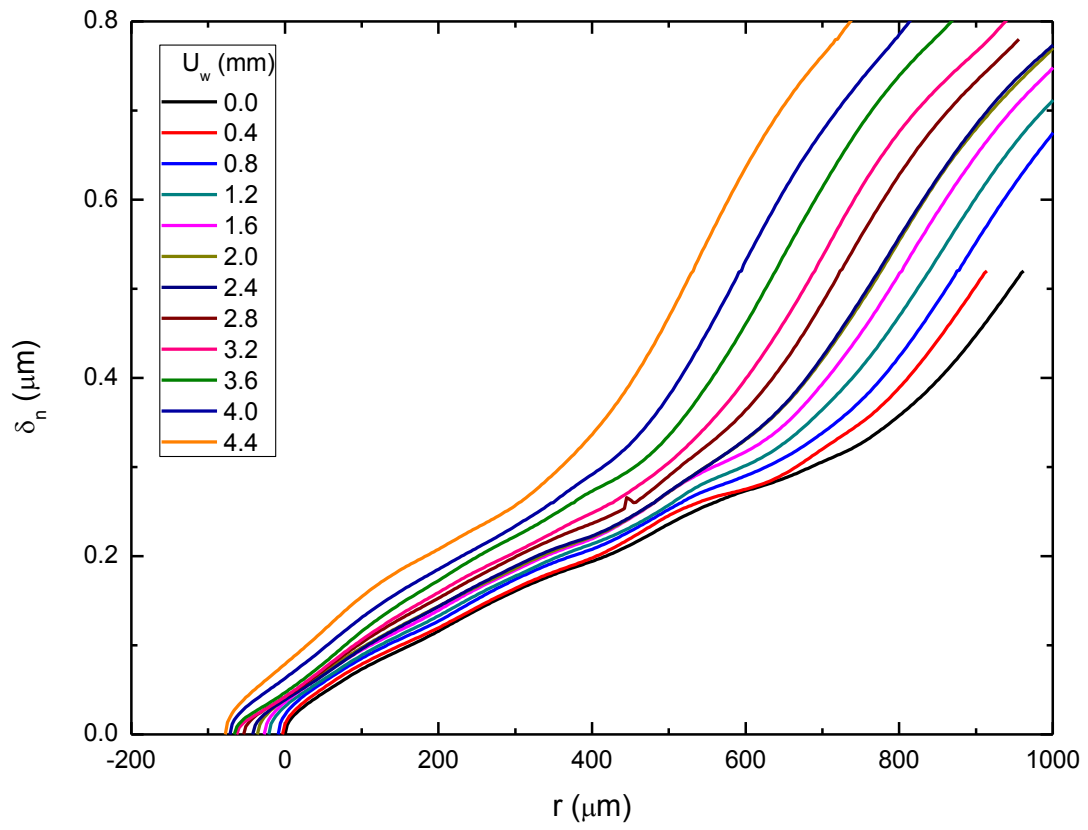


Figure 4.6 NCOD profiles as a function of wedge insertion.

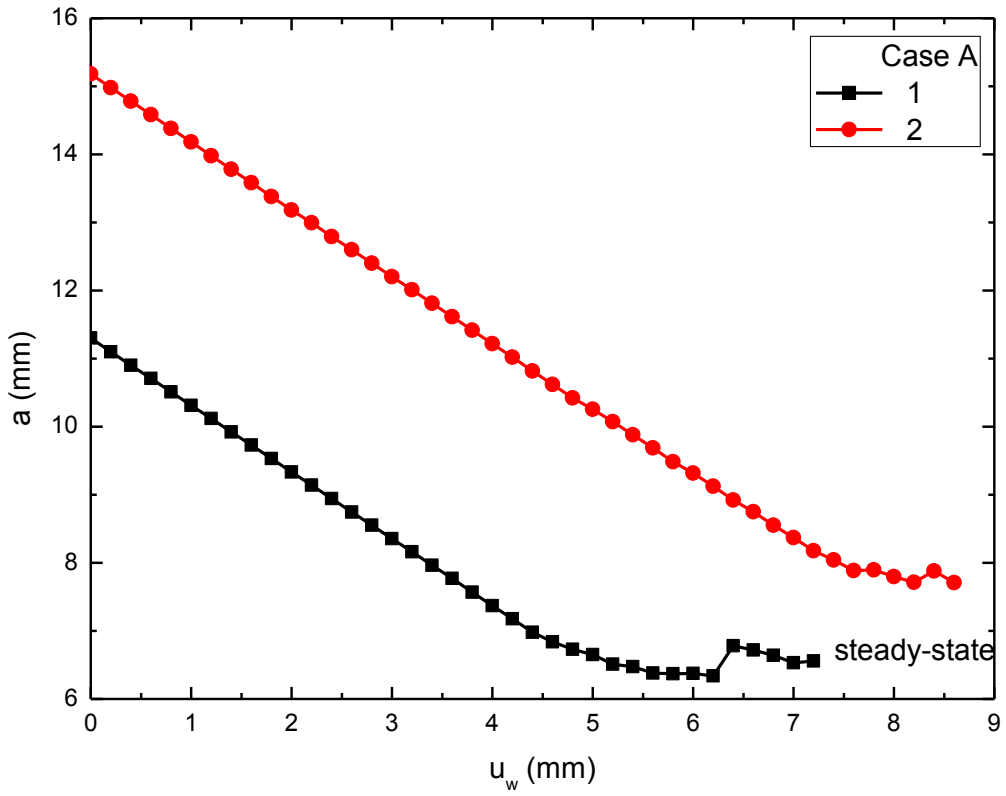


Figure 4.7 Crack length as a function of wedge insertion for two well bonded specimens.

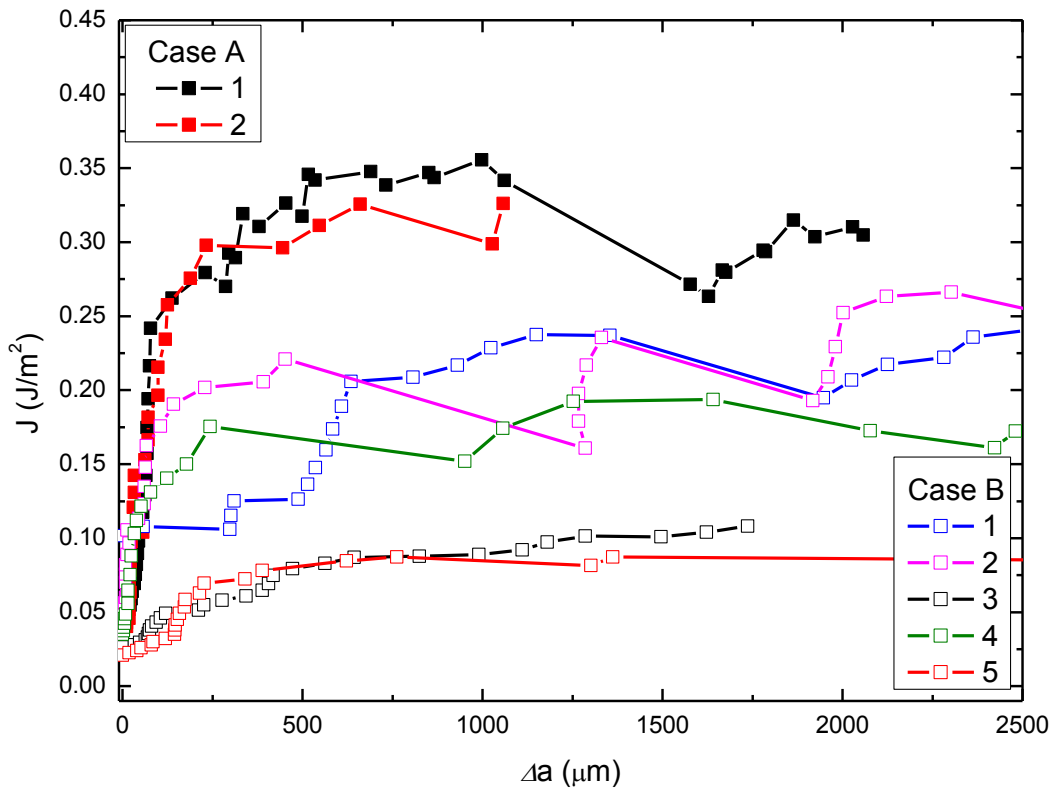


Figure 4.8 Delamination resistance curves for all the specimens with hydrophilic bonding.

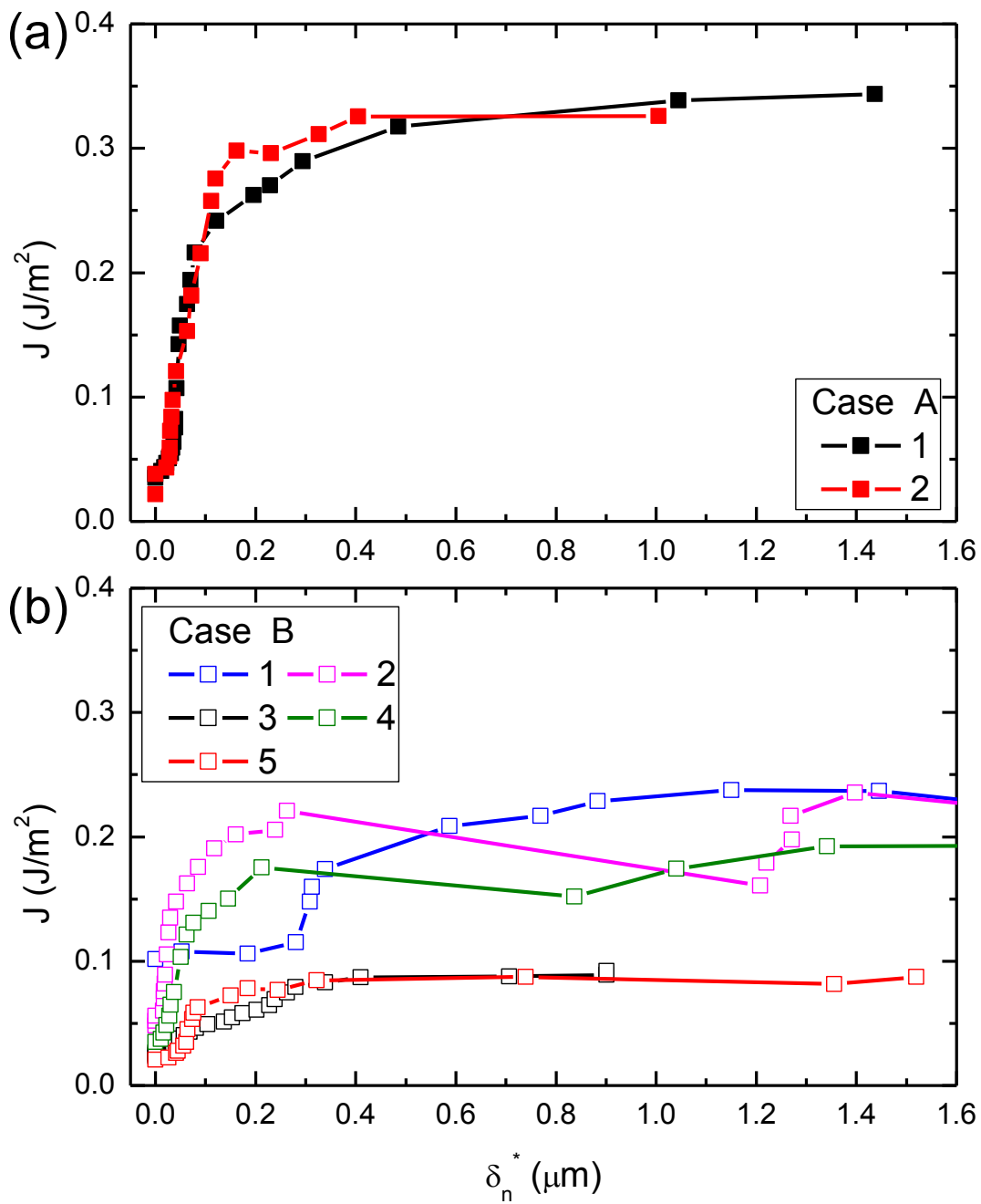


Figure 4.9 The variation of J-integral with end opening NCOD: (a) Case A for relatively strongly bonded specimens, (b) Case B for weaker bonding.

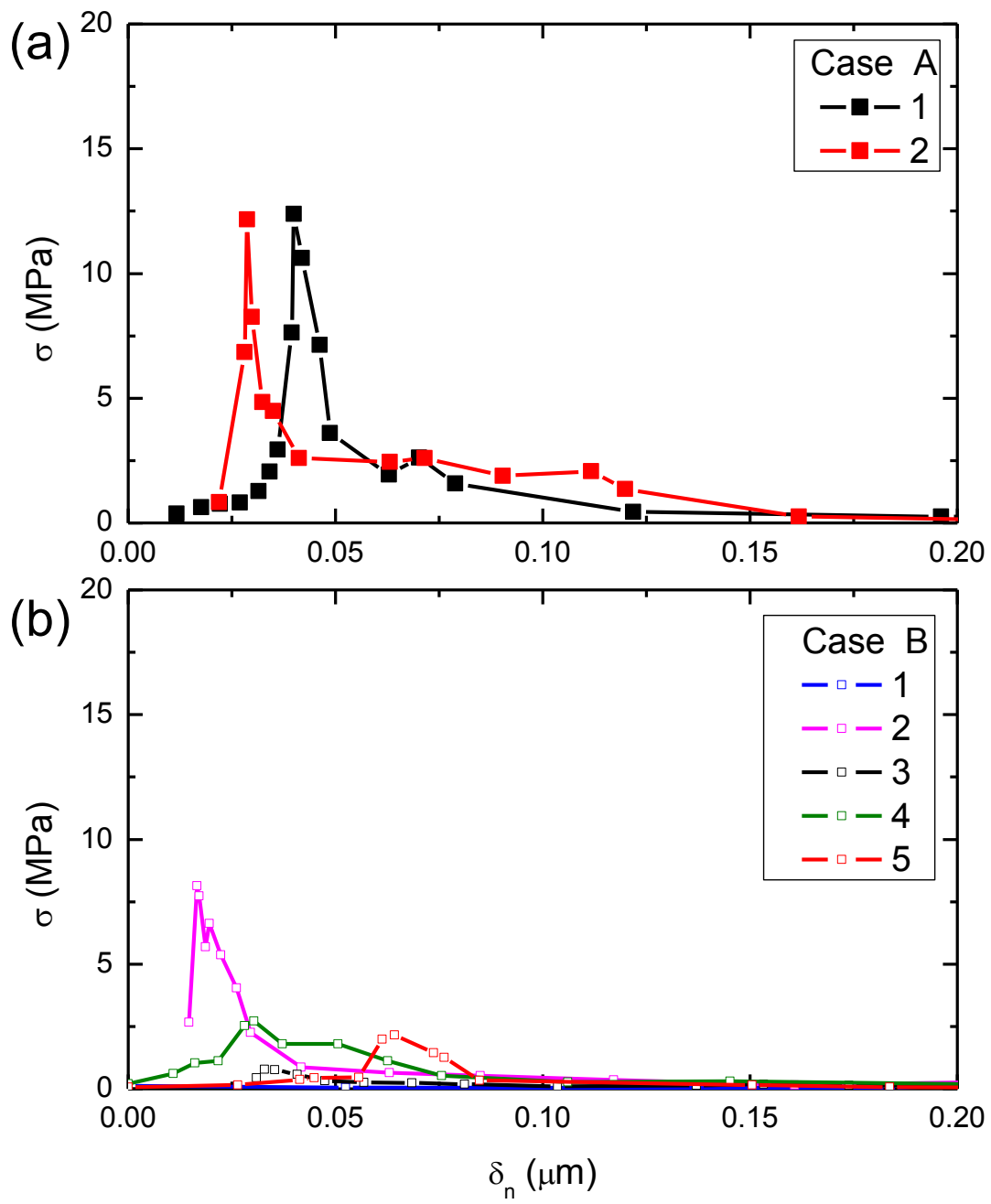


Figure 4.10 Traction-separation relations for hydrophilic bonding: (a) Case A. (b) Case B

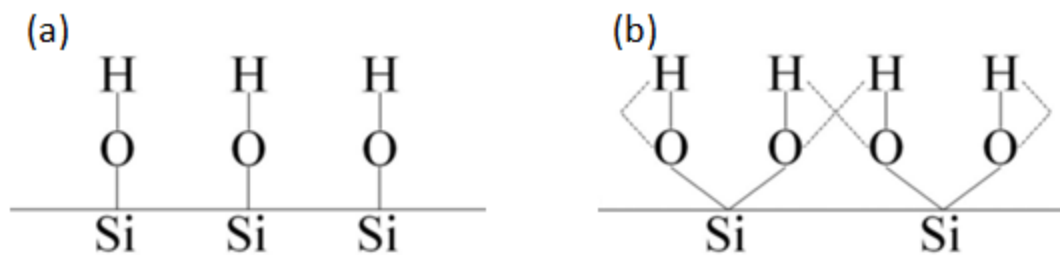


Figure 4.11 Two different hydroxyl groups on silicon wafers [176]. (a) Type A bonding without any hydrogen bonding between the hydroxyl groups. (b) Type B bonding with hydrogen bonding (dashed line) between hydroxyl groups.

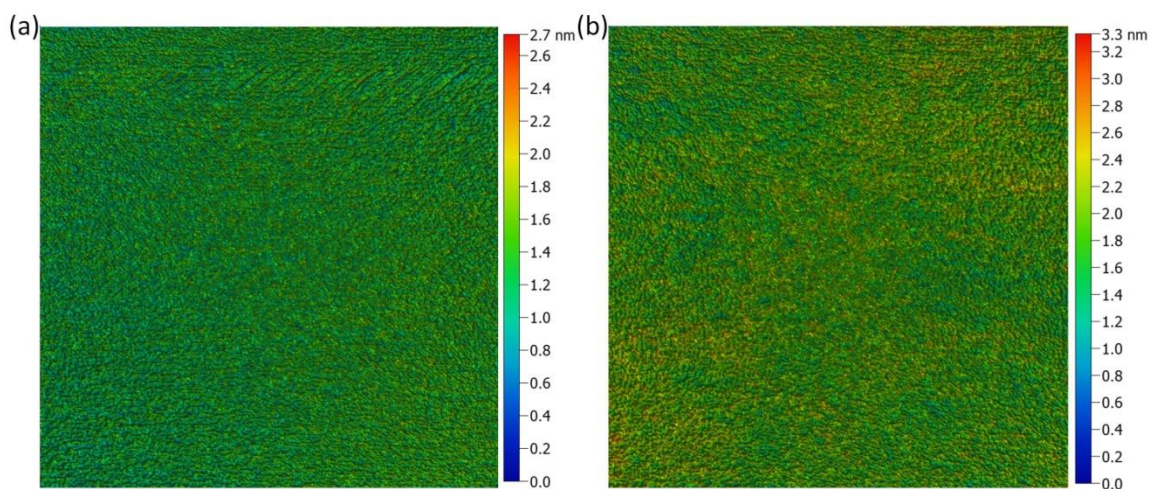


Figure 4.12 Topographical plot of  $5 \times 5 \mu\text{m}$  regions on a Si(111) surface. The overall roughness values in each case were (a) 0.255 nm and (b) 0.309 nm.

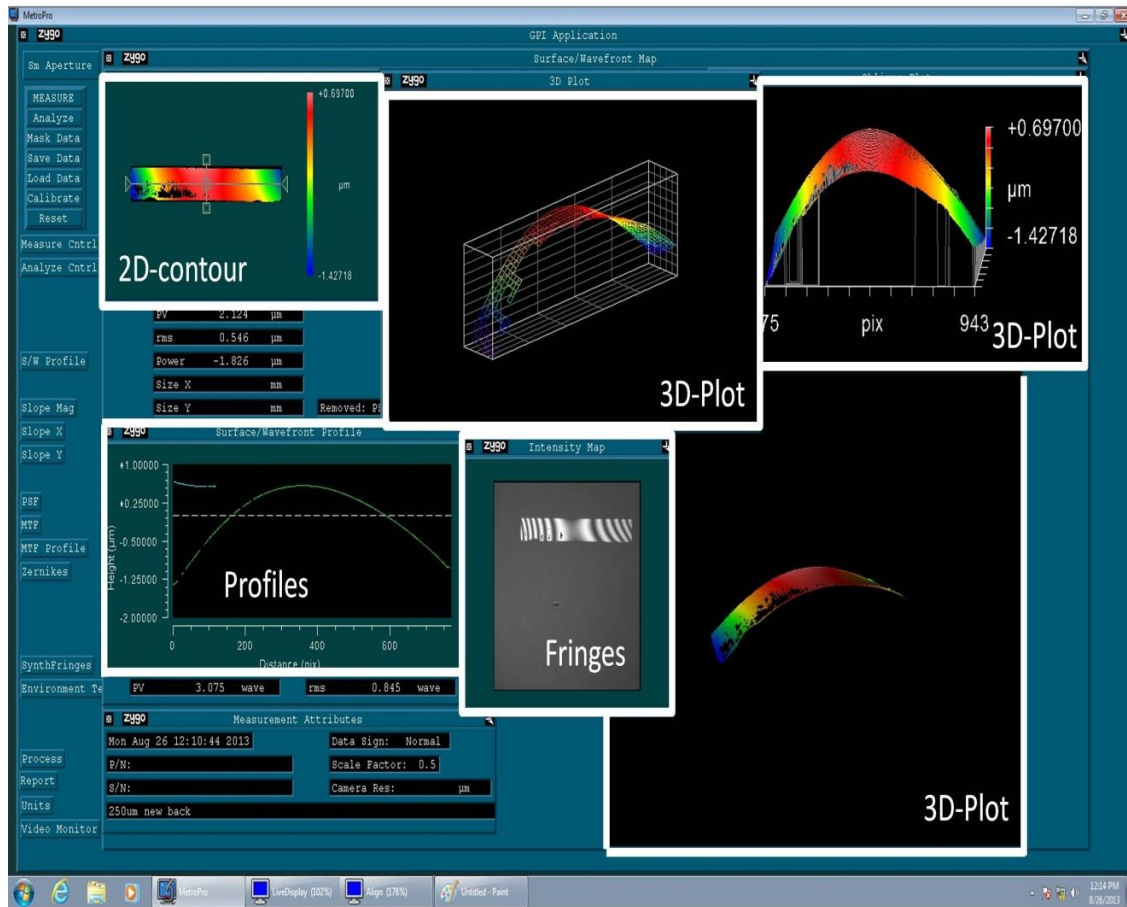


Figure 4.13 The surface topography of a silicon strip as seen by the Zygo interferometer and analyzed by MetroPro® software.

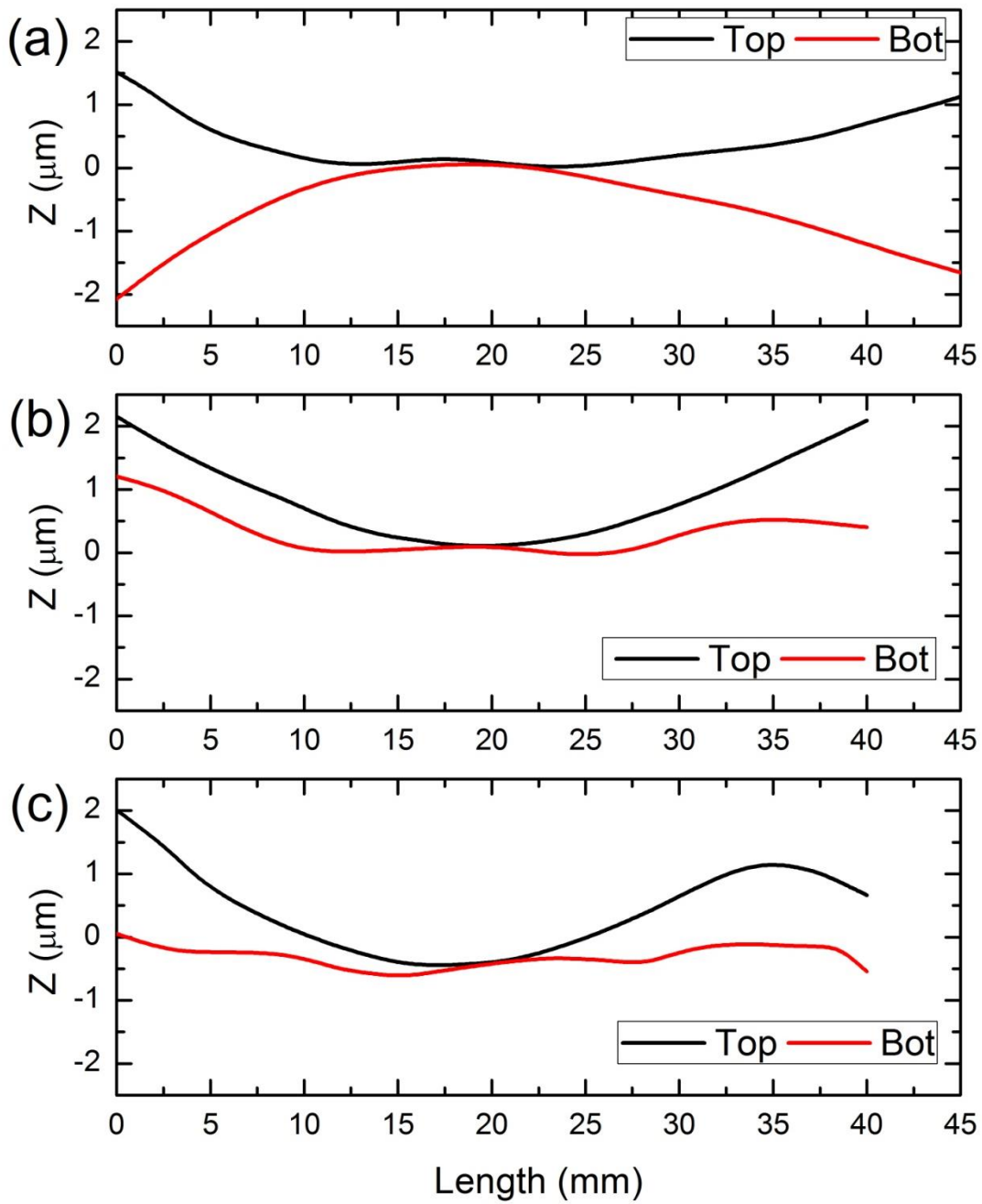


Figure 4.14 A series of bonding surface profiles for three pairs of silicon strips. (a) Case A-1 in Figure 4.8, (b) Case B-4 in Figure 4.8 and (c) Case B-5 in Figure 4.8.



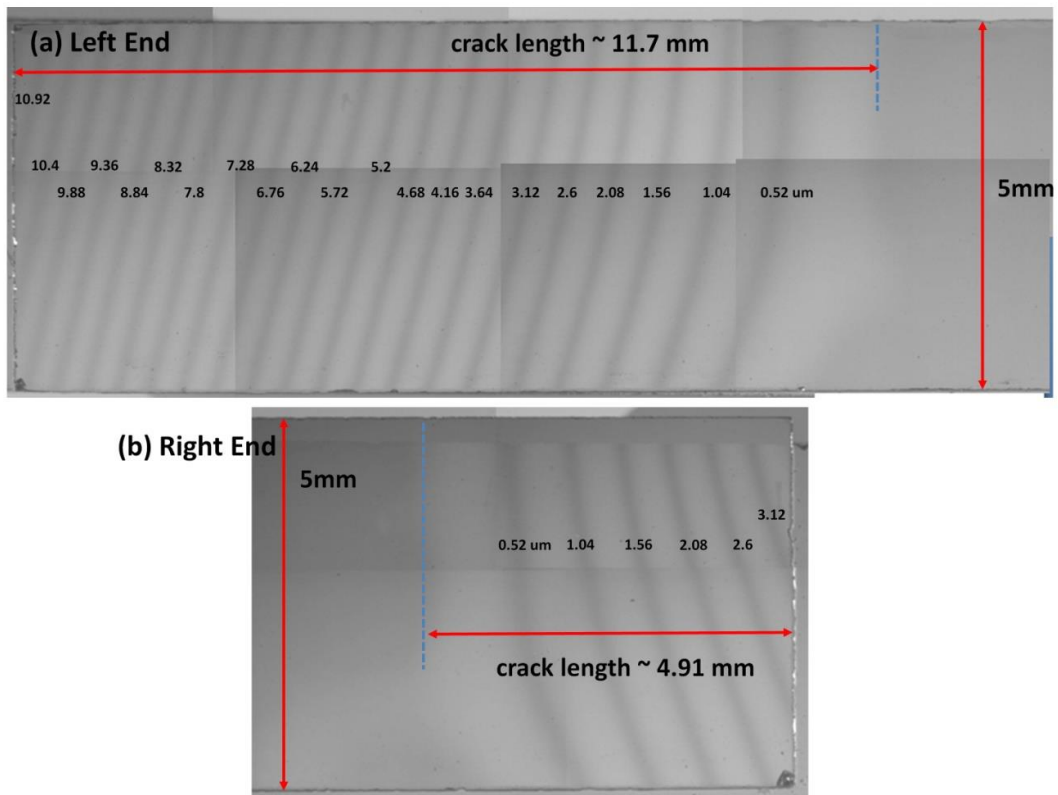


Figure 4.15 Opening displacements at the left and right ends after two silicon strips (Fig. 4.14a) were bonded. Open cracks at the (a) left and (b) right ends.

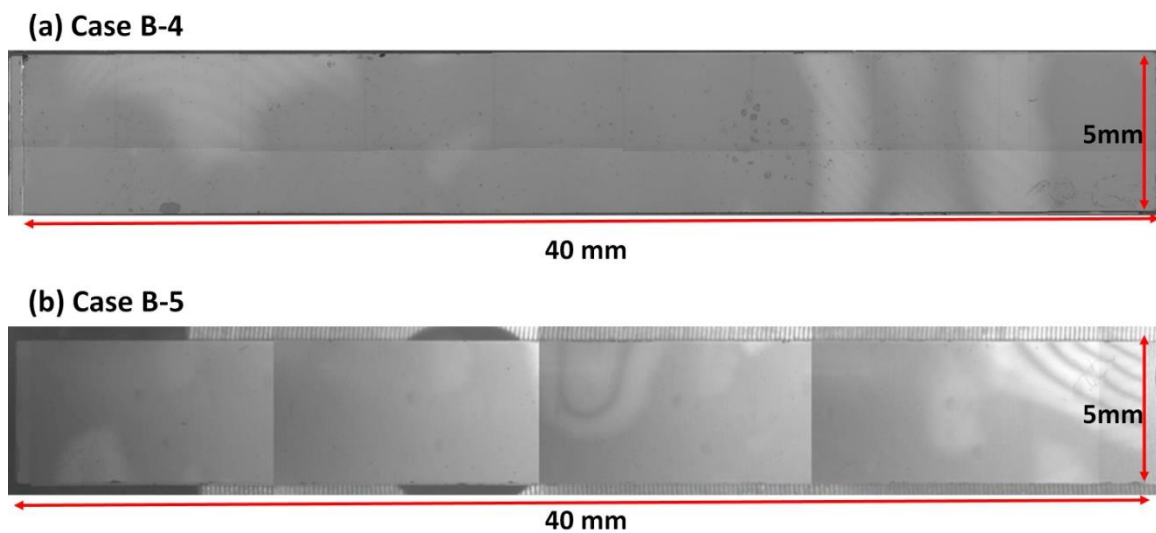


Figure 4.16 IR-COI images of bonded samples. (a) Case B-4, (b) Case B-5.

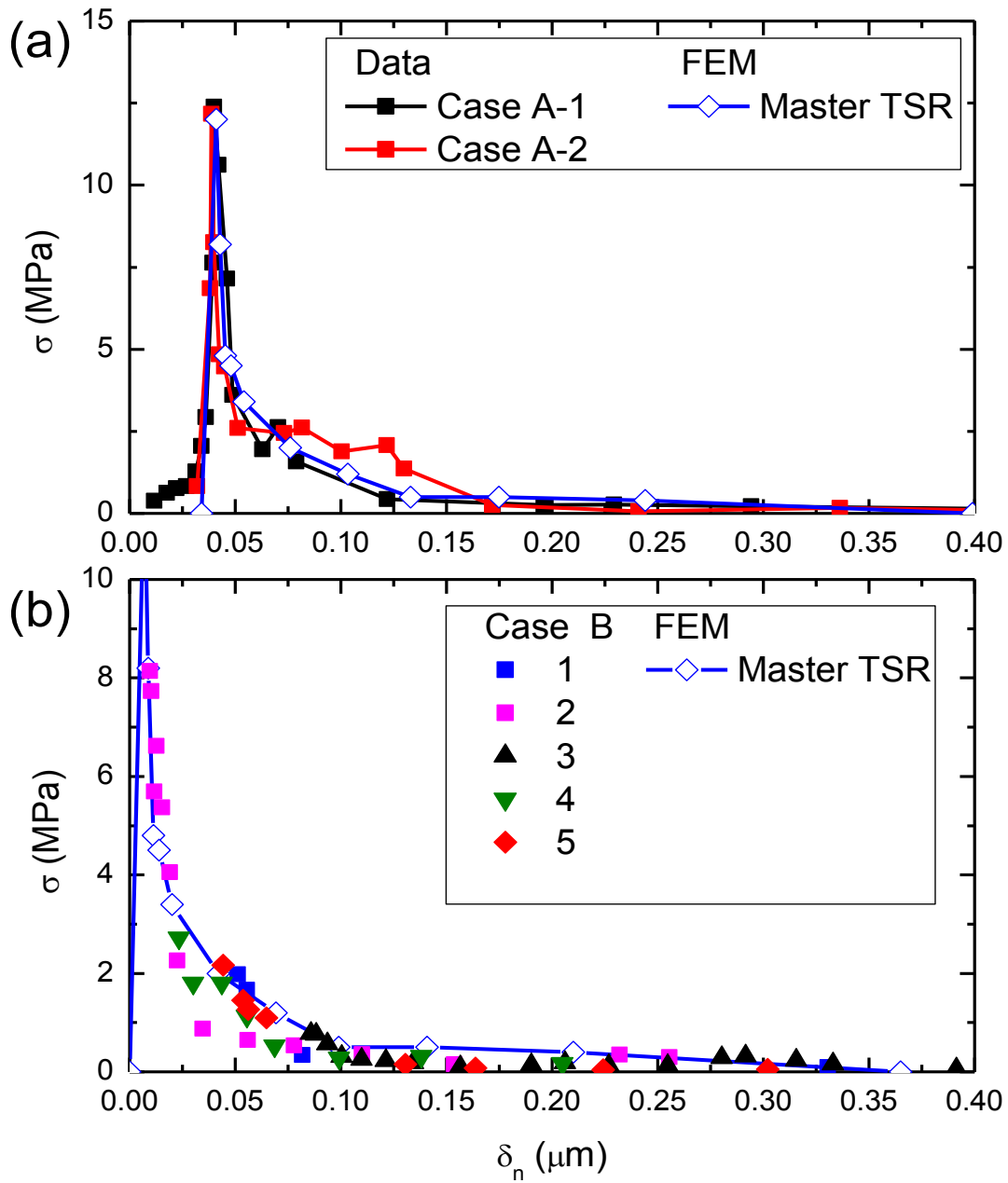


Figure 4.17 Comparison of the master traction-separation relation that was used in the finite element analyses and the data obtained from all specimens.

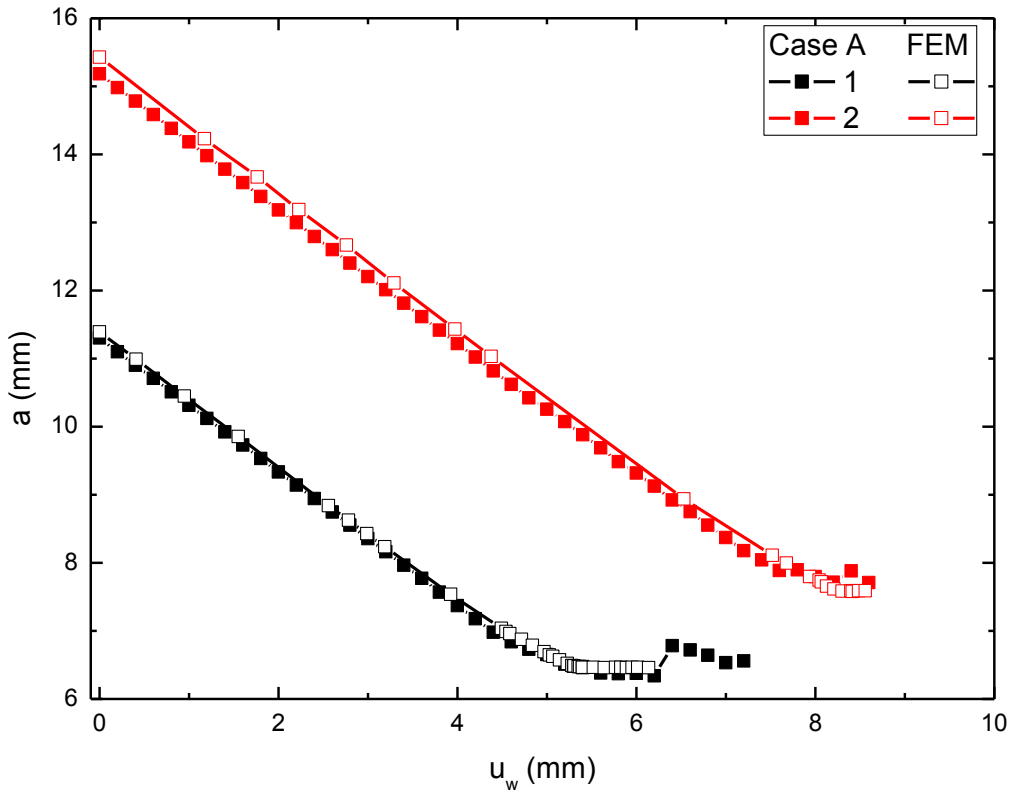


Figure 4.18 Predicting, based on the master traction-separation relation, the variation of the crack length with respect to wedge insertion for the well-bonded samples.

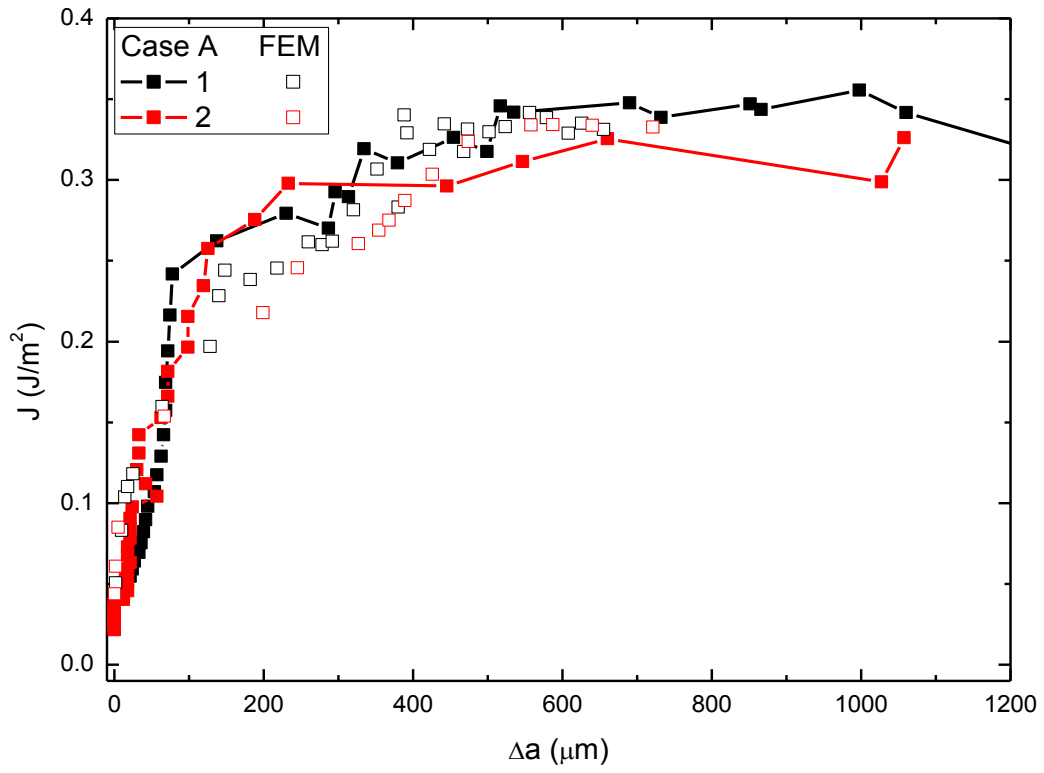


Figure 4.19 Comparing the predicted resistance curves based on the master traction-separation relation with the measured ones for well-bonded samples.

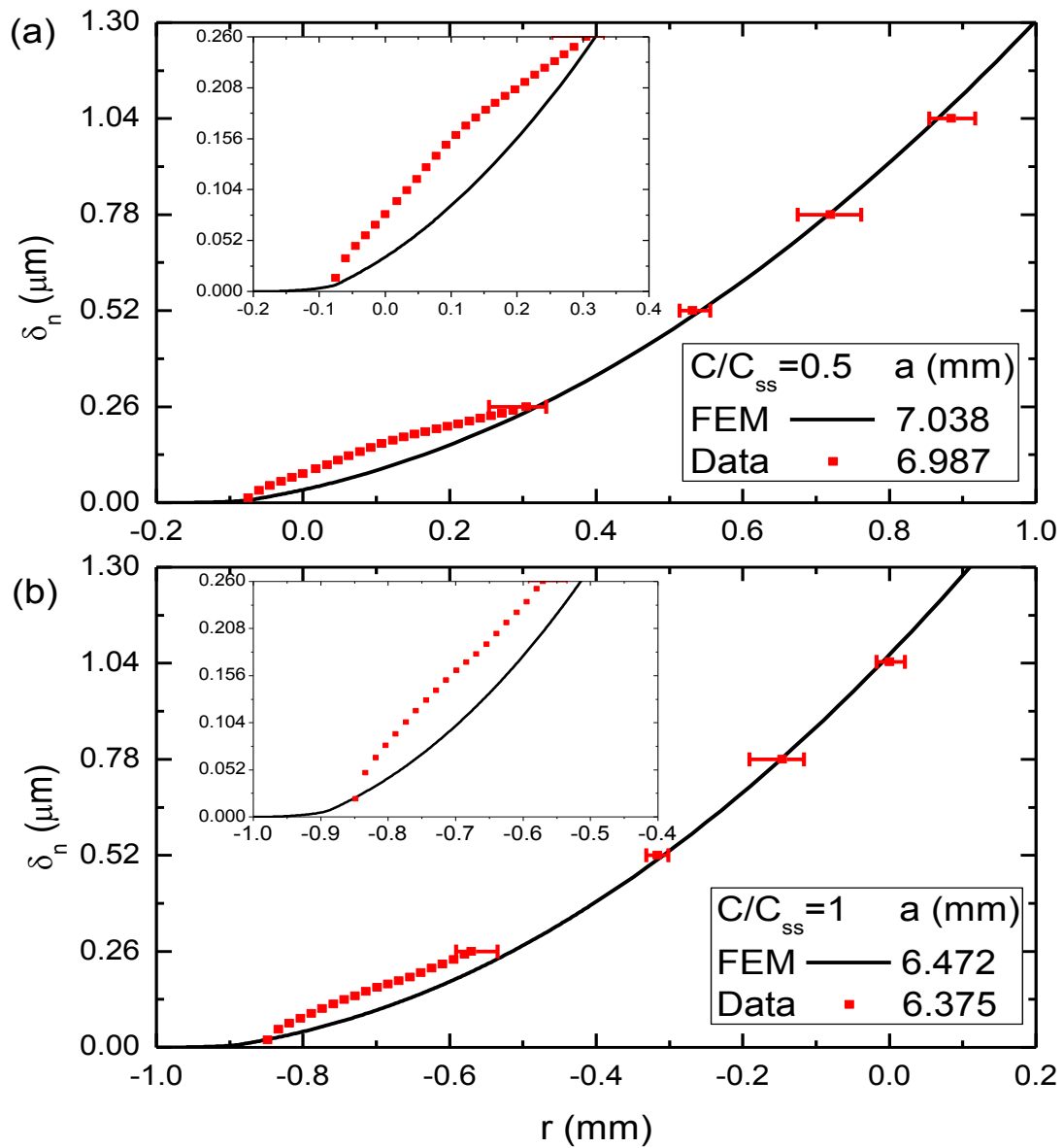


Figure 4.20 Comparing the predicted and measured NCOD profiles for well-bonded samples. (a) Prior to steady-state growth ( $a = 6.987$  mm) and (b) at steady-state ( $a = 6.375$  mm) based on the master traction-separation relation.

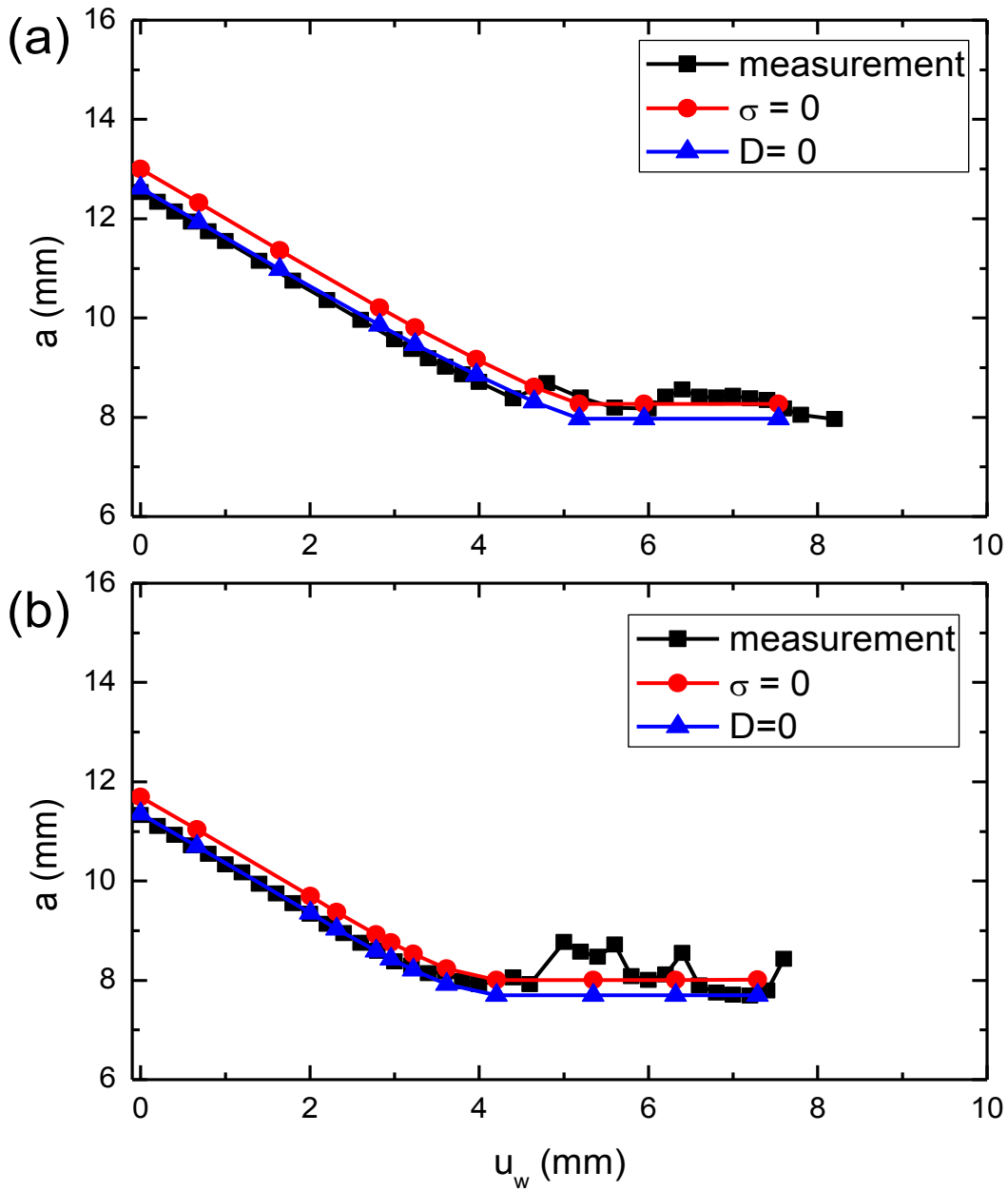


Figure 4.21 Predicting, based on the damaged master traction-separation relation, the variation of the crack length with respect to wedge insertion for (a) case B-4 and (b) case B-5.

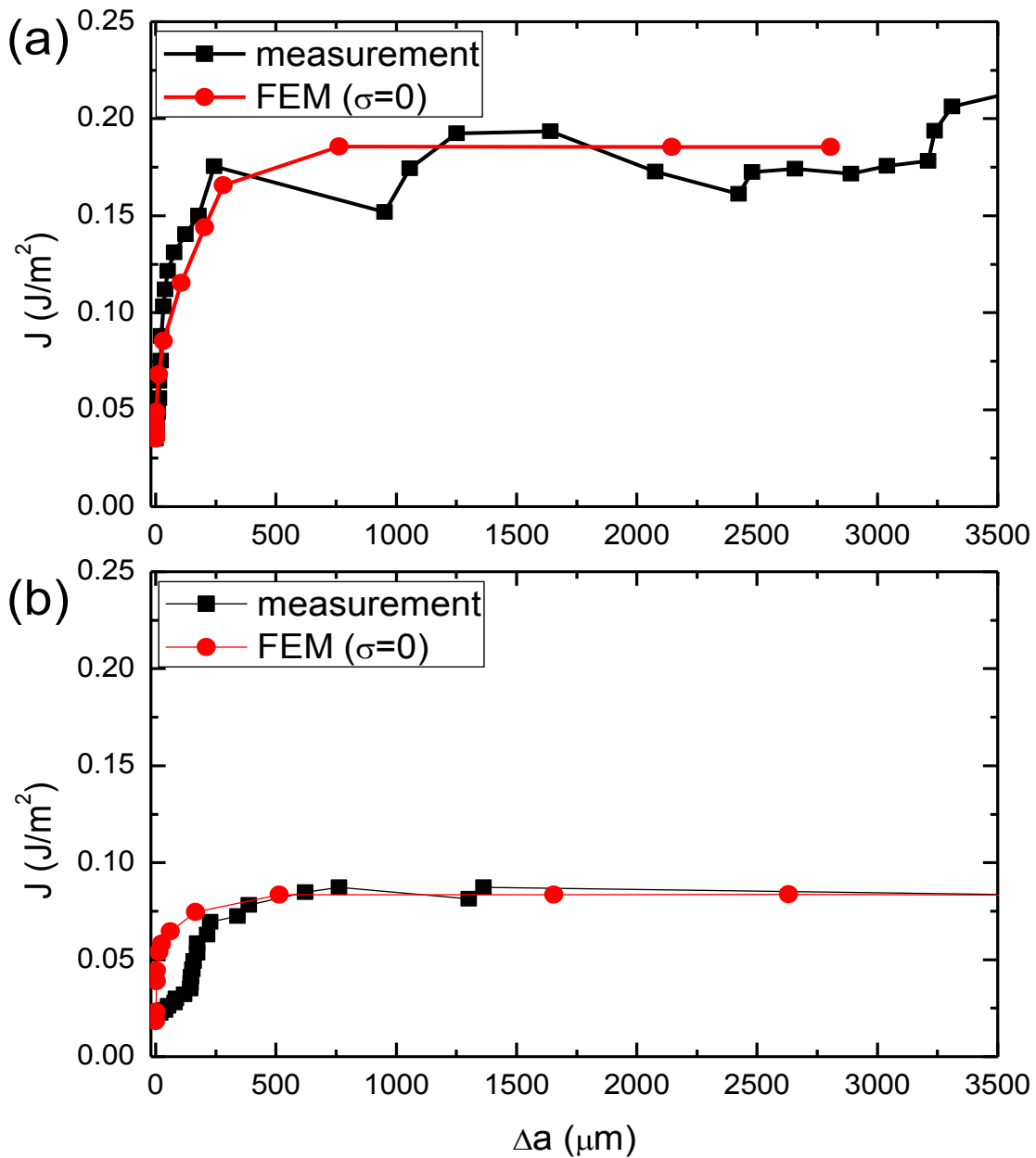


Figure 4.22 Comparing the predicted resistance curves based on the damaged master traction-separation relation with the measured ones for (a) case B-4 and (b) case B-5.

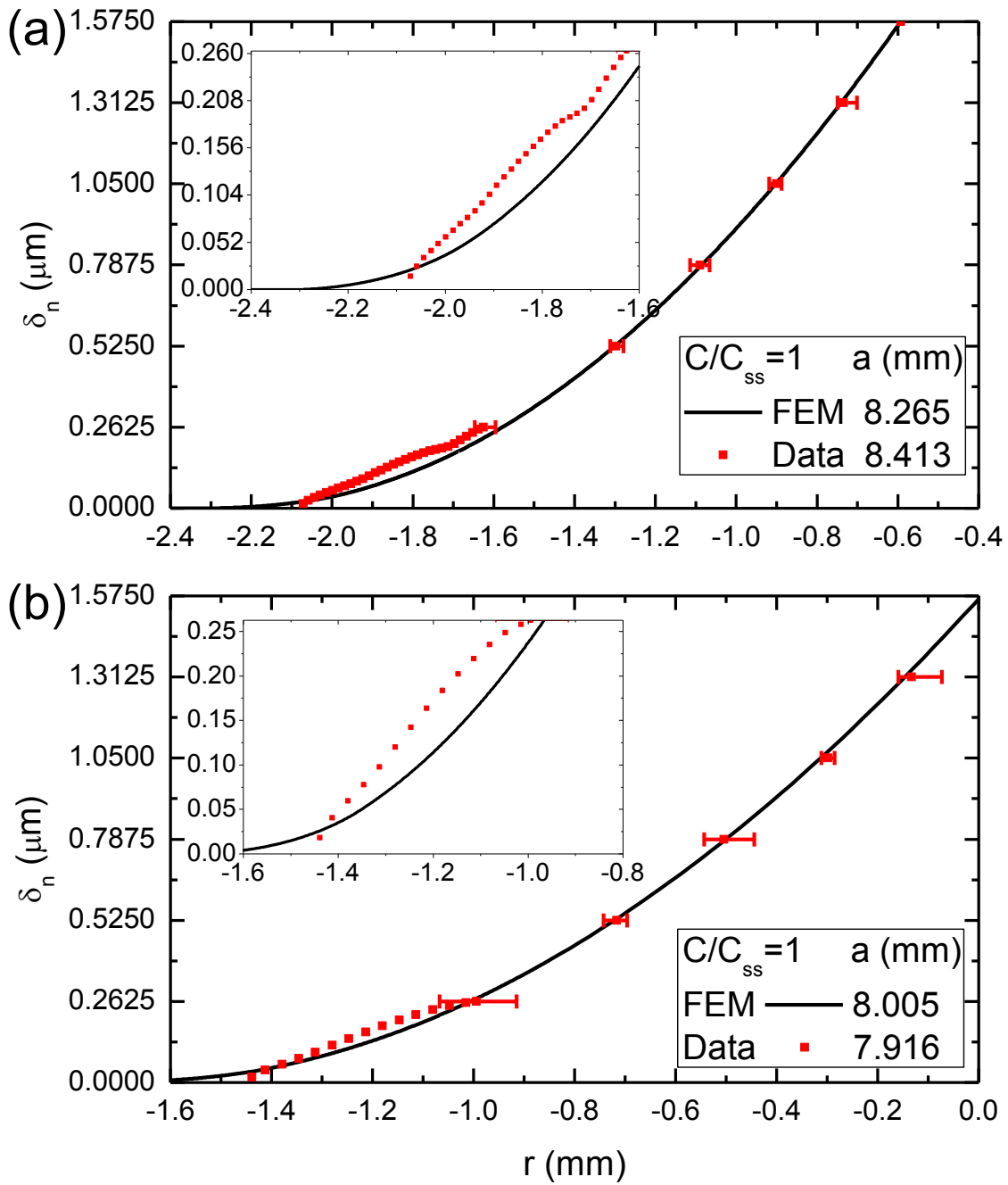


Figure 4.23 Comparing the predicted and measured NCOD profiles for (a) case B-4 and (b) case B-5, based on damaged master traction-separation relations.



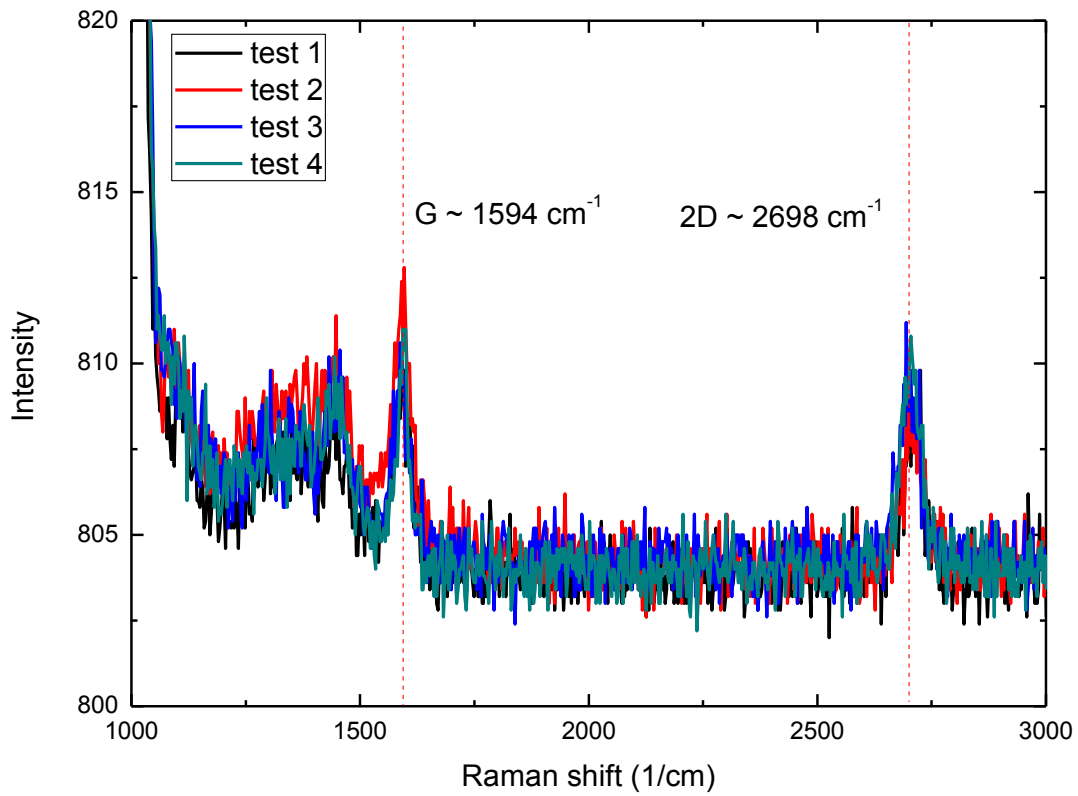


Figure 5.1 Raman spectra of graphene that had been wet-transferred to a Si(111) surface. The presence of the G and 2D-bands clearly indicates that graphene was successfully transferred to silicon.

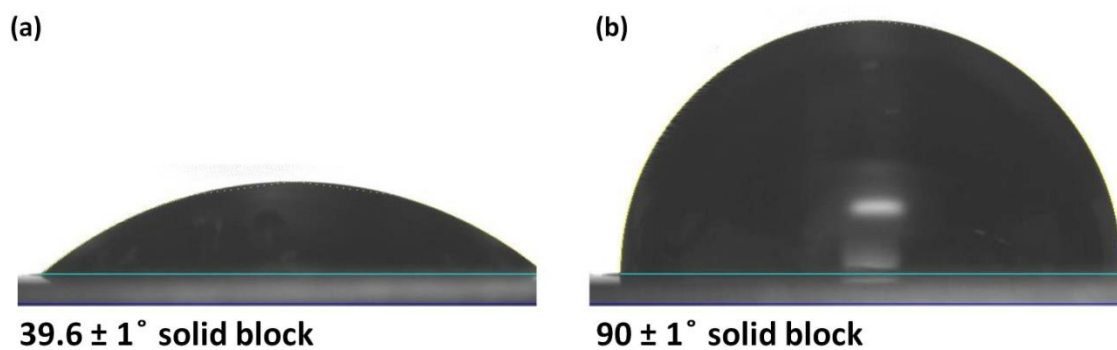


Figure 5.2 Calibration of the contact angle measuring system with calibration blocks of (a)  $39.6 \pm 1^\circ$  and (b)  $90 \pm 1^\circ$ . The respective measured values were  $39.9 \pm 0.25^\circ$  and  $90.1 \pm 0.6^\circ$ .

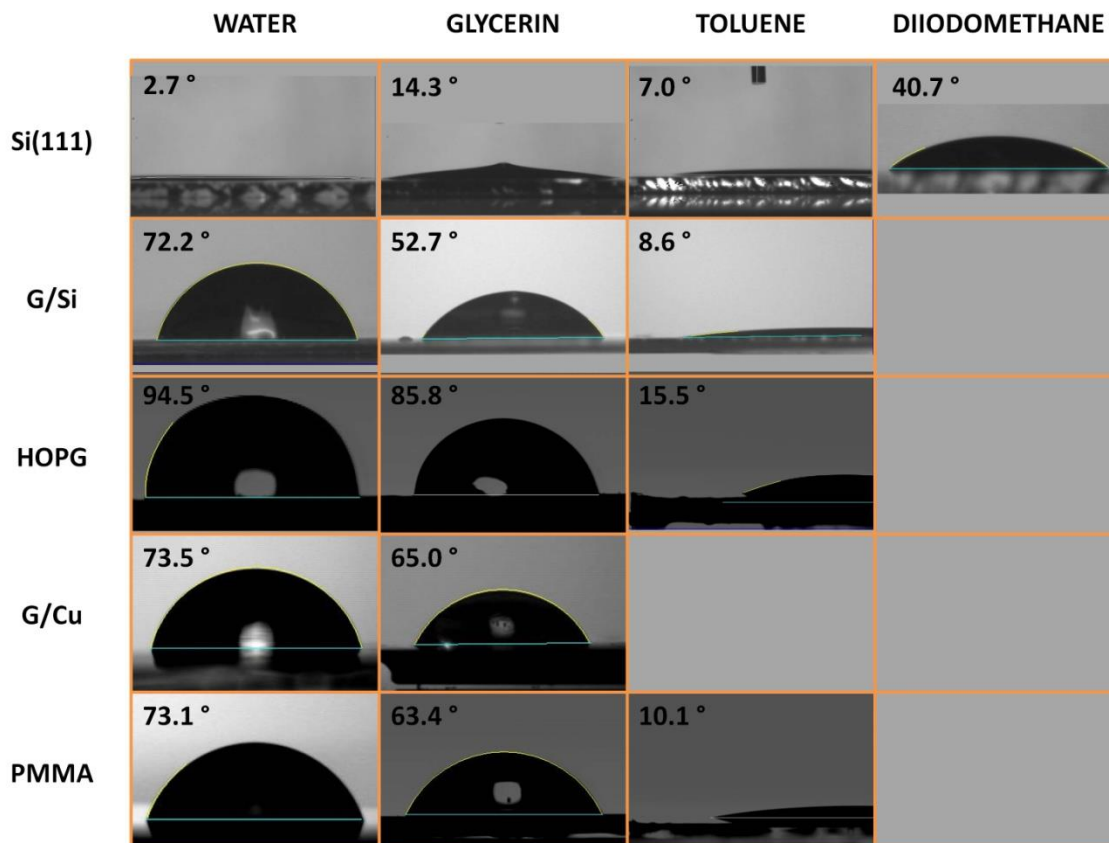


Figure 5.3 Contact angle measurements using four different liquids on Si(111) substrates, graphene on silicon, HOPG, graphene/ on copper and PMMA on silicon.

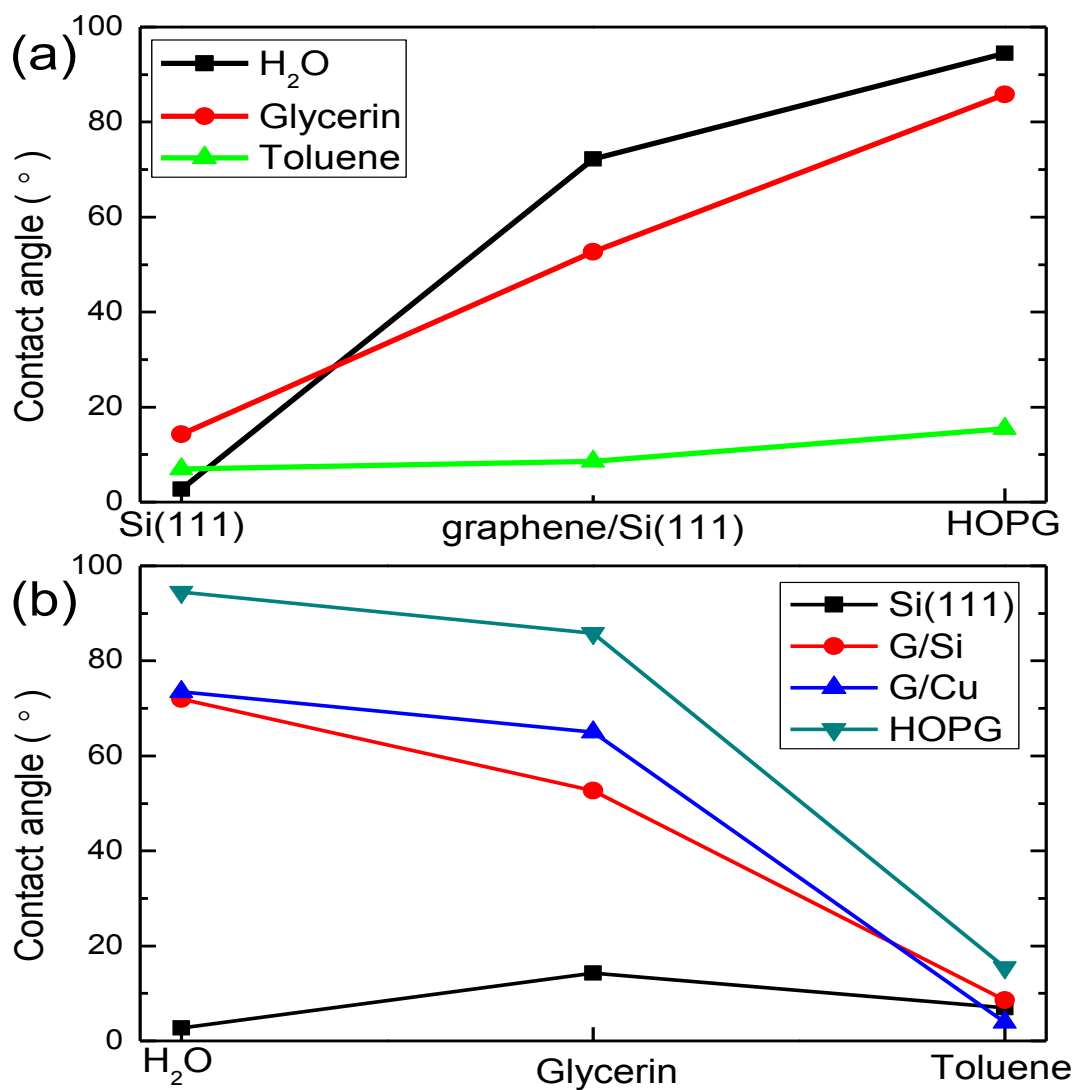


Figure 5.4 The variation of the contact angle with (a) the number of graphene layers and probe liquid and (b) the liquid and several substrates.

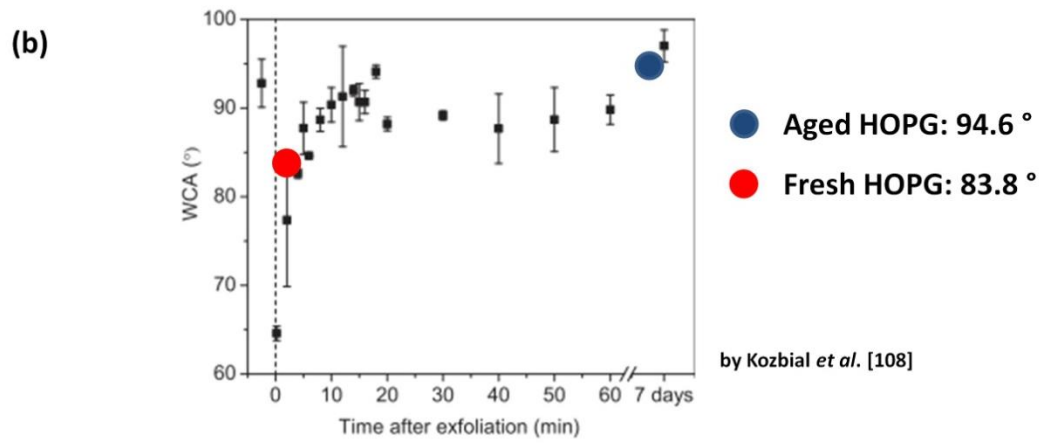
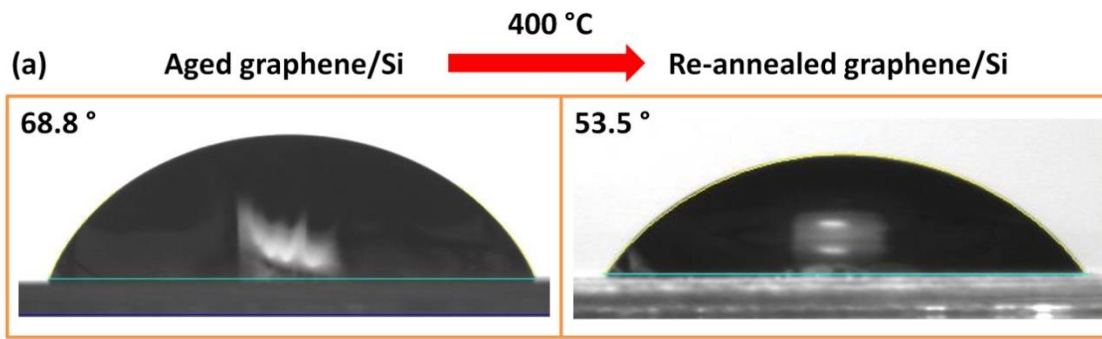


Figure 5.5 Variation of the contact angle associated with surface aging of (a) graphene on silicon and (b) HOPG [197].

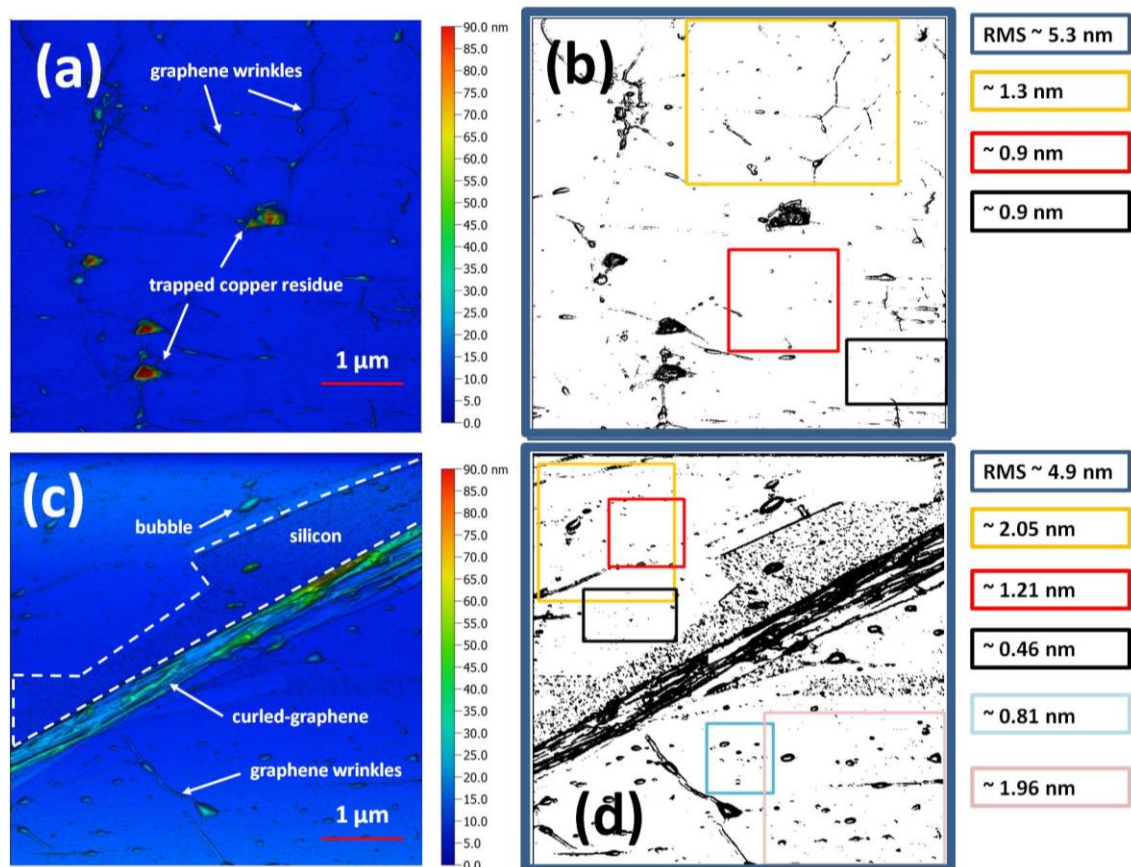


Figure 6.1 AFM scanning of wet-transferred graphene on silicon: (a) The topography of wet-transferred graphene on silicon, (b) measurements of the RMS roughness over various regions, (c) the topography of torn, wet-transferred graphene on silicon and (d) measurements of the RMS roughness over various regions.

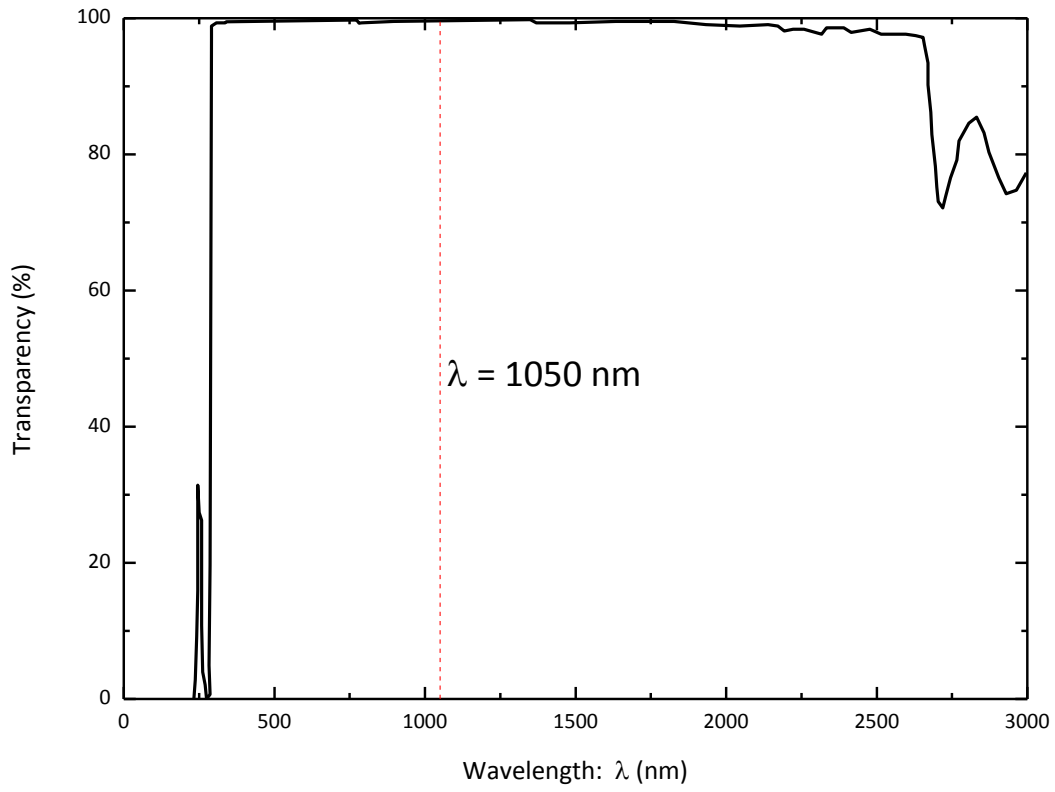


Figure 6.2 Optical transparency of the epoxy (EP30 from Master Bond Inc) particularly at 1050 nm.

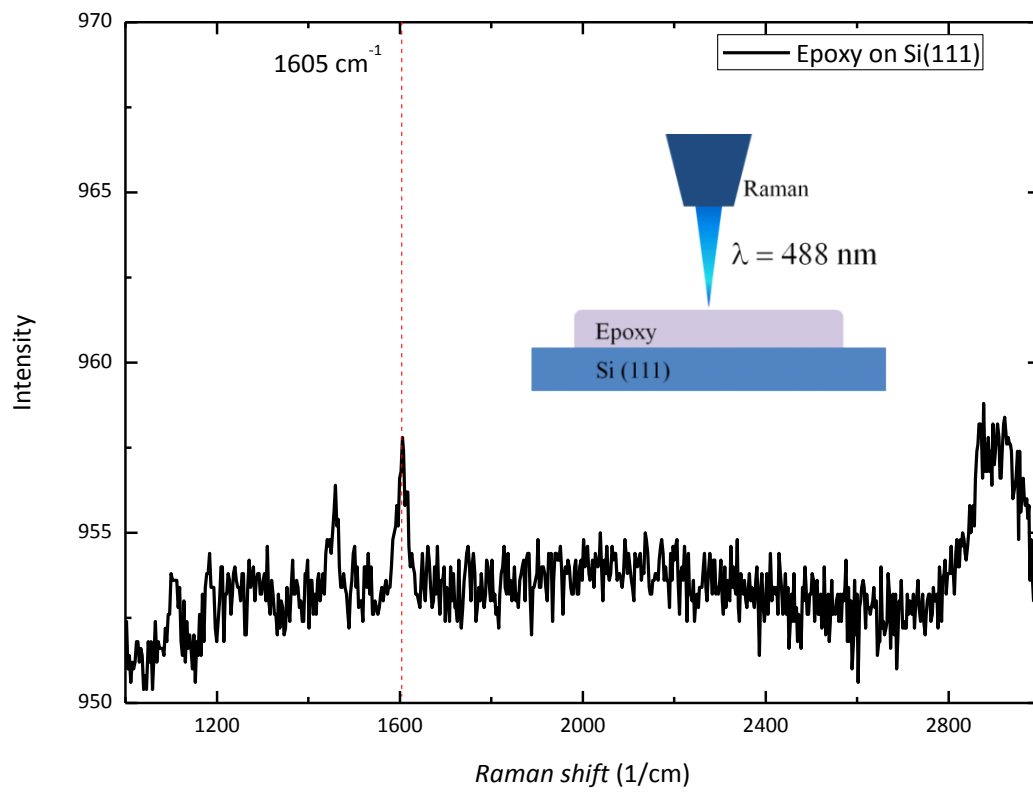


Figure 6.3 Raman spectrum of epoxy on silicon. This epoxy has a peak at  $1605 \text{ cm}^{-1}$ , which is close to the G band of the graphene.

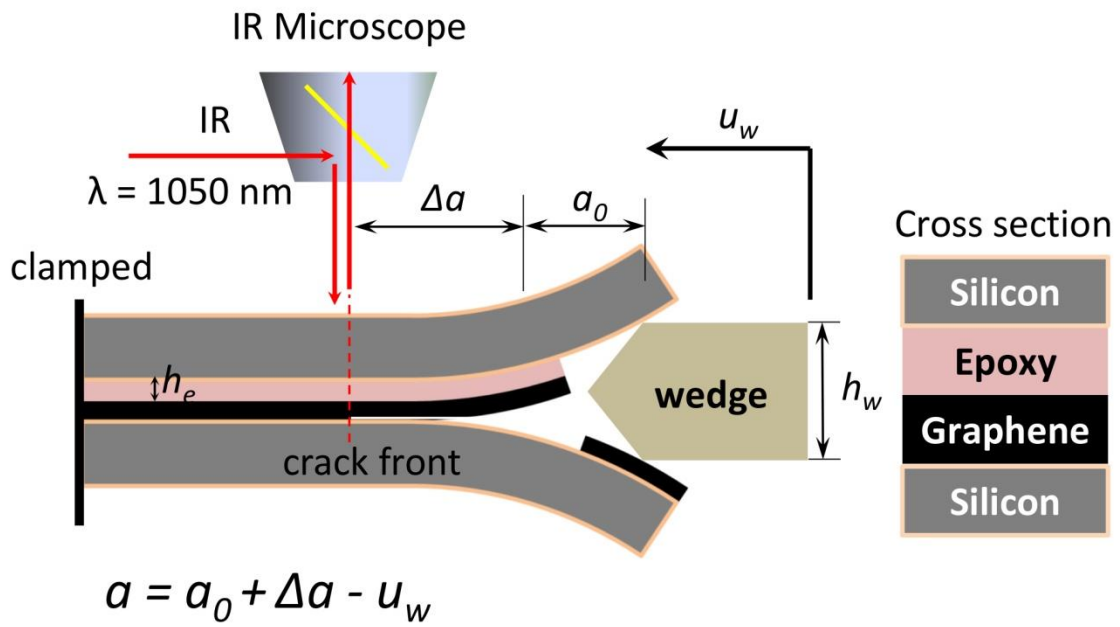


Figure 6.4 Infra-red crack opening interferometry in the fracture experiments.



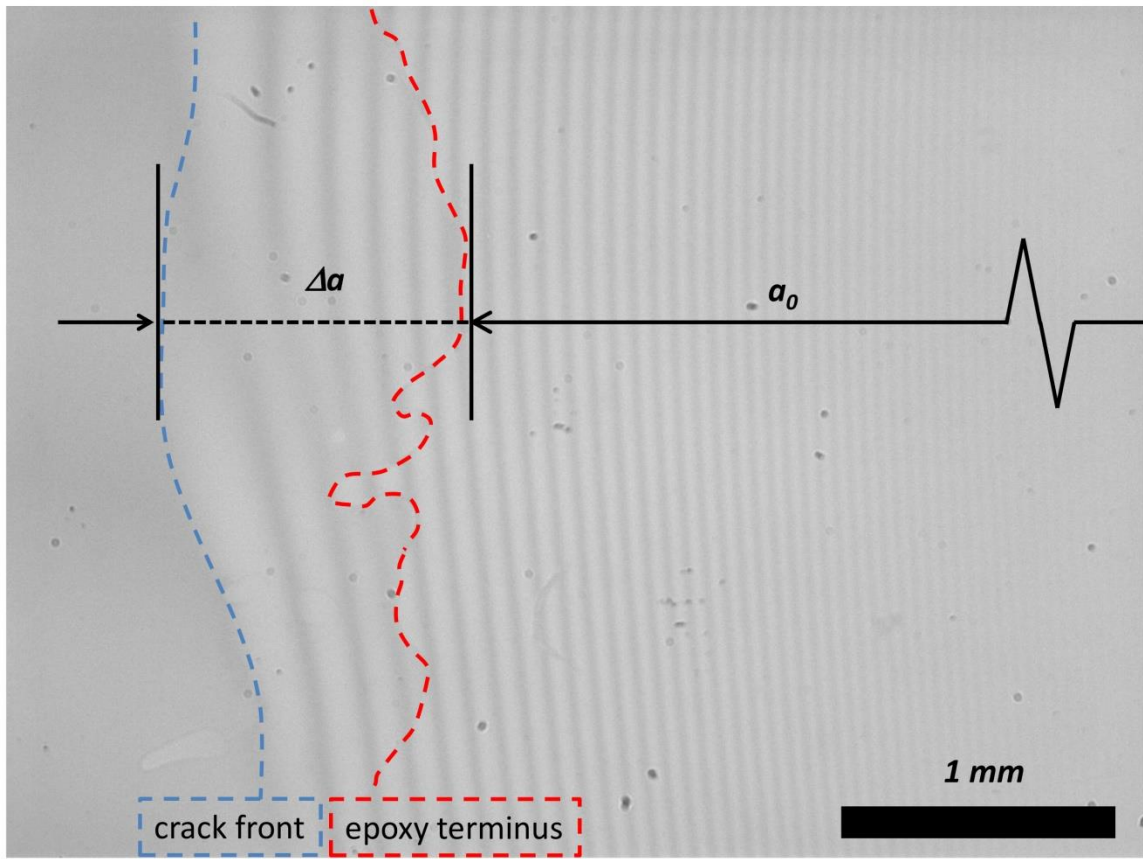


Figure 6.5 Defining the crack front and crack face separation from fringe patterns.

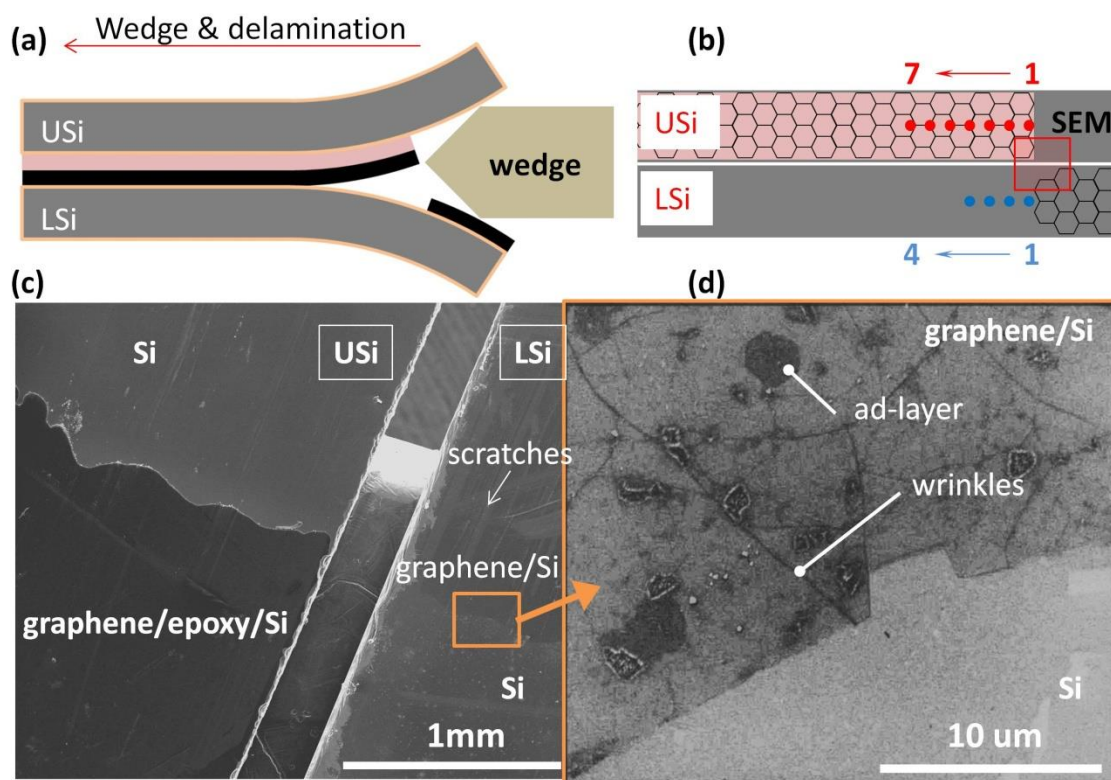


Figure 6.6 Characterization of the fracture surfaces: (a) Edge view schematic of graphene delamination from the lower silicon strip, (b) plan view schematic of the fracture surfaces of both silicon strips after complete separation, (c) low magnification SEM image of the fracture surfaces of both silicon strips, and (d) high magnification SEM image of the fracture surface of the lower silicon strip.

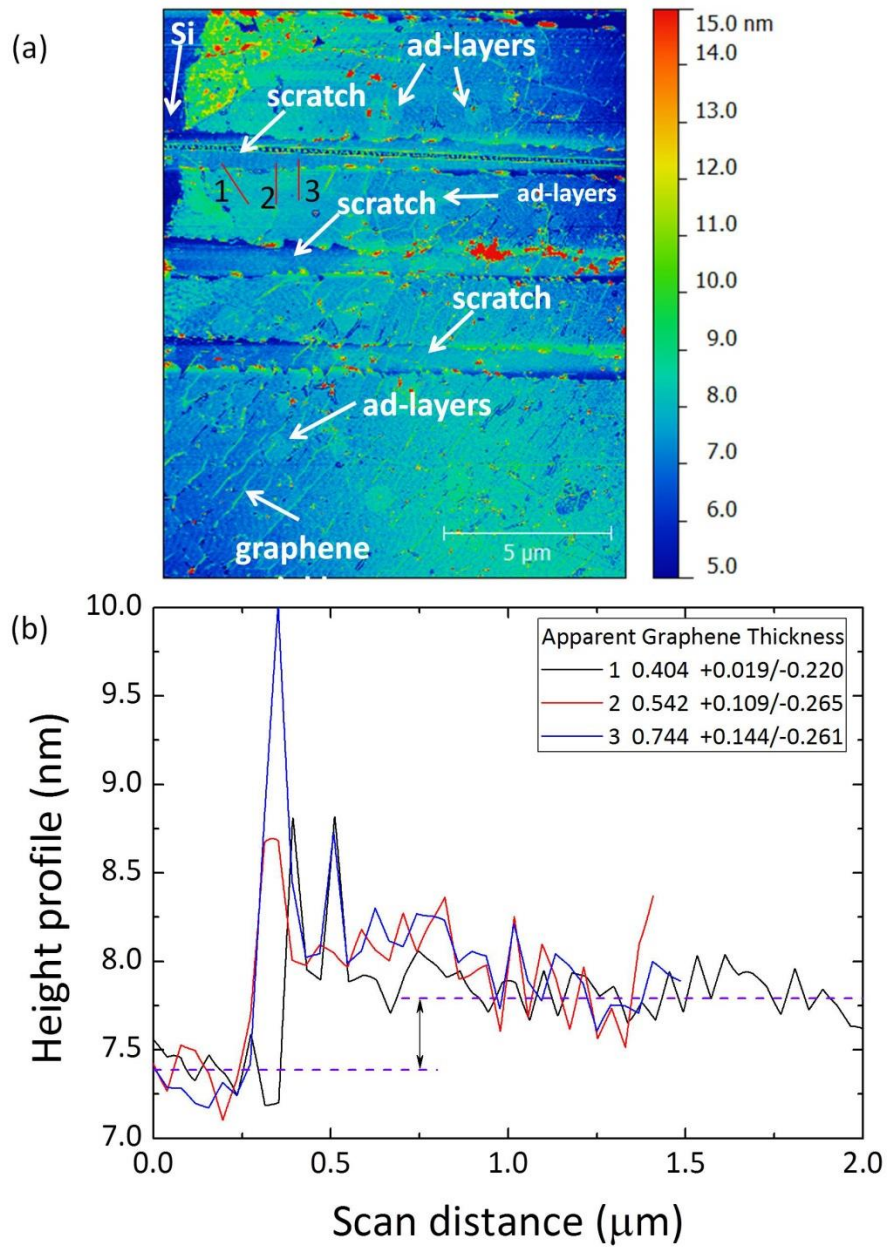


Figure 6.7 Scratches in graphene due to wedge insertion: (a) AFM topology images of graphene on Si(111) in the region where the wedge was inserted and (b) height variations of graphene on Si(111); nominal values are listed in the legend.

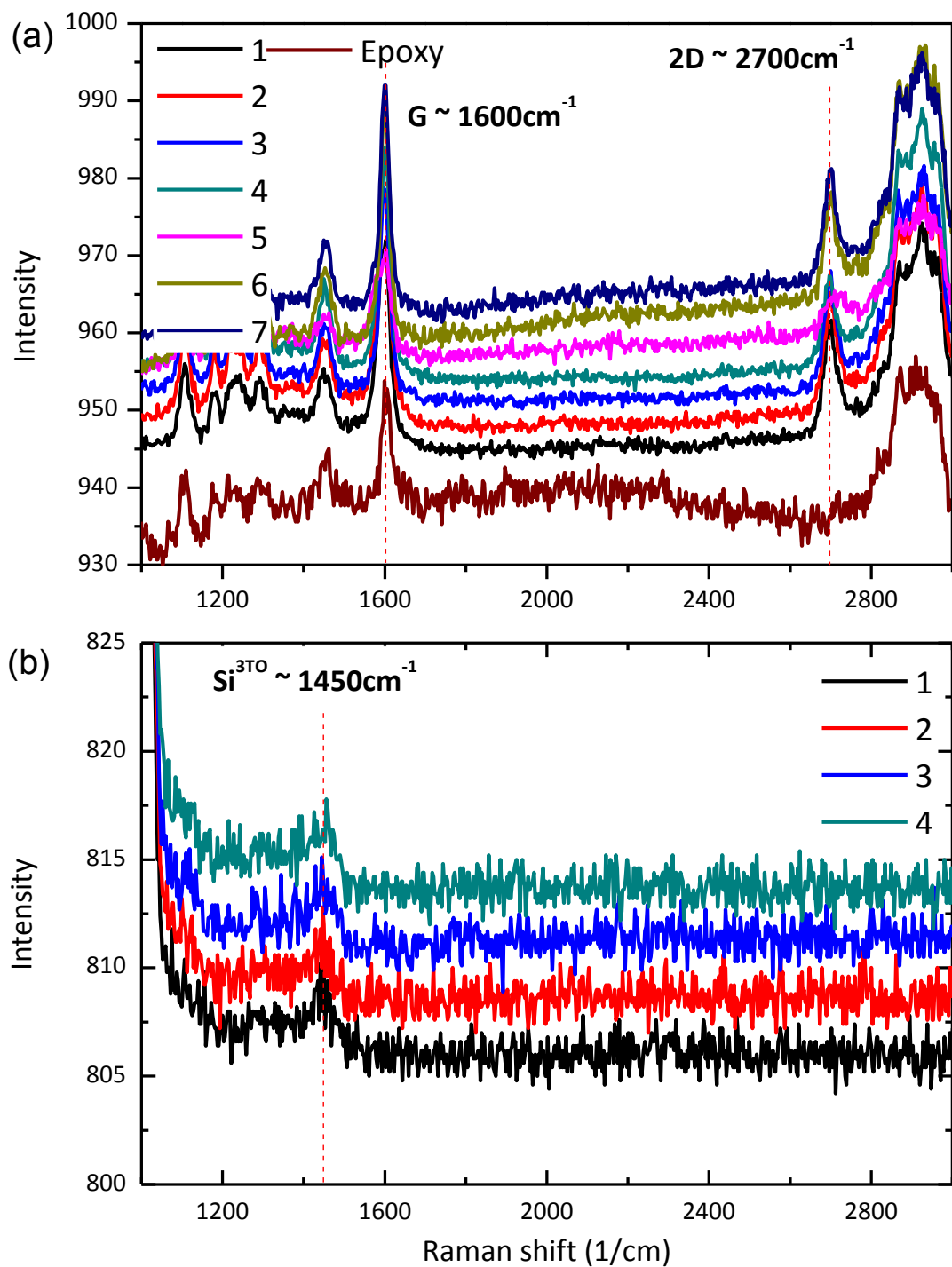


Figure 6.8 (c) and (d) continued on next page

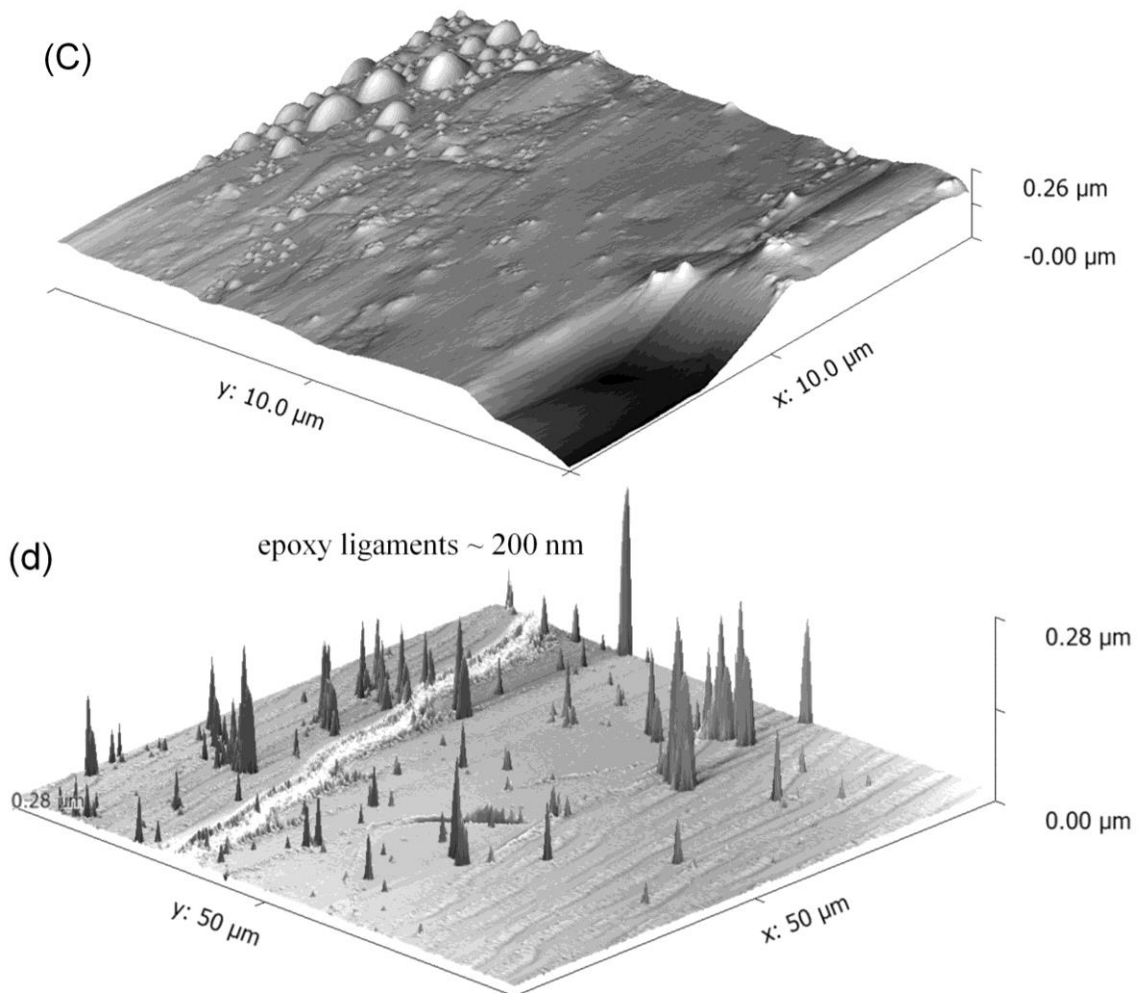


Figure 6.8 Characterization of the fracture surfaces: (a) Raman spectra of the fracture surface of the upper silicon strip at 7 different spots. (b) Raman spectra of the fracture surface of the lower silicon strip at 4 different spots. (c) Micro bubbles between graphene and epoxy on a  $10\ \mu\text{m}$  by  $10\ \mu\text{m}$  AFM scan of the fracture surface of the upper silicon strip. (d) Epoxy ligaments on a  $50\ \mu\text{m}$  by  $50\ \mu\text{m}$  AFM scan of the epoxy fracture surface of a silicon/epoxy/silicon specimen with no graphene.

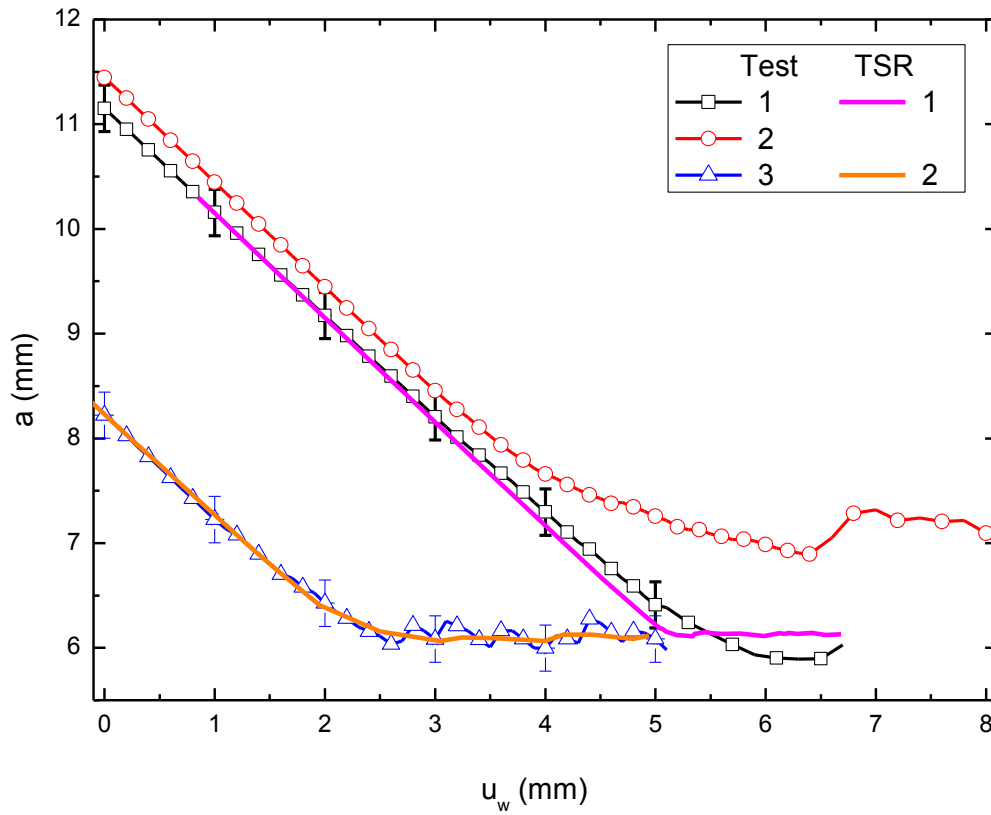


Figure 6.9 Variation of crack length with respect to wedge insertion. The initially linear response indicates that the crack was not growing as the wedge was inserted. Subsequent crack extension soon transitioned to steady state growth where each wedge insertion step produced the same amount of growth. Finite element solutions are shown as TSR1 and TSR2 as simulations of both tests 1 and 2 and test 3, respectively.

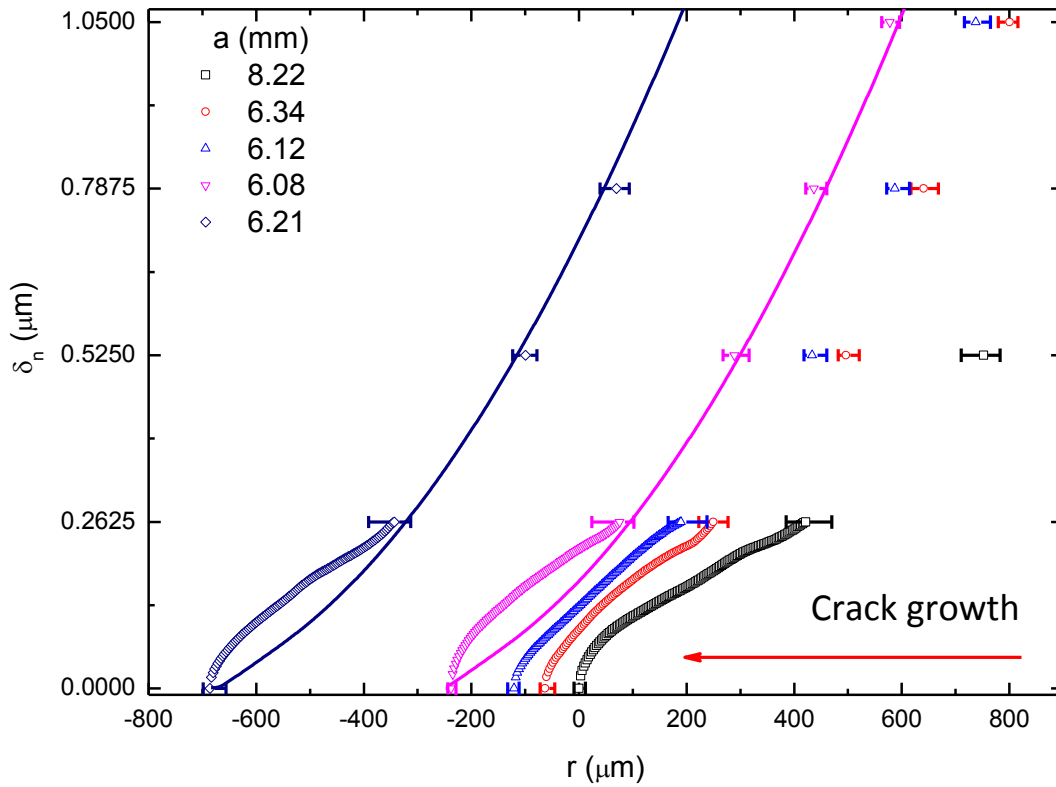


Figure 6.10 Crack face separation during crack opening and growth. NCOD profiles obtained by IR-COI as a function of crack length  $a$  as the wedge insertion progressed during test 3. Finite element solutions are shown as TSR2 for two steady state growth conditions.

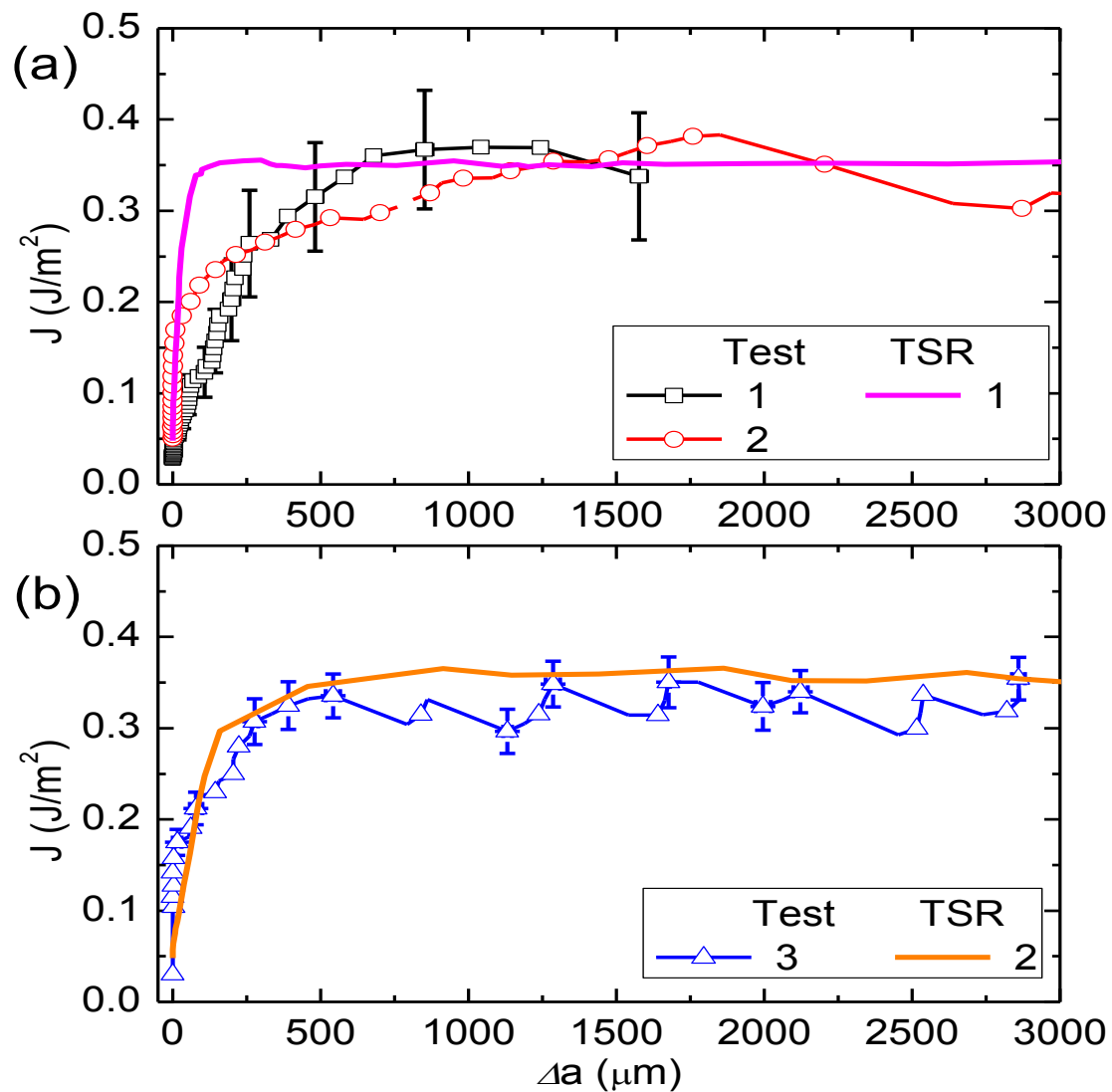


Figure 6.11 Delamination resistance behavior for graphene/silicon interactions. The resistance to fracture as represented by the  $J$ -integral initially rose steeply with small amounts of crack extension  $\Delta a$ . The resistance to crack growth eventually stabilized at the steady state toughness  $\Gamma_{ss}$  of the graphene/silicon interface. (a) Comparison of the resistance response with respect to data from tests 1 and 2 and a finite element solution using TSR 1. (b) Comparison of the resistance response with respect to data from test 3 with a finite element solution using TSR 2.



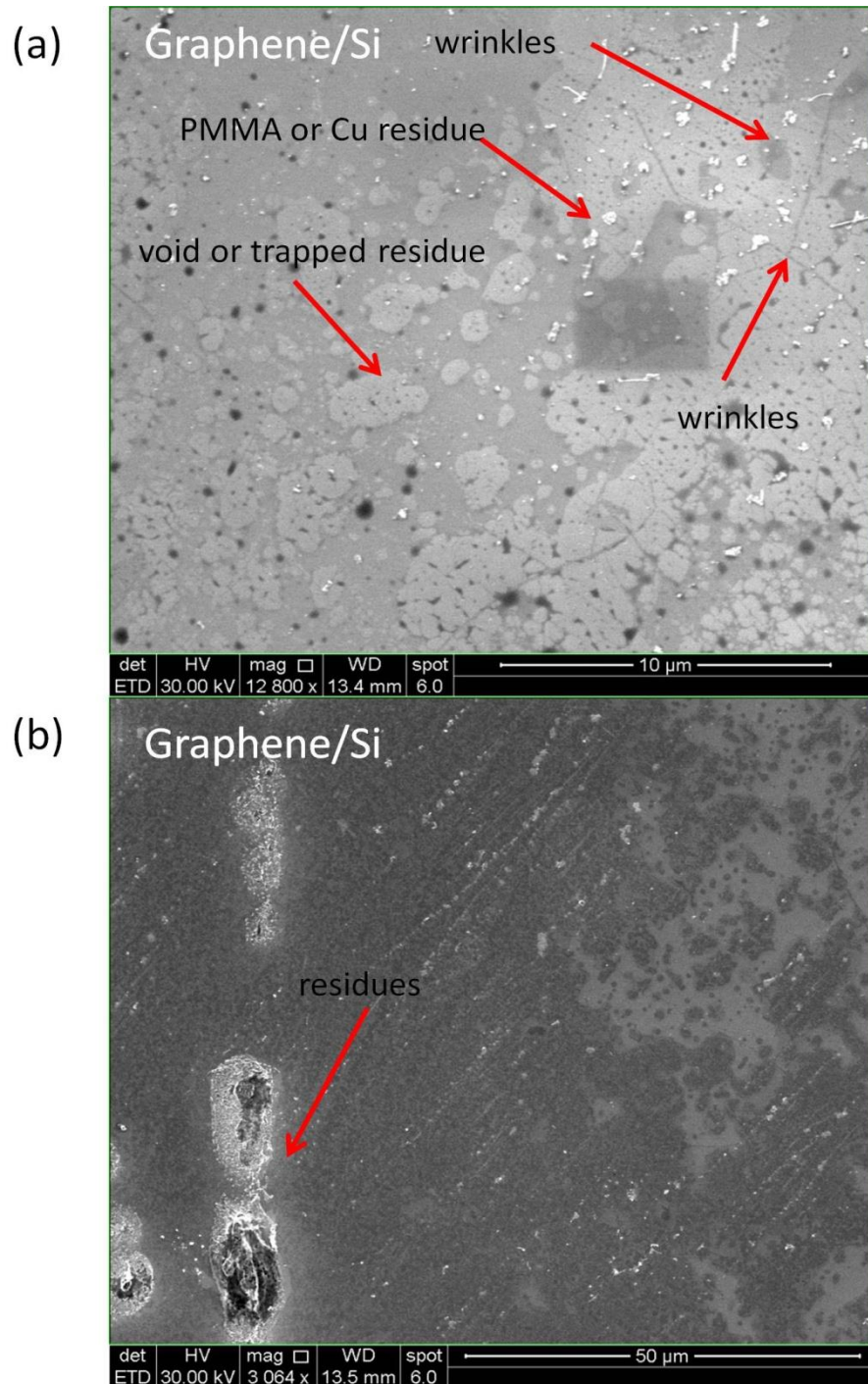


Figure 6.12 High-resolution SEM images of wet-transferred graphene on Si(111): (a) Wrinkles, trapped residues and PMMA or copper residues and (b) other residues and non-uniform transfer of graphene.

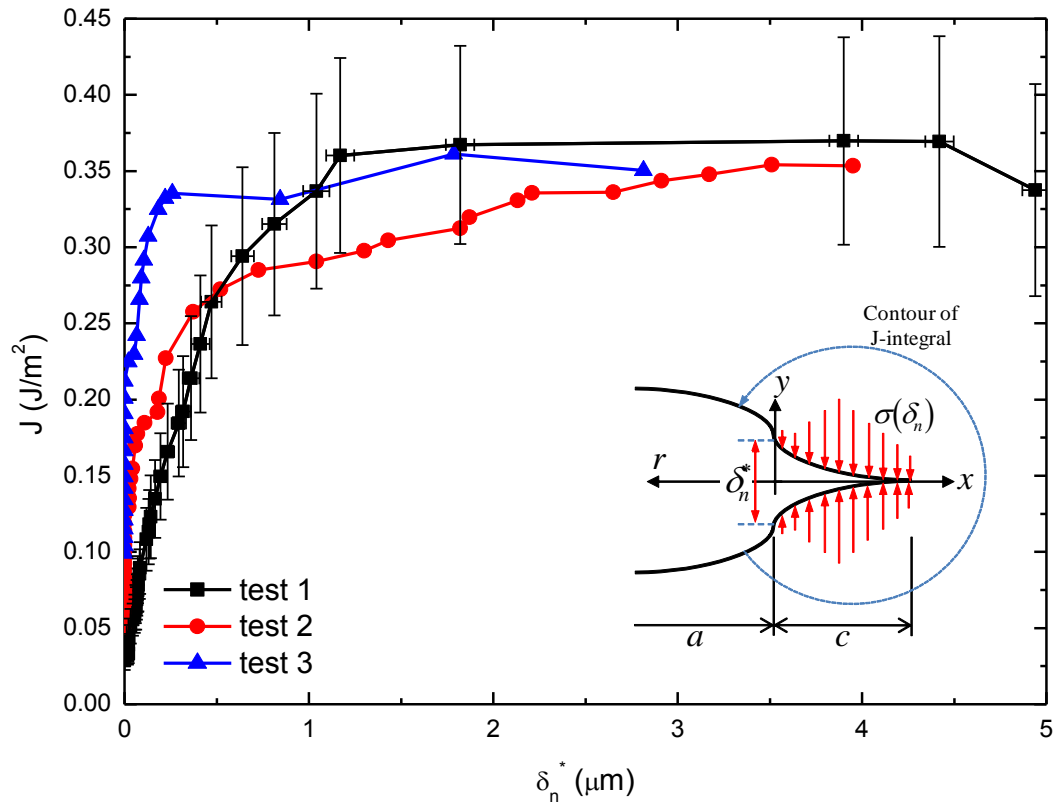


Figure 6.13 The variation of the J-integral with respect to the end opening displacement  $\delta_n^*$  (the inset defines the cohesive zone geometry and interactions).

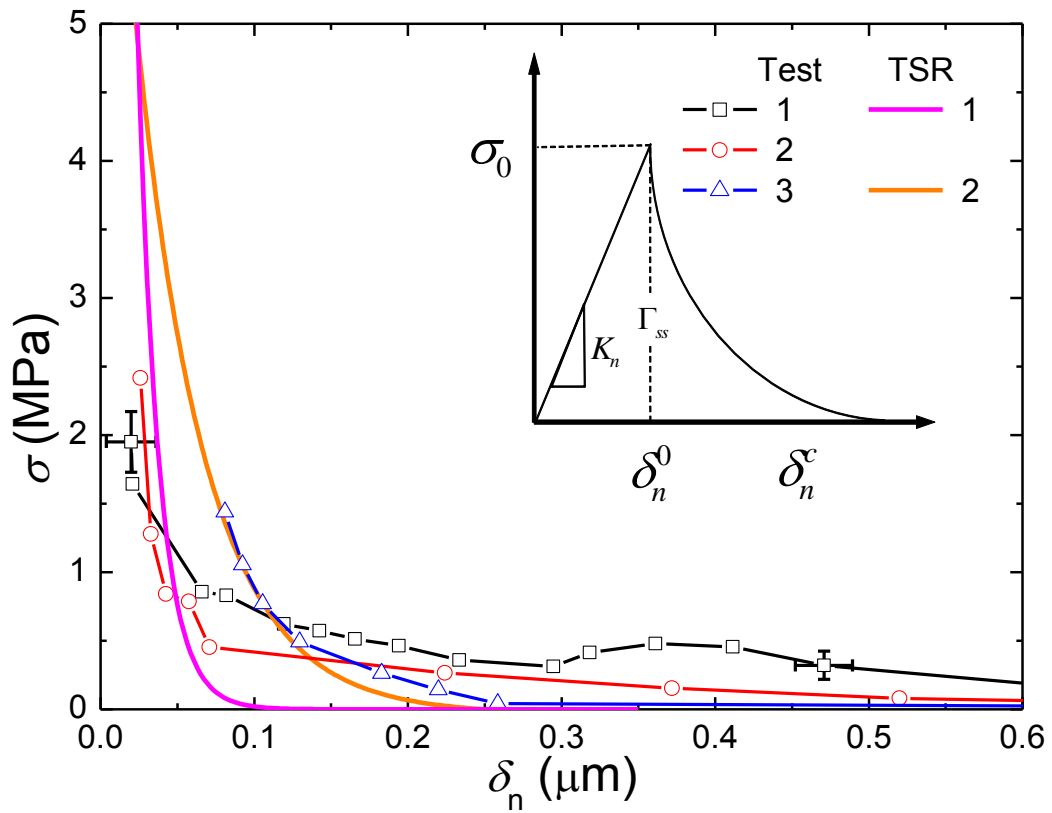


Figure 6.14 The traction-separation relations between wet-transferred graphene and silicon (the sketch identifies a typical shape of the traction-separation relation whose parameters are listed in Table 6.1). Traction-separation relations TSR1 and TSR2 were used in the finite element analyses of tests 1 & 2 and test3, respectively.

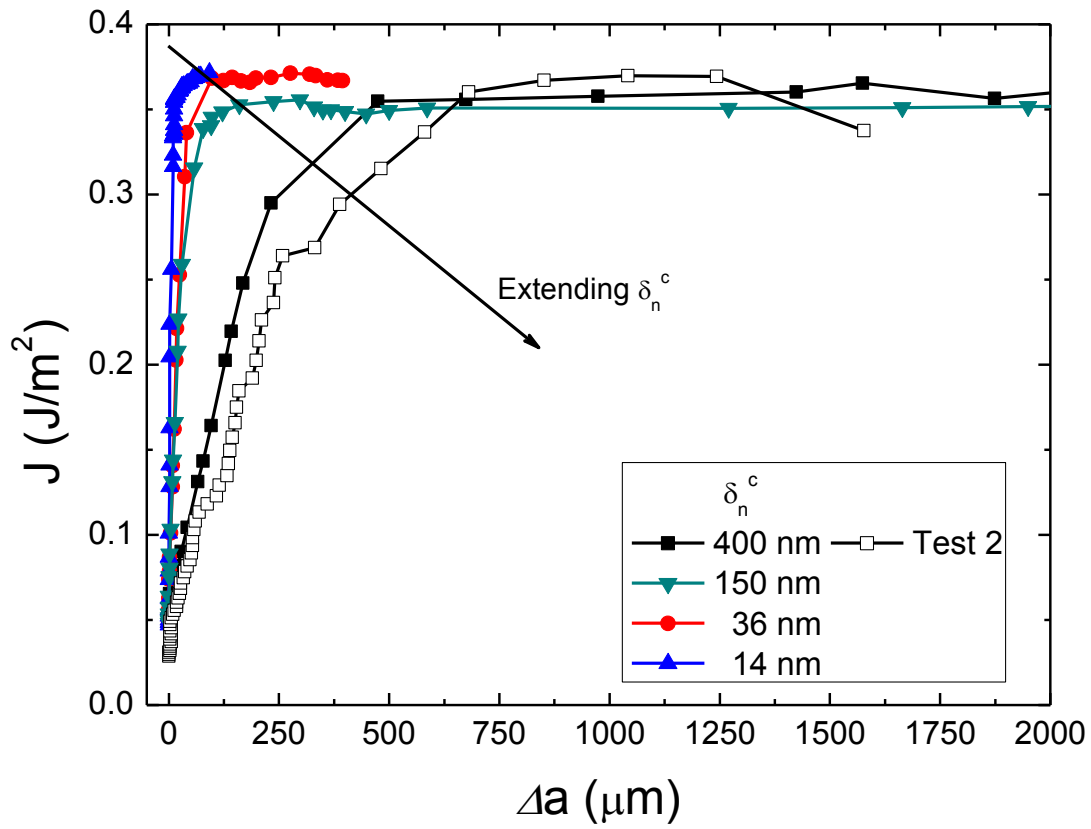


Figure 6.15 Effect of the interaction range on delamination resistance curves.

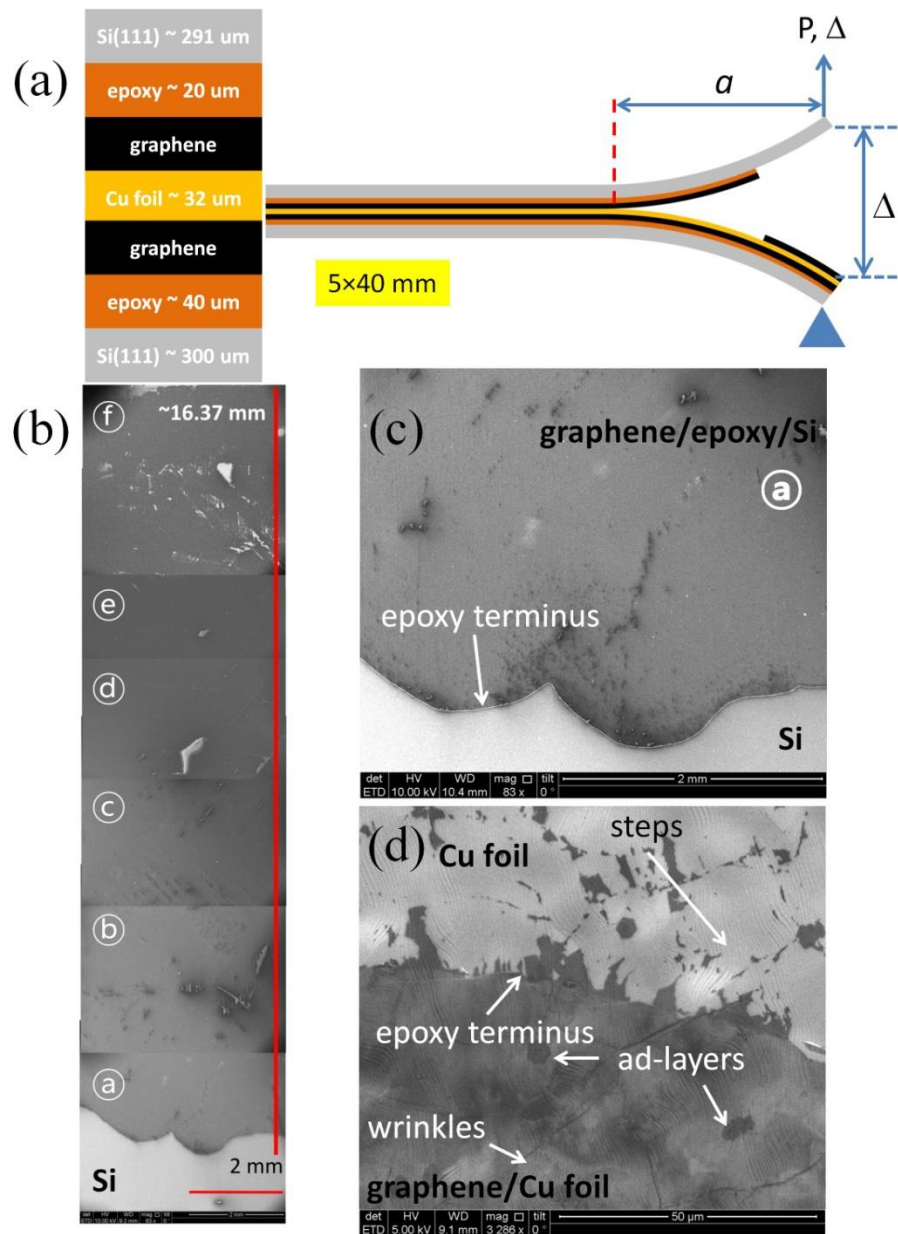


Figure 7.1 Schematics of the cross section of the specimen and experimental configuration are presented along with low and high resolution SEM images of the fracture surfaces: (a) Cross section and a specimen under load. The crack length  $a$  is defined as the distance from the crack front to the loading point. (b) Low resolution, stitched SEM images of graphene transferred to the epoxy. (c) High resolution SEM image of epoxy on silicon near the epoxy terminus after graphene transfer. (d) High resolution SEM of copper foil near the epoxy terminus after transfer.

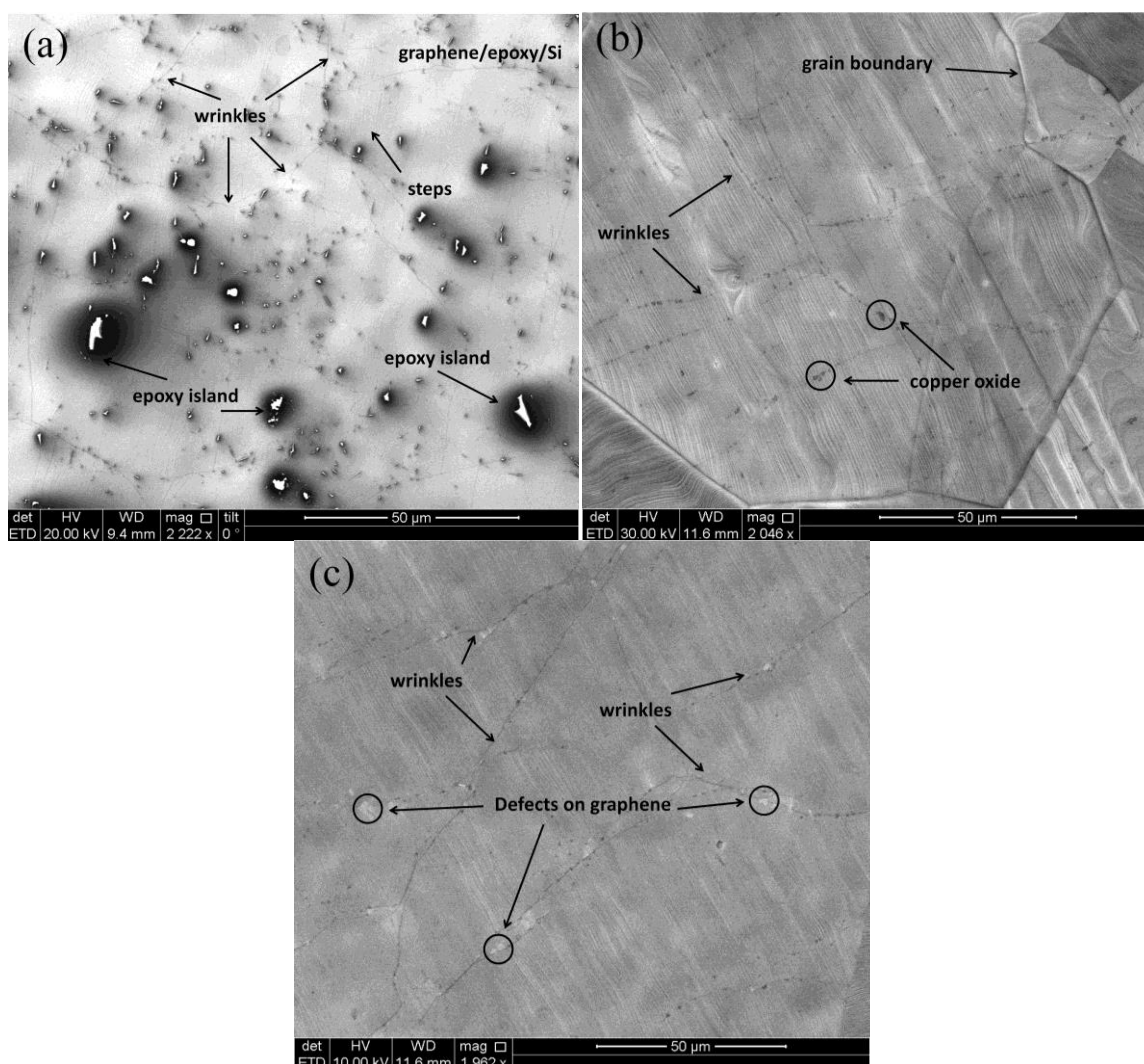


Figure 7.2 High resolution SEM images of graphene transferred to epoxy and on copper following growth. (a) Following transfer, steps, ad-layers, wrinkles and epoxy islands or holes in the graphene can be seen on the epoxy fracture surface. Before transfer, (b) graphene wrinkles, copper oxide, grain boundaries and steps can be seen on the copper. (c) Another region contains notable defects (most likely holes) in addition to graphene wrinkles and steps.

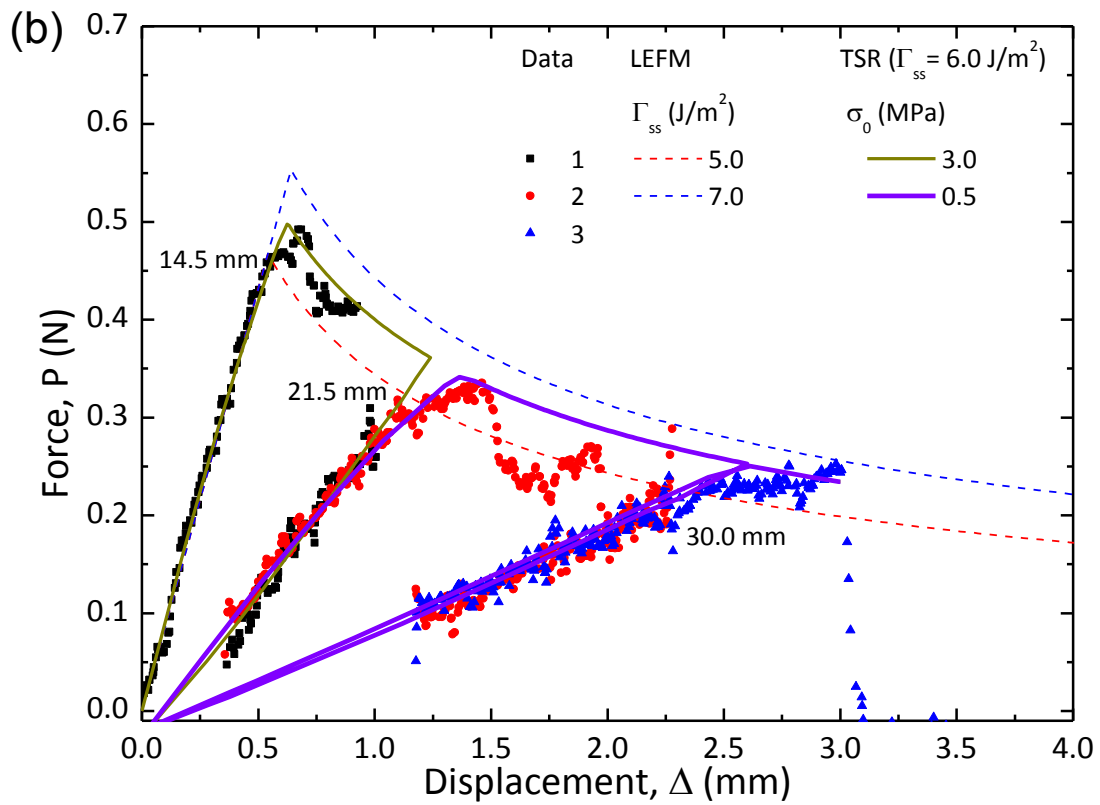
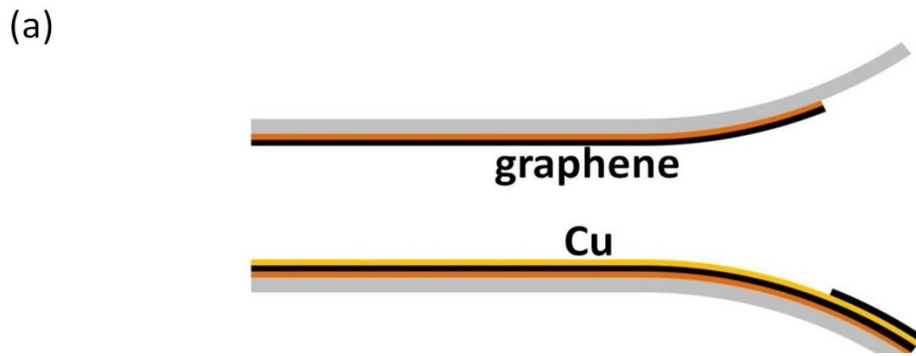


Figure 7.3 (c) and (d) continued on next page

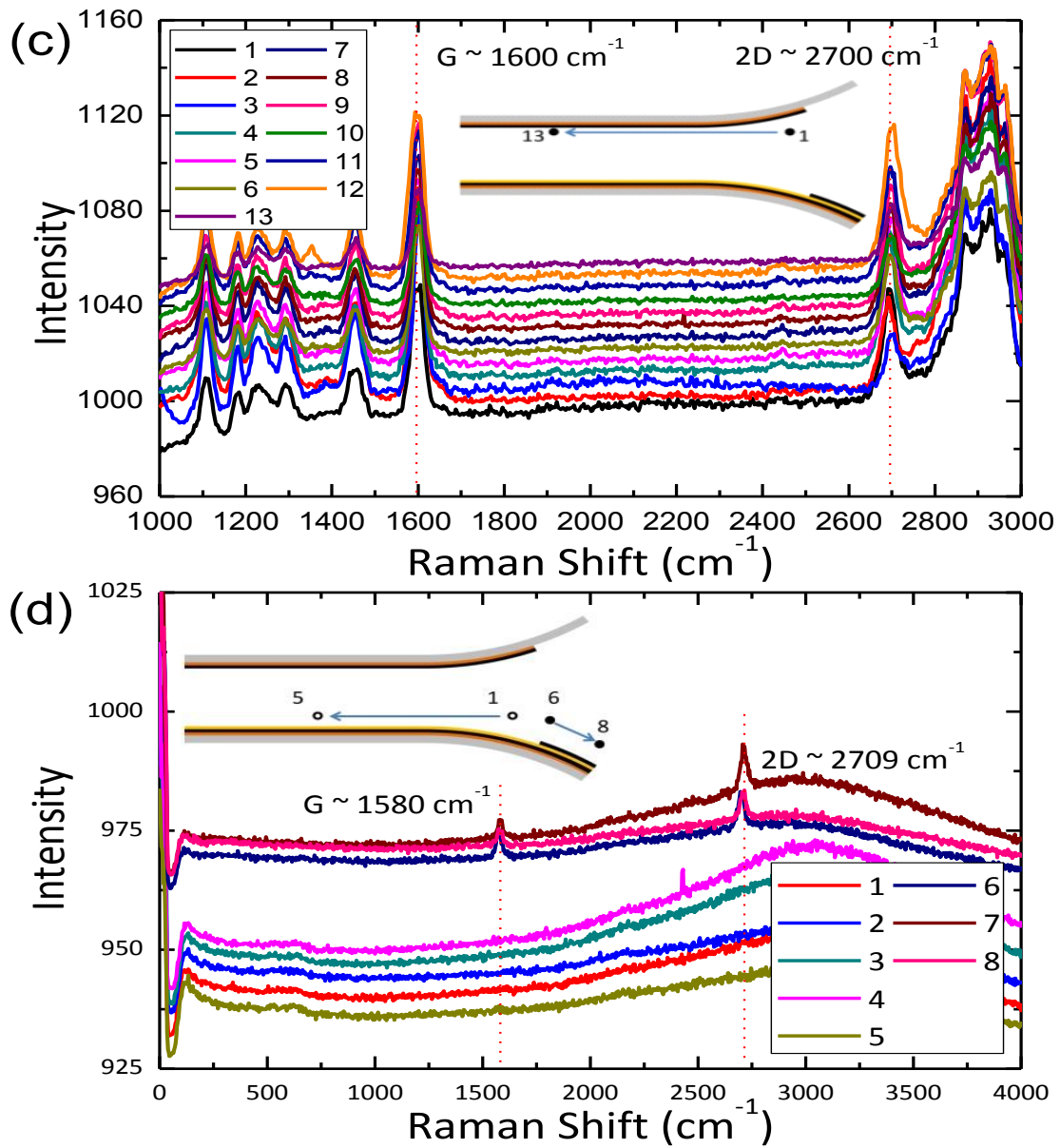


Figure 7.3 Results of experiments at an applied separation rate of 254.0  $\mu\text{m/s}$ : (a) A schematic of delamination along the graphene/copper interface. (b) Force-displacement response of three experiments and associated simulations. (c) Raman spectra of graphene transferred on epoxy and pure epoxy. (d) Raman spectra of copper foil after mechanical transfer; the series of spots from 1 to 5 shows no graphene because it was transferred to the epoxy while spots 6 to 8 indicate the presence of graphene in the pre crack region where there was no epoxy.



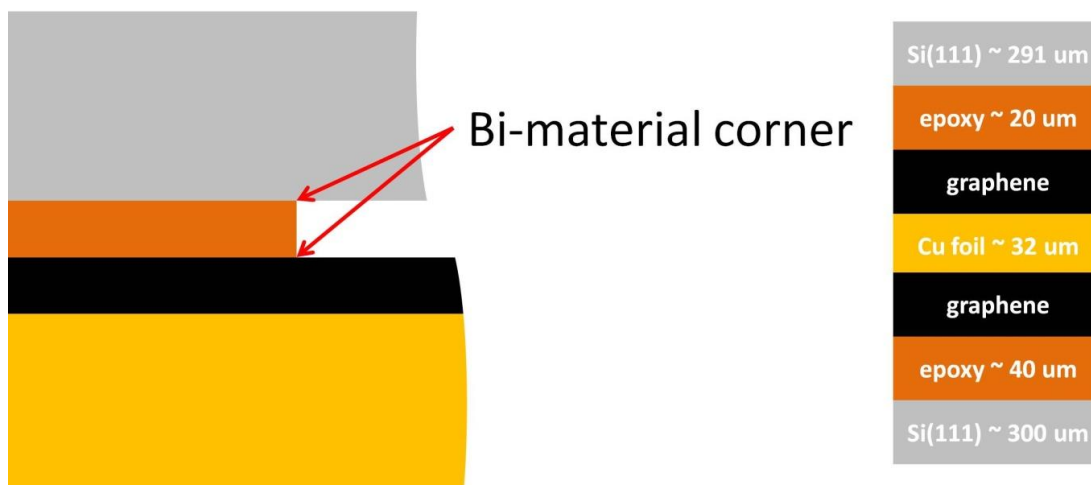


Figure 7.4 A schematic of the bi-material corners formed at the terminus of the top epoxy layer.

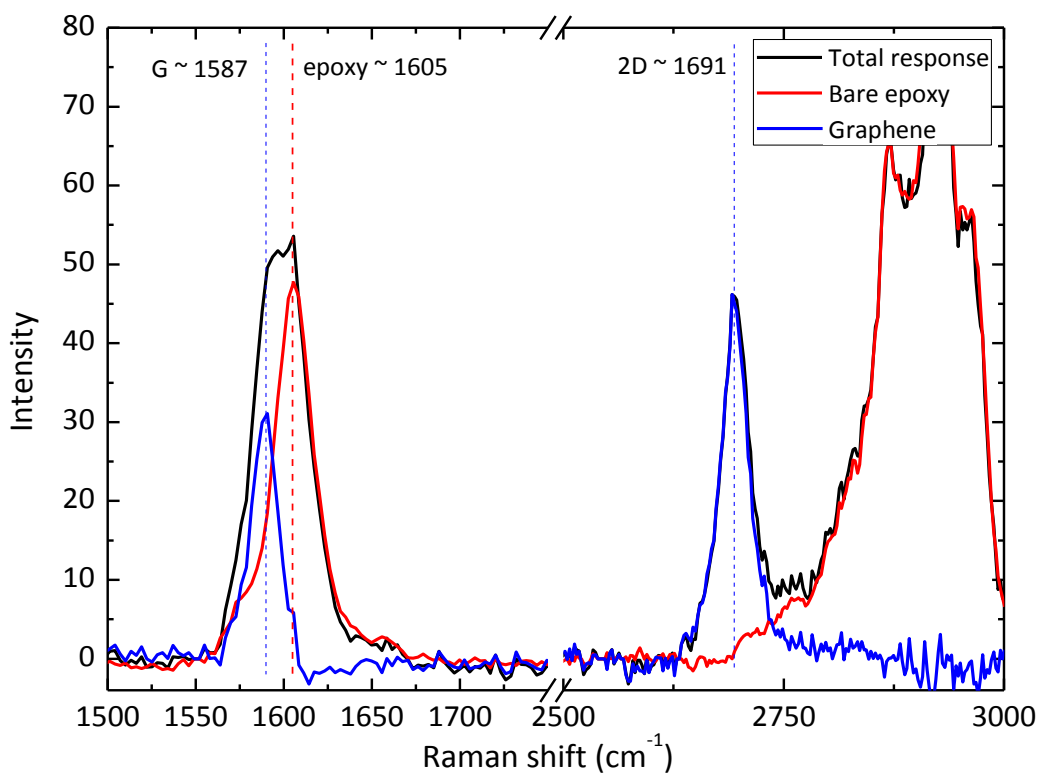


Figure 7.5 Raman spectra for graphene/epoxy (black), bare epoxy (red) and the subtracted response (blue).

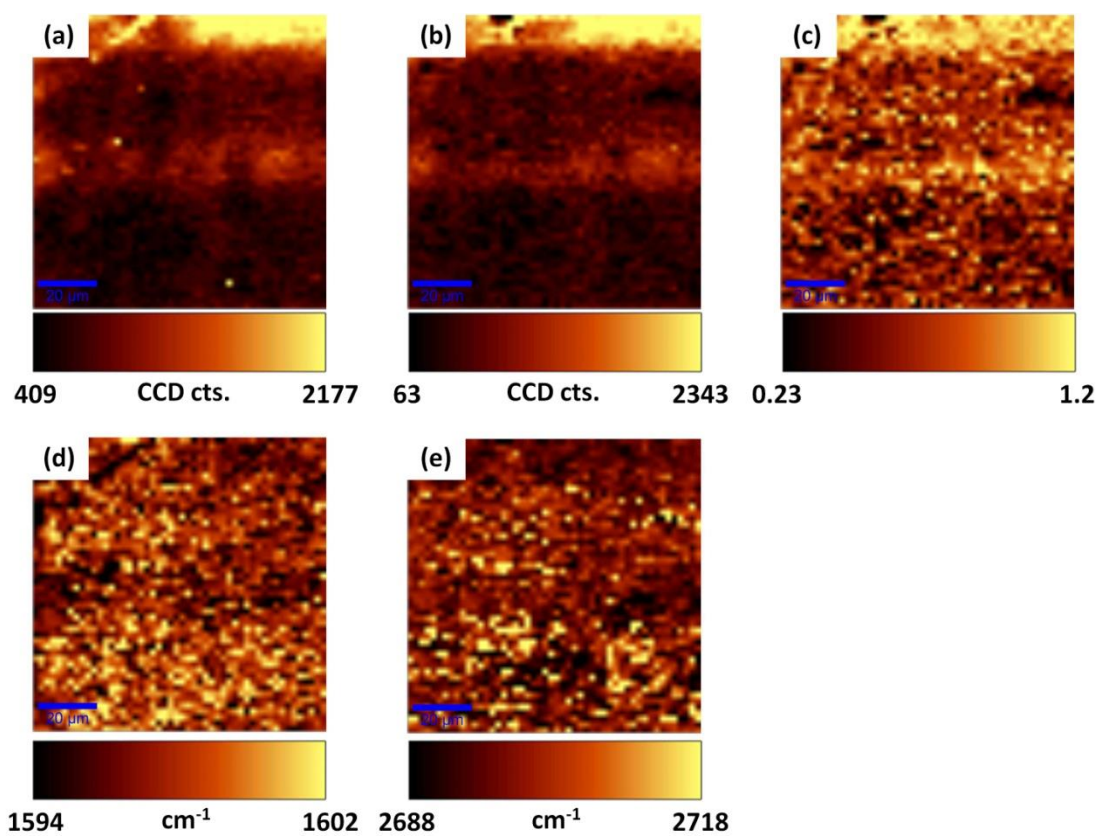


Figure 7.6 Raman maps of 100×100-μm regions of graphene on epoxy. (a) Intensity map of the G peak. (b) Intensity map of the 2D peak. (c) Map of the ratio of the intensities  $I_{2D}/I_G$  of the 2D and G peaks. (d) Map of the range of the G peak location. (e) Map of the range of the 2D peak location.

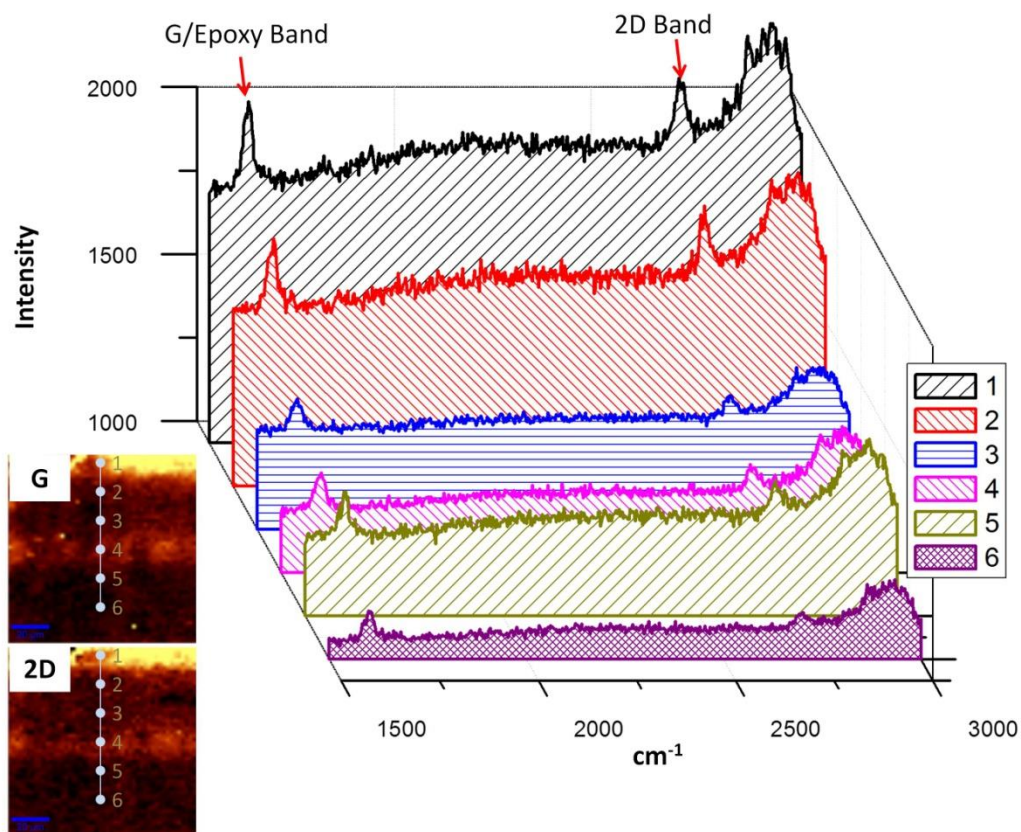


Figure 7.7 Variation of Raman spectra at 6 locations due to the topography of the epoxy fracture surface relative to the depth of field of the Raman microscope. Nonetheless, G and 2D peaks exist at every location, confirming the presence of graphene on epoxy.

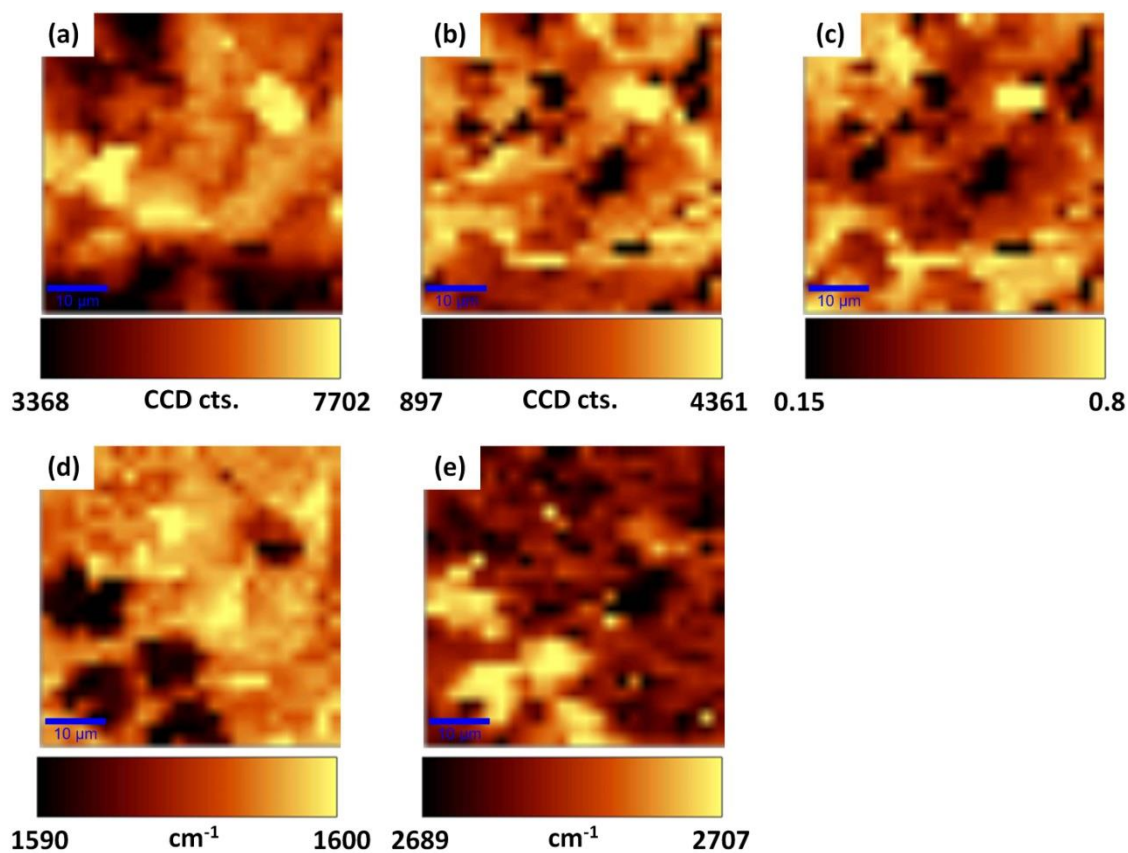


Figure 7.8 Raman maps of 50×50-μm regions of graphene on epoxy. (a) Intensity map of the G peak. (b) Intensity map of the 2D peak. (c) Map of the ratio of the intensities  $I_{2D}/I_G$  of the 2D and G peaks. (d) Map of the range of the G peak location. (e) Map of the range of the 2D peak location.

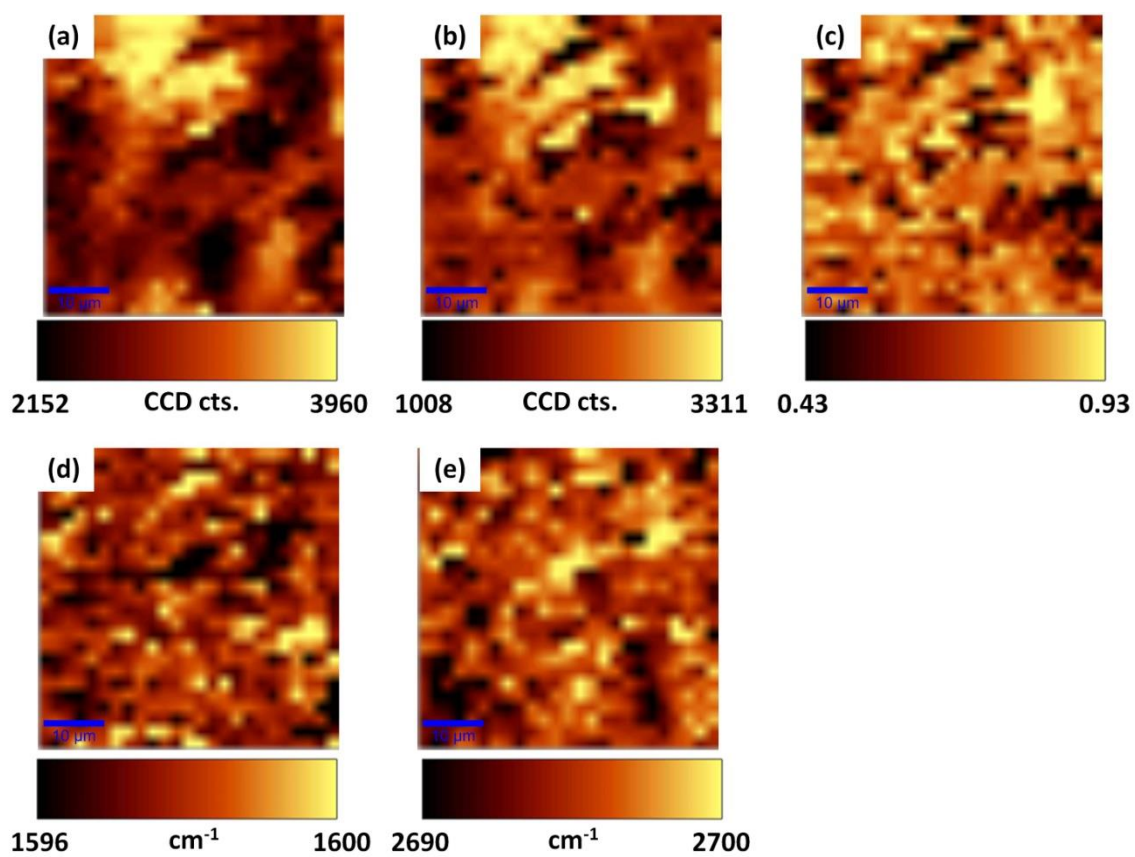


Figure 7.9 Raman maps of 50×50-μm regions of graphene on epoxy. (a) Intensity map of the G peak. (b) Intensity map of the 2D peak. (c) Map of the ratio of the intensities  $I_{2D}/I_G$  of the 2D and G peaks. (d) Map of the range of the G peak location. (e) Map of the range of the 2D peak location.

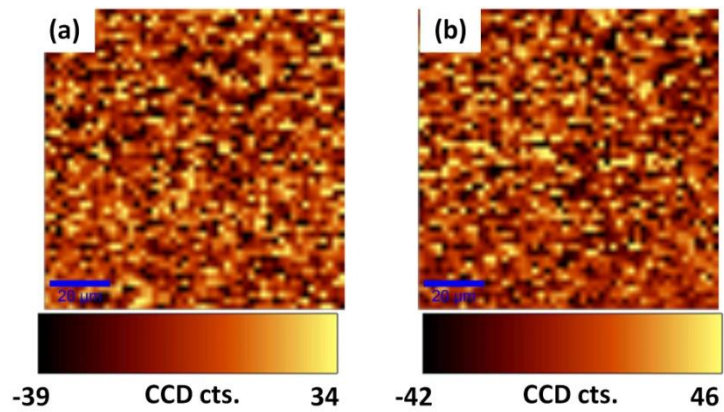


Figure 7.10 Raman maps over  $100\times 100\text{-}\mu\text{m}$  regions of the copper fracture surface following delamination. (a) Intensity map of the G peak. (b) Intensity map of the 2D peak. The essentially zero values indicate that there was no graphene on the copper



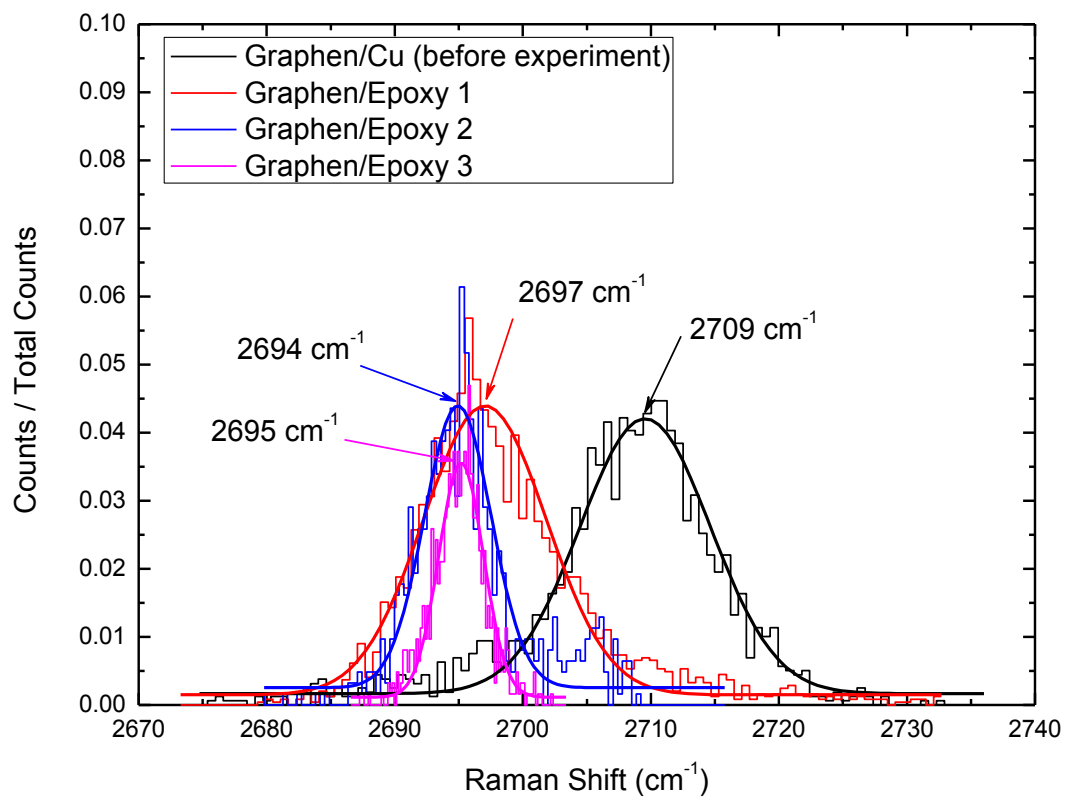


Figure 7.11 Distribution of Raman 2D peak locations from spectra obtained from graphene on copper following growth and the shift of the Raman 2D peaks from spectra obtained from graphene on epoxy following delamination.

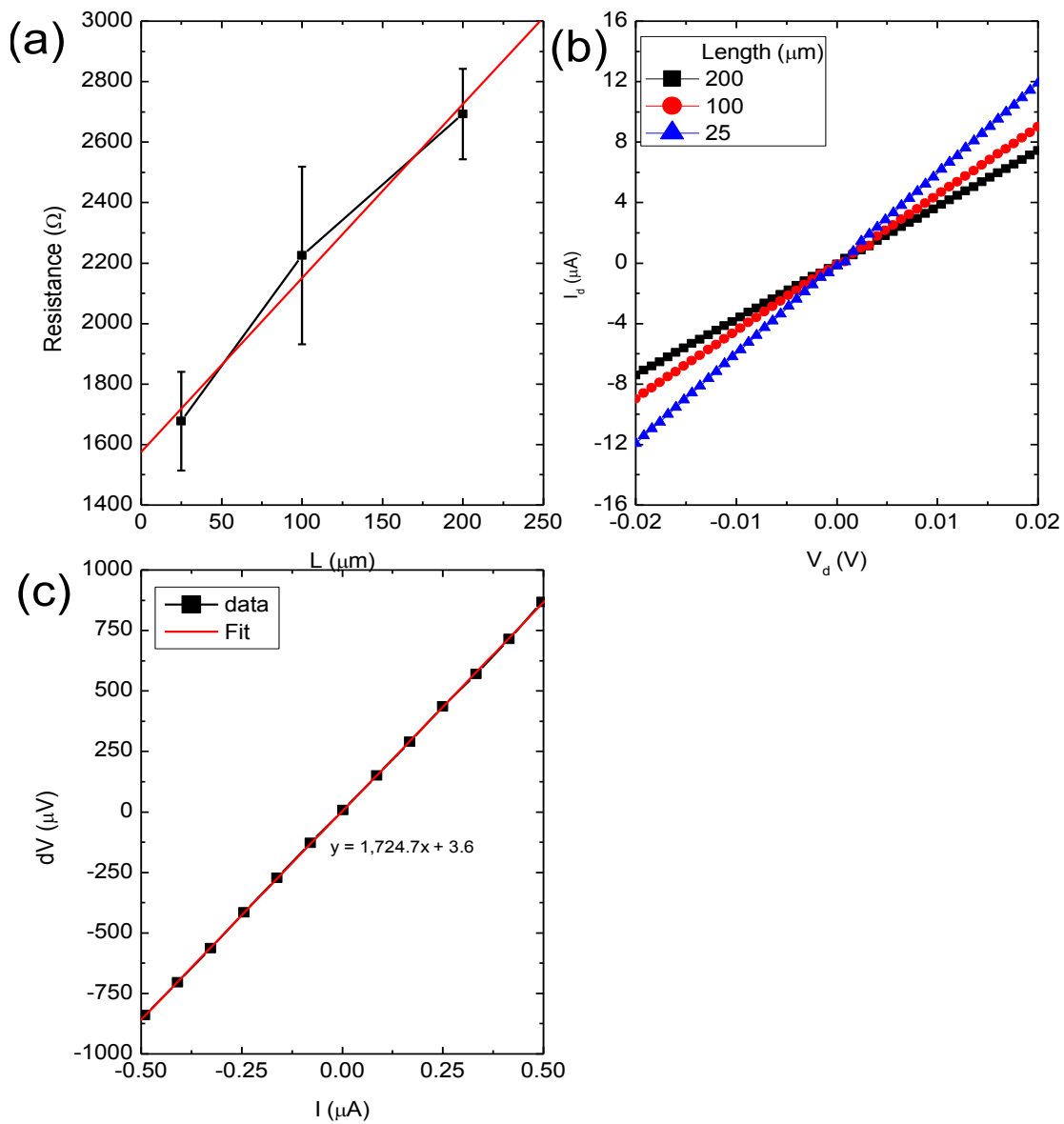


Figure 7.12: Electrical measurement of (a) Resistance vs. length and (b) Ohmic response during TLM experiments. (c) Results from four-point measurement.



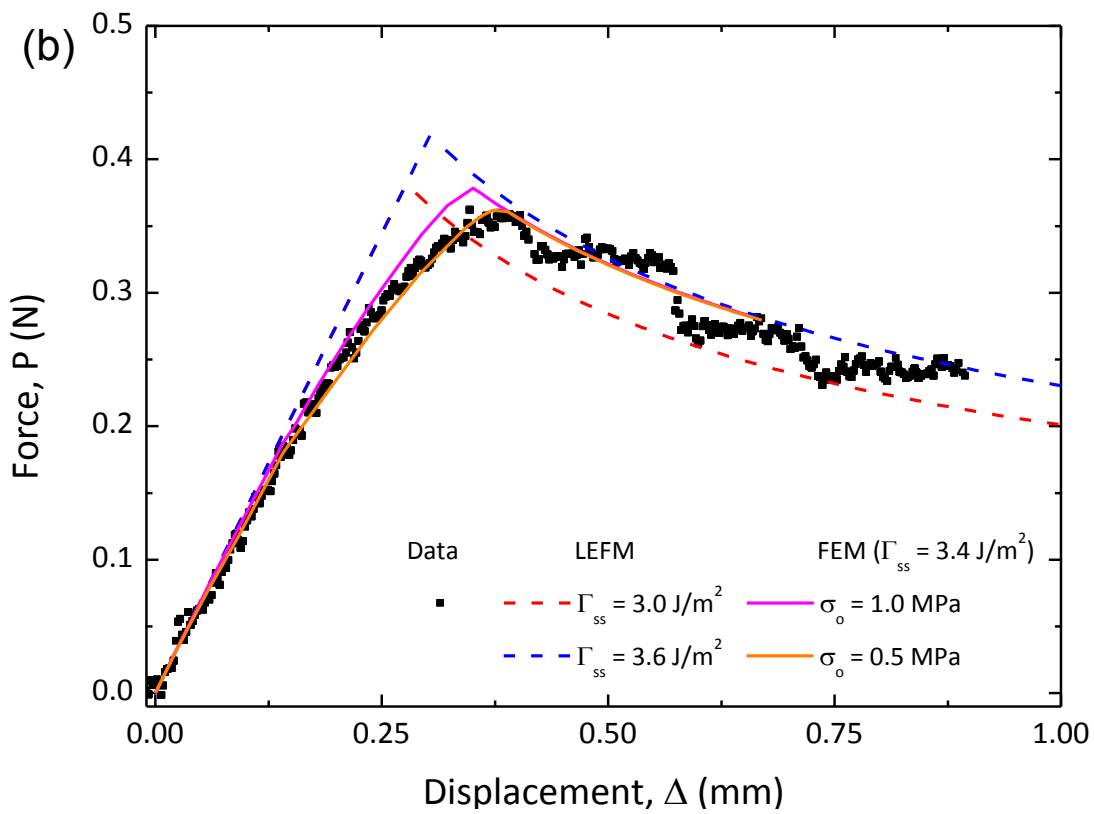
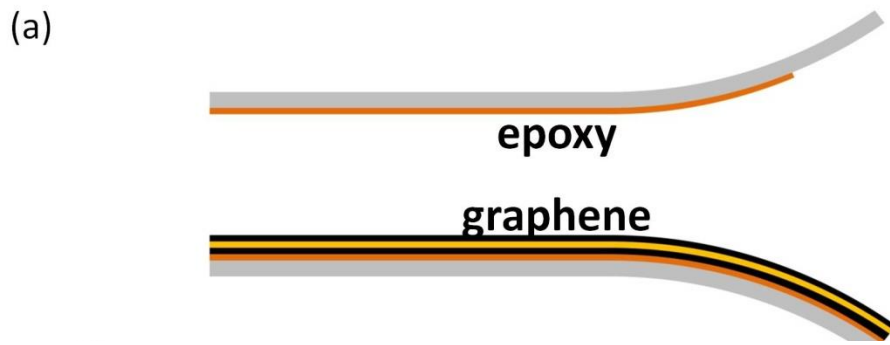


Figure 7.13 (c) and (d) continued on next page

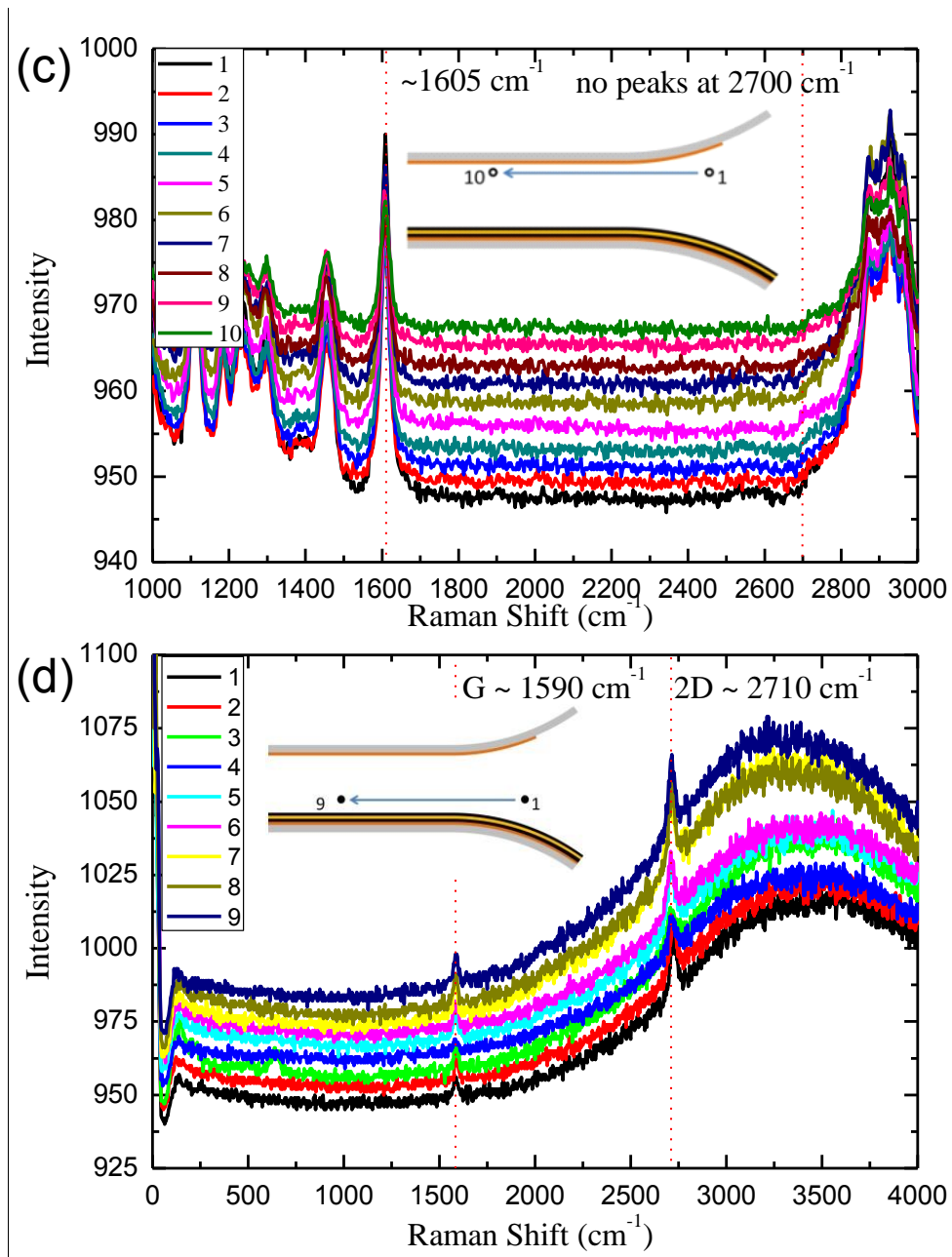


Figure 7.13 Results of experiments at an applied separation rate of 25.4  $\mu\text{m/s}$ : (a) A schematic of delamination along the graphene/epoxy interface. (b) Force-displacement response of an experiment and associated simulations. (c) Raman spectra of ten spots on the epoxy with no graphene on it. (d) Raman spectra of copper foil after separation; the series of spots from 1 to 9 confirm the presence of graphene because it was not transferred to the epoxy.

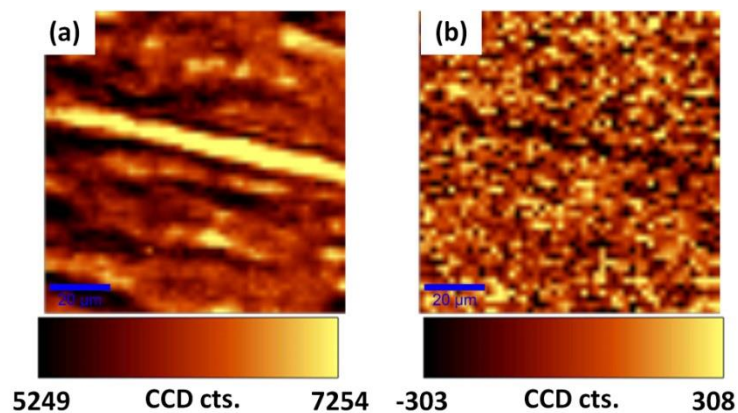


Figure 7.14 Raman maps over  $100 \times 100 \mu\text{m}$  regions on the epoxy fracture surface. (a) Intensity map of the epoxy peak at approximately  $1600 \text{ cm}^{-1}$ . (b) Intensity map of the 2D peak.

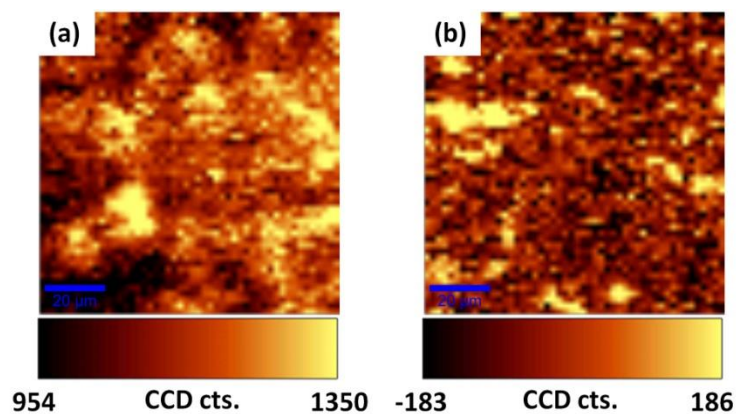


Figure 7.15 Raman maps over  $100 \times 100 \mu\text{m}$  regions on the epoxy fracture surface. (a) Intensity map of the epoxy peak at approximately  $1600 \text{ cm}^{-1}$ . (b) Intensity map of the 2D peak.

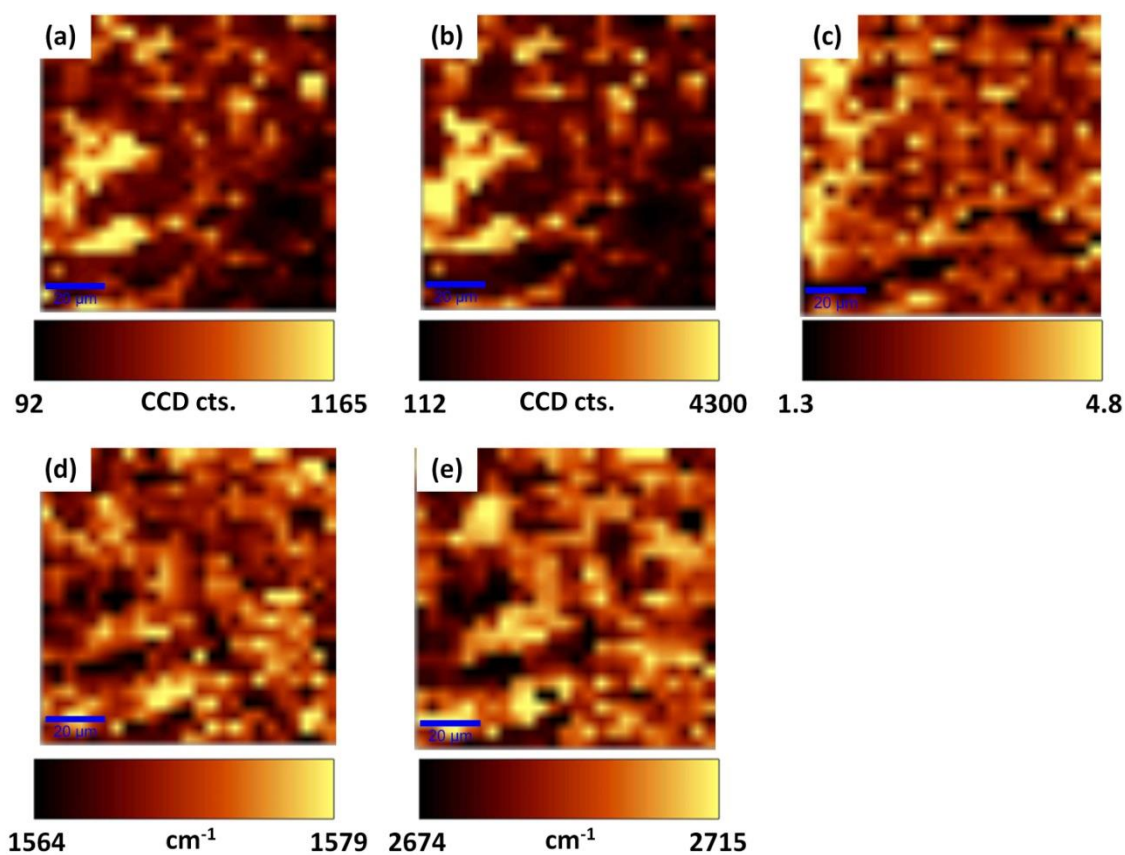


Figure 7.16 Raman maps over  $100 \times 100 \mu\text{m}$  regions on the copper fracture surface. (a) Intensity map of the G peak. (b) Intensity map of the 2D peak. (c) Map of the ratio of the intensities  $(I_{2D} / I_G)$  of the 2D and G peaks. (d) Map of the range of the G peak location. (e) Map of the range of the 2D peak location.

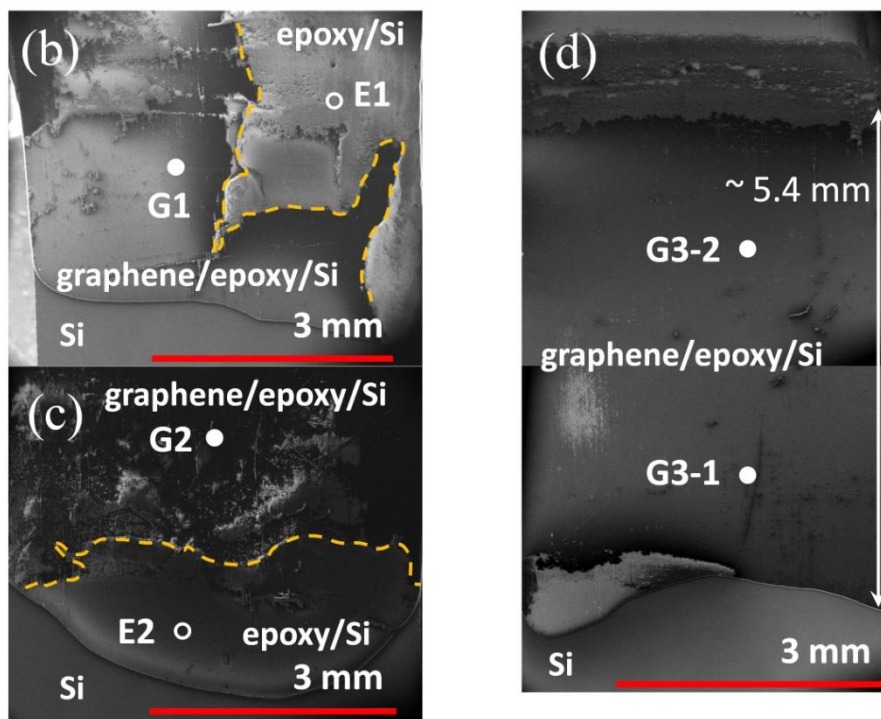
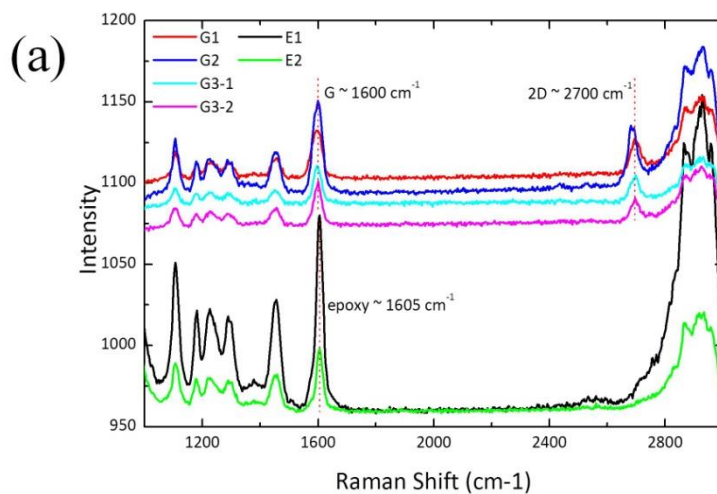


Figure 7.17 Raman spectra and low resolution SEM images were prepared to track the transfer of graphene at intermediate loading rates: (a) Raman spectra of the epoxy fracture surface following experiments at 42.3, 84.6 and 169.3  $\mu\text{m/s}$ . (b) Low resolution SEM image of the epoxy fracture surface following an experiment at 42.3  $\mu\text{m/s}$  which shows small patches of graphene transferred to the epoxy. (c) Low resolution SEM image of the epoxy fracture surface following experiments at 84.6  $\mu\text{m/s}$  which again shows small patches of graphene. (d) More continuous transfer of graphene (5 $\times$ 5.4 mm) was achieved at a loading rate of 169.3  $\mu\text{m/s}$ .

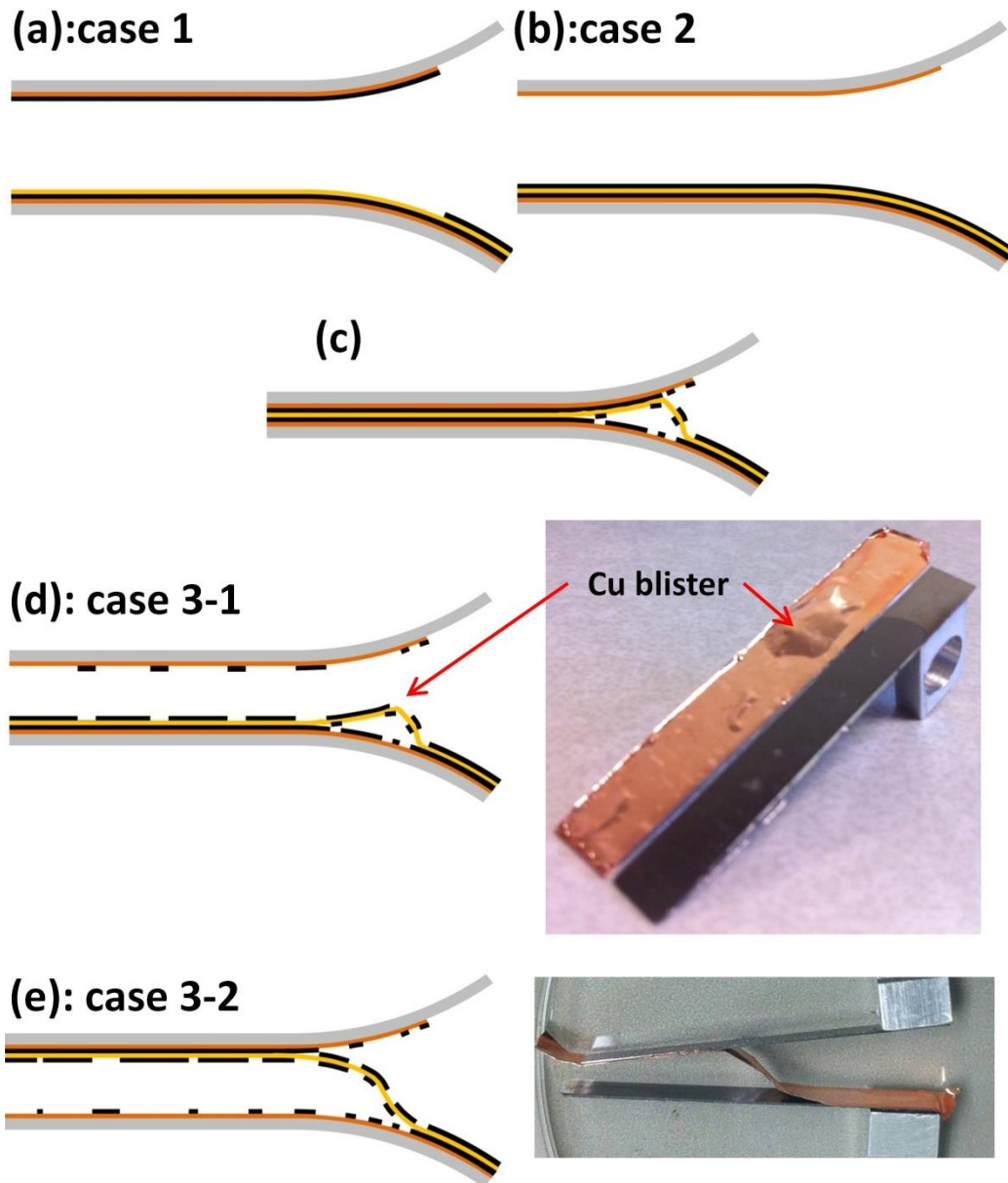


Figure 7.18 A summary of delamination modes: (a) delamination along the graphene/copper interface at  $254 \mu\text{m/s}$ . (b) Delamination along the graphene/epoxy interface at  $25.4 \mu\text{m/s}$ . (c) Onset of case 3 via the formation of a blister below the epoxy terminus on the bottom side the copper. (d) Case 3-1, where the blister arrested and delamination continued at one of the interfaces above the copper. (e) Case 3-2 where the blister continued to grow along one of the interfaces below the copper foil.

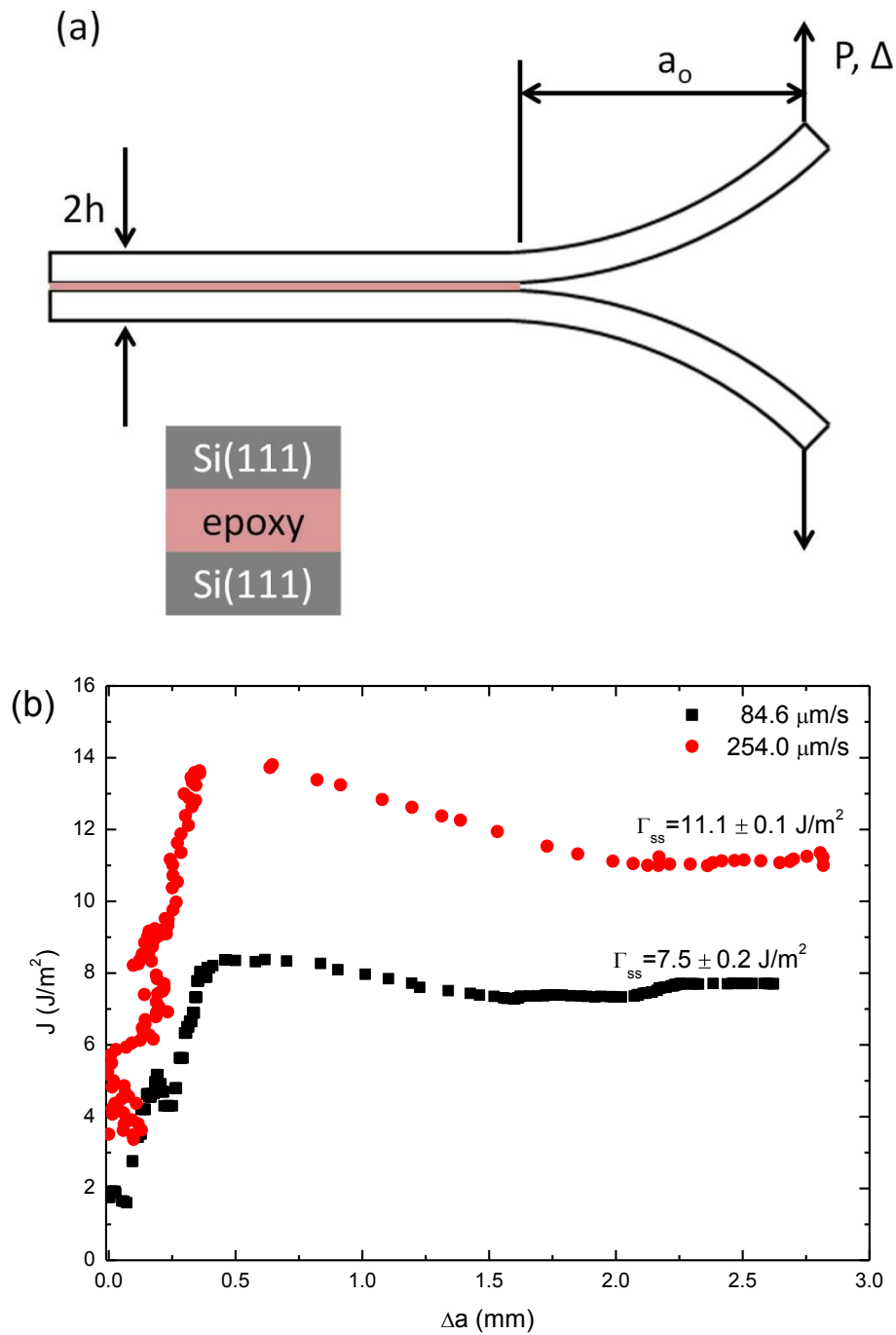


Figure 7.19 Schematic of Mode I fracture experiment in Si/epoxy/Si specimen and its fracture toughness in terms of load rate: (a) Double cantilever beam fracture experiment and (b) resistance response; the J-integration with respect to the crack propagation  $\Delta a$ .



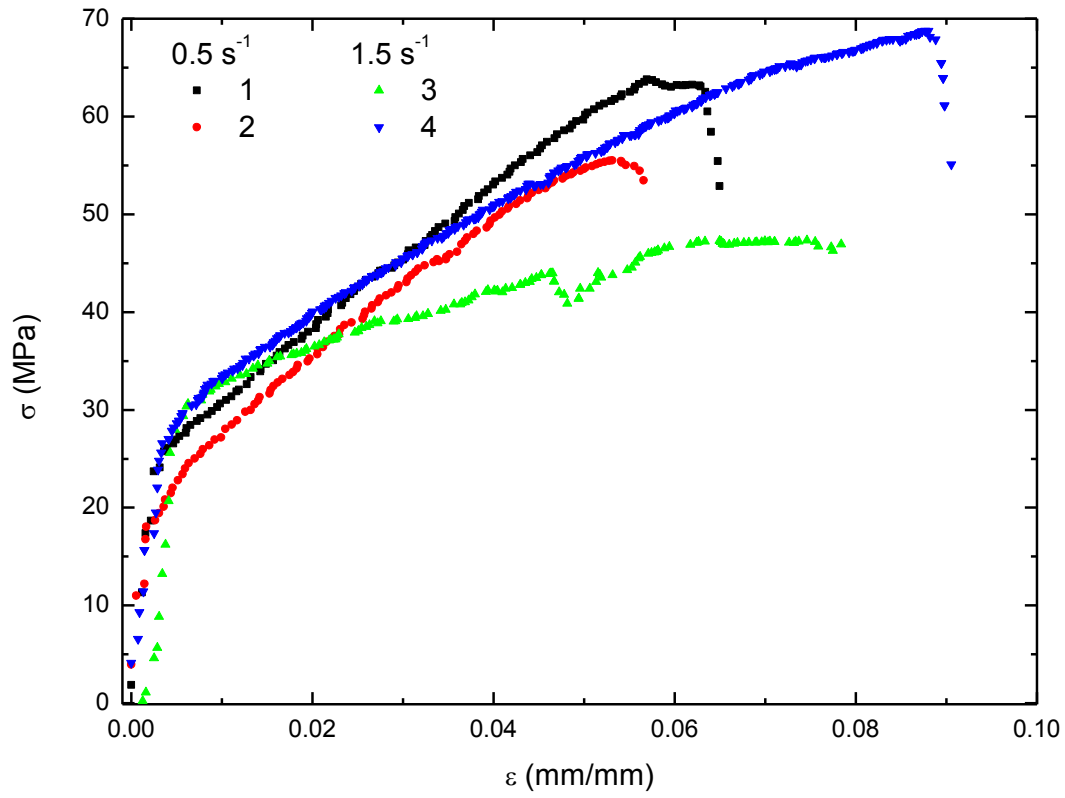


Figure 7.20 The stress-strain curves of annealed copper foils for 0.5 /s and 1.5 /s loading rates. The yield strength of all four copper foils is  $23.3 \pm 3.5$  MPa



(a)

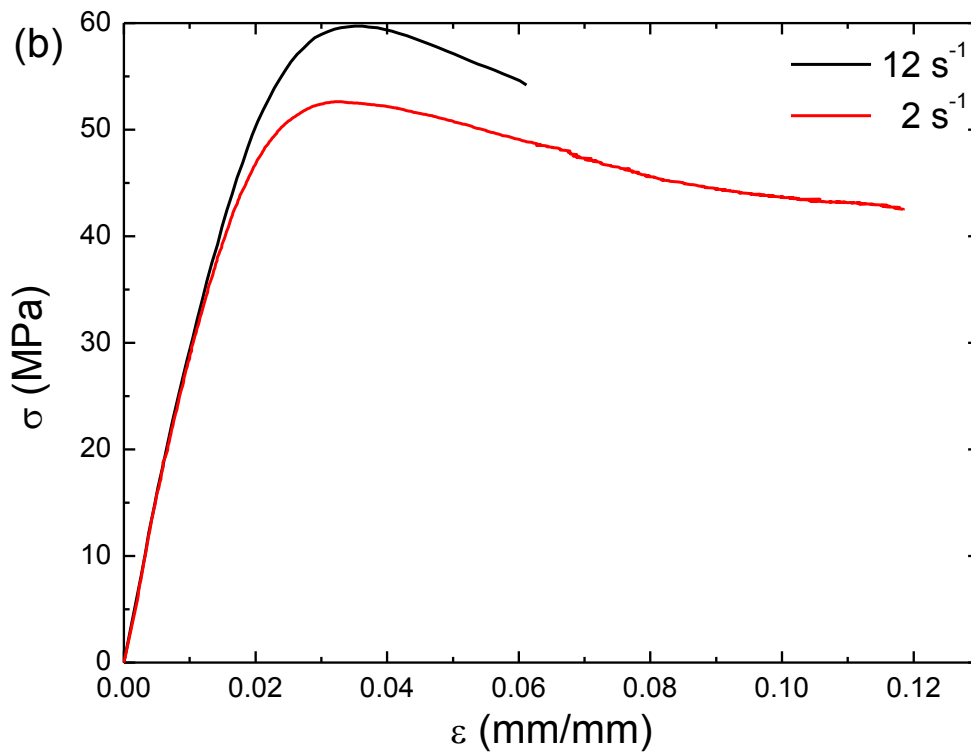
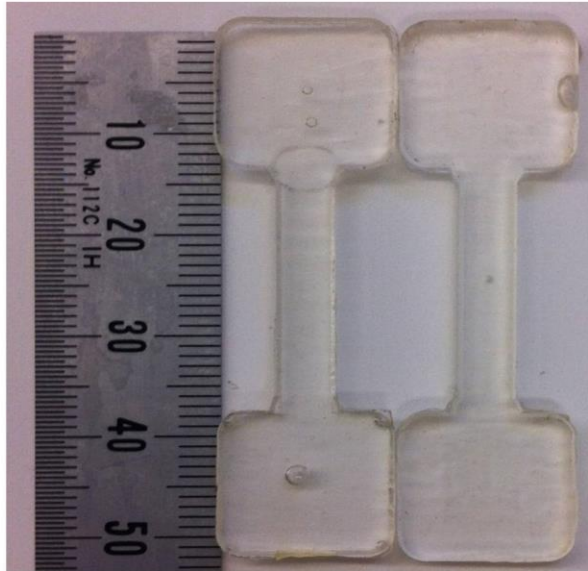


Figure 7.21 Uniaxial tension test at room temperature: (a) An epoxy tensile specimen and (b) the stress-strain curve at two different loading rates:  $2 \text{ /s}$  and  $12 \text{ /s}$ .

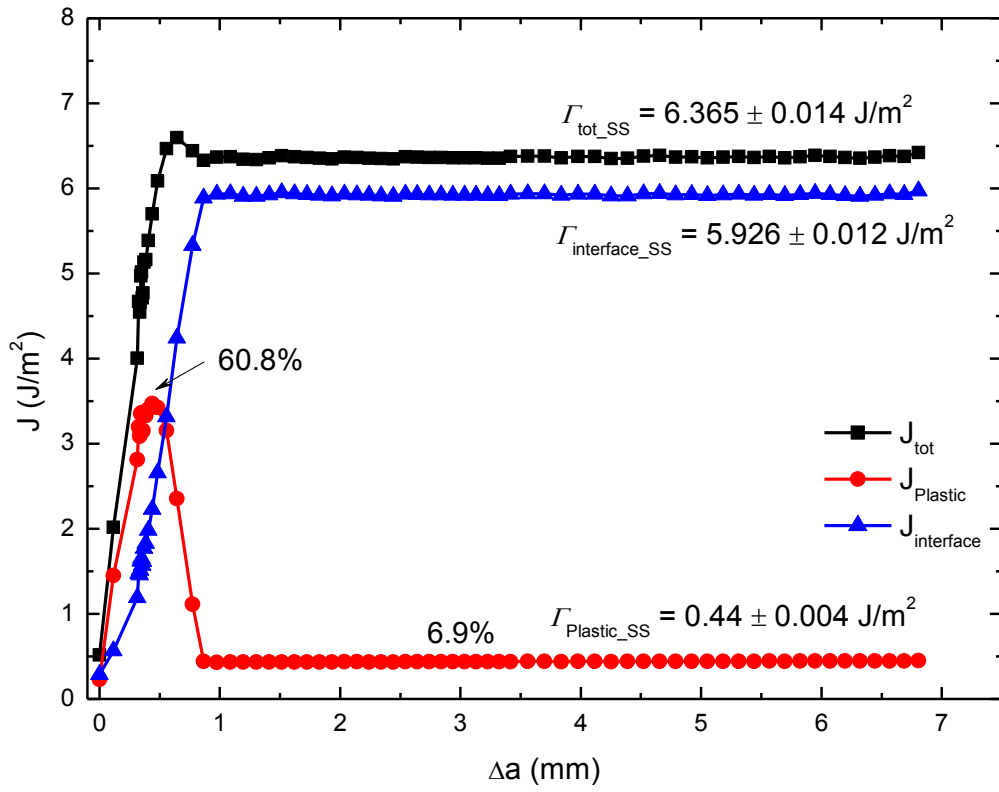


Figure 7.22 The decomposition of the J-integral with respect to the work of plasticity for the graphene/copper interface.

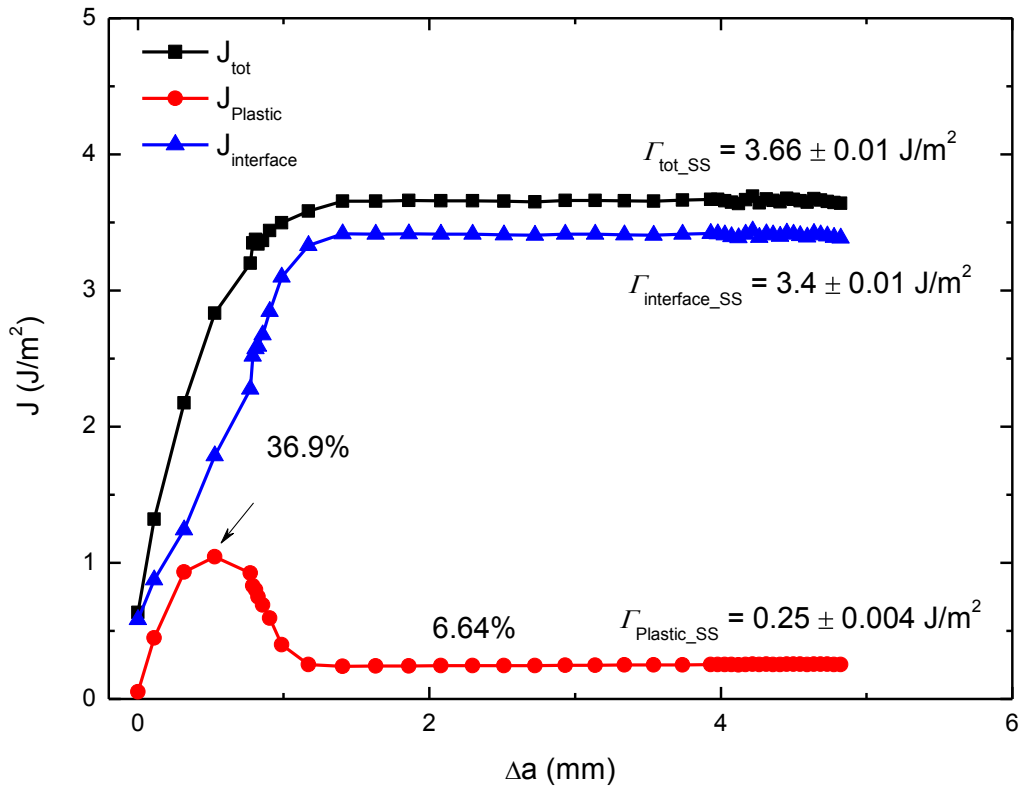


Figure 7.23 The decomposition of the J-integral with respect to the work of plasticity for the epoxy/graphene interface.

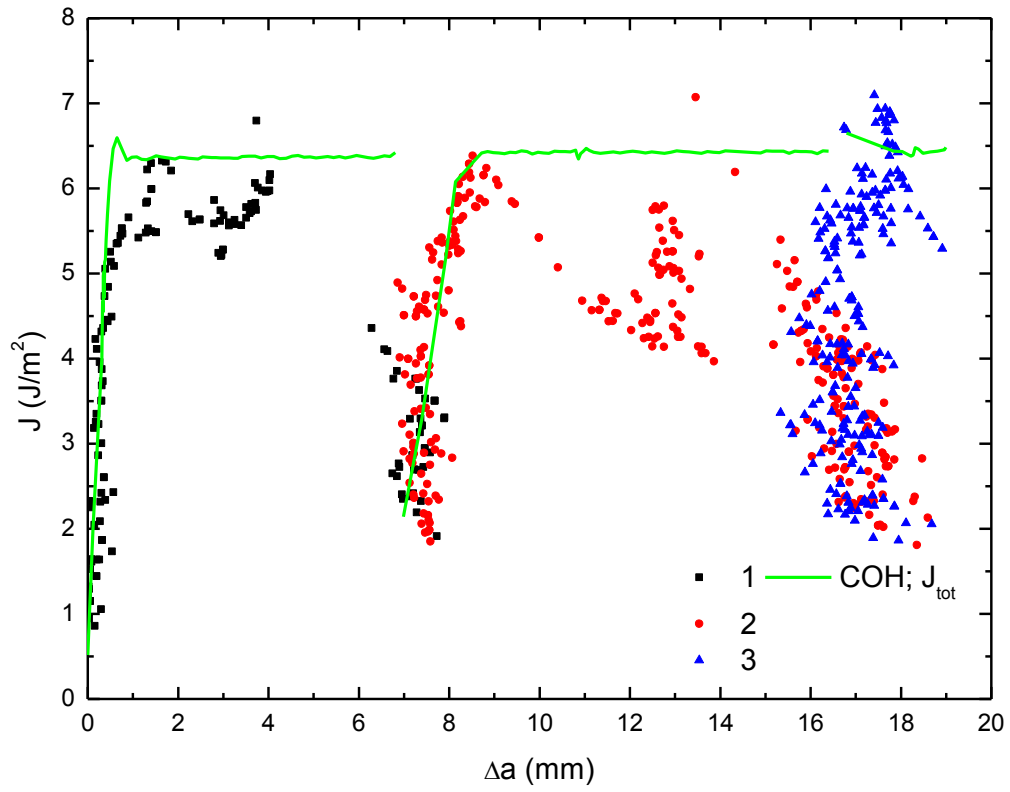


Figure 7.24 The delamination resistance curve for the graphene/copper interface.

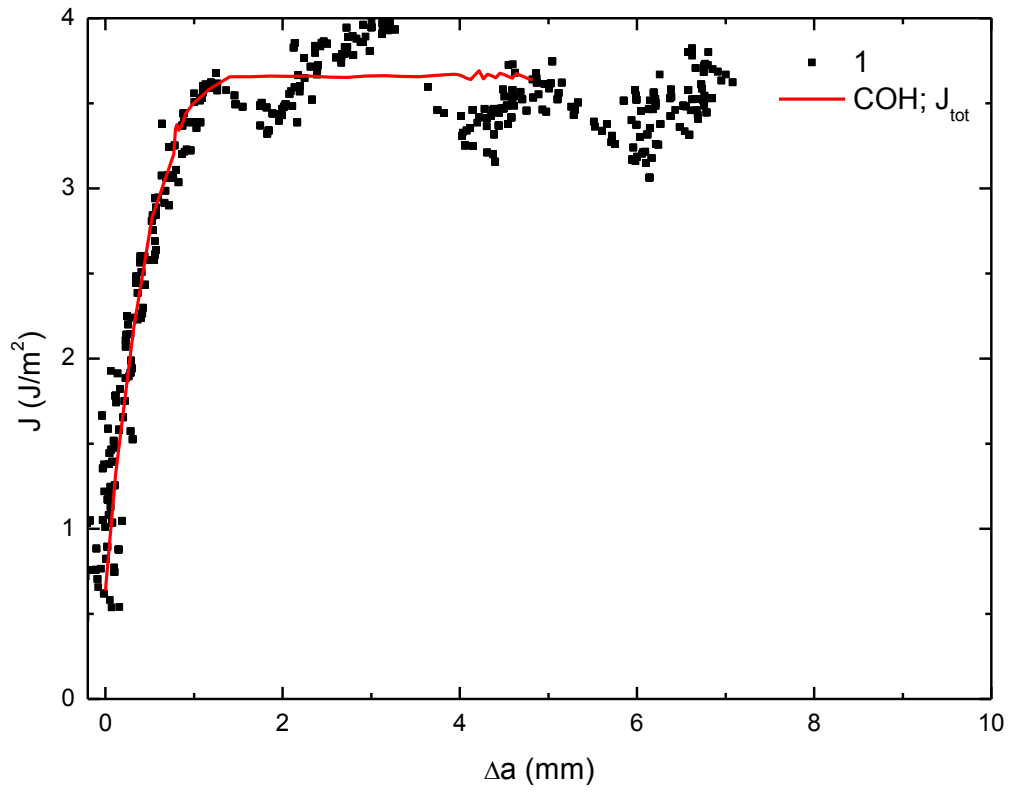


Figure 7.25 The delamination resistance curve of the epoxy/graphene interface.

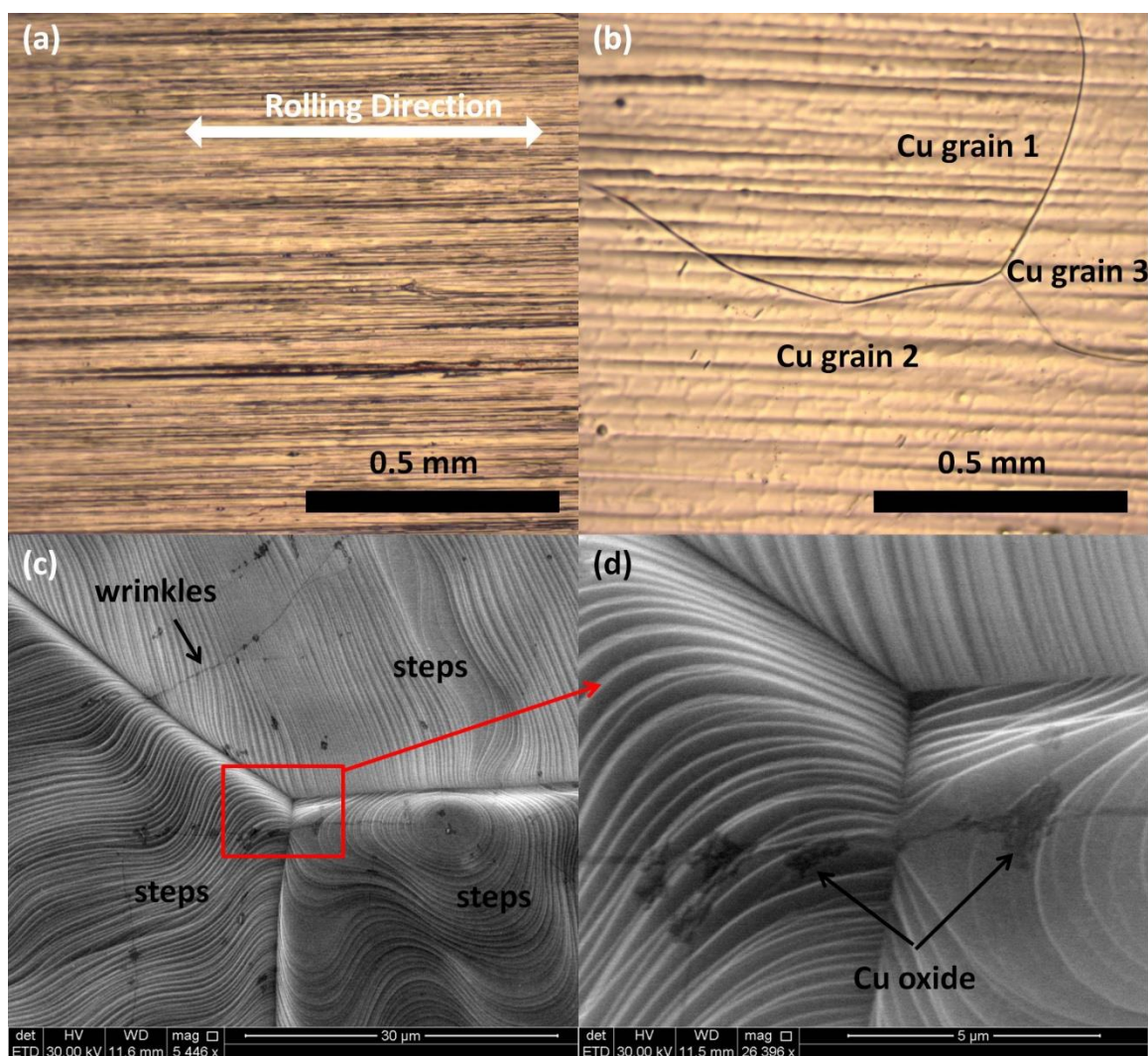


Figure 7.26 Variety of features on copper foil. (a) Before graphene growth, (b) after graphene growth, (c) grains, steps and graphene wrinkles on copper foil and (d) high-resolution image observation at the junction of three copper grains.

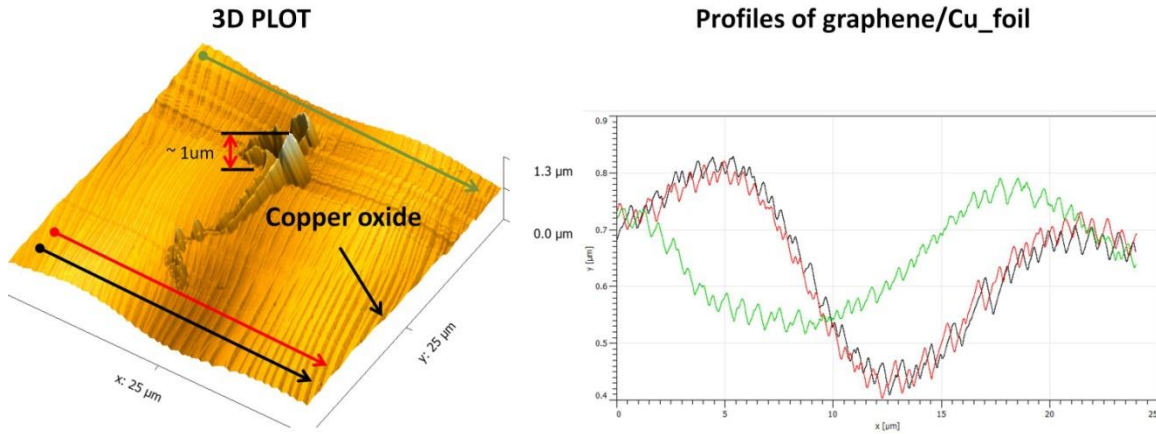


Figure 7.27 (a) An AFM scan over a  $25 \times 25 \mu\text{m}$  region of graphene on copper foil with a copper oxide trace growing through the graphene. (b) The topography profiles taken along each of the colored lines bring out steps and rolling marks in the foil.

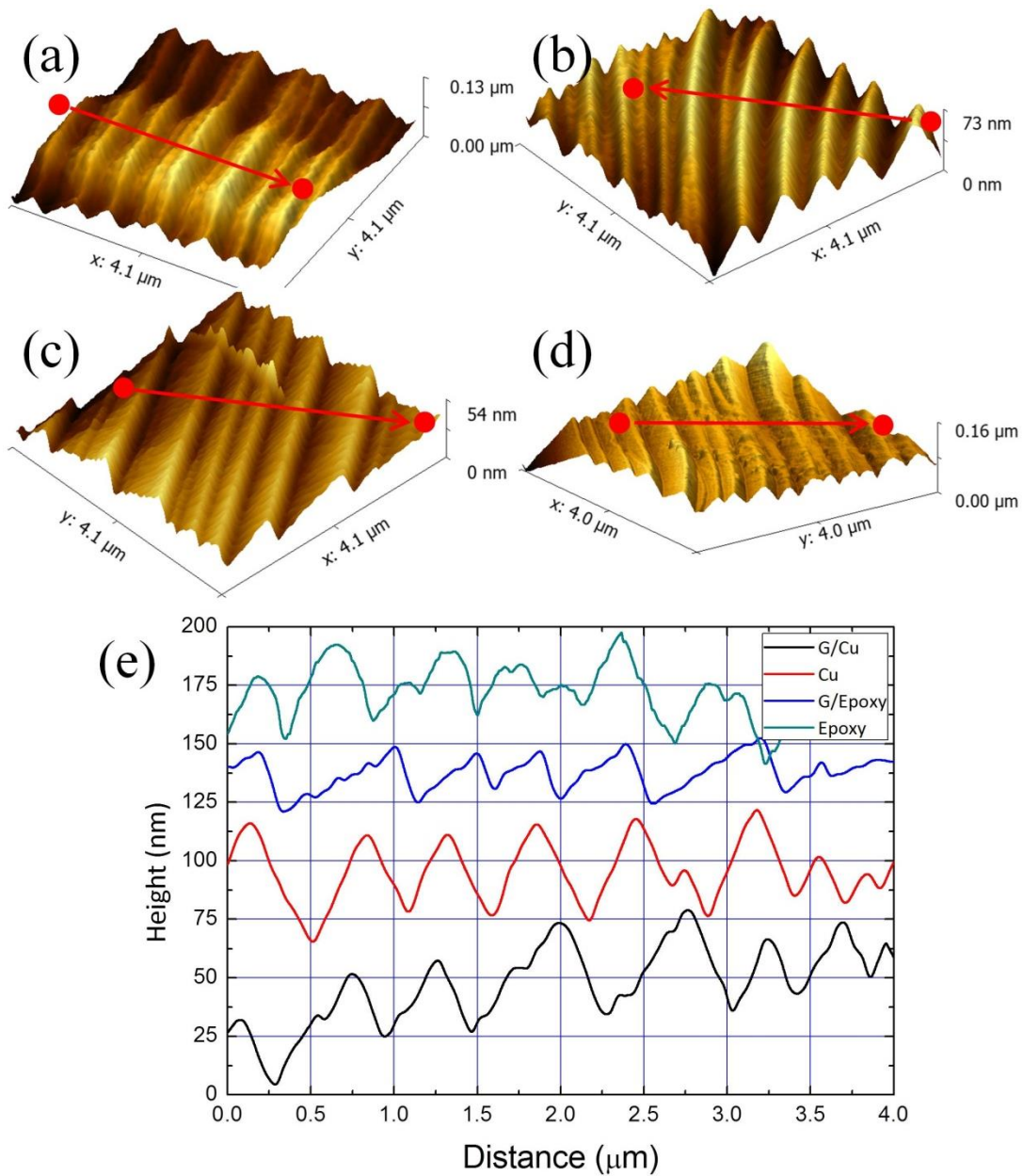


Figure 7.28 AFM scans prior to and following transfer of graphene: (a) The initial state of graphene on copper foil following deposition. The RMS roughness was 11.4 nm. (b) Copper without graphene after transfer had an RMS roughness of 12.3 nm. (c) The RMS roughness of the graphene-coated epoxy surface was 7.35 nm. (d) The RMS roughness of epoxy without graphene was 11.3 nm. (e) Profiles indicate that the wavelength of the surface roughness was quite similar in all cases.



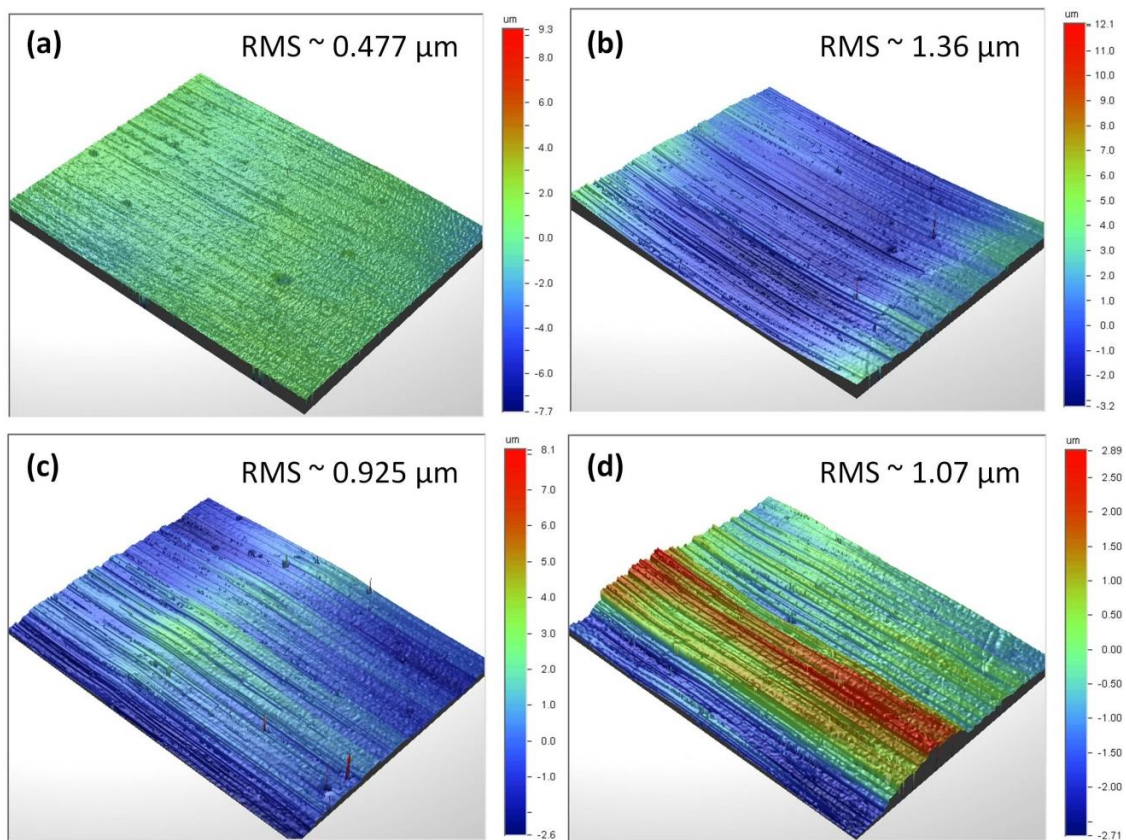


Figure 7.29 Scans of  $1 \times 1.3$ -mm regions graphene on epoxy obtained with a Veeco Optical Profilometer. The overall RMS roughness of each region is noted on each image.

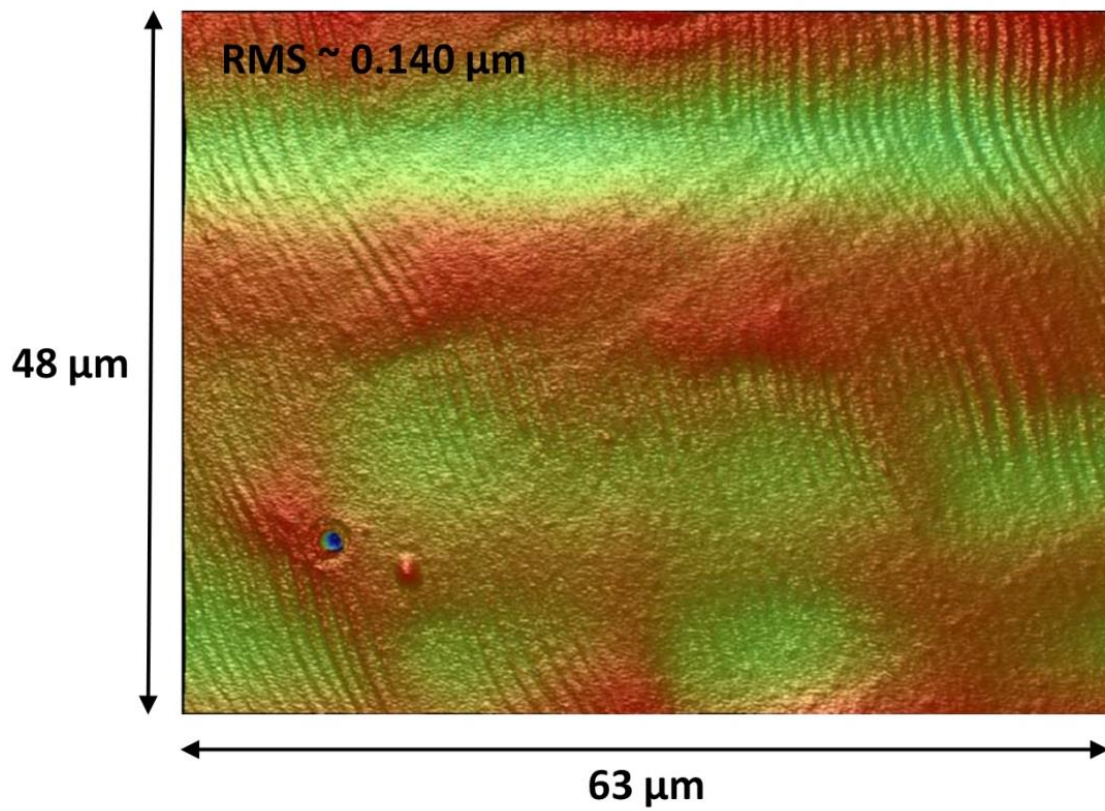


Figure 7.30 A higher resolution image of the surface topology of graphene on epoxy obtained with a Veeco Optical Profilometer.

## TABLES

Table 2.1 The surface energy components of four liquids.

Unit (mJ/m <sup>2</sup> )	Total ( $\gamma$ )	Dispersion ( $\gamma^d$ )	Polar ( $\gamma^p$ )	Acid ( $\gamma^+$ )	Base ( $\gamma^-$ )
Water	73.1	22.1	51	25.5	25.5
Glycerin	64	34	30	3.92	57.4
Toluene	28.5	28.5	0	0	0.72
Diiodomethane	50.8	50.8	0	0.01	0.0

Table 3.1 The RMS roughness of CF<sub>3</sub>, COOH, and NMe<sub>2</sub>-terminated SAMs.

Scan Area ( $\mu\text{m}^2$ )	CF <sub>3</sub> (nm)	COOH (nm)	NMe <sub>2</sub> (nm)
6×6	0.512	0.363	0.147
0.6×0.6	0.289	0.12	0.108

Table 3.2 Comparisons of the measured and expected thickness of the SAMs [161].

	Theoretical thickness (nm)	Ellipsometry measurement (nm)	
CF <sub>3</sub>	2.238	2.21	
COOH	2.04	1.94	
NMe <sub>2</sub>	2.57	2.46	

Table 4.1 Material properties of silicon and a summary of the key parameters of the traction-separation relations for hydrophilic bonding.

Material	Young's Modulus (GPa)	Poisson's Ratio	Yield Strength (MPa)
Silicon	169	0.22	N/A

TSR	$K$ (MPa/mm)	$\sigma_0$ or $\delta_n^0$ (MPa or nm)	$\delta_n^c$ ( $\mu\text{m}$ )	$\Gamma_{ss}$ ( $\text{mJ/m}^2$ )
1	1714290	12 or 0.007	365	325

Table 4.2 Master traction separation relation for hydrophilic bonding.

$\delta_n$ ( $\mu\text{m}$ )	Stress (MPa)	Damage ( $D$ )	Displacement ( $\mu\text{m}$ )
0	0	N.A	N.A
0.007	12	0	0
0.0088	8.2	0.456439394	0.0000018
0.01	6.568	0.616866667	0.000003
0.02	3.417742	0.90031586	0.000013
0.03	2.77	0.946138889	0.000023
0.04	2.133636	0.96888447	0.000033
0.05	1.767647	0.979377451	0.000043
0.06	1.473529	0.98567402	0.000053
0.07	1.183446	0.99013795	0.000063
0.08	0.946959	0.993095087	0.000073
0.09	0.710473	0.995395083	0.000083
0.1	0.5	0.997083333	0.000093
0.11	0.5	0.997348485	0.000103
0.12	0.5	0.997569444	0.000113
0.13	0.5	0.99775641	0.000123
0.14	0.5	0.997916667	0.000133
0.15	0.486705	0.998107258	0.000143
0.16	0.472254	0.998278239	0.000153
0.17	0.457803	0.998429106	0.000163
0.18	0.443353	0.998563209	0.000173
0.19	0.428902	0.998683196	0.000183
0.2	0.414451	0.998791185	0.000193
0.21	0.4	0.998888889	0.000203
0.22	0.374194	0.99900782	0.000213
0.23	0.348387	0.99911641	0.000223
0.24	0.322581	0.99921595	0.000233
0.25	0.296774	0.999307527	0.000243
0.26	0.270968	0.99939206	0.000253
0.27	0.245161	0.999470331	0.000263
0.28	0.219355	0.999543011	0.000273
0.29	0.193548	0.999610679	0.000283
0.3	0.167742	0.999673835	0.000293
0.31	0.141935	0.999732917	0.000303
0.32	0.116129	0.999788306	0.000313
0.33	0.090323	0.999840339	0.000323
0.34	0.064516	0.999889311	0.000333
0.35	0.03871	0.999935484	0.000343
0.365	0	1	0.000358

Table 5.1 Summary of the surface free energy components of four solid surfaces. The liquids used in the tests were water (W), glycerin (G), toluene (T) and diiodomethane (D), the latter two being apolar liquids. T and D indicate apolar liquid used in the calculation. The two liquid method was used for graphene on copper.

mJ/m <sup>2</sup>	Liquid	$\gamma^d$	$\gamma^+$	$\gamma^-$	$\gamma^p$	$\gamma$
Si(111)	W.G.T	23.9±0.2	7.0±0.6	52.6±1.2	38.4±1.6	62.3±1.4
	W.G.D	38.0±0.2	3.05±0.4	48.7±0.6	24.4±0.5	62.4±0.9
G/Si(111)	W.G.T	24.4±0.2	5.4±0.4	6.4±0.4	11.6±0.2	36±0.1
G/Cu	W.G	21.4±0.9	X	X	12.5±0.4	33.9±0.6
HOPG	W.G.T	27.4±0.3	0±0.01	3.0±0.3	0.3±1.3	27.6±2.3

Table 6.1 Summary of key parameters for the traction-separation relations of graphene on silicon in each of the three experiments.

	Test 1	Test 2	Test 3	Average
$\sigma_0$ (MPa)	1.951	2.415	1.4	1.922±0.414
$\delta_n^0$ (nm)	19.84	25.9	81.01	42.25±33.7
$\delta_n^c$ (nm)	820	530	300	550±260
$\Gamma_{ss}$ (mJ/m <sup>2</sup> )	366±4	377±5	343±8	357±16



Table 6.2 The traction-separation relation parameters that were used in the finite element analysis of graphene/silicon interactions.

	<b>TSR1</b>	<b>TSR2</b>
$\sigma_0$ (MPa)	24	8
$\delta_n^0$ (nm)	2	2
$\delta_n^c$ (nm)	350	250
$\alpha$	25	5.5
$\Gamma_{ss}$ (mJ/m <sup>2</sup> )	358	360

Table 7.1 The effect of loading rate on the fracture path in the selective separation of graphene from copper or epoxy.

Loading Rate	< 25.4 $\mu\text{m/s}$	42.3 $\mu\text{m/s}$	84.6 $\mu\text{m/s}$	127 $\mu\text{m/s}$	169.3 $\mu\text{m/s}$	254 $\mu\text{m/s}$ >
Main Fracture Path	Epoxy/G	Mixed	Mixed	Mixed	G/Cu foil	G/Cu foil
Total Samples	6	1	1	1	4	35
Continuity of graphene film	0.5x4 cm (on Cu foil)				0.5x0.6 cm (on Epoxy)	0.5x1.6 cm (on epoxy)
Fracture mode	1	1	1		4	23
	2	1		1		
	3-1	4				4
	3-2	1				8

Table 7.2 Material properties of epoxy at different loading rates of 2 /s and 12 /s.

rate	$E$ (GPa)	$\nu$	$\sigma_y$ (MPa)	$\sigma_u$ (MPa)	$\epsilon_f$
2 $\mu\text{m/s}$	3.161	N/A	36.4	52.6	0.118
12 $\mu\text{m/s}$	2.963	N/A	46.1	59.6	0.061

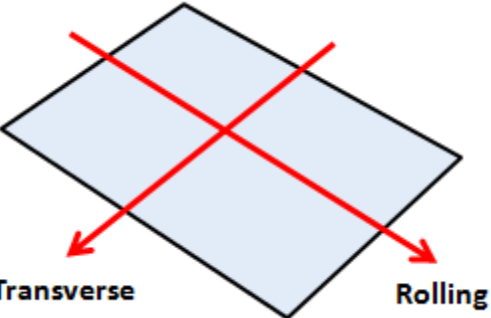
Table 7.3 Material properties and geometry of each material

	Young's Modulus (GPa)	Poisson's Ratio	Yield Strength (MPa)	Thickness ( $\mu\text{m}$ )	Size ( $\text{cm} \times \text{cm}$ )
Silicon	169	0.2	N/A	291 $\pm$ 5	0.5 $\times$ 4
Epoxy	3.0 $\pm$ 0.02	0.4	41.8 $\pm$ 2.9		
Graphene	$\sim$ 1000				0.5 $\times$ 4
Cu foil	110	0.33	23.3 $\pm$ 3.5	31.8 $\pm$ 4.8	0.5 $\times$ 4

Table 7.4 The values of the parameters associated with the traction-separation relations that were extracted by simulation.

Interaction Pair	TSR	$\Gamma_{ss}$ ( $\text{J}/\text{m}^2$ )	$\sigma_o$ (MPa)	$\delta_n^0$ ( $\mu\text{m}$ )	$\delta_n^c$ ( $\mu\text{m}$ )
Graphene/Cu	1	6	3	0.03	4
	2		0.5	0.005	24
Graphene/epoxy	1	3.4	1	0.01	6.8
	2		0.5	0.005	13.6

Table 7.5 The RMS roughness along the rolling and transverse directions of graphene on epoxy.

	RMS roughness ( $\mu\text{m}$ )	
Figure 7.28	Rolling Direction	Transverse Direction
a	0.444 $\pm$ 0.124	0.391 $\pm$ 0.187
b	1.226 $\pm$ 0.144	0.598 $\pm$ 0.049
c	0.566 $\pm$ 0.145	0.779 $\pm$ 0.071
d	0.262 $\pm$ 0.071	1.057 $\pm$ 0.147

## References

1. Feynman, R.P., *There's plenty of room at the bottom*. Engineering and science, 1960. **23**(5): p. 22-36.
2. Ulman, A., *Formation and structure of self-assembled monolayers*. Chemical reviews, 1996. **96**(4): p. 1533-1554.
3. Si, O., *An Introduction to SAMs: Self-Assembled Monolayers in Organic Chemistry*. 2001.
4. Linford, M.R. and C.E. Chidsey, *Alkyl monolayers covalently bonded to silicon surfaces*. Journal of the American Chemical Society, 1993. **115**(26): p. 12631-12632.
5. Sullivan, T.P. and W.T. Huck, *Reactions on monolayers: organic synthesis in two dimensions*. European Journal of Organic Chemistry, 2003. **2003**(1): p. 17-29.
6. Langner, A., et al., *Controlled silicon surface functionalization by alkene hydrosilylation*. Journal of the American Chemical Society, 2005. **127**(37): p. 12798-12799.
7. Wikipedia. *X-ray photoelectron spectroscopy*. wikipedia [Web Article]; Available from: [http://en.wikipedia.org/wiki/X-ray\\_photoelectron\\_spectroscopy](http://en.wikipedia.org/wiki/X-ray_photoelectron_spectroscopy).
8. Wang, M., et al., *Self-assembled silane monolayers: fabrication with nanoscale uniformity*. Langmuir, 2005. **21**(5): p. 1848-57.
9. Wikipedia. *Ellipsometry*. Wikipedia; Available from: <http://en.wikipedia.org/wiki/Ellipsometry>.
10. Inc., J.A.W.C., *Optical Constants*. 2014: p. [http://www.jawoollam.com/tutorial\\_7.html](http://www.jawoollam.com/tutorial_7.html).
11. Xiao, X., et al., *Chain length dependence of the frictional properties of alkylsilane molecules self-assembled on mica studied by atomic force microscopy*. Langmuir, 1996. **12**(2): p. 235-237.
12. Kim, H.I., et al., *Systematic studies of the frictional properties of fluorinated monolayers with atomic force microscopy: comparison of CF<sub>3</sub>-and CH<sub>3</sub>-terminated films*. Langmuir, 1997. **13**(26): p. 7192-7196.
13. Masuko, M., H. Miyamoto, and A. Suzuki, *Tribological characteristics of self-assembled monolayer with siloxane bonding to Si surface*. Tribology International, 2007. **40**(10): p. 1587-1596.
14. Hild, W., et al., *Microtribological properties of silicon and silicon coated with self-assembled monolayers: effect of applied load and sliding velocity*. Tribology Letters, 2007. **25**(1): p. 1-7.
15. Cui, B., J. Zhang, and J. Chen, *Tribological properties of poly (amide amine) and small molecule composite self-assembled monolayers: Influence of functional group of small molecule*. Tribology International, 2013. **62**: p. 149-154.
16. Carpick, R.W. and M. Salmeron, *Scratching the surface: fundamental investigations of tribology with atomic force microscopy*. Chemical Reviews, 1997. **97**(4): p. 1163-1194.

17. Zhuk, A.V., et al., *The adhesion energy between polymer thin films and self-assembled monolayers*. Journal of materials research, 1998. **13**(12): p. 3555-3564.
18. Tsukruk, V.V., I. Luzinov, and D. Julthongpiput, *Sticky molecular surfaces: epoxysilane self-assembled monolayers*. Langmuir, 1999. **15**(9): p. 3029-3032.
19. Burns, A., et al., *Molecular level friction as revealed with a novel scanning probe*. Langmuir, 1999. **15**(8): p. 2922-2930.
20. Maugis, D., *Adhesion of spheres: the JKR-DMT transition using a Dugdale model*. Journal of Colloid and Interface Science, 1992. **150**(1): p. 243-269.
21. Maugis, D. and B. Gauthier-Manuel, *JKR-DMT transition in the presence of a liquid meniscus*. Journal of adhesion science and technology, 1994. **8**(11): p. 1311-1322.
22. Gandhi, D.D., et al., *Annealing-induced interfacial toughening using a molecular nanolayer*. Nature, 2007. **447**(7142): p. 299-302.
23. Mello, A.W. and K.M. Liechti, *The effect of self-assembled monolayers on interfacial fracture*. Journal of applied mechanics, 2006. **73**(5): p. 860-870.
24. Swadener, J. and K. Liechti, *Asymmetric shielding mechanisms in the mixed-mode fracture of a glass/epoxy interface*. Journal of applied Mechanics, 1998. **65**(1): p. 25-29.
25. Swadener, J., K. Liechti, and A.d. Lozanne, *The intrinsic toughness and adhesion mechanisms of a glass/epoxy interface*. Journal of the Mechanics and Physics of Solids, 1999. **47**(2): p. 223-258.
26. Schmidt, M.A., *Wafer-to-wafer bonding for microstructure formation*. Proceedings of the IEEE, 1998. **86**(8): p. 1575-1585.
27. Plöbßl, A. and G. Kräuter, *Wafer direct bonding: tailoring adhesion between brittle materials*. Materials Science and Engineering: R: Reports, 1999. **25**(1): p. 1-88.
28. Christiansen, S.H., R. Singh, and U. Gosele, *Wafer direct bonding: From advanced substrate engineering to future applications in micro/nanoelectronics*. Proceedings of the IEEE, 2006. **94**(12): p. 2060-2106.
29. Bengtsson, S., K. Ljungberg, and J. Vedde, *The influence of wafer dimensions on the contact wave velocity in silicon wafer bonding*. Applied Physics Letters, 1996. **69**(22): p. 3381.
30. Rieutord, F., B. Bataillou, and H. Moriceau, *Dynamics of a bonding front*. Physical review letters, 2005. **94**(23): p. 236101.
31. Navarro, E., et al., *Direct silicon bonding dynamics: A coupled fluid/structure analysis*. Applied Physics Letters, 2013. **103**(3): p. 034104.
32. Martini, T., J. Steinkirchner, and U. Gösele, *The Crack Opening Method in Silicon Wafer Bonding How Useful Is It?* Journal of the Electrochemical Society, 1997. **144**(1): p. 354-357.
33. Tong, Q.Y., et al., *Low vacuum wafer bonding*. Electrochemical and solid-state letters, 1998. **1**(1): p. 52-53.

34. Miki, N. and S. Spearing, *Effect of nanoscale surface roughness on the bonding energy of direct-bonded silicon wafers*. Journal of applied physics, 2003. **94**(10): p. 6800-6806.
35. Turner, K.T. and S. Spearing, *Modeling of direct wafer bonding: effect of wafer bow and etch patterns*. Journal of Applied Physics, 2002. **92**(12): p. 7658-7666.
36. Turner, K.T., *Wafer bonding: mechanics-based models and experiments*. 2004, Massachusetts Institute of Technology.
37. Cole, D.J., et al., *Development of a classical force field for the oxidized Si surface: Application to hydrophilic wafer bonding*. The Journal of chemical physics, 2007. **127**(20): p. 204704.
38. Wang, J.-T., C. Chen, and Y. Kawazoe, *New carbon allotropes with helical chains of complementary chirality connected by ethene-type  $\pi$ -conjugation*. Scientific reports, 2013. **3**.
39. Delhaes, P., *Graphite and precursors*. Vol. 1. 2000: CRC Press.
40. Fecht, H.J. and K. Brühne, *Carbon-based Nanomaterials and Hybrids: Synthesis, Properties, and Commercial Applications*. 2014: CRC Press.
41. Wikipedia, *Amorphous carbon*. Wikipedia: p. [http://en.wikipedia.org/wiki/Amorphous\\_carbon](http://en.wikipedia.org/wiki/Amorphous_carbon).
42. Novoselov, K.S., et al., *Electric field effect in atomically thin carbon films*. science, 2004. **306**(5696): p. 666-669.
43. Novoselov, K., et al., *Two-dimensional gas of massless Dirac fermions in graphene*. nature, 2005. **438**(7065): p. 197-200.
44. Zhang, Y., et al., *Experimental observation of the quantum Hall effect and Berry's phase in graphene*. Nature, 2005. **438**(7065): p. 201-204.
45. Brodie, B.C., *On the atomic weight of graphite*. Philosophical Transactions of the Royal Society of London, 1859: p. 249-259.
46. May, J.W., *Platinum surface LEED rings*. Surface Science, 1969. **17**(1): p. 267-270.
47. Wikipedia, *Graphite oxide*. Wikipedia: p. [http://en.wikipedia.org/wiki/Graphite\\_oxide](http://en.wikipedia.org/wiki/Graphite_oxide).
48. Li, X., et al., *Transfer of large-area graphene films for high-performance transparent conductive electrodes*. Nano letters, 2009. **9**(12): p. 4359-4363.
49. Lee, Y.-H. and J.-H. Lee, *Scalable growth of free-standing graphene wafers with copper (Cu) catalyst on SiO<sub>2</sub>/Si substrate: Thermal conductivity of the wafers*. Applied Physics Letters, 2010. **96**(8): p. 083101.
50. Tao, L., et al., *Synthesis of high quality monolayer graphene at reduced temperature on hydrogen-enriched evaporated copper (111) films*. ACS nano, 2012. **6**(3): p. 2319-2325.
51. Kang, B.J., et al., *Monolayer graphene growth on sputtered thin film platinum*. Journal of Applied Physics, 2009. **106**(10): p. 104309.
52. Lahiri, J., et al., *Graphene growth on Ni (111) by transformation of a surface carbide*. Nano letters, 2010. **11**(2): p. 518-522.

53. Sun, J., et al., *Large-area uniform graphene-like thin films grown by chemical vapor deposition directly on silicon nitride*. Applied Physics Letters, 2011. **98**(25): p. 252107.
54. Lee, C., et al., *Measurement of the elastic properties and intrinsic strength of monolayer graphene*. science, 2008. **321**(5887): p. 385-388.
55. Kim, K., et al., *Grain boundary mapping in polycrystalline graphene*. ACS nano, 2011. **5**(3): p. 2142-2146.
56. Lee, G.-H., et al., *High-Strength Chemical-Vapor-Deposited Graphene and Grain Boundaries*. Science, 2013. **340**(6136): p. 1073-1076.
57. Zong, Z., et al., *Direct measurement of graphene adhesion on silicon surface by intercalation of nanoparticles*. Journal of Applied Physics, 2010. **107**(2): p. 026104-026104-3.
58. Koenig, S.P., et al., *Ultrastrong adhesion of graphene membranes*. Nature nanotechnology, 2011. **6**(9): p. 543-546.
59. Boddeti, N.G., et al., *Mechanics of Adhered, Pressurized Graphene Blisters*. Journal of Applied Mechanics, 2013. **80**(4): p. 040909.
60. Cao, Z., et al., *A blister test for interfacial adhesion of large-scale transferred graphene*. Carbon, 2014. **69**: p. 390-400.
61. Yoon, T., et al., *Direct measurement of adhesion energy of monolayer graphene as-grown on copper and its application to renewable transfer process*. Nano letters, 2012. **12**(3): p. 1448-1452.
62. Das, S., et al., *Measurements of the adhesion energy of graphene to metallic substrates*. Carbon, 2013. **59**: p. 121-129.
63. Das, S., et al., *Interfacial bonding characteristics between graphene and dielectric substrates*. Nanotechnology, 2014. **25**(4): p. 045707.
64. Li, Q., et al., *Substrate effect on thickness-dependent friction on graphene*. physica status solidi (b), 2010. **247**(11-12): p. 2909-2914.
65. Lee, C., et al., *Frictional characteristics of atomically thin sheets*. Science, 2010. **328**(5974): p. 76-80.
66. Kim, K.-S., et al., *Chemical vapor deposition-grown graphene: the thinnest solid lubricant*. ACS nano, 2011. **5**(6): p. 5107-5114.
67. Blake, P., et al., *Making graphene visible*. Applied Physics Letters, 2007. **91**: p. 063124.
68. Nair, R., et al., *Fine structure constant defines visual transparency of graphene*. Science, 2008. **320**(5881): p. 1308-1308.
69. Bunch, J.S., et al., *Impermeable atomic membranes from graphene sheets*. Nano letters, 2008. **8**(8): p. 2458-2462.
70. Stolyarova, E., et al., *Observation of graphene bubbles and effective mass transport under graphene films*. Nano letters, 2008. **9**(1): p. 332-337.
71. Chen, S., et al., *Oxidation resistance of graphene-coated Cu and Cu/Ni alloy*. ACS nano, 2011. **5**(2): p. 1321-1327.
72. Novoselov, K.S., et al., *Electric field effect in atomically thin carbon films*. Science, 2004. **306**(5696): p. 666-669.



73. Li, X.S., et al., *Large-area synthesis of high-quality and uniform graphene films on copper foils*. Science, 2009. **324**(5932): p. 1312-1314.
74. Li, X., et al., *Large-area graphene single crystals grown by low-pressure chemical vapor deposition of methane on copper*. Journal of the American Chemical Society, 2011. **133**(9): p. 2816-2819.
75. Li, X., et al., *Graphene Films with Large Domain Size by a Two-Step Chemical Vapor Deposition Process*. Nano Letters, 2010. **10**: p. 4328-4334.
76. Chen, S., et al., *Oxidation resistance of graphene-coated Cu and Cu/Ni alloy*. ACS Nano, 2011. **5**(2): p. 1321-1327.
77. *Commercial scale large-area graphene now available from Bluestone Global Tech in 24"x300" films*. 2013; Available from: <http://www.azonano.com/news.aspx?newsID=26553>.
78. Rupp, F., et al., *Enhancing surface free energy and hydrophilicity through chemical modification of microstructured titanium implant surfaces*. Journal of Biomedical Materials Research Part A, 2006. **76A**(2): p. 323-334.
79. Suk, J.W., et al., *Transfer of CVD-Grown Monolayer Graphene onto Arbitrary Substrates*. ACS Nano, 2011. **5**(9): p. 6916-6924.
80. Wang, Y., et al., *Electrochemical delamination of CVD-grown graphene film: toward the recyclable use of copper catalyst*. ACS nano, 2011. **5**(12): p. 9927-9933.
81. Dugdale, D., *Yielding of steel sheets containing slits*. Journal of the Mechanics and Physics of Solids, 1960. **8**(2): p. 100-104.
82. Barenblatt, G.I., *The mathematical theory of equilibrium cracks in brittle fracture*. Advances in applied mechanics, 1962. **7**(1): p. 55-129.
83. Hillerborg, A., M. Modéer, and P.-E. Petersson, *Analysis of crack formation and crack growth in concrete by means of fracture mechanics and finite elements*. Cement and concrete research, 1976. **6**(6): p. 773-781.
84. Ungsuwarungsri, T. and W.G. Knauss, *The role of damage-softened material behavior in the fracture of composites and adhesives*. International Journal of Fracture, 1987. **35**(3): p. 221-241.
85. Needleman, A., *A continuum model for void nucleation by inclusion debonding*. Journal of applied mechanics, 1987. **54**(3): p. 525-531.
86. Scheider, I., *Cohesive model for crack propagation analyses of structures with elastic-plastic material behavior Foundations and implementation*. GKSS research center, Geesthacht, 2001.
87. Elices, M., et al., *The cohesive zone model: advantages, limitations and challenges*. Engineering fracture mechanics, 2002. **69**(2): p. 137-163.
88. Li, S., et al., *Use of mode-I cohesive-zone models to describe the fracture of an adhesively-bonded polymer-matrix composite*. Composites Science and Technology, 2005. **65**(2): p. 281-293.
89. Alfano, G., *On the influence of the shape of the interface law on the application of cohesive-zone models*. Composites Science and Technology, 2006. **66**(6): p. 723-730.

90. Li, S., et al., *Mixed-mode cohesive-zone models for fracture of an adhesively bonded polymer–matrix composite*. Engineering Fracture Mechanics, 2006. **73**(1): p. 64-78.
91. Pohlitz II, D.J., *Dynamic mixed-mode fracture of bonded composite joints for automotive crashworthiness*. 2007, Virginia Polytechnic Institute and State University.
92. Song, K., C.G. Davila, and C.A. Rose. *Guidelines and parameter selection for the simulation of progressive delamination*. in *abaqus User's Conference, Newport, Rhode Island (Hibbit Karlsson and Sorensen, USA, 2008)*. 2008.
93. De Moura, M., R. Campilho, and J. Goncalves, *Mixed-mode cohesive damage model applied to the simulation of the mechanical behaviour of laminated composite adhesive joints*. Journal of Adhesion Science and Technology, 2009. **23**(10-11): p. 1477-1491.
94. Ridha, M., V. Tan, and T. Tay, *Traction–separation laws for progressive failure of bonded scarf repair of composite panel*. Composite structures, 2011. **93**(4): p. 1239-1245.
95. Stutz, S., J. Cugnoni, and J. Botsis, *Studies of mode I delamination in monotonic and fatigue loading using FBG wavelength multiplexing and numerical analysis*. Composites Science and Technology, 2011. **71**(4): p. 443-449.
96. Needleman, A., *An Analysis of Tensile Decohesion Along an Interface*. Journal of the Mechanics and Physics of Solids, 1990. **38**(3): p. 289-324.
97. Tvergaard, V. and J. Hutchinson, *Effect of strain-dependent cohesive zone model on predictions of crack growth resistance*. International Journal of Solids and Structures, 1996. **33**(20): p. 3297-3308.
98. Geubelle, P.H. and J.S. Baylor, *Impact-induced delamination of composites: a 2D simulation*. Composites Part B: Engineering, 1998. **29**(5): p. 589-602.
99. Na, S.R., et al., *Ultra Long-Range Interactions between Large Area Graphene and Silicon*. ACS nano, 2014.
100. Stigh, U. and T. Andersson, *An experimental method to determine the complete stress-elongation relation for a structural adhesive layer loaded in peel*. European Structural Integrity Society, 2000. **27**: p. 297-306.
101. Sørensen, B.F. and T.K. Jacobsen, *Determination of cohesive laws by the  $\int J$  integral approach*. Engineering fracture mechanics, 2003. **70**(14): p. 1841-1858.
102. Sørensen, B.F. and P. Kirkegaard, *Determination of mixed mode cohesive laws*. Engineering fracture mechanics, 2006. **73**(17): p. 2642-2661.
103. Högberg, J.L., B.F. Sørensen, and U. Stigh, *Constitutive behaviour of mixed mode loaded adhesive layer*. International Journal of Solids and Structures, 2007. **44**(25): p. 8335-8354.
104. Lundsgaard-Larsen, C., et al., *A modified DCB sandwich specimen for measuring mixed-mode cohesive laws*. Engineering Fracture Mechanics, 2008. **75**(8): p. 2514-2530.

105. Sørensen, B.F. and T.K. Jacobsen, *Characterizing delamination of fibre composites by mixed mode cohesive laws*. Composites science and technology, 2009. **69**(3): p. 445-456.
106. Gowrishankar, S., et al., *A comparison of direct and iterative methods for determining traction-separation relations*. International Journal of Fracture, 2012. **177**(2): p. 109-128.
107. Liechti, K.M., et al., *A High Vacuum Fracture Facility for Molecular Interactions*. Experimental Mechanics, 2013. **53**(2): p. 231-241.
108. Gowrishankar, S., *Characterization of Delamination in Silicon/Epoxy Systems*. 2014, University of Texas: Austin, Tex.
109. Na, S.R., et al., *Selective Mechanical Transfer of Graphene from Seed Copper Foil Using Rate Effects*. ACS Nano, 2015.
110. S. R. Na, J.W.S., Rodney S. Ruoff, Rui Huang, Kenneth M. Liechti, *Ultra Long-Range Interactions between Large Area Graphene and Silicon*. ACS Nano, 2014.
111. Binggeli, M. and C. Mate, *Influence of capillary condensation of water on nanotribology studied by force microscopy*. Applied physics letters, 1994. **65**(4): p. 415-417.
112. Binggeli, M., *Influence of water vapor on nanotribology studied by friction force microscopy*. Journal of Vacuum Science & Technology B: Microelectronics and Nanometer Structures, 1995. **13**(3): p. 1312.
113. Thomas, R.C., et al., *Probing adhesion forces at the molecular scale*. Journal of the American Chemical Society, 1995. **117**(13): p. 3830-3834.
114. Wakamatsu, M., *Fracture at the Molecular Level*. 2008, University of Texas at Austin.
115. Wortman, J. and R. Evans, *Young's modulus, shear modulus, and Poisson's ratio in silicon and germanium*. Journal of applied physics, 1965. **36**(1): p. 153-156.
116. Kim, J., D. Cho, and R.S. Muller. *Why is (111) silicon a better mechanical material for MEMS*. in *Transducers*. 2001.
117. Higashi, G.S., et al., *Ideal hydrogen termination of the Si (111) surface*. Applied Physics Letters, 1990. **56**(7): p. 656.
118. Higashi, G., et al., *Comparison of Si (111) surfaces prepared using aqueous solutions of NH<sub>4</sub>F versus HF*. Applied physics letters, 1991. **58**(15): p. 1656-1658.
119. Wikipedia, *Hydrofluoric acid*. p. [http://en.wikipedia.org/wiki/Hydrofluoric\\_acid](http://en.wikipedia.org/wiki/Hydrofluoric_acid).
120. Ciampi, S., J.B. Harper, and J.J. Gooding, *Wet chemical routes to the assembly of organic monolayers on silicon surfaces via the formation of Si-C bonds: Surface preparation, passivation and functionalization*. Chemical Society Reviews, 2010. **39**(6): p. 2158-2183.
121. Burrows, V., et al., *Infrared spectroscopy of Si (111) surfaces after HF treatment: Hydrogen termination and surface morphology*. Applied physics letters, 1988. **53**(11): p. 998-1000.
122. Hsiao, G.S., J.A. Virtanen, and R.M. Penner, *Scanning tunneling microscopy investigations of the Si (111) topography produced by etching in 40% NH<sub>4</sub>F*:

- observation of an optimum etch duration*. Applied physics letters, 1993. **63**(8): p. 1119-1121.
123. Li, X., et al., *Large-area synthesis of high-quality and uniform graphene films on copper foils*. Science, 2009. **324**(5932): p. 1312-1314.
  124. Suk, J.W., *Fabrication and mechanical characterization of graphene based membranes and their use in thermoacoustics*. 2011, University of Texas: Austin, Tex. p. 1 online resource (xx, 127 leaves).
  125. Zhang, B., et al., *Low-temperature chemical vapor deposition growth of graphene from toluene on electropolished copper foils*. ACS nano, 2012. **6**(3): p. 2471-2476.
  126. Magnuson, C.W., et al., *Copper oxide as a “self-cleaning” substrate for graphene growth*. Journal of Materials Research, 2014. **29**(03): p. 403-409.
  127. Suk, J.W., *Fabrication and mechanical characterization of graphene based membranes and their use in thermoacoustics*. 2012.
  128. Suk, J.W., et al., *Enhancement of the electrical properties of graphene grown by chemical vapor deposition via controlling the effects of polymer residue*. Nano letters, 2013. **13**(4): p. 1462-1467.
  129. Wikipedia. *AFM*. Wikipedia [Web Article]; Available from: [http://en.wikipedia.org/wiki/Scanning\\_electrochemical\\_microscopy](http://en.wikipedia.org/wiki/Scanning_electrochemical_microscopy).
  130. Co., J.A.W. *Ellipsometry FAQ*. [Web Article]; Available from: <http://www.jawoollam.com/faq.html>.
  131. Porter, M.D., et al., *Spontaneously organized molecular assemblies. 4. Structural characterization of n-alkyl thiol monolayers on gold by optical ellipsometry, infrared spectroscopy, and electrochemistry*. Journal of the American Chemical Society, 1987. **109**(12): p. 3559-3568.
  132. Lee, S., et al., *The influence of packing densities and surface order on the frictional properties of alkanethiol self-assembled monolayers (SAMs) on gold: a comparison of SAMs derived from normal and spiroalkanedithiols*. Langmuir, 2000. **16**(5): p. 2220-2224.
  133. Wang, Y.y., et al., *Raman studies of monolayer graphene: the substrate effect*. The Journal of Physical Chemistry C, 2008. **112**(29): p. 10637-10640.
  134. Malard, L., et al., *Raman spectroscopy in graphene*. Physics Reports, 2009. **473**(5): p. 51-87.
  135. Saito, R., et al., *Raman spectroscopy of graphene and carbon nanotubes*. Advances in Physics, 2011. **60**(3): p. 413-550.
  136. He, R., et al., *Large physisorption strain in chemical vapor deposition of graphene on copper substrates*. Nano letters, 2012. **12**(5): p. 2408-2413.
  137. Ferrari, A.C. and D.M. Basko, *Raman spectroscopy as a versatile tool for studying the properties of graphene*. Nature nanotechnology, 2013. **8**(4): p. 235-246.
  138. Tuinstra, F. and J.L. Koenig, *Raman spectrum of graphite*. The Journal of Chemical Physics, 1970. **53**(3): p. 1126-1130.

139. Ferrari, A., et al., *Raman spectrum of graphene and graphene layers*. Physical review letters, 2006. **97**(18): p. 187401.
140. al, Y.y.W.e., *Raman Studies of Monolayer Graphene: The Substrate Effect*. 2008.
141. Ni, Z.H., et al., *Uniaxial strain on graphene: Raman spectroscopy study and band-gap opening*. ACS nano, 2008. **2**(11): p. 2301-2305.
142. Spizzirri, P., et al., *Nano-Raman spectroscopy of silicon surfaces*. arXiv preprint arXiv:1002.2692, 2010.
143. Frank, O., et al., *Raman 2D-band splitting in graphene: theory and experiment*. Acs Nano, 2011. **5**(3): p. 2231-2239.
144. Zabel, J., et al., *Raman spectroscopy of graphene and bilayer under biaxial strain: bubbles and balloons*. Nano letters, 2012. **12**(2): p. 617-621.
145. Tong, Q.Y., et al., *The role of surface chemistry in bonding of standard silicon wafers*. Journal of The Electrochemical Society, 1997. **144**(1): p. 384-389.
146. Ventosa, C., et al., *Hydrophilic low-temperature direct wafer bonding*. Journal of Applied Physics, 2008. **104**(12): p. 123524.
147. Fowlkes, C.W., *Crack opening interferometry—The effects of optical refraction*. Engineering Fracture Mechanics, 1975. **7**(4): p. 689-692.
148. Liechti, K.M., *On the use of classical interferometry techniques in fracture mechanics*. Experimental techniques in fracture, 1993: p. 95-124.
149. Liang, Y.-M. and K. Liechti, *Toughening mechanisms in mixed-mode interfacial fracture*. International journal of solids and structures, 1995. **32**(6): p. 957-978.
150. Brantley, W., *Calculated elastic constants for stress problems associated with semiconductor devices*. Journal of Applied Physics, 1973. **44**(1): p. 534-535.
151. Dolbow, J. and M. Gosz, *Effect of out-of-plane properties of a polyimide film on the stress fields in microelectronic structures*. Mechanics of materials, 1996. **23**(4): p. 311-321.
152. Hopcroft, M.A., W.D. Nix, and T.W. Kenny, *What is the Young's Modulus of Silicon?* Microelectromechanical Systems, Journal of, 2010. **19**(2): p. 229-238.
153. Hutchinson, J.W. and Z. Suo, *Mixed mode cracking in layered materials*. Advances in applied mechanics, 1991. **29**: p. 63-191.
154. Martinez, N., *Wettability of silicon, silicon dioxide, and organosilicate glass*. 2009, University Of North Texas.
155. Chehimi, M.M., A. Azioune, and E. Cabet-Deliry, *Acid-Base Interactions: Relevance to Adhesion and Adhesive Bonding*. Handbook of Adhesive Technology, 2003: p. 95.
156. Israelachvili, J.N., *Intermolecular and surface forces: revised third edition*. 2011: Academic press.
157. Fowkes, F.M., *Attractive forces at interfaces*. Industrial & Engineering Chemistry, 1964. **56**(12): p. 40-52.
158. Van Oss, C., R. Good, and M. Chaudhury, *Additive and nonadditive surface tension components and the interpretation of contact angles*. Langmuir, 1988. **4**(4): p. 884-891.

159. Na, S.R., et al., *Ultra Long-Range Interactions between Large Area Graphene and Silicon*. ACS nano, 2014. **8**(11): p. 11234-11242.
160. Strother, T., et al., *Synthesis and characterization of DNA-modified silicon (111) surfaces*. Journal of the American Chemical Society, 2000. **122**(6): p. 1205-1209.
161. Godawat, R., S.N. Jamadagni, and S. Garde, *Characterizing hydrophobicity of interfaces by using cavity formation, solute binding, and water correlations*. Proceedings of the National Academy of Sciences, 2009. **106**(36): p. 15119-15124.
162. Brown, W.F., C. Iverson, B., *Organic Chemistry . Fourth Edition. Belmont, CA. (2005)*.
163. Liechti, K. and Y. Chai, *Asymmetric shielding in interfacial fracture under in-plane shear*. Journal of Applied Mechanics, 1992. **59**(2): p. 295-304.
164. Evans, A.G. and J.W. Hutchinson, *Effects of non-planarity on the mixed mode fracture resistance of bimaterial interfaces*. Acta Metallurgica, 1989. **37**(3): p. 909-916.
165. Tirosh, E., et al., *Direct monitoring of opto-mechanical switching of self-assembled monolayer films containing the azobenzene group*. Beilstein journal of nanotechnology, 2011. **2**(1): p. 834-844.
166. Zhang, T., H. Wang, and Y. Hu, *Atomic stick-slip friction between commensurate self-assembled monolayers*. Tribology Letters, 2003. **14**(2): p. 69-76.
167. Wang, H., Y.-Z. Hu, and T. Zhang, *Simulations on atomic-scale friction between self-assembled monolayers: Phononic energy dissipation*. Tribology international, 2007. **40**(4): p. 680-686.
168. Aureau, D., et al., *The titration of carboxyl-terminated monolayers revisited: In situ calibrated Fourier transform infrared study of well-defined monolayers on silicon*. Langmuir, 2008. **24**(17): p. 9440-9448.
169. Moraillon, A., et al., *Amidation of monolayers on silicon in physiological buffers: A quantitative IR study*. The Journal of Physical Chemistry C, 2008. **112**(18): p. 7158-7167.
170. Tong, Q.Y., et al., *Hydrophobic silicon wafer bonding*. Applied physics letters, 1994. **64**(5): p. 625-627.
171. Gösele, U., et al., *What determines the lateral bonding speed in silicon wafer bonding?* Applied Physics Letters, 1995. **67**(6): p. 863.
172. Gösele, U., et al., *Self-propagating room-temperature silicon wafer bonding in ultrahigh vacuum*. Applied physics letters, 1995. **67**(24): p. 3614-3616.
173. Suni, T., et al., *Effects of plasma activation on hydrophilic bonding of Si and SiO<sub>2</sub>*. Journal of the Electrochemical Society, 2002. **149**(6): p. G348-G351.
174. Tong, Q.-Y., et al., *Fluorine-enhanced low-temperature wafer bonding of native-oxide covered Si wafers*. Applied physics letters, 2004. **85**(17): p. 3731-3733.
175. Naumenko, V. and Y.D. Skrypnik. *Steady-state measurement of the interface fracture resistance in wafer bonding*. in *ECF15, Stockholm 2004*. 2013.
176. Masteika, V., et al., *A review of hydrophilic silicon wafer bonding*. ECS Journal of Solid State Science and Technology, 2014. **3**(4): p. Q42-Q54.

177. Horn, G., T. Mackin, and J. Lesniak, *Residual Stresses from Interface Defects in Wafer Bonded Silicon*.
178. Majumdar, A. and I. Mezić, *Instability of ultra-thin water films and the mechanism of droplet formation on hydrophilic surfaces*. Journal of heat transfer, 1999. **121**(4): p. 964-971.
179. Sander, D. and H. Ibach, *Experimental determination of adsorbate-induced surface stress: oxygen on Si (111) and Si (100)*. Physical Review B, 1991. **43**(5): p. 4263.
180. Leplan, H., J. Robic, and Y. Pauleau, *Kinetics of residual stress evolution in evaporated silicon dioxide films exposed to room air*. Journal of applied physics, 1996. **79**(9): p. 6926-6931.
181. Colombi Ciacchi, L., et al., *Stress-driven oxidation chemistry of wet silicon surfaces*. The Journal of Physical Chemistry C, 2008. **112**(32): p. 12077-12080.
182. Sabio, J., et al., *Electrostatic interactions between graphene layers and their environment*. Physical Review B, 2008. **77**(19): p. 195409.
183. Pallares, G., et al., *Quantitative Analysis of Crack Closure Driven by Laplace Pressure in Silica Glass*. Journal of the American Ceramic Society, 2011. **94**(8): p. 2613-2618.
184. Wang, M., et al., *Self-assembled silane monolayers: fabrication with nanoscale uniformity*. Langmuir, 2005. **21**(5): p. 1848-1857.
185. Weeks, B.L., M.W. Vaughn, and J.J. DeYoreo, *Direct imaging of meniscus formation in atomic force microscopy using environmental scanning electron microscopy*. Langmuir, 2005. **21**(18): p. 8096-8098.
186. Sirghi, L., R. Szoszkiewicz, and E. Riedo, *Volume of a nanoscale water bridge*. Langmuir, 2006. **22**(3): p. 1093-1098.
187. Bäcklund, Y., K. Hermansson, and L. Smith, *Bond-Strength Measurements Related to Silicon Surface Hydrophilicity*. Journal of the Electrochemical Society, 1992. **139**(8): p. 2299-2301.
188. Legtenberg, R., et al., *Stiction of surface micromachined structures after rinsing and drying: model and investigation of adhesion mechanisms*. Sensors and Actuators A: Physical, 1994. **43**(1): p. 230-238.
189. Rafiee, J., et al., *Wetting transparency of graphene*. Nature Materials, 2012. **11**(3): p. 217-222.
190. Taherian, F., et al., *What is the contact angle of water on graphene?* Langmuir, 2013. **29**(5): p. 1457-1465.
191. Shih, C.-J., et al., *Breakdown in the wetting transparency of graphene*. Physical review letters, 2012. **109**(17): p. 176101.
192. Raj, R., S.C. Maroo, and E.N. Wang, *Wettability of graphene*. Nano letters, 2013. **13**(4): p. 1509-1515.
193. Liechti, K., S. Schnapp, and J. Swadener, *Contact angle and contact mechanics of a glass/epoxy interface*. International journal of fracture, 1997. **86**(4): p. 361-374.
194. Wang, S., et al., *Wettability and surface free energy of graphene films*. Langmuir, 2009. **25**(18): p. 11078-11081.

195. Sirghi, L., et al., *Cleaning and hydrophilization of atomic force microscopy silicon probes*. The Journal of Physical Chemistry B, 2006. **110**(51): p. 25975-25981.
196. Sato, N. and Y. Shimogaki, *Adsorption Model of Organic Molecules on the Surface of Thermally Oxidized Silicon*. ECS Journal of Solid State Science and Technology, 2012. **1**(4): p. N61-N66.
197. Kozbial, A., et al., *Understanding the intrinsic water wettability of graphite*. Carbon, 2014. **74**: p. 218-225.
198. Schrader, M.E., *Ultrahigh vacuum techniques in the measurement of contact angles. III. Water on copper and silver*. The Journal of Physical Chemistry, 1974. **78**(1): p. 87-89.
199. Li, Z., et al., *Effect of airborne contaminants on the wettability of supported graphene and graphite*. Nature Materials, 2013. **12**(10): p. 925-931.
200. Pirkle, A., et al., *The effect of chemical residues on the physical and electrical properties of chemical vapor deposited graphene transferred to SiO<sub>2</sub>*. Applied Physics Letters, 2011. **99**(12): p. 122108-122108-3.
201. Lin, Y.-C., et al., *Graphene annealing: how clean can it be?* Nano letters, 2011. **12**(1): p. 414-419.
202. Gutfreund, P., et al., *Depletion at solid/liquid interfaces: Flowing hexadecane on functionalized surfaces*. The Journal of chemical physics, 2011. **134**(6): p. 064711.
203. Opitz, A., et al., *A comparative investigation of thickness measurements of ultra-thin water films by scanning probe techniques*. Journal of applied physics, 2007. **101**(6): p. 064310.
204. Li, D. and A. Neumann, *Contact angles on hydrophobic solid surfaces and their interpretation*. Journal of colloid and interface science, 1992. **148**(1): p. 190-200.
205. Li, D. and A. Neumann, *Equilibrium of capillary systems with an elastic liquid-vapor interface*. Langmuir, 1993. **9**(1): p. 50-54.
206. Rupp, F., et al., *Enhancing surface free energy and hydrophilicity through chemical modification of microstructured titanium implant surfaces*. Journal of Biomedical Materials Research Part A, 2006. **76**(2): p. 323-334.
207. Kozbial, A., et al., *Study on the surface energy of graphene by contact angle measurements*. Langmuir, 2014. **30**(28): p. 8598-8606.
208. Zong, Z., et al., *Direct measurement of graphene adhesion on silicon surface by intercalation of nanoparticles*. Journal of Applied Physics, 2010. **107**(2): p. 026104.
209. Boddeti, N.G., et al., *Mechanics of Adhered, Pressurized Graphene Blisters*. arXiv preprint arXiv:1304.1011, 2013.
210. Fan, X., et al., *Interaction between graphene and the surface of SiO<sub>2</sub>*. Journal of Physics: Condensed Matter, 2012. **24**(30): p. 305004.
211. Gao, W., et al., *Interfacial adhesion between graphene and silicon dioxide by density functional theory with van der Waals corrections*. arXiv preprint arXiv:1403.3751, 2014.



212. Paek, E. and G.S. Hwang, *A computational analysis of graphene adhesion on amorphous silica*. Journal of Applied Physics, 2013. **113**(16): p. 164901.
213. Obreimoff, J., *The splitting strength of mica*. Proceedings of the Royal Society of London. Series A, Containing Papers of a Mathematical and Physical Character, 1930. **127**(805): p. 290-297.
214. Gowrishankar, S., *Characterization of Delamination in Silicon/Epoxy Systems*. 2013, University of Texas: Austin, Tex.
215. DelRio, F.W., et al., *The role of van der Waals forces in adhesion of micromachined surfaces*. Nature materials, 2005. **4**(8): p. 629-634.
216. DelRio, F.W., et al., *Rough surface adhesion in the presence of capillary condensation*. Applied physics letters, 2007. **90**(16): p. 163104.
217. DelRio, F.W., M.L. Dunn, and M.P. de Boer, *Capillary adhesion model for contacting micromachined surfaces*. Scripta Materialia, 2008. **59**(9): p. 916-920.
218. Bae, S., et al., *Roll-to-roll production of 30-inch graphene films for transparent electrodes*. Nature nanotechnology, 2010. **5**(8): p. 574-578.
219. Wang, X., et al., *Direct Delamination of Graphene for High-Performance Plastic Electronics*. Small, 2014. **10**(4): p. 694-698.
220. Kanninen, M., *An augmented double cantilever beam model for studying crack propagation and arrest*. International Journal of Fracture, 1973. **9**(1): p. 83-92.
221. Frank, O., et al., *Interaction between graphene and copper substrate: The role of lattice orientation*. Carbon, 2014. **68**: p. 440-451.
222. Lee, J.U., D. Yoon, and H. Cheong, *Estimation of Young's modulus of graphene by Raman spectroscopy*. Nano Lett, 2012. **12**(9): p. 4444-8.
223. Lee, J.-U., D. Yoon, and H. Cheong, *Estimation of Young's modulus of graphene by Raman spectroscopy*. Nano letters, 2012. **12**(9): p. 4444-4448.
224. Kanninen, M.F. and C.L. Popelar, *Advanced fracture mechanics*. 1985.
225. Zhang, P., et al., *Fracture toughness of graphene*. Nature communications, 2014. **5**.
226. Hall, E., *The deformation and ageing of mild steel: III discussion of results*. Proceedings of the Physical Society. Section B, 1951. **64**(9): p. 747.
227. Petch, N., *The cleavage strength of polycrystals*. J. Iron Steel Inst., 1953. **174**: p. 25-28.
228. Meyers, M.A. and K.K. Chawla, *Mechanical behavior of materials*. Vol. 547. 2009: Cambridge University Press Cambridge.
229. Mohammed, I. and K.M. Liechti, *Cohesive zone modeling of crack nucleation at bimaterial corners*. Journal of the Mechanics and Physics of Solids, 2000. **48**(4): p. 735-764.
230. Chaudhury, M.K., *Rate-dependent fracture at adhesive interface*. The Journal of Physical Chemistry B, 1999. **103**(31): p. 6562-6566.
231. Lee, K.J., et al., *Large-Area, Selective Transfer of Microstructured Silicon: A Printing-Based Approach to High-Performance Thin-Film Transistors Supported on Flexible Substrates*. Advanced Materials, 2005. **17**(19): p. 2332-2336.

232. Meitl, M.A., et al., *Transfer printing by kinetic control of adhesion to an elastomeric stamp*. Nature Materials, 2005. **5**(1): p. 33-38.
233. Feng, X., et al., *Competing fracture in kinetically controlled transfer printing*. Langmuir, 2007. **23**(25): p. 12555-12560.
234. Sharpe, L.H., *The interphase in adhesion*. The Journal of Adhesion, 1972. **4**(1): p. 51-64.
235. Yoon, T., *Adhesion Energy Measurement and Interfacial Reliability Evaluation*. MS Thesis, KAIST Korea, 2013.
236. Lilliestråle, J.C.Å., *Structural properties of Ge doped multicrystalline Silicon wafers and Solar cells*. 2012.

## **Vita**

Na, Seung Ryul was born in Seoul, Republic of Korea in 1976. He received his B.S. and M.S degree in the Department of Mechanical Engineering from Chung-Ang University and KAIST in 2002 and 2004, respectively. His research during his M.S. degree was associated with plasticity and crash analysis using the commercial finite element codes, LS-Dyna 3D and ABAQUS. After graduating with his M.S. degree, he joined Samsung Electronics Ltd. for four and a half years as a FEM engineer and system designer. During this period, he expanded his interests to thin film mechanics and FEM simulations of cracks in the semiconductor industry. Following his industrial experience, he joined the Engineering Mechanics Ph.D. program in the Department of Aerospace and Engineering Mechanics at the University of Texas at Austin, and joined Liechti's group studying the adhesion properties of self-assembled monolayers (SAMs). During this period, his research covered not only SAMs but also other 2-dimensional materials such as graphene and others. His research focused on the adhesion properties of 2-dimensional materials and their applications. He will now continue this work as a postdoctoral researcher with Professor Liechti.

Email:Seungryul.na@gmail.com

This dissertation was typed by Seung Ryul Na.